High performance sailplane airbrake analysis using CFD

T. Potgieter

orcid.org/0000-0002-0972-676X

Dissertation accepted in fulfilment of the requirements for the degree *Master of Engineering* in Mechanical Engineering at the North-West University

Supervisor:	Dr J.J. Bosman
Graduation:	July - August 2023
Student number:	24212423

Acknowledgements

Firstly and most importantly, I would like to thank the Almighty and living God for the blessings and opportunities He has given me.

I would also like to thank the following people for their contributions to completing my study; Dr. J.J. Bosman and Mr L. le Grange for their support. Prof A. Jonker for the financial backing, and to Mr. M. Pekar for the wind tunnel data used in this study.

To my family, mother Marietjie, father Gerhard and brother Marco, together with my love and best friend Melissa, for their continuous support, love, patience and prayers. I would like to thank my friends, Peet and Ariane, among others, for their tough love and support.

Lastly, I want to thank Heinrich Huyser for his patience and understanding during my studies, as well as all the unnamed people who in any way contributed to the completion of this study. There are numerous of them, each playing a part.

Thank you all.

Abstract

Sailplane airbrakes are an essential part of sailplane control and safety. So much so that EASA, (European Aviation Safety Agency) has specific regulations specifically aimed at sailplane airbrake design. For sailplanes to be competitive, the latest in simulation software and techniques are required to design on the cutting edge of what is allowed. This is especially important in the airbrake design as flow over airbrakes is notoriously difficult to predict, leading to larger design margins and loss of performance gains.

The aim of this study is to focus on a methodology to achieve accurate, reliable and efficient CFD results, in particular for use during the concept design phase of sailplane aerodynamics. An overall strategy of starting simple and incrementally increasing the complexity was followed to achieve this.

The study started by using simple geometries and worked up to more complex geometries, such as the airbrakes. Generally, the methodology was to run mesh refinement studies as well refining meshes in crucial regions of high flow gradients in conjunction with time step and inner iteration independent studies. Once these simulations were completed, validations were done using CFD or wind tunnel data as a reference.

This methodology was first applied to unsteady flow over three cylinder cases. Two circular cylinders at Re $= 200$ and Re $= 3.6 \times 10^6$ and a square cylinder at Re $= 2.2 \times 10^4$. Secondly, validation simulations were done on two airfoils using wind tunnel data as a reference. These two airfoils are the FX66-17AII-182 and HPH yn1. Both airfoils are used in sailplane applications, making them suitable for this study. Thirdly the methodology was applied to the two airfoils with airbrakes extended.

A good correlation was achieved with the cylinder validation studies and the two FX66 airfoil and airbrake validations. Even though the simulations were only 2D, expected flow characteristics such as vortex shedding and recirculation were simulated and captured. The simulations on the HPH airfoil and airbrake cases did not give such good results and required further investigation. These investigations were done on various other constitutive options and the effects modifying the shear stress limiter and realizability coefficients in the $k - \omega$ SST model had on the simulation results. In addition to using more complex turbulence solvers, such as RST and Lag EB $k - \epsilon$, various techniques were studied that were especially used on anisotropic flows, such as recirculation, separation and vortex shedding.

The clean HPH airfoil force coefficients correlated well with the wind tunnel results in the linear range (AOA -6° up to 5°), after which the results deviated from that of the wind tunnel. None of these additionally investigated parameters increased the simulation accuracy of the clean airfoil from 8° nor the accuracy of the airfoil and airbrake configuration results.

Keywords: URANS; Unsteady flow; CFD; Vortex shedding; Sailplane airbrakes; Flow separation; Anisotropic flows; Recirculation

Contents

List of Figures

List of Tables

Table of abbreviations

A table containing a list of abbreviations that will be used throughout text.

2D	Two dimensional
3D	Three dimensional
AOA	Angle of attack
AR	Aspect Ratio
BS	Base size [m]
BSL	Baseline $k - \omega$ model
C	Airfoil chord [m]
CFD	Computational Fluid Dynamics
CFL	Courant–Friedrichs–Lewy
CS	Custom size [-]
DES	Direct Eddy Simulations
DNS	Direct Numerical Simulation
EARSM	Explicit Algebraic Reynolds Stress Model
EASA	European Aviation Safety Agency
EB	Elliptical Blending
GCI	Grid Convergence Index
II	Inner Iteration
JL	Jones-Launder
L/D	Lift to drag ratio
LE	Leading edge
LES	Large Eddy Simulation
PL	Prism layer
PSD	Power Spectral Density [s]
QCR	Quadratic constitutive option
RANS	Reynolds - Averaged Navier - Stokes
Re	Reynolds number
RST	Reynolds stress transport model
SF	Stretch Factor
SS	Surface size
SST	Shear stress transport
TE	Trailing edge
TKE	Turbulent Kinetic Energy [J/kg]

Nomenclature

A table containing a list of symbols that will be used throughout text.

a_1	Shear stress limiter[-]
c	Speed of sound through air [m/s]
C_L	3D Lift coefficient [-]
C_l	2D Lift coefficient [-]
C_D	3D Drag coefficient [-]
C_d	2D Drag coefficient [-]
C_p	Pressure coefficient [-]
C_T	Realizability coefficient [-]
D	Drag [N]
D_{cyl}	Cylinder diameter [m]
Δ_h	Element length in direction of flow [m]
Δ_x	Representative mesh spacing [-]
δ	Boundary layer thickness [m]
F_s	Relaxation factor [-]
f_1	Fine-grid numerical solution [-]
f_2	Coarse-grid numerical solution [-]
f_{vs}	Vortex shedding frequency [Hz]
$\gamma - Re\Theta$	Gamma - ReTheta
l	Characteristic length [m]
n_{total}	Total number of mesh elements [-]
PL_{NOC}	Number of prism layer cells
PL_T	Prism layer thickness [m]
R_{cyl}	Cylinder radius [m]
ρ	Fluid density [kg/m^3]
r	Refinement factor [-]
μ	Dynamic viscosity [Pa s]
S	Characteristic area [(m^2)]
V	Fluid velocity [m/s]
ν	Kinematic viscosity [m ^{2} / s]
y	Normal distance from surface [m]
u_τ	Wall friction velocity
τ_w	Wall shear stress [-]
σ	Courant number [-]

Chapter 1

Introduction

1.1 Background

Sailplanes, also called gliders, are unpowered aircraft used in leisure activities or competitive sporting events. The main difference between sailplanes and conventional aircraft is that sailplanes do not produce their own sustained thrust during flight. Some models contain sustainers that allow a short burst of thrust at the pilot's discretion.

Only three forces are acting on a sailplane as opposed to the four forces acting on conventional powered aeroplanes. Both aircraft are subjected to lift, drag and weight. Powered aircraft, on the other hand, uses thrust to negate the effects of drag where sailplanes cannot.

Sailplanes depend on converting potential energy into kinetic energy for forward movement [13]. Sailplanes gain potential energy in two main ways: at launch, when they are towed into the air by a tug plane or winch launched, and during flight, by using thermals that produce updrafts.

For sailplanes to produce lift, they need forward movement to allow the air to flow over their wings. This is where energy conversion comes into play. Sailplanes use their height above the ground (potential energy) and convert it into forward movement (kinetic energy), meaning that a sailplane will lose altitude to gain forward movement. The relationship between this loss in altitude and the forward movement is known as the glide slope, glide angle, or lift-to-drag ratio, also known as L/D [14].

The competitive nature of the sport pushes sailplane designers to design and manufacture sailplanes that endlessly push the boundaries of sailplane capabilities. The never-ending pursuit of drag reduction and understanding of aerodynamics cause sailplanes to reach faster average cross-country speeds and much higher L/D. The increase in lift and decrease in drag can thus lead to problems when pilots need to land or reduce speed. A solution is adding devices that the pilot can control to physically increase the drag of the sailplane.

These devices are called airbrakes, and their function is to increase the frontal area of the

sailplane, thus increasing the total drag. The drag increase reduces the glide slope and velocity of the sailplane, making landing approaches much safer. As the glide slopes and wingspans increased, more and more emphasis was placed on safety.

The high L/D of these high-performance gliders made the final approach stages very difficult without the use of airbrakes [10]. In the 1965 World Gliding Championships, two high-performance gliders were severely damaged due to field landings caused by the lack of effective airbrakes as well as bad visibility from the cockpit. It was evident that as the performance of gliders increased, airbrakes became an integral part of the safety aspect of sailplanes [15].

Airbrakes aid in landing by reducing the L/D. During landing, the lower L/D ratio means that pilots have enough altitude above the runway to pull out of the final approach if needed. With the high L/D, the sailplanes approached very low to the ground leaving little room for pilot error or unexpected situations.

High drag devices added to sailplanes can include flaps, spoilers and airbrakes, also known as dive brakes. These devices all serve the same purpose: increasing and controlling drag and decreasing the sailplane's glide slope. However, there are differences between how they achieve these goals and other effects that allow each device to be used for a specific purpose.

Spoilers (Point 1 in Figure 1.1) are found on the upper surfaces of wings, aiming to increase drag and reduce lift. When extended, spoilers increase the drag of a sailplane by altering and interrupting the flow over the wing, also resulting in less lift. This is especially useful in powered aeroplanes to increase the efficiency of the landing gear breaks [16].

Figure 1.1: Spoilers and Flaps extended of a Boeing 737-700 [1]

During landing or take-off, flaps (Point 2 in Figure 1.1) are used to increase the lift generated from the wing by physically changing the shape and surface area of the wing. This increase the efficiency of the wing during low speeds. The downside to the increase

in lift is an increase in drag produced by the wings [17]. Figure 1.1 beautifully illustrates both spoilers and extended flaps of a Boeing 737-700 during landing.

Airbrakes are ideal for sailplanes in that they are designed to increase the drag of a sailplane with minimal reduction in the lift and without dramatically changing the flight characteristics. Schempp–Hirth type airbrakes (Point 1 in Figure 1.2) are flat plates extending from the top of the wing (Point 2 in Figure 1.2) and perpendicular to the airflow direction.

Figure 1.2: Schempp-Hirth type airbrakes used on the JS3 sailplane.

The primary purposes of airbrakes on sailplanes are to reduce the glide slope and to limit the maximum airspeed in a dive (CS 22.73). According to CS-22 regulations [18], the airbrakes should be able to limit the glide slope to 1:7 at 1.3 times the stall speed of the glider (CS 22.75). This is a substantial reduction in glide slope, considering that some open-class sailplanes have glide slopes above 1:70.

1.2 Problem statement

In order to ensure the safety of pilots and bystanders, sailplanes need to be certified. The European Aviation Safety Agency (EASA) has a set of regulations specifically focused on sailplanes, and powered sailplanes [18]. The CS-22 contains all the requirements that sailplanes need to adhere to in order to be certified as airworthy. The certification process requires rigorous testing of all the glider systems, including structural and flight tests. Pushing the limits of design will also leave you on the edge of compliance or failure of the regulations.

This was evident in the design of the JS3, a highly competitive glider on the edge of the CS-22 regulations. The JS3 airbrakes are large enough to provide the drag to reduce the glide angle to 1:7 but just small enough to reduce the approach speed to 1.3 times the stall speed. During the final approach, the JS3 achieved the maximum allowable stall speed (CS 22.49), putting the current airbrake designs on its performance limit. If the airbrakes

frontal area were any larger, the stall speed will be too high, causing the JS3 to fail the CS 22 requirements.

Finding the ideal airbrake area can prove challenging, considering the seemingly contradicting nature of the regulations. CS 22.73 requires the airbrake area to be as large as possible to limit the never–exceed airspeed (V_{ne}) in a dive. CS 22.49 and CS 22.75, on the other hand, require the airbrake area to be as small as possible to have the stall speed of the glider as low as possible. Finding the optimum airbrake area without reliable aerodynamic properties, such as lift and drag ratios, will prove very difficult.

This is exponentially more difficult in the open sailplane classes. The larger sailplanes will require even larger airbrakes to account for the extra lift of the larger wings. Designing an airbrake system that produces enough drag to achieve a 1:7 L/D and adhering to the other requirements of the CS-22 will prove to be much more complex (CS 22.75).

Accurate and reliable calculations are required during the design process to ensure that future sailplane models easily comply with the regulations and be as competitive as possible. Accurately calculating important aerodynamic parameters, such as the drag and lift coefficients of the wing section where the airbrakes are located, is crucial. A slight deviation in calculated parameters can cause a discrepancy between the theoretical calculations and flight test data, leading to non-compliance with the CS-22 regulations. However, accurate and reliable calculations on airbrakes are challenging due to the large flow separation downstream. Computational Fluid Dynamics (CFD) analysis could be the only way these complex flow phenomena can be investigated numerically.

An in-depth study must be done to simulate the flow over the airbrake system to ensure accurate results of the fundamental aerodynamic properties needed during the design stages as efficiently and computationally inexpensively as possible.

1.3 Research aim and objectives

The aim of this study is to identify the key parameters required during the mesh generation and simulation setup to achieve efficient and accurate flow and force coefficient predictions of 2D unsteady airbrake simulations.

To achieve this goal, the following objectives must be accomplished:

- Unsteady flow validation
- Validation of airfoils at high angles of attack
- Validation of flow over an airfoil with extended airbrakes

1.3.1 Validated unsteady canonical flow cases

The first step is to run CFD validation on three canonical flow cases, starting simple and working up to more complex cases. The CFD data for the laminar circular cylinder was given in [11]. The reference CFD data of turbulent flow over a circular and square cylinder was given in [12].

1.3.2 Validate flow over a clean airfoil

The next logical step is to simulate and understand flow over a clean airfoil. The airfoils that will be used are an FX66-17AII-182 and an HPH yn1 airfoil. The clean FX66 and HPH airfoils wind tunnel results are given in [19] and [20], respectively. Additionally, these airfoils are used in sailplane design, making them well-suited for this study.

1.3.3 Validate flow over an airfoil with extended airbrakes

The final step is to apply the knowledge gained to airfoils with extended airbrakes. The two airfoils and airbrake cases, FX66 and HPH, have CFD data available. The FX66 and HPH reference CFD data are given in [9] and [10], respectively.

1.4 Chapter breakdown

The following section briefly summarises the chapter breakdown in this dissertation.

Chapter 2: The literature study is broken down into three sections, fundamental aerodynamic theory, CFD theory and a literature review of unsteady canonical cases and CFD studies on sailplane airbrakes.

Chapter 3: Unsteady validation is done on flow over bluff bodies of a laminar circular cylinder, a turbulent circular cylinder and a square cylinder. During these studies, emphasis is placed on mesh generation and the choice of time step and inner iterations.

Chapter 4: Using the identified mesh, time step and inner iterations parameters are studied on the FX66 and HPH airfoils through a CFD Validation.

Chapter 5: CFD validations are done on the FX66 and HPH airfoils with extended airbrakes. The identified mesh refinement, time step and inner iteration parameters are applied to the airbrake cases.

Chapter 6: The effect of the airbrake cap on the FX66 airfoil is studied. Unstructured and structured meshes are compared with the CFD data found in [9].

Chapter 7: This chapter gives a summary of all studies and simulations performed during this investigation and gives the overall conclusions and recommendations for further study.

Chapter 2

Literature study

2.1 Introduction

This chapter gives an overview of the background theory used in this study and the theory relevant to bluff bodies of highly separated flow conditions. The theoretical overview is divided into the following sections: Fundamental flow dynamics and Computational Fluid Dynamics (CFD) theory. The literature review focuses primarily on numerical studies of flow around bluff bodies and airfoils with extended airbrakes.

2.2 Fundamental aerodynamics

2.2.1 Reynolds number

The Reynolds number can be interpreted as the ratio between a fluid's inertia force and viscous force. Another use for the Reynolds number is as a measure to distinguish between laminar or turbulent flow. Equation 2.1 gives the dimensionless Reynolds number, with the fluid properties of density ρ, dynamic viscosity μ, kinematic viscosity ν, the characteristic length l and the fluid velocity V [21].

$$Re = \frac{\rho V l}{\mu} = \frac{V l}{\nu} \tag{2.1}$$

The Reynolds number can be used to compare and match flow properties. Different fluid conditions will exhibit the same fluid-flow characteristics if the Reynolds numbers are the same, even though the fluids have different material properties, velocities, and dimensionally different bodies [22].

Reynolds' similarity law states that force coefficients and flow patterns, which includes the boundary layer, are similar for bodies of different sizes but of similar shape or bodies of similar size but in different flow mediums if the Reynolds numbers are the same [2].

2.2.2 Lift

The lift coefficient used throughout this study is defined as

$$C_l = \frac{L}{\frac{1}{2}\rho V^2 S} \tag{2.2}$$

where L is the lift force, ρ is the density, V is the velocity and S the characteristic area. For a 2D drag coefficient, S can be replaced with the airfoil's chord length (C) [3].

2.2.3 Boundary layer

Prandtl conceived the boundary layer theory in 1904. His theory enabled the theoretical and experimental study of lift and drag. Prandtl theorised that the viscosity of the air only has to be considered within a limited sheet of fluid next to the body surface. This sheet of fluid is called the boundary layer. Outside the boundary layer, viscosity does not have a noticeable effect when considering the fluid particles relative to each other. The boundary layer will affect the surrounding flow, moving the flow outwards. This outward movement of a flow corresponds to the displacement thickness [2].

The boundary layer can be seen as a relatively thin layer of fluid that is slowed by friction with the surface of the body the fluid is moving over. The boundary layer can be in two states, namely laminar at low Reynolds numbers or turbulent at higher Reynolds numbers [2].

The critical Reynolds number for a flat plate parallel to the flow direction can vary depending on the turbulence of the outer flow. These critical Reynolds numbers are 3×10^5 for highly turbulent flows to as high as 3×10^6 for exceptionally smooth flows. A Reynolds number of 5×10^5 is a good generalisation for the critical Reynolds number in the application during this study. [23]

According to McCormick [3], the boundary layer thickness for laminar flow can be expressed as

$$\delta = 5.2x(\frac{Vx}{\upsilon})^{-1/2} = 5.2x(\frac{\rho Vx}{\mu})^{-1/2} \tag{2.3}$$

and for turbulent flow as

$$\delta = 0.37x(\frac{Vx}{\upsilon})^{-1/5} = 0.37x(\frac{\rho Vx}{\mu})^{-1/5} \tag{2.4}$$

Figure 2.1 illustrates the effect of the adverse (positive) pressure gradient and viscosity on the boundary layer. The fluid particles closest to the surface will travel along the body's surface, from the stagnation point at the front through the point where the velocity is at its maximum. Due to viscous losses along the path of travel, the particles closest to the

surface will not have enough kinetic energy to overcome the adverse pressure gradient at the rear of the body. These particles will come to rest, expending the remaining energy [2].

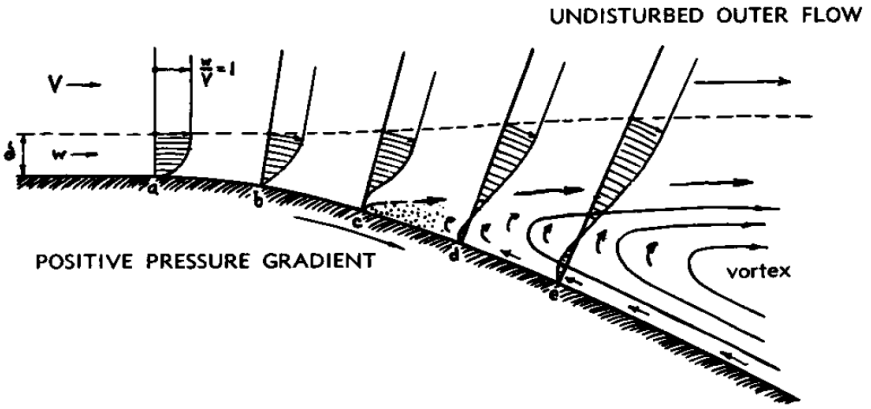

Figure 2.1: Velocity profile, flow development and separation due to a positive adverse pressure gradient [2]

At point a, the boundary layer will have a certain velocity profile and thickness. As the fluid continues along the surface and arrives at point b, the velocity profile will be slightly deformed due to the pressure gradient caused by the outer flow. As the fluid reaches point c, the particles with the lowest momentum will reach a velocity of zero. At point d, the adverse pressure will change the direction of the motion into the undisturbed flow. These particles are collected in the boundary layer, increasing the thickness of the layer and causing the outer flow to separate from the body surface. This separation leaves a zone of low pressure at the rear of the body and, at point e, low energy flow causes vortices that fill the low pressure area [2].

Turbulent boundary layer over a cylinder

In a turbulent boundary layer, there exists a transfer of mass and momentum between the adjacent sheets in the boundary layer. This transfer can be seen as a continuous mass and momentum transfer between the free flow and the body surface. The losses in the turbulent boundary layer are greater than in a laminar boundary layer. The sheets near the surface of the turbulent boundary layer, however, contain much more momentum than that in the laminar boundary layer. As the flow reaches the equator of the cylinder, the flow approaches the critical Reynolds number, where the boundary layer starts to transition from laminar to turbulent, imparting more velocity and momentum to the sheets closest to the surface [2].

2.2.4 Drag

Aerodynamic drag results when a body is moved or forced through the air. There are two main types of drag, namely parasitic and induced drag. Induced drag is the result

of a vortex system that is generated downstream of a lift generating surface and thus is proportional to the lift generated [3].

Parasitic drag can be seen as the drag that remains when the induced drag is removed. The parasite drag can also be denoted as viscous, emphasising that frictional and pressure drag are caused by the fluid viscosity [2]. Parasite drag includes drag components such as skin friction drag, pressure drag (form drag), interference drag, and cooling drag. Skin friction drag can roughly be defined as the drag force directly caused by the tangential shear force along the body's surface.

A bluff (or non-aerodynamic) body moving through the air is mainly affected by skin friction and pressure drag, where pressure drag is, by far, the most significant contributor to overall drag. To put this into perspective, a cylinder's skin friction drag coefficient, taking averaged velocity and corresponding wetted area into account, is approximately 0.01. On the other hand, a cylinder at subcritical and supercritical Reynolds numbers has a pressure drag coefficient between 0.3 -0.4 and 1.2, respectively. This means that the pressure drag component is between 30 and 120 times greater than the skin friction drag [2].

The overall drag coefficient (C_D) a body experiences can be expressed as:

$$C_d = \frac{D}{\frac{1}{2}\rho V^2 S} \tag{2.5}$$

Equation 2.5 can be rewritten to give the drag for a given area as

$$D = \frac{1}{2}\rho V^2 C_d S \tag{2.6}$$

where D is the drag force, ρ is the density, V is the velocity and S the characteristic area. For a 2D drag coefficient, S can be replaced with the airfoil's chord length (C) [2].

Pressure drag

Pressure drag is the drag acting on a body due to the combined effects of the static pressure distribution normal to the body's surface in the direction of drag. This is illustrated more clearly in an extreme case, a flat plate oriented normal to the flow direction, as shown in Figure 2.2. In this case, the drag caused by skin friction is negligible. Most of the drag is caused by an imbalance in the normal pressure distribution [3].

Pressure drag, and to an extent, skin friction drag, is difficult to predict. One must usually refer to experimental or numerical results for accurate drag estimations. Similar to skin friction drag, pressure drag depends on the Reynolds number. This phenomenon can be seen in Figures 2.5 for a cylinder and 2.6 for flat plates. The effect of the Reynolds number is visualised in Figure 2.3, illustrating the wake and separation point. Figure 2.3a is a low Reynolds number flow, whereas the flow in Figure 2.3b has a higher Reynolds number. A

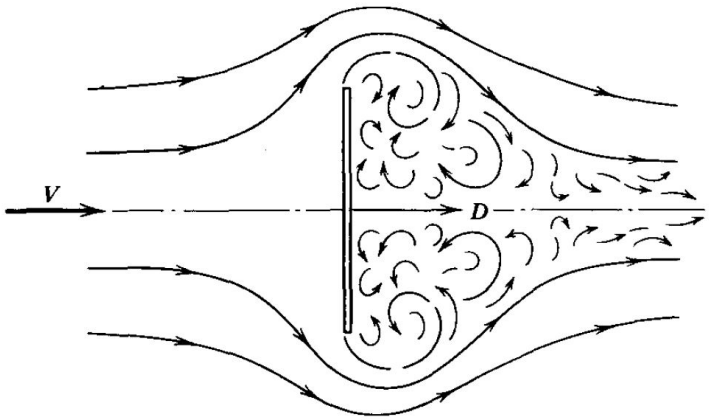

Figure 2.2: Flat plate normal to flow [3]

wider range of Reynolds numbers and the effect on the wake and vortex shedding is given in Figure 2.7 [2].

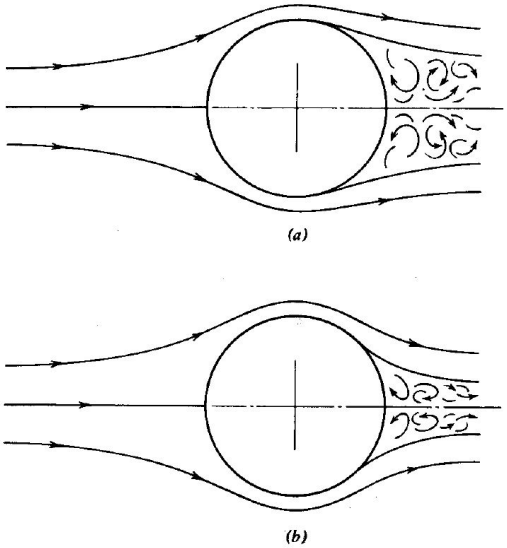

Figure 2.3: Flow over cylinder with low and high Reynolds numbers [3]

Figure 2.4 shows the pressure coefficient plot over a cylinder at three different Reynolds number regimes. These are at inviscid flow, subcritical Reynolds numbers ($2 - 10 \times 10^4$), and supercritical Reynolds numbers ($2 - 4 \times 10^5$).

This pressure difference between the stagnation point (at 0°) and downstream of the separation point is the primary driver of total pressure drag in these cases.

Separation

Flow separation, also called detached flow, occurs when the boundary layer leaves the body's surface. Adverse pressure gradients cause flow separation due to the frictional losses between the fluid particles in the boundary layer, as seen in Figure 2.1. Flow separation can also occur when a body has sharp geometric shapes such as corners.

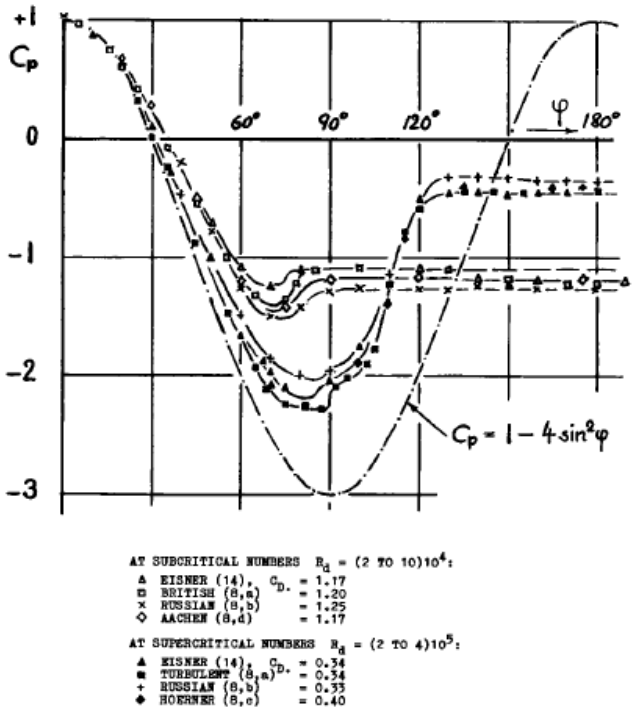

Figure 2.4: Pressure distribution on a Cylinder surface at various Reynolds numbers [2]

Flow separation can be seen at the front or rear of bluff bodies where the adverse pressure gradient is large enough or on the sides of bodies where the boundary layer is thick enough to cause detached flow. The wake behind a body, by itself, is not necessarily caused by flow separation. It is possible that flow can gather enough energy and momentum to reattach to the surface of a body [2].

Separation should not be confused with turbulence. In some instances, separation can be avoided or potentially reduced by forcing the flow to transition into a turbulent state. As explained in Section 2.2.3, the added velocity and momentum will allow the boundary layer to flow better against the adverse pressure gradient, keeping the flow attached for longer.

The delay in the separation and moving the separation point further downstream decreases the body's drag coefficient, as can be seen in Figure 2.5. The drag reduction corresponds to that of supercritical Reynolds numbers ($C_D = 0.1$) [2].

Figure 2.5, shows the drag coefficient against the Reynolds number. At Re $= 0.75 \times 10^6$, the drag coefficients drop significantly from $C_D \approx 0.8$ to $C_D \approx 0.1$. The critical Re is a function of how the boundary layer develops, from the stagnation point at the front of the body to the point of maximum thickness. Thus, the critical Re is a function of the upstream boundary layer, from maximum pressure to the minimum pressure[2].

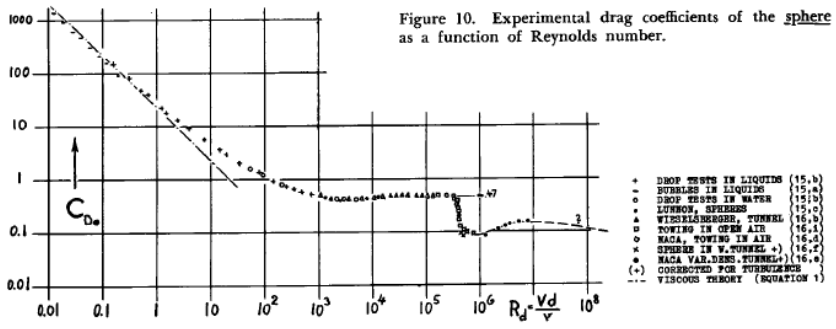

Figure 2.5: Experimental C_D vs Re of a sphere [2]

Drag of various plates

The information mentioned in Section 2.2.4 regarding the importance and role of the boundary layer on the drag of a body applies, in principle, only to sufficiently round bodies such as cylinders or airfoils at high angles of attack.

Bodies with sharp edges, on the other hand, such as flat plates with flow normal to their surface or extended sailplane airbrakes, do not exhibit the same drag decrease, as shown in Figure 2.5. The pressure gradient of the flow around the edges would be extremely high, compared to the flow pattern, if it was attached to the rear of the plate [2]. The edge of the plate prevents any boundary layer, whether laminar or turbulent, from flowing around the body in question and causing immediate flow separation.

Figure 2.6 shows the drag coefficients as a function of the Reynolds number, of a disk and a square plate, with flow normal to the surface. The flow over the bodies at Reynolds number below 100 is largely viscous. A peak C_D can be seen at Re $\approx$ 300, caused by the change in the vortex shedding pattern behind the body [2].

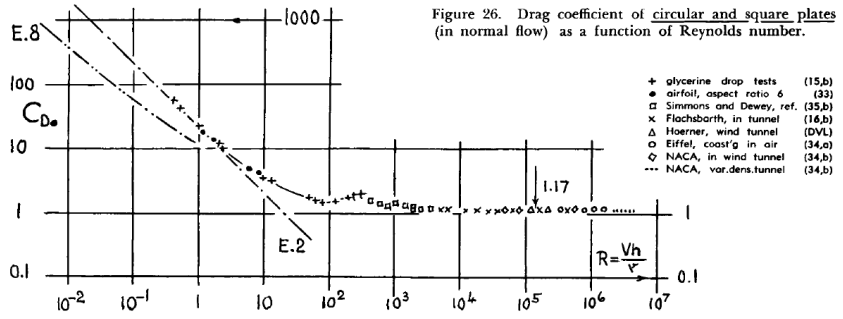

Figure 2.6: Experimental C_D vs Re of flat plates [2]

From Re $\approx$ 1000, the drag coefficients are mostly constant up to the highest tested Reynolds numbers ($Re \approx 10^7$). Even though the drag coefficient remains the same as the Reynolds number is increased, reported data from various wind tunnels do not report the same drag coefficient. This is partly due to blocking effects in closed-type wind tunnel installations, among other reasons [2].

2.2.5 Vortex shedding

As a body is forced through the air, some energy is transferred to the individual particles. These particles are in the body's wake in the form of momentum. This energy transfer accelerates the fluid particles, causing the particles to follow the body. These motions, and other vortex formations, consist of: turbulence, stationary vortices, induced vortices, and vortex streets [2].

There are a few various types of vortices applicable to this study:

- Turbulence can be seen as vortex formation without regular patterns. These vortices are within the turbulent boundary layer over a body and follow behind bodies in motion.
- Stationary vortices form in gaps or other holes in body surfaces. The freestream flow seals the vortex in place by the small amount of momentum transfer to the fluid particles. A classic example is the backward facing step.
- Induced vortices are created behind wings or other non-lifting bodies, such as fuselages. These vortices are the main drivers of induced drag.
- Large repeating vortex formations in the wake behind a moving bluff body.

Bluff bodies, such as cylinders and flat plates, leave a distinct type of vortex in their wake. The vortices are called vortex streets or double-row vortex trails. Vortices are periodically shed from the upper and lower side of a bluff body, as seen in Figure 2.7. The vortex street moves in the direction of the body. The vortex plays a big role in the drag of the body. It has been demonstrated that the vortex system of a bluff body can entirely contain the equivalent of the drag of the body [2].

At Re < 1, dynamic forces acting on a bluff body can be neglected Figure 2.7 (A). As Re ≈ 1, the fluid's dynamic forces need to be considered. There is an unsymmetrical flow pattern from Re < 10 between the front and rear of the body, where a stationary separation point forms as seen in Figure 2.7 (B).

At Re > 100, the periodic vortex shedding can be seen due to the dynamic forces being the dominant factor over the viscous forces. As the Reynolds number increases above $Re \approx 10^4$, the viscous forces decrease even further, and the dynamic forces increase. The constant flow pattern 2.7 (C) can be seen [2].

The frequency of the vortex shedding can be calculated using the following equation below:

$$f_{vs} = \frac{StV}{l} \tag{2.7}$$

Equation 2.7 was derived from Equation 2.8 described in more detail in Section 2.2.5.

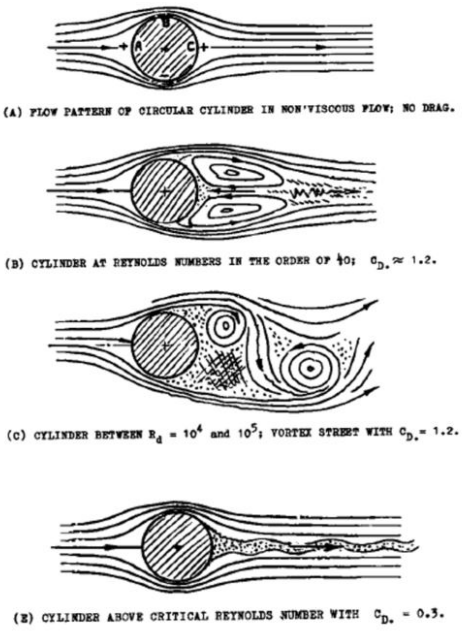

Figure 2.7: Vortex streets formed at various Reynolds numbers [2]

Strouhal number

The Strouhal number is primarily used in unsteady and oscillation flow cases and can be interpreted as the ratio between the local inertial force and the convective inertial force. The local inertial forces, or local accelerations, are due to the flow's unsteadiness. The convective inertial forces, or convective acceleration, are due to the change in velocity at different points in the flow field [21]. The dimensionless Strouhal number can be expressed in the form of Equation 2.8, where f_{vs} is the vortex shedding (oscillation) frequency, V the fluid velocity, and l is the characteristic length projected perpendicular to the flow [24].

$$St = \frac{f_{vs} l}{V} \tag{2.8}$$

Unsteady flow development depends on the Reynolds number and may develop when fluid flows past a body. This unsteady flow will trigger vortices downstream of the body, causing repeating periodic flow. This oscillating flow can be predicted by the shedding frequency in the equation. Bluff bodies are more susceptible to unsteady flow and vortex shedding, as can be seen by airfoils at large angles of attack, flow over cylinders and sailplane airbrakes. These vortices are called Von Kármán vortex trail or vortex street after Theodor von Karman [21].

The vortex shedding frequency f_{vs} is the number of vortices formed per unit time at one side of the body. According to experimental results of essentially 2D bodies at Reynolds numbers between 10^3 and 10^6, the drag coefficient and Strouhal numbers appear to be proportional. [2].

2.3 Computational Fluid Dynamics Theory

2.3.1 Mesh generation

A mesh and the creation of a mesh is a fundamental and essential part of any CFD simulation, thus great care must be taken to ensure adequate mesh quality. Poorly generated meshes directly impact the success or failure, the results' accuracy, and the simulation's stability and convergence [4].

Types of meshes

Meshes can be categorised into two categories, structured and unstructured meshes. The advantages and disadvantages of both types will be discussed below.

Structured mesh

A structured mesh (Figure 2.8) require remarkably less memory than an unstructured mesh with similar number of mesh elements [25]. Mesh generation around simple geometries, such as airfoils, is easier and less time consuming than unstructured elements [4]. Simulation time for less complex flows is also lower than that of unstructured meshes.

The disadvantages of structured meshes are the difficulty in generating meshes for more complicated geometries. Meshing complex shapes with a structured mesh tends to create skewed cells, leading to instabilities and erroneous results. More mesh elements may also be required due to structured meshes not being able to grow in size as rapidly as the unstructured variant [25]. Overall, structured meshes work better on simple geometries with the flow aligned with the mesh elements that have strong gradients in a single direction, with less intense gradients in other directions such as in the boundary or shear layers and the wake [26].

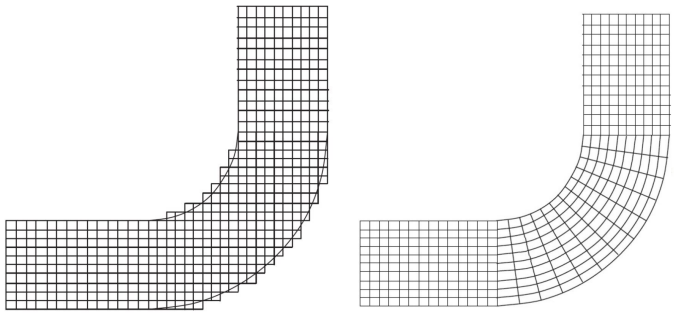

(a) Staircase-like steps (b) Body fitted

Figure 2.8: Examples of a structured mesh in a 90 ° bend pipe - adapted from [4]

Unstructured mesh

On the other hand, unstructured meshes (Figure 2.9) are much more flexible when used on more complex geometries. The mesh refinement is also simpler than structured meshes

with more rapid cell size growth available if required [25]. A drawback of unstructured mesh is that a single mesh cell may have several neighbouring cells, more than that of structured meshes. This increases the computational time when resolving the simulation. Another disadvantage is that unstructured mesh elements are inadequate to capture and resolve the boundary layer in viscous flows [4].

Polyhedral vs Tetrahedral

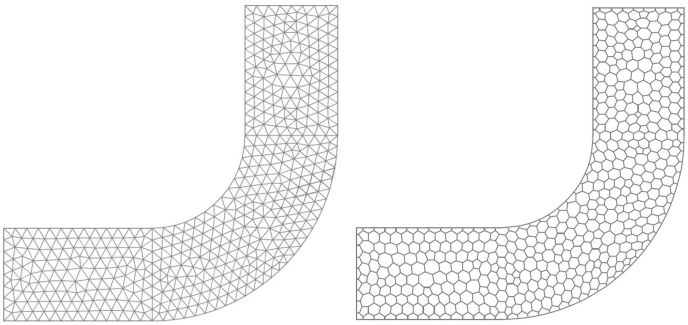

(a) Tetrahedral cells (b) Polyhedral cells

Figure 2.9: Examples of an unstructured mesh types in a 90 ° bend pipe - adapted from [4]

Two popular unstructured mesh types are tetrahedral and polyhedral meshes (Figures 2.9a and 2.9b respectively). Polyhedral meshes are created by merging tetrahedral cells. According to [4], fewer polyhedral cells are required compared to tetrahedral cells in a given volume. When using polyhedral cells, mesh quality can be improved by merging skewed tetrahedral cells into more ideal polyhedral cells. Increasing the mesh quality not only leads to improved accuracy and quicker convergence but also increased stability. A further benefit to using polyhedral is meshing complex geometries more efficiently than tetrahedral meshes.

The biggest benefit of polyhedral cells is the advantage when used in anisotropic flow cases such as recirculation or vortex shedding [26]. The larger amount of neighbouring cells and increased face counts increases the accuracy of polyhedral meshes without increasing the cell count.

Hybrid mesh

Hybrid grids (Figure 2.10) combine the strengths of both mesh types by using a structured mesh in the viscous boundary layer and generating an unstructured mesh in the free stream. Using a hybrid mesh is crucial when solving viscous flows, as it is used to capture the actual flow physics occurring in the boundary layer [4]. This structured mesh used to capture the boundary layer conditions is also known as the prism layer.

Prism layer

Using a prism layer is vital in the accurate resolution of the near wall flows. Flow features, such as transition and separation, are captured within the viscous sublayer of the turbulent boundary layer. The prism layer mesh is a convenient and efficient way to increase the

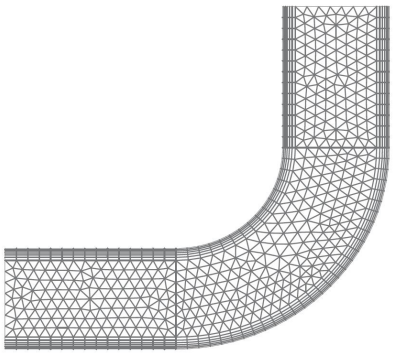

Figure 2.10: Examples of a hybrid mesh in a 90 ° bend pipe - adapted from [4]

mesh density in the important boundary layer. High aspect ratio cells are used, increasing cross-stream resolution whilst keeping the streamwise resolution to a minimum [5]. Using prism layers, numerical or false diffusion in the near wall area is reduced. Flow aligned meshes minimise the probability of numerical diffusion errors [5].

To fully capture the boundary layer, [5] suggests using between 10 - 20 cells in the cross-stream (normal to the flow) direction, where [4] suggests 30 - 60. In addition to the correct number of cells in the prism layer, the correct y^+ value is required. Both [5] and [4] suggests using $y^+ \approx 1$.

The dimensionless y^+ value can be defined as:

$$y^+ = \frac{yu_\tau}{\nu} \tag{2.9}$$

where u_τ is the wall friction velocity, y the normal distance from the wall and ν the kinematic viscosity.

The wall friction velocity (u_τ) can further be defined as

$$u_\tau = \sqrt{\frac{\tau_w}{\rho}} \tag{2.10}$$

with τ_w the wall shear stress and ρ the density [4].

Generated mesh assessment

Due to the importance of a high quality mesh, it is essential to assess the quality of a mesh. This can be divided into inspections on a local and global level. Inspecting a mesh on a local level is vital to remove any simulation errors and convergence problems. Incorrect meshes on a global scale will affect simulation time and overall simulation accuracy.

Inspection on a local level takes individual mesh elements into account. Important factors to consider when assessing individual element quality are the elements' aspect ratio (AR) and the skewness angles.

A global inspection includes inspecting the mesh density, distribution, and near wall layers. An optimal mesh has sufficient mesh elements at areas where high flow gradients occur to accurately capture these phenomena. The distribution of mesh elements between these high and low gradient regions should be gradual and smooth. Near wall layer elements are crucial for capturing flow phenomena such as the viscous effects [5]. In addition to the importance of the y^+ value, the Courant–Friedrichs–Lewy (CFL) number should also be considered when generating a mesh. The CFL condition is important to ensure the simulation is stable and accurate.

Aspect ratio

The aspect ratio (AR) of a cell is a measure of the overall shape of the cell. The aspect ratio is defined as $AR = \Delta y/\Delta x$, where Figure 2.11 describes these terms.

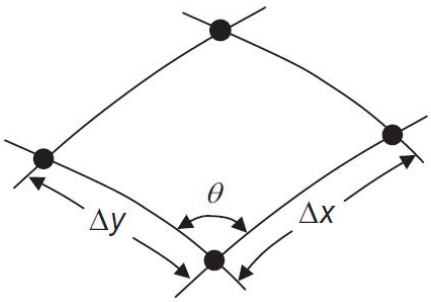

Figure 2.11: Quadrilateral mesh element (cell) with mesh spacing Δy and Δx [4].

During the mesh generation process, cells with large aspect ratios should be avoided in areas of importance. Large aspect ratios can cause degraded solution accuracy and poor iterative convergence. Ideally, the aspect ratio should be in the range of $0.2 < AR < 5$ in the flow field. The aspect ratio in the prism layer can deviate from this. For a flow in the y direction, choosing a sufficient Δx value in the x direction for an acceptable y^+ value would result in $AR > 5$. This is not a problem because the gradient change in the boundary layer is mainly in the x direction, in this specific case [4].

Skewness angle

The skewness angle is a measure used to evaluate generated cells on both sides of a common face that allows the diffusion of quantities, between these cells, without the quantities becoming unbounded. Figure 2.12 illustrates two cell centroids on either side of a common face.

The skewness angle can be defined as the angle (θ) between the face normal vector ($\mathbf{a}$) and the vector connecting the centroids of the two cells ($d\mathbf{s}$). A skewness angle of 0° would thus indicate a completely orthogonal mesh. Cells with a skewness angle greater than 85° are seen as bad and must be attended to. Convergence errors start to occur at a skewness angle of 90° and higher. These errors are due to the zero value of $\mathbf{a} \cdot d\mathbf{s}$ at an angle of 90°. This dot product is contained in the denominator of the diffusion term for the transported scalar variables. Higher skewness angles reduce the accuracy of the calculations and, with that, the robustness of the simulation. Skewness angles of less than 85° are advised to

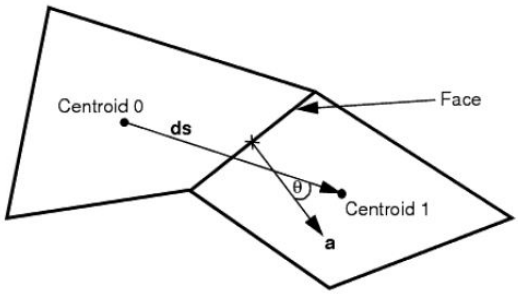

Figure 2.12: Two quadrilateral mesh elements with cell centroids on either side of a common face [5].

reduce the impact on the simulation robustness [5]

False (Numerical) diffusion

Another aspect that needs to be addressed during mesh generation is the importance of adequate concentration of mesh elements in areas of high flow gradients. Accurately capturing these areas is crucial in accurate and stable simulations. Coarse grids will increase the chances of numerical, artificial or false diffusion, which gives a diffusion-like effect. False diffusion is the phenomenon that occurs when flow lines are not aligned with the grid lines, which leads to the smearing of the transport properties. According to [6], the error caused by false diffusion is largest at coarser grids, and adequate mesh refinement would, in theory, reduce these effects. Figure 2.13 below illustrates the effects of grid refinement on the accuracy of the solution. The solution of finer grids moves towards the exact solution.

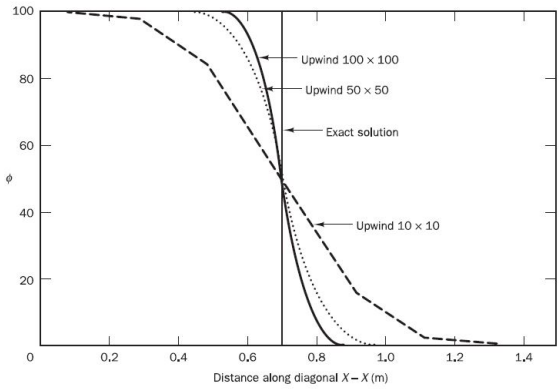

Figure 2.13: Grid density effect on false diffusion [6].

In practice, Mesh refinement to eliminate the effects of false diffusion can become computationally expensive. To overcome this, more emphasis can be placed on refining mesh elements at critical locations, such as locations of high flow gradience, or choosing a higher order discretisation scheme.

Courant number and CFL condition

The Courant number

The Courant number is a dimensionless number used to evaluate the required time step and cell sizes for a given flow velocity in an unsteady (transient) study. The Courant number is linked to the CFL (Courant–Friedrichs–Lewy) condition stability evaluations.

The Courant number can be defined as [27]

$$\sigma = \frac{V\Delta t}{\Delta h} \tag{2.11}$$

where V is the the flow velocity, Δt the time step and Δh the mesh element length.

The Courant number roughly indicates the amount of information travel across the mesh within a specific time step. As shown in Figure 2.14, a Courant number greater than one indicates the information moves through more than a single cell per time step, decreasing simulation accuracy. This can also lead to instability and divergence but also to nonphysical flow phenomena to occur.

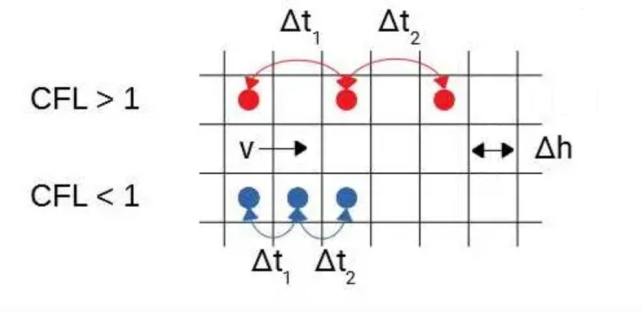

Figure 2.14: Illustration of the Courant number and CFL condition on an example mesh [7]

Choosing the correct time step is crucial in a transient simulation where capturing the time dependent flow structures is the primary goal. This is better illustrated in Figure 2.15.

For a given V and Δh, the change in time step can affect the behaviour of a captured variable of interest. The upper portion of Figure 2.15 illustrates a chosen time step too large to capture the flow physics fully. The ideal case is a smaller time step that fully resolves the flow physics, with 10 - 20 points per period [8].

The CFL condition

The CFL condition is a simulation stability requirement expressed in terms of the Courant number as:

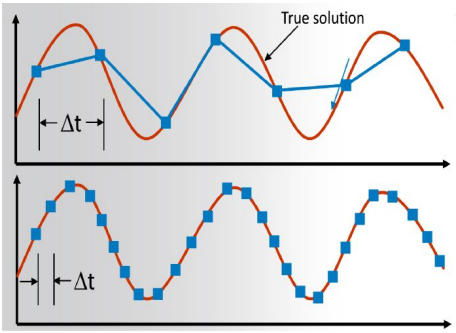

Figure 2.15: Illustration of the Courant number and CFL condition on an example mesh [8]

$$\sigma = \frac{V\Delta t}{\Delta h} \leq \sigma_{max} \tag{2.12}$$

where σ_{max} can vary depending on the type of time integration scheme used. However, a general rule is that $\sigma_{max} \leq 1$ [4].

The CFL stability condition is of much more importance in explicit-type procedures. These types can be considered conditionally stable due to being greatly influenced by the temporal resolution of the simulation setup. On the other hand, implicit-type solutions can usually be considered unconditionally stable [4].

2.3.2 CFD physics

k-ω SST Turbulence model

The $k-\omega$ shear stress transport (SST) solver is a two-equation eddy viscosity turbulence model introduced by F.R. Menter [28]. The $k-\omega$ SST turbulence model uses two turbulence models, namely $k-\epsilon$ in the wake region of the boundary layer and free stream regions and $k-\omega$ in the sublayer and logarithmic regions of the boundary layer. The $k-\omega$ model is a simple model that leads to numerical stability, which plays a significant role in CFD simulations.

Baseline model

The standard high Reynolds version of the $k-\epsilon$ model is transformed into a $k-\omega$ formulation. This $k-\omega$ formulation differs from the original $k-\omega$ model in two ways, namely, the addition of a cross-diffusion term in the ω equation and different modelling constants. On the left of the equations below is the Lagrangian derivative in the form $D/Dt := d/dt + u_i d/dx_i$. The original $k-\omega$ model is defined in equations 2.13 and 2.14 below.

$$\frac{D\rho k}{Dt} = \tau_{ij}\frac{du_i}{dx_j} - \beta^*\rho\omega k + \frac{d}{dx_j}[(\mu + \sigma_{k1}\mu_t)\frac{dk}{dx_j}] \tag{2.13}$$

$$\frac{D\rho\omega}{Dt} = \frac{\gamma_1}{v_t}\tau_{ij}\frac{du_i}{dx_j} - \beta_1\rho\omega^2 + \frac{d}{dx_j}[(\mu + \sigma_{\omega 1}\mu_t)\frac{d\omega}{dx_j}] \tag{2.14}$$

The transformed $k-\epsilon$ model is defined in equations 2.15 and 2.16 below.

$$\frac{D\rho k}{Dt} = \tau_{ij}\frac{du_i}{dx_j} - \beta^*\rho\omega k + \frac{d}{dx_j}[(\mu + \sigma_{k2}\mu_t)\frac{dk}{dx_j}] \tag{2.15}$$

$$\frac{D\rho\omega}{Dt} = \frac{\gamma_2}{v_t}\tau_{ij}\frac{du_i}{dx_j} - \beta_2\rho\omega^2 + \frac{d}{dx_j}[(\mu + \sigma_{\omega 2}\mu_t)\frac{d\omega}{dx_j}] + 2\rho\sigma_{\omega 2}\frac{1}{\omega}\frac{dk}{dx_j}\frac{d\omega}{dx_j} \tag{2.16}$$

After the transformation, the newly transformed $k-\epsilon$ model (Eq 2.15 and Eq 2.16) is multiplied by a blending function in the form of $(1-F_1)$ and the original $k-\omega$ model (Eq 2.13 and Eq 2.14) is multiplied by a blending function F_1. After the multiplication of the blending functions, the models are added together and given in equations 2.17 and 2.18 below. This blending function F_1 is set up in such a way that it has a value of 1 in the sublayer and logarithmic region of the boundary layer, which activates the original $k-\omega$ model. The blending function then gradually changes to 0 in the wake region, which in turn activates the transformed $k-\epsilon$ model [28].

$$\frac{D\rho k}{Dt} = \tau_{ij}\frac{du_i}{dx_j} - \beta^*\rho\omega k + \frac{d}{dx_j}[(\mu + \sigma_k\mu_t)\frac{dk}{dx_j}] \tag{2.17}$$

$$\frac{D\rho\omega}{Dt} = \frac{\gamma}{v_t}\tau_{ij}\frac{du_i}{dx_j} - \beta\rho\omega^2 + \frac{d}{dx_j}[(\mu + \sigma_\omega\mu_t)\frac{d\omega}{dx_j}] + 2\rho(1-F_1)\sigma_{\omega 2}\frac{1}{\omega}\frac{dk}{dx_j}\frac{d\omega}{dx_j} \tag{2.18}$$

To simplify the equations mentioned above, let ϕ represent any constants of the new derived model (σ_k...), ϕ_1 the constants in the original $k-\omega$ model (σ_{k1}...) and ϕ_2 the constants in the transformed $k-\epsilon$ model (σ_{k2}...). The relationship between these is given in equation 2.19 below [28].

$$\phi = F_1\phi_1 + (1-F_1)\phi_2 \tag{2.19}$$

Shear stress model

Menter modified the definition of the eddy viscosity to take the transport of the principal turbulent shear stress into account. This modification to the model is known as the SST model and is a considerable improvement over the standard $k-\epsilon$ and original $k-\omega$ models [28].

The shear stress in conventional two-equation models is calculated from Eq 2.20 below

$$\tau = \mu_t\Omega \tag{2.20}$$

where $\Omega = (du/dy)$. Eq 2.20 can be rewritten as

$$\tau = \rho\sqrt{\frac{Production_k}{Dissipation_k}}a_1 k \tag{2.21}$$

The ratio of production to dissipation can be larger than 1 in adverse pressure gradient flows. This will cause an overprediction of τ. The eddy viscosity in an eddy-viscosity model is redefined as

$$v_t = \frac{a_1 k}{max(a_1\omega; \Omega F_2)} \tag{2.22}$$

where F_2 is another blending function with value 1 for flow in the boundary layer and 0 for flow in the shear layer. F_2 can be defined as

$$F_2 = \tanh(arg_2^2) \tag{2.23}$$

The added computational costs for utilising this modified model lie mainly in calculating the added cross diffusion term and the two blending functions F_1 and F_2. These blending functions are a function of the distance from the geometry surface. This distance is calculated only once if the generated mesh remains the same or if there are no mesh deformations [28].

Application and Validation

The model has different applications in the article by Menter [28]. The applications of interest for this study are adverse pressure gradient flows, the backward facing step and flow over a NACA 4412 airfoil. In these validation cases, Menter compared four turbulent models, namely Jones-Launder $k-\epsilon$ model (JL) and variations of the $k-\omega$ model (SST, original and the baseline model (BSL)) with experimental data.

Adverse pressure gradient

The flow along the axial direction of a circular cylinder was considered to evaluate the accuracy of the SST model with regard to sufficiently strong adverse pressure gradients. Flow separation was achieved due to the strong pressure gradients in the experiment. When comparing the wall pressure results, it was found that, due to the ability of the SST model to take the transport of the principal shear stress into account, the results were superior to that of the other models. The SST model predicts the most significant amount of separation when comparing the wall shear stress distributions. In comparison, the JL $k-\epsilon$ model does not predict flow separation. The SST model outperforms the other models regarding the prediction of the velocity profiles and the reduction of the eddy-viscosity due to the adverse pressure gradients [28].

Backwards facing step

The flow over a backwards facing step was considered. Two parameters were used to compare the turbulence models with the experimental results: the skin friction distribution and the reattachment length downstream of the step. When comparing the skin friction distributions, the $k-\omega$ models delivered better results than the JL $k-\epsilon$ model. The percent error of the reattachment length predictions are as follows: 1.56% (SST), 7.81% (BSL), 0% (Original), 14.06% (JL $k-\epsilon$). All models failed to capture the relaxation downstream of the reattachment accurately. The failure to accurately capture this phenomenon is also prevalent in more complex turbulent models, which take anisotropy into account [28].

NACA 4412 Airfoil

A NACA 4412 airfoil was used at an AOA of 13.87° and Reynolds number of 1.52×10^6 relative to the chord. The velocity profiles at various streamwise stations were used as means of comparison. The displacement effects predicted by the SST model correspond very well with that of the experiment. The velocity profile predictions of the original $k-\omega$ model are even further from the experiment than that of the JL $k-\epsilon$ model. The poor performance of the original $k-\omega$ model was due to the freestream dependency. Menter did additional simulations with a ω value of about 50 times larger, and the results were significantly different. The large ω value had a minimal impact on the results of the SST model [28].

When considering these test cases, the $k-\omega$ SST model is the better option for predicting flow separation, adverse pressure gradients, pressure recovery behind a bluff body and, in general, aerodynamic applications such as an airfoil at moderate to high angles of attack. These complex flow phenomena play a significant role in the flow over bluff bodies and, in turn, behind an airfoil with extended airbrakes.

2.4 Literature review

In order to understand the flow over airfoils with extended airbrakes, the first step was to understand the flow over a simpler yet similar geometry. This chosen geometry was the flow over cylinders. These canonical cases are widely studied, and information is widely available.

Similar to airfoils with extended airbrakes, both are bodies in free stream conditions with predictable and periodic vortex shedding. Circular cylinders separate due to adverse pressure gradients, whereas square cylinders separate due to sharp corners. These separation mechanisms are present in high angle of attack airfoils and extended airbrakes, respectively. It was essential to capture the flow around a body, which is crucial in the pressure drag. A cylinder, whether circular or square, has more similarities to the extended airbrake case and was chosen to form the bases of this study.

Another classic case is a verticle flat plate on a floor. These cases are in the presence of the boundary layer, meaning that already turbulent flows reach the body. In addition to this, the floor does not allow the air to move around the body. The cylinder cases are a

better match than the flat plate on a floor.

The literature review is divided into two sections. These sections are unsteady flow over a cylinder and literature on sailplane airbrakes and the numerical studies thereof. The main focus of the literature study in Chapter 2.4.1 is the numerical simulation setup and parameters. This ensures the correct use and understanding of the available tools and how these problems are solved in literature.

2.4.1 Unsteady flow over a cylinder

Flow over a cylinder is widely studied and applicable in various fields, such as heat transfer, civil engineering and aerodynamics applications. These cases are also widely used as validation cases. In addition to the various applications of these cylinder flow cases, several configurations are studied at a wide Reynolds number range. Most of these studies are done at low Reynolds numbers: thus, the focus was on single cylinders at high Reynolds numbers ($Re > 1 \times 10^4$). High Reynolds numbers are more applicable in the end goad of flow over an airbrake.

The simulations in [29] are of a 3D circular cylinder at Reynolds numbers $RE = 10^6$. A structured mesh with $k - \epsilon$ RANS and URANS eddy viscosity models and LES turbulence models were used. A non-dimensional time step of 0.01 was chosen for the RANS and URANS studies. The LES time step was varied between 0.003 and 0.0045 with a maximum CFL of 1.5. The LES simulation pressure coefficient had good agreement with the experimental results. The URANS pressure coefficient was, according to [29], satisfactory but with poor RANS pressure coefficient results. The LES model had better C_D predictions, with RANS and URANS being similar. There are no RANS Strouhal results; however, the URANS Stouhal results are closer to that of the LES model. Overall, the LES model gave better results than both RANS and URANS.

The study done in [30] is of flow over smooth 2D circular cylinders in the Reynolds number range $10^4 < Re < 10^7$. Constant density and viscosity were selected with low mainstream turbulence. An unstructured mesh was used with a structured mesh in the near wall region to capture the boundary layer, ensuring $y^+ = 1$. Both standard and realizable $k - \epsilon$ URANS eddy viscosity models were used with two-layer near wall treatment. The second-order discretization scheme was used with the segregated implicit solver. The time step was chosen to be 0.05 times the vortex shedding period, derived from the Strouhal number, with 10 inner iterations. Both mesh and temporal refinements were done in this study. This study compares the numerical C_D and separation angle with experimental results. According to [30], the results show discrepancies between the computational and experimental results.

In [12], flow over a 3D square and circular cylinder was investigated. The Reynolds numbers for the circular cylinder were 1.4×10^5 and 3.6×10^6, with that of the square cylinder being 2.2×10^4. The Spalart Allmaras DES turbulence model was used in both cases. A structured prism layer mesh was generated with an unstructured mesh away from the body. The average y^+ was reported as 0.065 and 0.4 for the circular cylinder

at Reynolds numbers 1.4×10^5 and 3.6×10^6, respectively. The square cylinder had a y^+ of 0.065. A non-dimensional time step of 0.01 was used for both circular and square cylinders. Two circular cylinder cases were investigated at 3.6×10^6, laminar and turbulent inlet flow. The laminar case had a trip function at $\pm$ 65° to $\pm$ 85° from the stagnation point. The 3.6×10^6 cases underpredicted C_D by roughly 25%, with an overpredicted Strouhal number. As mentioned in [12], other numerical simulations indicate that the aerodynamic parameters are insensitive to the trip location. The pressure coefficients compare well to that of the selected experimental data. On the other hand, the square cylinder overpredicted the Strouhal number and underpredicted the time average C_D.

In [31], the flow over a circular cylinder at $10^4 < Re < 5 \times 10^5$ was simulated. The 2D RANS and URANS models were $k - \epsilon$ and $k - \omega$ SST. The 3D URANS and DES $k - \omega$ solvers were used with the LES turbulence model. A structured mesh was used, with the y^+ adjusted according to the required value for each turbulence model. The 3D simulations used a time step of 1×10^{-5}, ensuring that the Courant number is smaller than one. The importance of three-dimensionality is shown in [31]. The averaged C_D results, compared to the experimental case (at Re = 10^4), are as follows: 33.04% underprediction using 2D RANS, 45.22% overprediction using 2D URANS, 9.57% overprediction using 3D URANS, 2.61% underprediction using DES and 0.87% prediction using LES.

A square cylinder with an aspect ratio of 4:1 was numerically investigated in [32] for $7.8 \times 10^3 < Re < 1.9 \times 10^4$. Both 2D and 3D simulations were done with $k-\omega$ SST URANS and the Spalart-Allmaras DDES turbulence models, respectively. The non-dimensional time step used in the 2D URANS simulation was 10^{-3} with second-order implicit, spacial and upwind schemes. Both structured and unstructured meshes were used in the near and far wall domains, respectively, with $y^+ = 0.7$. The same mesh setup used in the 2D study was used during the 3D study, only extruded in the z-direction. Similar second-order schemes were used as in the 2D case, except for the Linear Upwind Stabilised Transport scheme. The time step was adjusted to 6.25×10^{-4} for stability. The study in [32] focuses on comparing the experimental and numerical results due to the change in angle of attack. Both URANS and DDES studies overpredicted the C_L values for angles higher than 0° but adequately captured the C_D values. It was found that the URANS solver performed better at angles below the stall angle than the DDES simulation. However, the DDES model accurately predicted the stall angle, whereas the URANS model could not.

Flow over a 2D and 3D square cylinder was studied in [33], with a Reynolds number of 2.14×10^4. The simulation used a structured mesh with a y^+ less than one. The $k - \omega$ SST RANS model was used in the 2D URANS and 3D hybrid LES/RANS and IDDES simulations. A time step of 1×10^{-10} was chosen. It was found that the 2D URANS model performed very poorly compared to the hybrid LES/RANS and IDDES solvers. Aerodynamic characteristics studied included the Strouhal number, time-averaged base pressure and drag coefficients.

The flow over a smooth circular cylinder was investigated in [34]. The $k - \omega$ SST 2D URANS study was in the Reynolds number range $1.5 \times 10^6 < Re < 3.6 \times 10^6$. A structured mesh was used with a $y+ = 1$. A transient first-order implicit simulation was used due

to the more lenient stability requirements. A second-order upwind scheme was selected to discretize the pressure and momentum equations. On the other hand, the turbulent kinetic energy and the specific dissipation rates were discretized using the first-order upwind scheme. A temporal sensitivity study was done with time steps between 2×10^{-4} and 9×10^{-4} with a CFL number between 13 and 16. The results were that the 2D URANS $k-\omega$ SST model used predicted the C_D and Strouhal numbers adequately close to experimental results.

The literature above varies from 2003 to 2020, from square to circular cylinders and from 2D to 3D simulations. Results show that complex flows can be numerically captured despite some discrepancies between the numerical and experimental. The discrepancies between numerical and experimental studies can be explained by the complex real-world flows as well as the slight differences in the simulation setup.

It is abundantly clear that 3D simulations using LES or DES solvers give overall better results than 2D URANS simulations. The difference between 2D and 3D is emphasized in [31], increasing the accuracy without using more advanced models such as LES or DES. It is also clear that the 3D effects of separation and turbulence in the wake directly impact the predicted results. However, due to the current study's limitations, the focus is on 2D simulations.

Based on the above literature and the turbulent model giving the best results, the most popular choice is $k - \omega$ SST. Even though both structured and unstructured meshes were used, structured meshes were prevalent at the near wall regions of the body in question. The literature also revealed that both forms of separation, due to adverse pressure gradients or the geometric shape of the body, can reasonably accurately be captured.

2.4.2 Sailplane airbrake literature

This literature review section primarily focuses on numerical and experimental studies of flow over sailplane airbrakes. The literature surrounding these cases is challenging to obtain. Sailplane design is a very competitive and commercial sport, with sailplane manufacturers not wanting the opposition to gain an advantage. This might be the reason why sailplane airbrake literature is so sparsely available.

As with the literature review of flow over a cylinder, it is essential to know and understand what current literature is available. Below is a summary and a brief discussion of the literature on sailplane airbrakes.

A study on a NACA 23012 and FX66-17AII-182 airfoil with retracted and extended airbrakes is conducted in [35]. The simulations were done at a Reynolds number of 3.33×10^5 and were compared with experimental results. Both studies had structured meshes on the body with unstructured meshes in the free stream, with a second-order upwind discretization scheme. A 2D steady $k - \epsilon$ RANS solver was used in an incomparable viscous flow regime. The focus of the study was on the difference in lift slopes rather than the absolute values, and the experimental results support the conclusions. It is acknowledged in [35]

that the results accuracy is problematic and that it is essential to use unsteady simulations with a time step corresponding to the vortex shedding frequency of the airfoil and airbrake geometry.

In [9], flow over three airbrake configurations extended out of an FX66-17AII-182 was numerically tested, with a reference airbrake configuration used as a validation case. All of these configurations were variations on the Schempp-Hirth type airbrakes. The 2D study was conducted using the URANS solver and the $k-\omega$ SST turbulence model. The time step was set to 0.01 with a central discretization approach. A structured overset mesh was used, dividing the domain into two sections: close to the airbrake and the surrounding domain. The overset mesh allowed the generation of separate high-quality meshes. However, the problem with this method is that the mesh elements at the intersections between the two overset regions need to merge gradually. This can be seen to be the case in [9]: however, the mesh refinement downstream of the airbrake might still be too coarse when taking the vortex shedding of square cylinders into account. The boundary layer was captured with 32 cells in the prism layer, with a $y^+ < 1$. The reference simulations compare well with the experimental case.

Two studies, [10] and [36], were done on the HPH yn1 airfoil designed specifically for sailplane use. The first study, [10], is an experimental and numerical study on the aerodynamic effects of flow over a top mounted airbrake and the effect of the gap between the airfoil and airbrake. The second study, [36], is divided into an experimental and numerical study. The experimental study focused on the effects of a top-mounted airbrake and a top and bottom-mounted airbrake. In addition to these, various design changes were investigated. These studies include the effects of the airbrake chordwise mounting position, airbrake gap and the effect of airbrake height. The numerical study supplemented the experimental study by simulating the effect of the airbrake box, as the experimental model was not equipped with this box. Both studies assumed 2D flows through the addition of endplates to the test section. The experimental study was conducted in the 3m low speed wind tunnel at VZLU in Prague. The numerical setup was 2D URANS with the $k-\omega$ solver at a Reynolds number of 1.5×10^6. The addition of the Hellsten explicit algebraic Reynolds-stress model was used in both studies. A hybrid unstructured mesh with a structured mesh in the prism layer was used with a $y^+ \approx 1$. It is not disclosed what the selected time step for the URANS solver was, only that it was chosen to satisfy the CFL stability condition. Neither of the studies shows what the generated mesh looked like: however, it is mentioned in [10] that local refinement was done close to the actuators and the flaps. The total used mesh elements were given in [36] as ≈450000 elements, but conclusions are difficult to make without a domain size or indication of the level of refinement. Nevertheless, a good pressure distribution comparison between the numerical and experimental studies was reported in [10], with the force coefficients, especially C_L, being in good agreement. The numerical model overpredicted the recirculation in [36], but it did not have a large impact on the results. The CFD simulation of the second study, [36], showed little difference between the flow prediction for the airfoil with and without the airbrake box. This was used to conclude that the experimental results, without the airbrake box, were representative.

Two studies, [37] and [38], were done on the airbrakes of the GL-1 Indonesian designed sports glider. Both studies follow similar methodologies and simulation setups, with very little information on the numerical simulation setup. The $k-\omega$ SST turbulence model is used with the RANS solver. Using RANS, as seen in Section 2.4.1, is not an ideal solver to use in the largely separated and turbulent flows expected downstream of an extended airbrake. An unstructured mesh was used in [37], with no mention of the mesh used in the boundary layer. Two cases were studied in [38]: 2D and 3D. A structured mesh was used in the 2D case, with an unstructured mesh in the 3D case. As within [37], no mention was made as to the mesh type in the boundary layer. Due to the little information given on the mesh setup, mesh independence study, validation study or all the other important parameters in a CFD simulation, the results will not be considered moving forward. It is still important to add these studies in this section to thoroughly evaluate the state of numerical simulation literature on sailplane airbrakes.

The studies done on the FX66-17AII-182 [9] and the HPH yn1 [10], [36] airfoils will form the main focus points in the study moving forward. Both the numeric results in these studies correlate very well with experimental results.

The simulation and mesh setups are given in such a way as to give a solid starting point going forward. Unfortunately, neither of these studies goes into too much detail about the mesh generation and setup. Some details are given in [9], but as mentioned, the mesh seems questionable when taking the information in Section 2.3.1 into account. The most significant point of concern is the relatively abrupt element size change downstream of the airbrake. This lends itself to numeric errors such as false diffusion. The literature around sailplane airbrakes shows that 2D simulations are sufficient and the prevalence of the $k-\omega$ SST solver.

Chapter 3

Unsteady CFD validation

3.1 Introduction

Flow past airfoils at high angles of attack, landing gear and airbrakes will cause interesting and chaotic flow. Due to the nature of the flow, it is crucial to understand these complex flow phenomena by simulating these simple geometries and investigating and comparing the results. Afterwards, the same methodology can be extended to more complex geometries, such as sailplane airfoils with extended airbrakes with confidence.

The flow around a cylinder, similar to airbrakes, is complex and can lead to complicated and challenging flow phenomena. The simple geometry cause flow phenomena such as transition, boundary-layer separation, Reynolds number (Re) dependency, geometry–dependant vortex shedding in the wake and recirculation. These flow phenomena are widespread in the aerospace industry and on aircraft. Over the years, the flow past cylinders have intrigued and challenged researchers. There is a wide range of studies conducted at various Reynolds numbers that will ease in selecting applicable flow conditions. [12]

The flow separation and the vortex shedding are significant parts of the flow around a cylinder and bluff bodies in general. Chapter 2.2 discusses the mechanisms that lead to separation and vortex shedding. These phenomena are considered to be unsteady or time-dependent. Unsteady CFD (Computational Fluid Dynamics) simulations are needed to capture these effects accurately [4]. In order to ensure accurate and reliable simulation results, the tools available need to be understood and used correctly. This chapter focuses on the fundamental setup and the effects of various parameters on the accuracy of unsteady CFD simulations.

An effort was made to ensure economic simulations concerning computational resources, including time spent to study the effects of different parameters on simulation. This effort would yield dividends when faced with more complex geometries and in 3D cases where computation requirements are much higher.

In this chapter, the CFD simulations done where only to see the effect varying specific

parameters will have on the simulation accuracy and the vortex shedding frequency of the cylinder. It is crucial to understand which parameters are more important and what effect these variations will have on the aerodynamic parameters such as the lift and drag coefficients (C_l, C_d) and the vortex shedding frequency (f_{vs}).

A methodology of starting simple and gradually moving to more complex geometry and flows were chosen. Various parameters were tested in a laminar 2D circular cylinder simulation. Other aspects were tested in a turbulent circular cylinder, resembling the flow over an airfoil at high angles of attack. The last case was turbulent flow over a square cylinder. This is a critical distinction due to the mechanics of flow separation over a circular and square cylinder. The increase in simulation complexity ensured that the basic parameters of an unsteady simulation were understood and that the aerodynamic parameters C_l, C_d and f_{vs} were calculated correctly.

3.2 CFD verification and validation

Verification and validation are essential to ensure the results obtained from the CFD software are accurate and trustworthy [39]. The AIAA [40] defines verification and validation as the following:

Verification: The process of determining that a model implementation accurately represents the developer's conceptual description of the model and the solution to the model.

Validation: The process of determining the degree to which a model accurately represents the real world from the perspective of the intended uses of the model.

The verification process entails identifying and quantifying errors in any given computational model and its solutions. In other words, verification is the process of evaluating if the results given by a computational model make sense in terms of the application of the model and whether the results are within a selected range. Validation, on the other hand, is a comparison between adequately accurate simulation results and experimental data. The accuracy of computational results is measured against experimental, physical results. Assuming that it is done correctly, experimental measurements are the most reliable reflection of reality for these purposes. [39]

Siemens STAR-CCM+ provides its customers with access to the verification suite[41], which contains all of the verifications done for each software version. The Verification Suite is a collection of cases from the Simcenter STAR-CCM+ quality assurance process. The process includes STAR-Test. STAR-Test is an internal test system that is continuously used in the development of software packages. The version of Star CCM+ used in this study was Simcenter STAR-CCM+ 2019.1 Build 14.02.010.

This chapter's verification cases of interest were; Karman vortex shedding, turbulent flow over a surface mounted rib and transitional boundary layer. The verification case of the Karman Vortex Shedding of a cylinder in laminar flow was that the vortex shedding frequency was within 0.1% of the theoretical value, and thus the test was considered

passed. The SST $k-\omega$ solver's results were considered for the turbulent flow over a surface-mounted rib. The velocity profile was compared against the required values and was found to be within a tolerance of 1×10^{-2} m/s. This verification case passed and was considered acceptable. The final verification case was that of a transitional boundary layer. The $k-\omega$ turbulence model results were considered. The acceptance criteria of the verification case were that the average unsigned relative differences in the laminar skin friction coefficient be within 15%, and it was found to be 4.84%. In contrast, the turbulent skin friction coefficient was 10.57%. Both the skin friction coefficients were within tolerance, and thus the verification was adequate [41]. It can be concluded that the software is verified and that a verification study is not necessary for the current study.

Verification is only one part of ensuring accurate and reliable results. The other part, as mentioned above, is validating the simulation. The validation cases done in Chapter 3 were a circular cylinder in fully laminar flow (Section 3.3), a circular cylinder in turbulent flow (Section 3.4) and a square cylinder (Section 3.5).

3.3 Circular cylinder in laminar flow

A circular cylinder was chosen for several reasons. There is an abundance of information available on flow over a cylinder, the geometry is simple, and the flow characteristics closely resemble that which would occur when air flows past an airfoil and airbrake setup of a sailplane. These flow characteristics include flow transition, boundary-layer separation, Reynolds number dependency, geometry–dependant vortex shedding in the wake, and recirculation [12].

Only a numerical comparison was of interest for this section to ensure a proper benchmark to compare the results and an understanding of unsteady flow simulations. The chosen CFD reference data, [11], provided enough information to compare results and applicable aerodynamic parameters correctly, focusing on laminar flow over a circular cylinder at Re = 200. The reference study in [11] was a good choice as the Strouhal number of the CFD simulation was within 2% - 13% of experimental results.

The methodology followed was to choose specific parameters that affect the mesh, such as prism layer thickness and the number of prism layer cells. Only one parameter was varied at a time to evaluate the changes of these parameters on the simulation results in isolation. The lift-and-drag coefficients (C_l (Eq 2.2), C_d (Eq 2.5)) and the vortex shedding frequency (f_{vs} (Eq 2.7)), were used to compare these parameter variations.

The vortex shedding frequency is a good measure of the accuracy of the simulation because it describes the flow characteristics and is not dependent on the accuracy of C_l and C_d. The vortex shedding frequency was also the variable used in the verification case mentioned in Section 3.2 and thus provides a suitable means of comparison [41].

The aim of the studies done in Chapters 3.3 and 3.4 was to see which parameters had the most prominent effects on the aerodynamic characteristics (C_d, C_l, and f_vs), as well as to

get a good starting point of mesh sizes, time steps and inner iterations for further studies. These parameters were applied to the validation cases for the different flow cases.

3.3.1 Initial setup

It is relatively simple to calculate an adequate time step when the Strouhal number is known. Equation 2.8 can be used to derive the vortex shedding frequency. This shedding frequency can then be used to calculate an adequately small time step to capture the shedding behaviour as shown in Figure 2.15. However, this is not the case with geometries with unknown Strouhal numbers. An initial time step sweep was run to overcome this, giving a starting time step to use.

The important aerodynamic parameters of the reference study [11] used as a baseline for the validation are tabulated in Table 3.1.

Table 3.1: Aerodynamic properties used as laminar validation baseline [11]

Reynolds number	Strouhal number	Lift coefficient	Drag coefficient
200	0.192	0 +- 0.698	1.376 +- 0.048

Geometry

The flow domain, expressed in terms of the cylinder diameter (D_{cyl}) [m], is a rectangular area of 20 D_{cyl} by 30 D_{cyl}, containing a circle with a diameter D_{cyl}, with the centre point of the circle 10 D_{cyl} above and downstream of relative to the lower left corner of the flow domain. The setup can be seen in Figure 3.1 below.

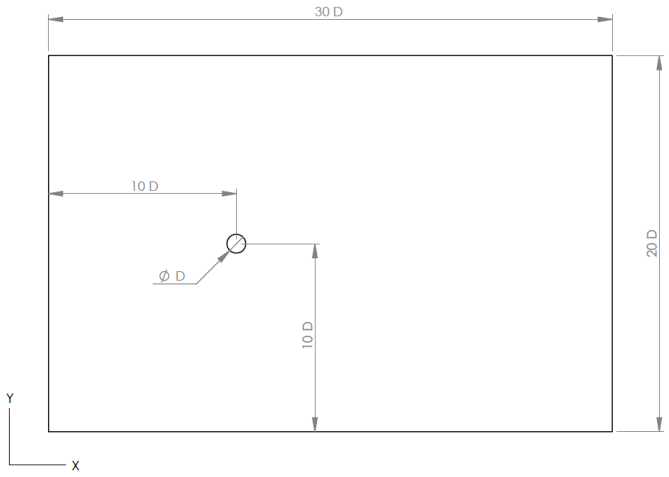

Figure 3.1: Flow domain dimensions

Figure 3.2 below illustrates the boundary conditions selected for the simulations. The left boundary was a velocity inlet with a uniform velocity profile and default turbulence intensity, whereas the right boundary was a pressure outlet. The upper and lower walls were set as slip walls, and the cylinder surface was left as a default wall boundary.

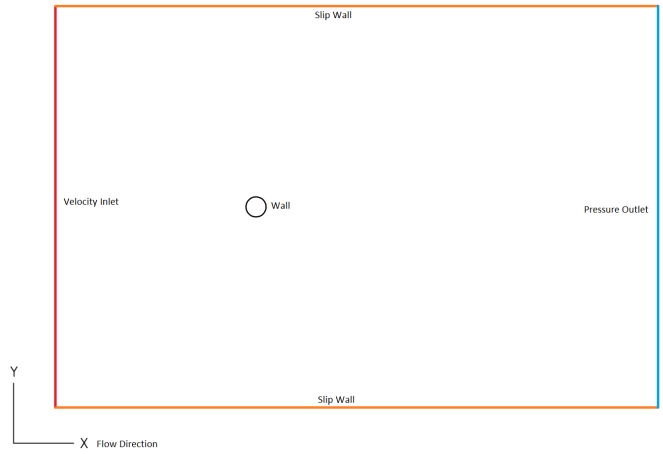

Figure 3.2: Flow domain boundary conditions

Physics setup

The reference study case in [11] provides the Reynolds number (Re) and Strouhal number (St). The Reynolds and Strouhal numbers are defined in Eq 2.1 and 2.8. These equations were used to calculate the unknown parameters not explicitly given in the reference study case. The diameter of the cylinder was chosen as 0.25 m, corresponding to the height of the airbrakes on the JS3 sailplane. For simplicity, the density was set to 1 kg/m^3, ambient pressure as 101.325 kPa and a vortex shedding frequency of 2 Hz was used to avoid time steps in the order of $1 \times 10^{-4} s$ and smaller. As discussed in Chapter 2.3, 10 - 20 points per period is required to start capturing the flow physics and using 2 Hz will yield a starting time step of 0.025 s. This was only the initial time step and no time step dependence studies have yet been done, the selected time step would still decrease, which would lead to increased simulation time.

Table 3.2 below list all the physical properties of the flow used in the initial setup.

Table 3.2: Physical properties used in the simulation of the laminar flow over a cylinder

Variable	Value [Unit]
Reynolds number [Re]	200 [-]
Strouhal number [St]	0.192 [-]
Cylinder diameter [D_{cyl}]	0.25 [m]
Density [ρ]	1 [kg/m^3]
Pressure	101.325 [kPa]
Vortex shedding frequency [$f_v s$]	2 [Hz]
Velocity [V]	2.604 [m/s]
Dynamic viscosity [μ]	3.2552×10^{-3} [Pa.s]

The physics continuum setup was as follows; a 2D setup was chosen using the implicit unsteady solver. Gas was used as the fluid medium with segregated solver. The constant density equation of state was selected using the laminar viscous regime. The Reynolds number of 200 required the use laminar flow regime. The simulation was set up as 2D for the ease and speed at which results would be attained, and changes in setup would deliver these results. The second-order temporal discretization was selected due to the accuracy

and speed of unsteady solutions. The stability of the higher-accuracy discretization scheme was not a problem due to the simplicity of the geometry and mesh. Initially, an arbitrary value of 5 inner iterations was used.

Table 3.3 gives the time steps at various iterations. This time step sweep was done to determine at which time step unsteady flow effects started forming.

Table 3.3: Initial time step sweep

Iterations	Time step [s]
0	1
2000	0.8
4000	0.6
6000	0.4
8000	0.2
10000	0.1
12000	0.08
14000	0.06
16000	0.04
18000	0.02
20000	0.01

Mesh setup

STAR-CCM+ uses a powerful automated mesher to generate the meshes used in the simulations. Different mesh setups were done to see what effects the changes in different parameters had on the accuracy and outcome of the simulation. The initial mesh setup described below is only the starting point, and all other studies will vary from this point. A more detailed description of these variations will be given in each different section.

An unstructured polyhedral mesh was generated with a structured prism layer to capture boundary layer effects. The mesh was generated using the automated 2D mesher. The stretch factor distribution mode was selected with a prism layer stretching factor of 1.0 and a near core layer aspect ratio (AR) of 10. This was to remove the forced prism layer reduction to comply with a given prism layer ratio. Having the near core aspect ratio, for example 0.75, will limit the prism layer thickness as the surface size is reduced.

The default controls for the mesh were as follows; the base size (BS) was the diameter of the cylinder (D_{cyl}). Custom sizes (CS) is a percentage value of the mesh base size, allowing uniform refinement by only changing a single value. This is a very convenient way of running mesh refinement studies and was used throughout this section and simulations.

The cylinder surface used a custom size of 15%. The surface growth rate was chosen as 1.1 to ensure an adequate gradual transition from the finer mesh near the cylinder to the free stream mesh. The other parameters were redefined in dedicated surface controls for the cylinder nodes and flow domain boundaries.

Custom volume controls were added to control the mesh setup further. A maximum

surface custom size of 15% was used as an initial starting point. The prism layer thickness was set to the absolute value of $0.5D_{cyl}$ or 50% of the base size (125mm). An arbitrary number of prism layers of 9 were chosen as a starting point.

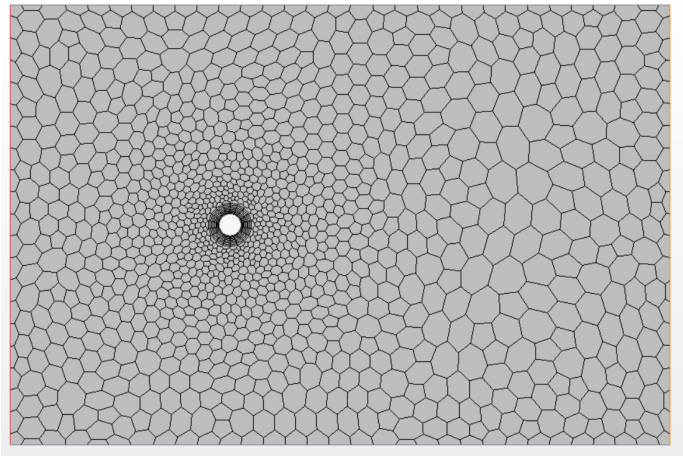

Figure 3.3: Initial generated mesh

Figure 3.3 illustrates the initial mesh used for this initial simulation.

Results and discussion

An initial simulation was done to determine the time step at which unsteady flow characteristics would start appearing. The initial simulation results are shown in Figure 3.5 with the simulation run until all the residuals converged below 0.01 for each inner iteration. The vortex shedding frequency was calculated using a power spectral density (PSD) plot.

The PSD is used to analyse signals and, according to [42], is mostly used to analyse random singles. The PSD is used to normalise the signal in the frequency bandwidth, giving the strength of the frequency content. This is ideal for determining the dominant frequencies in the signal, thus giving the vortex shedding frequency.

The vortex shedding frequency is a function of the Strouhal number, as seen in Eq 2.8 in Section 2.2. The vortex shedding frequency is used for flow validation in the Star CCM+ verification suite [41] and will be an adequate means to measure and compare the flow characteristics of the cylinder. The Strouhal number is used as a means of flow validation in literature summarised in Section 2.4.1. As the Strouhal number remains the same for the given Reynolds number, only the vortex shedding frequency will change and converge as mesh refinement is done.

This can be explained by the Nyquist criteria [43], stating simply that a time step of at least half of the shedding frequency is required to capture a signal or the unsteady behaviour in this case. However, [44] mentions that more points are required to capture the behaviour of the studied wave. This is illustrated in Figure 3.5, where convergence only started after 16000 iterations at a time step of 0.04 s, more than ten times smaller than the expected shedding frequency.

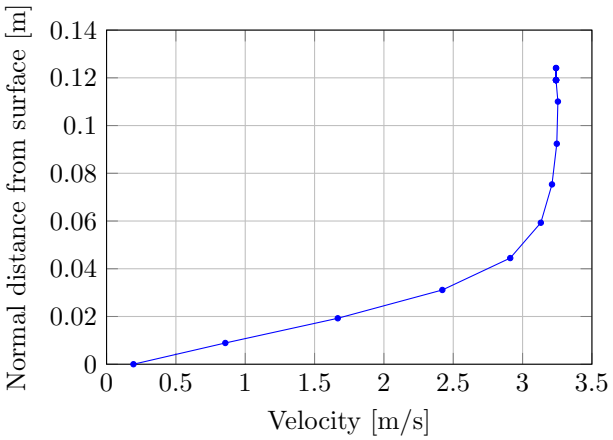

Figure 3.4: Boundary layer velocity profile at the top of a circular cylinder at Re = 200

Figure 3.4 shows the flow's velocity profile normal to the cylinder's surface at the top of the cylinder. The prism layer thickness of 0.5 D_{cyl} (125mm) was sufficient to fully capture the boundary layer as the laminar velocity profile has fully developed inside the prism layer. The velocity near the surface is close enough to 0, and these results will only improve as further prism layer refinements are made.

The initial mesh generated had a base size of 0.25 m using a custom surface size of 15%. This resulted in 1506 elements and had a vortex shedding frequency of 1.699 Hz. The expected time for a single vortex from one of the surfaces (upper or lower) was 0.589s. This corresponds well with the results in Figure 3.5. The unsteady phenomena started to appear as soon as the time step was smaller than the vortex shedding time. It is clear that decreasing the time step affects the C_d value.

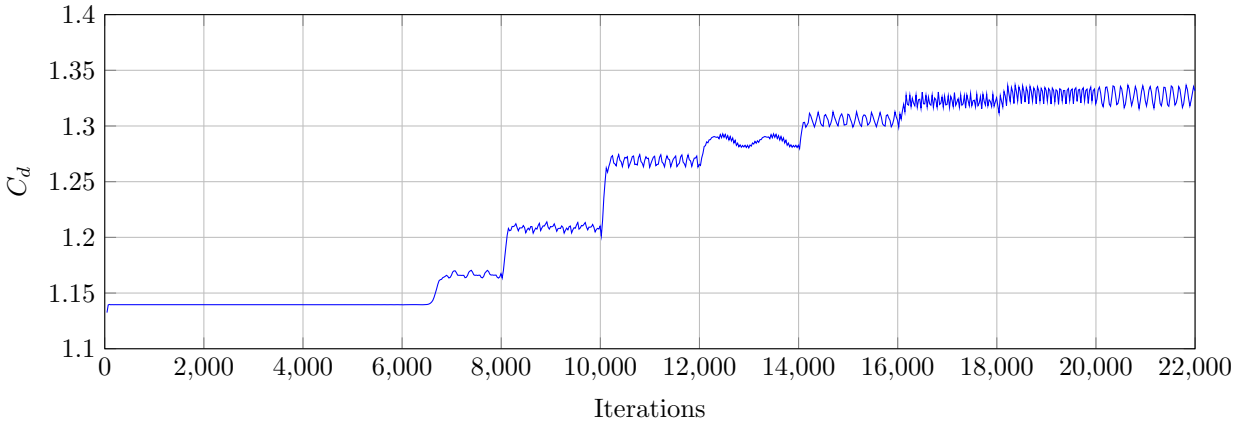

Figure 3.5: Drag coefficient variations due to changing time steps

A time step independence for this generated mesh was reached at a time step of 0.04s. Both the C_l and C_d values remained the same. These results clearly illustrate that a time step dependence should be considered within a given mesh.

3.3.2 Key mesh refinement regions

Arguably the most important part of a CFD setup is the mesh elements around the surface of the geometry. These elements are crucial in accurately capturing and predicting the boundary layer. STAR-CCM+ provides an option to activate the prism layers, which add cells to the surface of the geometry. These structured mesh elements are very customisable to ensure complete control. Second to the prism layer, especially in these highly separated flow conditions, is the wake refinement downstream of a body. It is essential to capture the low pressure region and vortices to ensure accurate results.

The parameters studied were broken down into two larger groups, the parameters affecting the boundary layer and the parameters affecting the wake downstream of the cylinder. The parameters affecting the boundary layer were the surface size of the body and the number of prism layer elements. By fully capturing the laminar boundary layer, the prism layer thickness was seen to be adequate in Figure 3.4.

The downstream length and mesh density of the wake refinement volume control was identified as the parameter of interest. An arbitrary wake refinement region was set up, capturing the wake formed in the initial simulation.

The laminar flow cylinder simulations only serve as a starting point for the more important and relatively more complex turbulent flow simulations in Sections 3.4 and 3.5. This section only served to identify the sensitivity of each parameter and a starting point for the mesh during the mesh refinement study. Only a brief overview of the work done, the setup used and a discussion of the results are given in this section. The results are summarised and given in Appendix A.1.

Simulation setup

Table 3.4: Time step variations at different physical times

Time step [s]	Simulation time [s]
0.06	0
0.04	5
0.02	10
0.01	15
0.008	20

The simulation time of the studies was 30 seconds to ensure completely developed and repeating flow patterns. The vortex shedding frequency was calculated using the power spectral density (PSD) plot of the lift coefficient between 20 s – 30 s. A PSD of C_d yields a plot with a peak at twice the shedding frequency thus, C_l was used. This is due to the shedding frequency being defined as the vortex shedding on a single side of the body (Section 2.2.5). The drag coefficient is affected by the vortices shed from both sides of the body, twice that of the lift coefficient.

Surface size study

Initially, only the effect of the surface size was studied. The surface size directly affects the resolution of the cylinder. The more nodes on the cylinder, the closer the geometry tends to a perfect circle. Fewer points on the geometry lead to the cylinder more closely representing a polygon, and the flow will not represent the flow over a circular cylinder.

This is especially important when the focus of a study is the separation due to adverse pressure gradients. Figure 2.1 illustrates the complex flows in the boundary layer, which must be captured to ensure accurate simulations.

The mesh used in the initial simulations (Section 3.3.1) formed the starting point. The surface size varied from a custom size of 15% of the mesh base size ($D_{cyl} = 0.25m$) to 3% in decrements of 3% per step. A custom surface size of 9% was used, the largest size where the vortex shedding frequency started to converge.

Prism layer element study

Besides the surface size, the number of prism layers affects how many elements are radially in the prism layer. This is an important parameter to capture the velocity change accurately, and momentum loss due to the viscous effects of the flow in the boundary layer [26].

The prism layer study was done to understand the effect of the number of prism layer cells on the simulation's accuracy and the prediction of the flow around the cylinder. The number of prism layer elements used was altered from 3 to 15 in increments of 3.

All of the simulations had the same vortex shedding frequency showing that, in the laminar flow regime, the flow characteristics around the cylinder are not as sensitive to the amount of prism layers cells. The average lift and drag coefficients of 6 and 15 prism layer cells stayed relatively the same, all within 2% of each other. At 3 prism layer cells, the average C_d dropped significantly. Based on this, 9 prism layer cells were chosen for the inner iteration and mesh refinement simulations to follow.

3.3.3 Inner iteration and mesh refinement study

As the study approached the overall mesh refinement phase, the finer meshes required more inner iterations for accurate solutions. Up to this point, only 5 inner iterations (II) were used. This allowed the focus to be on mesh generation and identifying the key parameters that would affect the accuracy.

The inner iterations and mesh dependency studies were done in tandem due to the reliance of the simulation results on the mesh density, the number of inner iterations and the time step used. As the mesh becomes finer, the time steps and inner iterations must be adjusted to reach an independent solution.

Mesh setup

As mentioned above, the wake refinement chosen for the inner iteration and mesh refinement studies had a downstream length of 8 D_{cyl} with a custom size of 20%. This setup allowed all the parameters to scale down as the base size was reduced. The studies were done at different inner iterations, as discussed in the physics setup below. The mesh size inner iteration studies were set to have custom sizes of 20%, 15%, and 10%.

The parameters studied above boiled down to the following choices; the custom surface size of the cylinder was 9%, and the prism layer thickness used was 125mm (0.5 D_{cyl}) with the prism layer stretching factor as 1.0. The number of prism layer cells was calculated using equation 3.2 below and was noted in Table 3.5.

Figure 3.6 below shows the generated mesh of 10% base size. The mesh incorporates all of the elements studied up to this point and added refinement upstream of the cylinder.

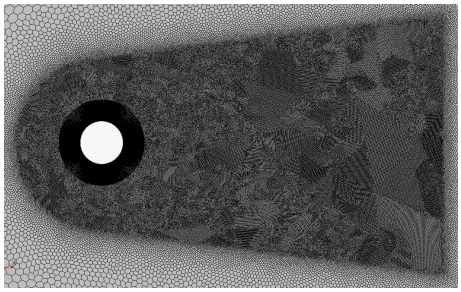

Figure 3.6: Generated mesh for inner iteration and mesh refinement simulations with base size 10%

An area of note was the number of prism layer elements used in the finer meshes. As the base size decreased, the length of each prism layer cell was reduced. This led to the aspect ratio (AR) of the prism layer cells increasing due to the prism layer thickness and the number of cells remaining the same. To counteract this, the same aspect ratio of the prism layer cells in Section 3.3.2 was used to adjust the number of prism layer cells in the finer meshes. The aspect ratio was calculated to be 0.62. An aspect ratio of 0.7 was selected for ease of calculation.

$$AR = \frac{\frac{PL_T}{PL_{NOC}}}{SS_{\%} \times BS} \tag{3.1}$$

Where PL_T is the prism layer thickness [m], PL_{NOC} is the number of prism layer cells, $SS_{\%}$ is the percentage of the minimum surface size (in terms of $0-1$) and BS is the base size of the mesh [m]. The numerator, consisting of the 2 prism layer terms (PL_T and PL_{NOC}), gives a rough approximation of the average cell height in the prism layer, as the stretch factor was kept at 1.0. The denominator gives the approximate minimum length of the prism layer cell. This term is an estimation factor to keep the ratio between these parameters consistent as the base size changes.

Equation 3.1 can be written in terms of the number of prism layer cells as seen in equation

3.2.

$$PL_{NOS} = \frac{PL_T}{AR \times SS_{percentage} \times BS} \tag{3.2}$$

The number of prism layers at base sizes 100% to 30% range from 9 to 27, respectively. This ensured that all cells in the prism layer had an aspect ratio lower than 1. The number of prism layers at the lower base sizes is shown in Table 3.5.

Table 3.5: Number of prism layer cells per mesh base size

Mesh base size [%]	Number of PL cells
20	40
15	53
10	80

Physics setup

The initial inner iteration study was done at 20% D_{cyl} base size at inner iterations ranging from 5 - 20 with increments of 5. This was done to determine which inner iterations to use for the mesh refinement study at base sizes 1 D_{cyl} - 0.3D_{cyl}. The Second part of the inner iterations study focused on the finer meshes of 0.15 D_{cyl} and 0.1 D_{cyl}. These meshes used inner iterations ranging from 15 - 30 in increments of 5.

As the base size decreased, the chosen time steps mentioned in Table 3.4 were inadequate to ensure time step independence. The time steps used for the inner iterations study were chosen as shown in Table 3.6. To ensure time step independence, the time steps were changed to 0.002 s lower than what was necessary. This ensured the C_d and C_l values converged and that the change in time steps didn't alter these values.

Table 3.6: Time steps used at various mesh densities during inner iteration study

Physical	Time step [s]	
time [s]	20% D	15% D - 10% D
0	0.04	0.02
5	0.02	0.01
10	0.01	0.008
15	0.008	0.006
20	0.006	0.004

The variation in time steps plays two different roles, namely ensuring time step independence and the flow fully developed using initial larger time steps. Table 3.7 summarises the time steps used at the different meshes in the mesh refinement study. The inner iterations of base sizes 1 D_{cyl} - 0.3 D_{cyl} were set at 15.

Table 3.7: Time steps used at various mesh densities during mesh refinement study

Physical	Time step [s]		
time [s]	100% D - 30% D	20% D	15% D - 10% D
0	0.06	0.04	0.02
5	0.04	0.02	0.01
10	0.02	0.01	0.008
15	0.01	0.008	0.006
20	0.008	0.006	0.004

Results and discussion for the inner iteration study

The C_l plots were very sporadic and inconsistent. Little could be learned when looking at the C_l plots, and thus the focus was placed on the effects of the inner iteration, time steps and mesh changes on the C_d values.

Figure 3.7 clearly illustrates the changes the time steps and inner iterations have on the accuracy of the simulation. Even at a time step of 0.006 s and with a time step independence solution, more than 5 inner iterations are required for an accurate solution. The inaccuracy of the solution due to the inner iterations are reduced as the time steps are decreased so that it is possible to achieve accurate results using smaller time steps or more inner iterations.

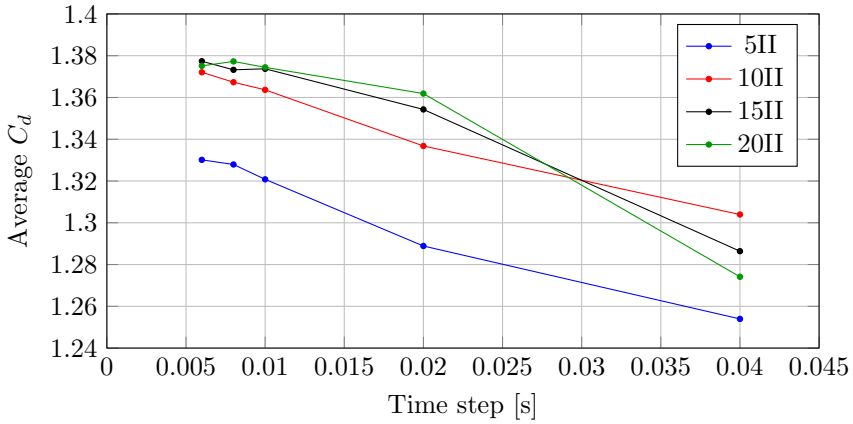

Figure 3.7: Average C_d results at various time steps for different inner iterations - mesh base size 20% D_{cyl}

Figure 3.8 gives the average C_d results for the different time steps as mentioned in Table 3.7 as the change in inner iterations effected it. It is clear to see in Figure 3.8 that the average C_d values converged as both the time step was decreased and as the inner iterations were increased. Figure 3.8b shows the significant difference in average C_d values at a time step of 0.02 s and what a dramatic difference only changing the inner iterations had on these values.

The inner iteration independence study results are given in Figure 3.9. The results show the average C_d values at the various inner iterations for base sizes 20% - 10%. These results are at a time step of 0.006 s, where independence was reached for the higher inner

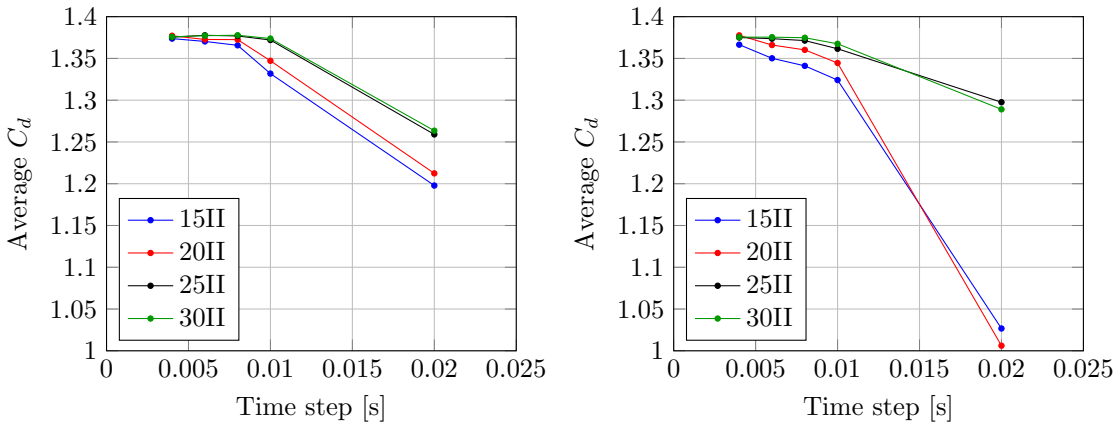

(a) base size 15% (b) base size 10%

Figure 3.8: Average C_d values at various time steps for different inner iterations of a) 15% and b) 10% base sizes

iterations.

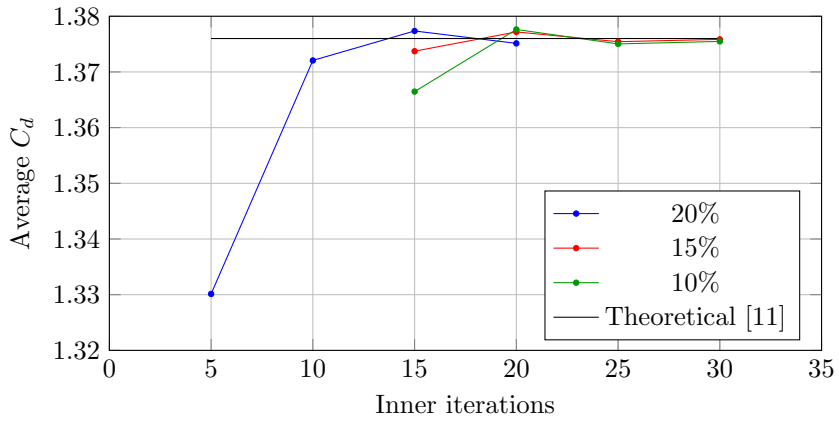

Figure 3.9: Average C_d vs Inner Iterations of base sizes 20% D_{cyl} to 10% D_{cyl} at time step 0.006 s

The vortex shedding frequency for all the cases mentioned above was 2.0996 Hz except for 1.9996 Hz at 5 inner iterations and a base size of 20%. The inner iterations used in the mesh refinement study at base sizes 20% D_{cyl}, 15% D_{cyl} and 10% D_{cyl} were 15, 25 and 25, respectively.

Results and discussion for the mesh refinement study

Figure 3.10 below shows the results of the average C_d values vs time steps at six chosen mesh densities from 1 D_{cyl} - 0.1 D_{cyl}. As expected, as the mesh is refined, the results tend towards the theoretical C_d value (1.376). A time step independence was reached at 0.02 s for base sizes 1 D_{cyl} to 0.3 D_{cyl} and 0.04 s for base sizes 15% D_{cyl} and 0.1 D_{cyl}. The maximum CFL number was 1.4 at base size 1 D_{cyl} and 8.2 at base size 0.1 D_{cyl}. The results show that, even though the ideal CFL is > 1, the results converged with high accuracy even at larger CFL values.

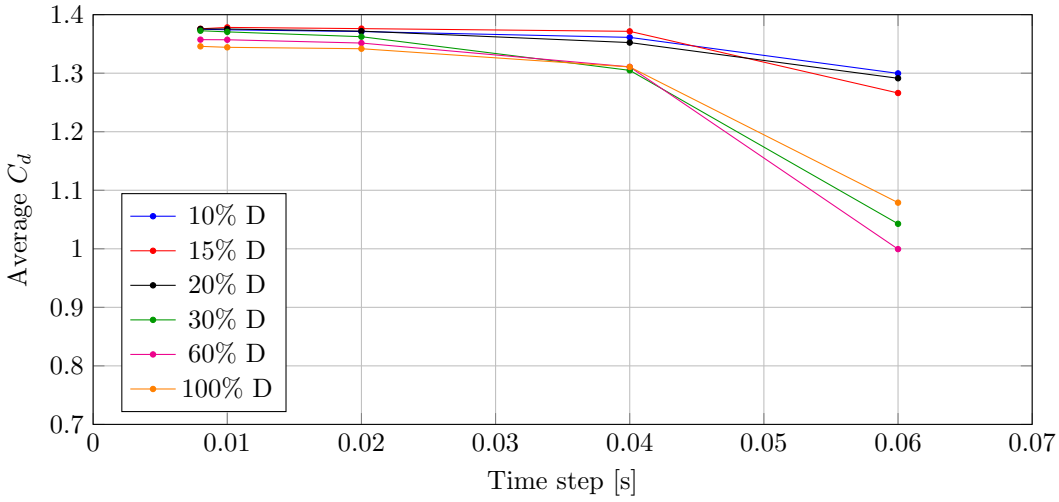

Figure 3.10: Average C_d values vs time steps of different base sizes

Table 3.8 below summarises the results obtained during the complete mesh refinement study. The results were taken at a time step of 0.008 s to ensure complete independence was reached. Due to the nature of the simulation, results were achieved in very little time, and the most efficient combination of time steps and inner iterations was not considered for this study. The primary consideration was the effects of time steps, inner iterations and mesh densities on the results.

Table 3.8: Laminar cylinder mesh dependency results at time step 0.008 s

Base size (% D_{cyl}) / (m)	Element count	f_{vs} [Hz]	Average C_l	Average C_d
100 / 0,25	4028	1.9	0.0024	1.3459
90 / 0,225	4693	1.9	0.0055	1.3533
80 / 0,2	5523	2.0	-0.0031	1.3490
70 / 0,175	6825	2.0	-0.0046	1.3558
60 / 0,15	8593	2.0	0.0032	1.3573
50 / 1,125	11127	2.0	-0.0055	1.3636
40 / 0,1	16070	2.0	-0.0189	1.3689
30 / 0,075	26880	2.1	-0.0177	1.3726
20 / 0,05	53912	2.1	-0.0248	1.3756
15 / 0,075	88697	2.1	-0.0035	1.3758
10 / 0,025	191213	2.1	0.0055	1.3751
Reference CFD [11]			0 +- 0.698	1.376 +- 0.048

The 5% deviation in the vortex shedding frequency can be explained by how the theoretical frequency, in Section 3.3.1, was calculated. The truncation of the chosen parameters used in the simulation physics setup (velocity, density and dynamic viscosity) may cause the deviation at finer meshes. However, the shedding frequency is close to the expected frequency; thus, the PSD method of calculating the frequency can be used in further studies. The slight deviation of the average C_d at 10% base size, in Figure 3.11 can be attributed to the mesh becoming too fine, which can cause other unforeseen numerical problems.

Figures 3.12a and 3.12b shows the C_d and C_l values vs physical time. As mentioned in

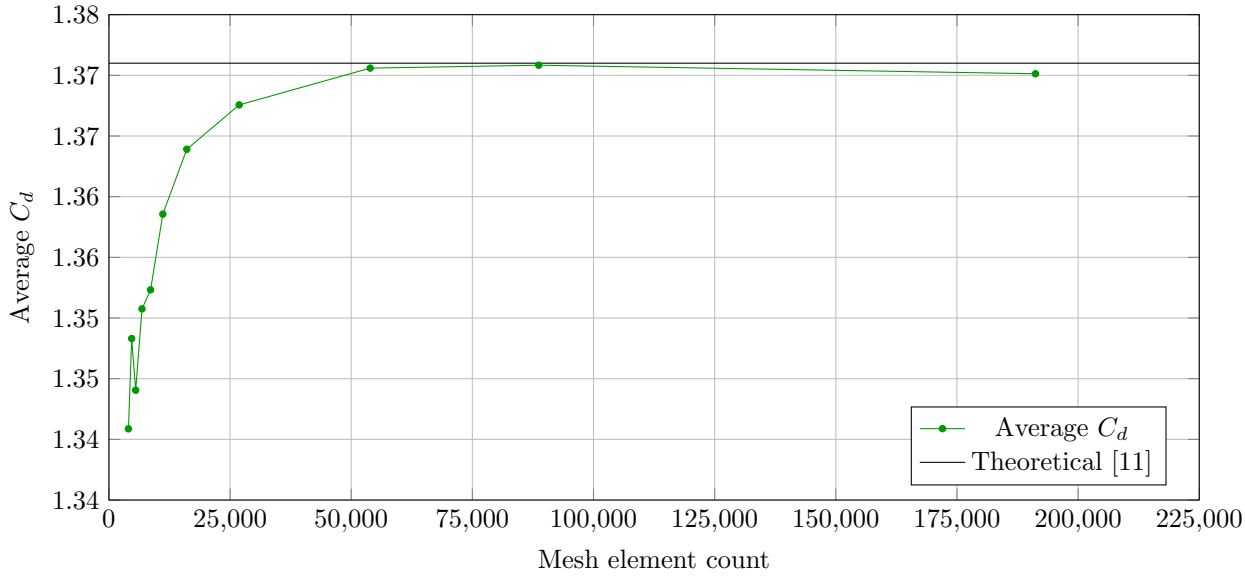

Figure 3.11: Average C_d values vs number of mesh elements at time step of 0.008 s

Table 3.7, the time steps change after every 5 seconds. The change in time steps is not as prominent due to the fine mesh and relatively high inner iterations used. It is clear to see the good correlation with the theoretical values[11] when taking the average lift and drag coefficients and the amplitude of the waves into consideration, with the points illustrating the maximum, minimum and average values.

Figure 3.13 shows the velocity contours of the flow past the cylinder. It is clear to see the Von Karman vortex shedding in the wake of the cylinder. Figure 3.14 clearly shows the recirculation downstream of the cylinder.

The C_d and Strouhal number of the laminar circular cylinder simulation was 1.375 and 0.2016, respectively. This compared well with the numerical results of [11]. The average C_d is within 0.07%, and the Strouhal number is within 5%. The slight deviation of the Strouhal number can be explained by rounding or numerical errors.

3.3.4 Summary

The work done in chapter 3.3 lays the groundwork for all of the work to follow in this study. The fundamentals of unsteady flow simulations regarding bluff bodies had to be learned and understood to progress to high angle of attack airfoils and airfoils with extended airbrakes.

The overall process followed was that for each new case, an initial time step sweep was done to identify at which time steps the characteristic flow phenomena would occur. Choosing an adequate time step is simple when the Strouhal number is known, but more complex geometries or obscure cases will not give this luxury. After the initial time step run, work was done on an adequate mesh for the specific case. Areas of interest were the boundary layer and the wake of the geometry.

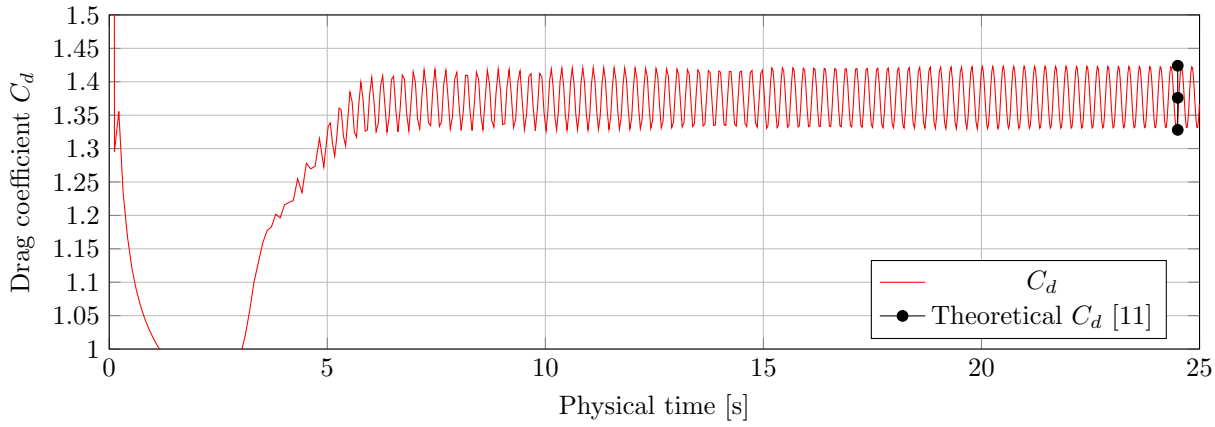

(a) Drag coefficient C_d

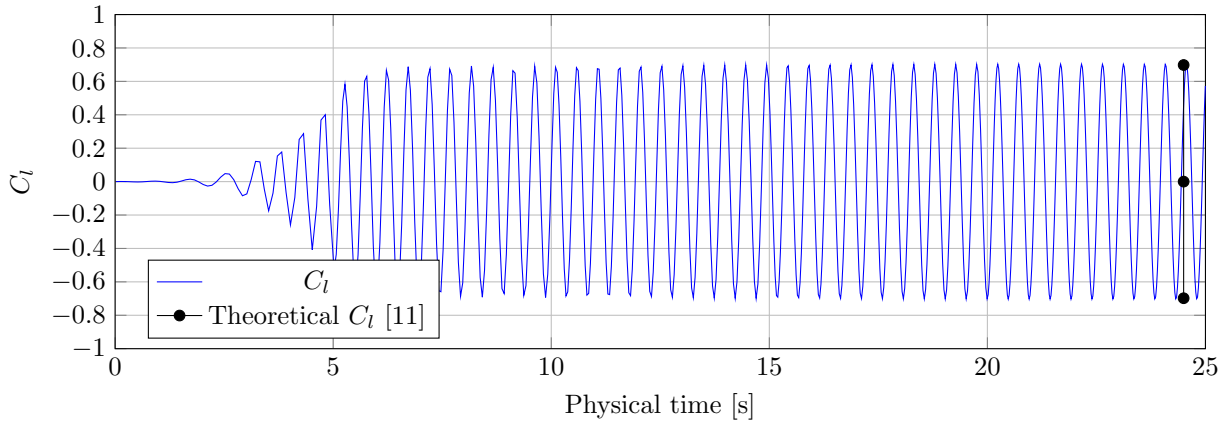

(b) Lift coefficient C_l

Figure 3.12: C_d (a) and C_l (b) vs physical time [s] at base size15% of laminar flow (Re = 200) over a circular cylinder

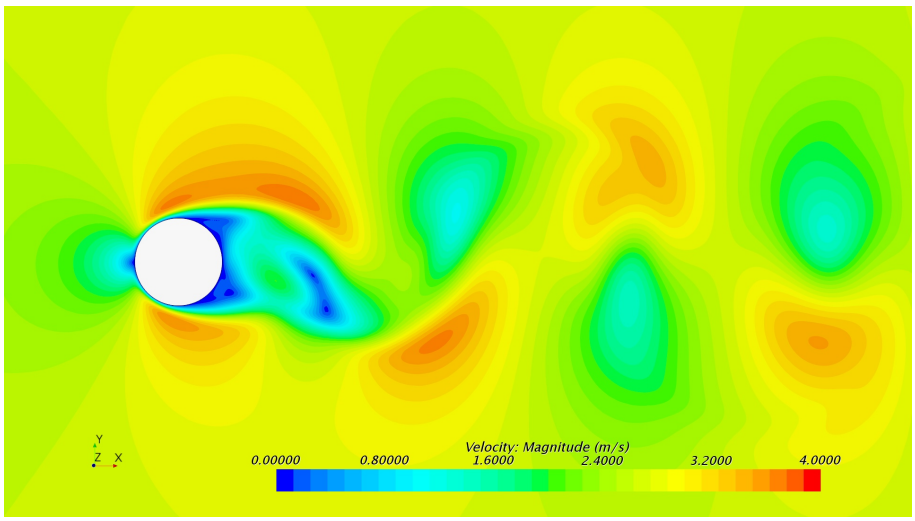

Figure 3.13: Velocity contours at base size 15%

The initial simulations illustrated the effects of using a time step that is sufficiently small enough, at least twice the period of the vortex shedding. In this case, this was at a time step 10 times smaller than the shedding period where the force coefficient convergence started. Once the time step range has been identified, the vortex shedding frequency was not sensitive to the changes made to the mesh parameters studies as it remained within 5% of the initially selected frequency of 2 Hz.

The mesh parameters studied prior to the time step and inner iteration independence studies were the surface size refinement, the number of prism layer cells and the wake refinement length and density. The force coefficients were more sensitive to these parameters as the mesh density increased with mesh cells. The change in surface size significantly affected the force coefficients, as they changed linearly as the surface mesh size decreased. The number of prism layers and wake refinement resulted in force coefficients converging after a certain point (as seen in A.1, indicating less sensitivity.

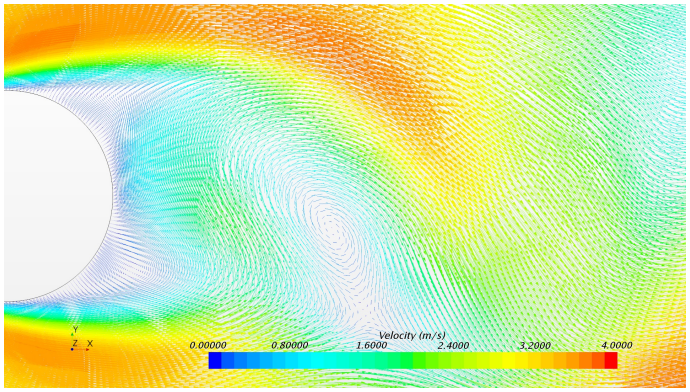

Figure 3.14: Velocity vectors at base size 15%

The parameters causing the most significant change in the force coefficients are the combination of inner iteration, time step and mesh density. This is most clearly indicated in Figures 3.7 and 3.8. Even after force coefficient convergence has been attained for a given time step sweep, changing the inner iterations further changes the simulation results.

Even though these studies have been done only in the laminar regime, light has been shed on the important parameters going forward. This gave a good starting point when more complexity, in the form of turbulence, was introduced.

3.4 Circular cylinder in turbulent flow

The next step in understanding unsteady flow simulations, and a step closer to the ultimate goal of accurately simulating the flow over an airfoil and airbrake, is the flow over a cylinder in a turbulent flow regime. The change from a laminar to a turbulent flow regime is significant. The added unpredictability makes solving turbulent simulations much more complicated than pure laminar flow analyses.

In addition to the key parameters studied in chapter 3.3, namely the time step, inner iterations and the density of the overall mesh, more focus was placed on mesh generation

at various key locations, which will be described in more detail below. These focus areas are prism layer parameters and various volume refinements around the cylinder body, followed by a more in-depth study of the wake refinement. Afterwards, inner iteration and mesh refinement simulations were done and compared with numerical results given in [12].

3.4.1 Initial setup

The initial simulation was used as a starting point to see what effects the turbulent solver had on the baseline simulation. An initial simulation was done based on the parameters in chapter 3.3. The baseline simulation also evaluated if the initial Strouhal number was close enough to what was expected.

The reference results is flow over a circular cylinder at Reynolds number 3.6×10^6, with a drag coefficient of 0.535 and Strouhal number of 0.311 [12]. The specific case used had low turbulence incoming flow with a forced trip at 65°. The average C_d of the reference CFD results in [12] are between 13.7% and 29.6% of the experimental data, whereas the Strouhal number is within 15.2%. This illustrates that capturing these highly separated and turbulent flows is inherently difficult.

The aerodynamic parameters used as the validation baseline case, found in [12], are tabulated in Table 3.16.

Table 3.9: Aerodynamic properties used as turbulent validation baseline [12]

Reynolds number	Strouhal number	Drag coefficient
3.6×10^6	0.311	0.535

Mesh setup

This initial study's flow domain and boundary conditions were identical to those used in chapter 3.3.1. The mesh needed to be adapted for the turbulent flow and the higher Reynolds number. Contrary to the mesh used in the laminar simulation in Section 3.3.3, the mesh in the turbulent simulation required more fine-tuning and customisation. Additional volumetric refinement zones were added to ensure sufficient variability during the initial simulation. The initial mesh was kept relatively simple.

As with the initial mesh in Section 3.3.1, the mesh was generated using the automated 2D mesher. Polygonal volume mesh and the prism layer mesher were used. The additional prism layer options can be found in Table 3.10. These options were from [45].

The default controls used in the mesh generation were as follows; the base size of the mesh was varied to find a good starting point for the simulation and is explained in Section 3.4.1. The base size was set as the cylinder diameter (D_{cyl}), and the surface growth rate used was 1.

Various custom controls were set up for more customisation and control of the mesh.

Table 3.10: Additional prism layer options

Property	Value
Stretching factor	Hyperbolic tangent
Distribution mode	Stretch Factor
Gap fill percentage	25
Minimum thickness percentage	0.01
Layer reduction percentage	0
Boundary march angle	85
Near core Aspect Ratio	10

These custom controls include a custom surface control for the cylinder: volume controls to have more control over the mesh around the cylinder and a surface control on the edges of the flow domain. Figure 3.15 shows the generated mesh used in the initial simulation at 10% base size. It is clear to see the different volume controls used.

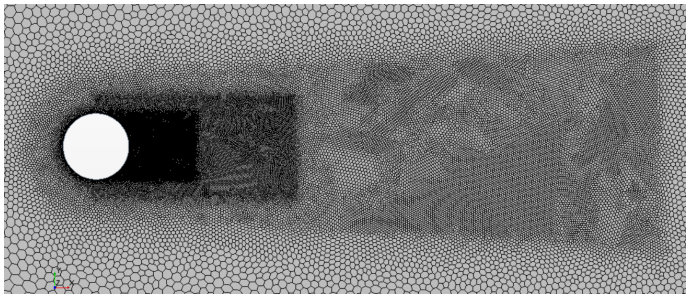

Figure 3.15: Generated mesh of initial simulation at base size 10%

The custom surface control used for the cylinder surface had a custom target and minimum surface sizes, and custom surface curvature selected. The prism layer setup used the custom number of prism layers, total thickness, and distribution parameters. The target and minimum custom surface sizes were set to 9% of the base, as selected in Section 3.3.3. The surface curvature was set to 85 points/circle. The custom prism layer properties used were; 25 prism layers, 1.05 prism layer stretching, and a prism layer thickness of 0.01 D_{cyl} (2.5mm).

The volume controls were added to capture the flow separation, recirculation and vortex streets. The volume control directly downstream of the body was added to capture the recirculation and the significant pressure drop at the rear of the cylinder. The volume control further downstream was used to capture the separation more accurately and the effects on the flow. The final volume control, the wake refinement, was used to capture the vortex streets and their effect on downstream flow. The custom sizes for these volume controls were 10%, 20% and 40% of the base, respectively. These arbitrary values were chosen as a logical start, and further tests on ideal base sizes and their effects were done later in this section.

Physics setup

Most of the differences between the laminar and turbulent solvers can be found during the setup of the physics continuum. As with the CFD reference data in Section 3.3.1, only the Reynolds and Strouhal numbers were given. Using these values with equations Eq 2.1 and 2.8, the physical properties of the flow were calculated and are given in Table 3.11. The same assumptions for the diameter, density, ambient pressure and vortex shedding frequency made as in Section 3.3.1 also apply in this section.

Table 3.11: Physical properties in the simulation of the turbulent flow over a cylinder

Variable	Value [Unit]
Reynolds number [Re]	3.6×10^6 [-]
Strouhal number [St]	0.311 [-]
Cylinder diameter [D_{cyl}]	0.25 [m]
Density [ρ]	1 [kg/m^3]
Pressure	101.325 [kPa]
Vortex shedding frequency [f_{vs}]	2 [Hz]
Velocity [V]	1.608 [m/s]
Dynamic viscosity [μ]	1.1165×10^{-7} [Pa.s]

The physics continuum was set up as follows; a 2D setup was chosen using the implicit unsteady time step. Gas was the material of choice, using segregated flow and constant density. The RANS (Reynolds-Averaged Navier-Stokes) turbulence model with the $k-\omega$ SST turbulence and Gamma - ReTheta ($\gamma - Re_\theta$) transition model was chosen. Direct Eddy Simulations (DES) were not an option for a 2D simulation. The all y^+ wall treatment was used. The $k-\omega$ SST turbulence model is well suited for this type of application, as discussed in detail in Section 2.3.2. This section did not focus on generating a mesh with a low y^+. The focus on low y^+ and a $y^+ < 1$ was done in a following section.

The $\gamma - Re_\theta$ Transition model requires a free stream edge value. This value is a user defined field function that was set to be above the prism layer. The field function was set as the same value as the chosen prism layer thickness. All other physics continuum properties, except material properties, were left as default.

The implicit unsteady solver was set to 2nd-order temporal discretisation as discussed in Section 3.3.1. The stopping criteria formed part of the variables tested in the simulations and will be further discussed later in this section. The initial inner iterations were set to 25. Table 3.12 gives the chosen time steps at various mesh densities. The time steps change at 5 and 10 seconds.

Table 3.12: Time steps used at various mesh densities during initial simulation

Simulation	Time step [s]	
time [s]	40% D, 30% D	20% D, 15% D, 10% D
0	0.01	0.01
5	0.008	0.008
10	N/A	0.006

Results and discussion

The drag coefficient values were not as important in the initial simulation. The results merely served as a starting point for the studies to come. The flow characteristics were, however, meaningful, and it was essential to ensure that the starting mesh predicted the flow correctly. For this, the vortex shedding frequency (f_vs) was used to represent the fully developed flow. Nevertheless, the results of average C_d values at the various time steps and different meshes can be found in Figure 3.16.

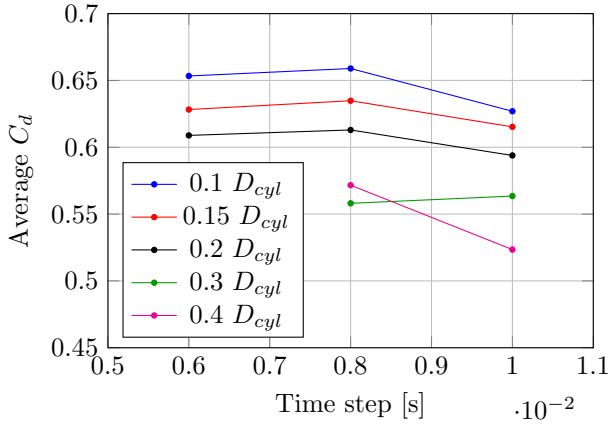

Figure 3.16: Average C_d values vs time steps of the initial high Re simulation

Table 3.13: Results of the initial simulation for turbulent flow over a circular cylinder

Base size [m] (% D)	Element count	f_{vs} [Hz]	Average C_d at 0.01	at 0.008	at 0.006
0.1 (40%)	9648	2	0.523	0.572	-
0.075 (30%)	13794	2	0.563	0.558	-
0.05 (20%) *	24169	1.9996	0.594	0.613	0.609
0.0375 (15%)	63120	1.9996	0.615	0.635	0.628
0.025 (10%)	68778	1.9996	0.627	0.659	0.653
Reference CFD [12]			0.535		

* Representing the chosen parameter for following studies

Important parameters such as the vortex shedding frequencies (f_{vs}), the number of elements and the average C_d at the different time steps can be found in Table 3.13. The vortex shedding frequency corresponds well with the expected shedding frequency (2 Hz), indicating that the initial mesh is a good starting point to capture the flow characteristics. On the other hand, the average C_d values deviated from the theoretical value (0.535) as the mesh density increased. Figure 3.16 represents the average C_d at the various time steps. A mesh with a base size 0.2 D_{cyl} was used as the starting point for further studies.

The chosen prism layer thickness (2.5mm) was sufficient to capture the fully developed boundary layer initially. The velocity profile in Figure 3.17 was captured at the cylinder top. The fact that the velocity at the surface of the cylinder, according to Figure 3.17, is not 0 m/s, illustrates that more refinement and work needed to be done on the prism layer. This work is described in more detail in Section 3.4.2.

The time steps chosen corresponded with the finding at the finer meshes in Section 3.3.1.

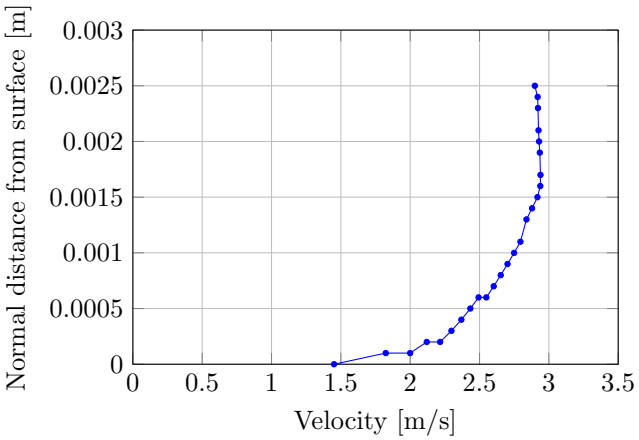

Figure 3.17: Boundary layer velocity profile of flow over a cylinder at for Re = 3.6×10^6

This was expected as the vortex shedding frequency was similar, and velocities were in the same order.

3.4.2 Key prism layer refinement regions

The key parameters and focus areas in mesh generation studied in this section are broken down into two parts. These are the prism layer parameters and mesh refinement around and behind the cylinder.

The parameters focused on in the prism layer were the prism layer stretching and the number of prism layer elements. Prism layer stretching wasn't considered in the previous section. In conjunction with the prism layer stretching, the number of prism layer elements will be revisited. As shown in Figure 3.17, the initial prism layer setup could not fully capture the boundary layer of the turbulent flow.

The second group of parameters are volume controls in key regions around the cylinder. These are in the predicted separation region, the recirculation zone and further mesh refinement simulations in the wake. Only a brief overview of the mesh setup and results are discussed in this section. More detail on the mesh and the results can be found in Appendix A.2.

Prism layer stretching

The Prism layer stretching parameter controls the growth rate of successive cells in the prim layer. This was vital in accurately capturing the velocity profile of the boundary layer flow.

The mesh used in the prism layer study was similar to that in Chapter 3.4.1. The only difference was the variation of the prism layer stretching. The initial step was from 1.05 to 1.1 and then to 1.8 in steps of 0.1.

Figure A.10 summarises the average C_d results of the prism layer simulations. There was

no discernible difference in the average C_d as the time steps (Table 3.12) decreased, thus the average C_d for the entire duration was taken. The vortex shedding frequencies were the same for all stretching factors (1.9996 Hz).

Even though the average C_d values have not converged, it can be seen that the average C_d was directly proportional to the prism layer stretching factor. Increasing the prism layer stretching further, however, will cause the aspect ratio of the prism layer cells to be not ideal and cause other unforeseen complications. Another aspect of increasing the stretching factor is that the cells near the top of the prism layer will become more coarse, and the cells near the wall, too fine. This may lead to false diffusion, which could affect the results. A prism layer stretch factor of 1.5 was chosen, being a good compromise between these factors, and is more than sufficient for the purposes of the following simulations.

Number of prism layers

The mesh used in this section was essentially the same, except for the change in the number of prism layer cells. The number of cells started at 20 and was increased in increments of 5 up to 60.

The effect the number of prism layer cells had on the C_d is given in Table A.11. There is a steady increase in the C_d value as the number of prism layer cells reaches 40. The C_d between 40 and 60 prism layer cells are within 8% of each other, whereas the C_d between 20 and 40 cells are within 22%. The remainder of this section used 20 prism layer cells; however, 40 prism layer cells were used in Section 3.4.4.

3.4.3 Key wake refinement regions

This section is a collection of simulations done at different key locations around the cylinder. The adverse pressure gradient triggers the separation in the boundary layer and will drastically affect the wake of the cylinder. As soon as separation occurs, the region behind the bluff body has a very low-pressure zone compared to the surrounding pressure. This pressure difference, also known as pressure drag, is the most significant contributor to the total drag of a bluff body [2]. Recirculation occurs approximately one diameter behind the bluff body and must be accurately captured. The vortex streets also need to be accurately captured between three and eight diameters behind the bluff body. All of these flow phenomena affect the total drag of the body.

The focus areas in the wake are divided into three overall groups. These groups are the flow separation, the recirculation region behind the cylinder (1 D_{cyl}) downstream from the surface, and the wake further downstream.

Separation zone mesh refinement

The mesh setup and results of the two studies are briefly summarised below. These studies were the effect of the mesh density on a volume control with set dimensions (study 1) and the effect of changing the volume control dimensions while keeping the custom mesh size constant (study 2).

The mesh used in study 1 (Section 3.3.3) was similar to the mesh in Section 3.4.2, except for the addition of circular volume control. The radius of the volume control was arbitrarily chosen as $3R_{cyl}$ (0.375m). The generated mesh can be seen in Figure A.12. The custom mesh size (CS) of the volume control was varied from 10% to 2% using steps of 2%, after which the size was set to 1%. Initially, 20 inner iterations were used. This was not a problem until a sudden drop in the average C_d was seen at a mesh with custom size 1%. The studies at 2% and 1% were repeated using 40 inner iterations. The results at a custom size of 1% returned to an expected C_d. The sudden drop at 1% and 20 inner iterations can be explained by the significant increase of mesh elements and the insufficiency of the simulation using 20 inner iterations to capture the complex flow structures. This emphasises the need for an inner iteration test, especially at higher mesh densities. The simulation of mesh density at 6% of the base size resulted in a vortex shedding frequency of 1.9996 Hz and thus was chosen for mesh refinement simulations.

The mesh used in study 2, was similar to that of study 1, except that the custom size was 4%. These variations were from 1.5 R_{cyl} (0.1875m) down to 1.1 R_{cyl} (0.1375) with steps of 0.1 and then further down to 1.05 R_{cyl} (0.13125m). Figure A.13 gives a visualisation of the generated meshes. All these studies were done at 25 inner iterations, as the mesh was not dense enough to warrant more inner iterations. The average C_d converged at a volume control of 1.3 R_{cyl}, resulting in a 1.9997 Hz vortex shedding frequency.

Recirculation zone mesh refinement

The volume control surrounding the cylinder had a radius of 1.5 R_{cyl} with a custom size of 10%. The added volume control and the generated mesh can be seen in Figure A.15. This volume control originates from the centre of the cylinder and extends to 1 D_{cyl} behind the cylinder (0.25m). The custom sizes started at 10% and were reduced by 2% down to 2% and further down to 1%. The inner iterations were kept at 25.

Figure A.16 plots the average C_d values vs the element count at each volume control custom size. A gradual convergence of C_d can be seen, indicating that a mesh independent solution was achieved. The vortex shedding frequency remained the same at 1.9996 Hz except at data point 1% of the base size, which was 1.4997 Hz. This can be explained by the phenomenon observed in the mesh refinement in the separation zone above.

Wake refinement study

The following section studied the effects of adding a volume control further downstream of the body to capture vortex streets fully. This section combined two studies, the effect of mesh refinement with a constant volume control size and the effect of the length of the wake refinement zone on the solution.

The first study (study 1) focused on the effect mesh refinement had on a volume control with length 3 D_{cyl} (0.75m) downstream from the surface of the cylinder. The generated mesh can be seen in Figure A.17. The custom sizes were varied from 20% down to 10% with steps of 2%. The average C_d values converged from the custom size of 16%. There is a 1.7% difference between the average C_d values at custom sizes of 20% and 16%, indicating that the flow downstream of the body was sufficiently captured and that no real benefits were added by increasing the mesh density.

The second study (study 2) used the same volume control except for the varying lengths. The lengths were varied from 3 D_{cyl} to 8 D_{cyl} in steps of 1 D_{cyl}. The custom mesh sizes for all the various volume control lengths were kept at 20%. Figure A.18 shows the generated meshes of lengths 3 D_{cyl} and 8 D_{cyl} respectively. There were no discernible changes in the average C_d values, indicating that a wake refinement zone of 3 D_{cyl} (0.75m) was adequate.

However, there was a discrepancy in two points (seen in Figure A.19) in the simulation that the automated mesher may have caused. These points, at a custom size of 18% during study 1 and a wake length of 5 R_{cyl} during study 2, were rerun using the double precision version of STAR-CCM+ with similar results. These points did not affect the overall conclusions and can be ignored for the purposes of the wake refinement study.

3.4.4 Inner iteration and mesh refinement study

The final mesh was a combination of the refinement regions and parameters studied in Sections 3.4.2 and 3.4.3. Up to this point, all the studies varied each parameter in isolation to identify which aspects had the most significant overall effect on the simulation results. During the inner iteration and mesh refinement study, the generated mesh was varied by changing the overall base size. The simulation was then run at various time steps and inner iterations to ensure a time step and inner iteration independent solution was achieved.

Mesh setup

The generated mesh consisted of a combination of the above mentioned volume controls with the addition of a wider wake refinement and refinement upstream of the cylinder. It was also essential to capture the high pressure ahead of the cylinder. The custom sizes can be found in Table 3.14 with Figure 3.18 illustrating the generated mesh using base size 10%.

The base sizes for the simulation started at 0.4 D_{cyl} and decreased to 0.05 D_{cyl} in decre-

Table 3.14: Custom sizes of volume controls (% of base sizes))

Volume control	Custom size
Separation zone refinement	6 %
Recirculation zone refinement	10 %
Wake refinement	16 %
Wider wake refinement	20 %

ments of 5%. The number of prism layer cells was set at 40, based on earlier prism layer study (Section 3.4.2) and shown in Figure A.11.

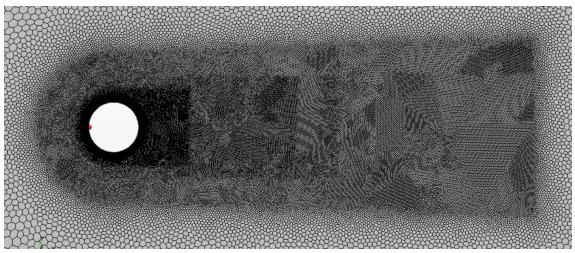

Figure 3.18: Generated mesh with base size 10%

Physics setup

Simulations with base sizes between 0.4 D_{cyl} and 0.25 D_{cyl} used 25 inner iterations, where simulations with base sizes of 0.2 D_{cyl} to 0.05 D_{cyl}, used 40 - 55 inner iterations with increments of 5. However, the two simulations with base sizes of 0.2 D_{cyl} and 0.15 D_{cyl} started with 25 inner iterations before continuing to 40 inner iterations. All the simulations used a time step of 0.008 s for the first 5 seconds, which changed to 0.006 s for the remaining 15 seconds.

Results and discussion

Figures 3.19 show the average C_d of base sizes 0.4 D_{cyl} to 0.1 D_{cyl} using 25 inner iterations. The average C_d results and power spectral density calculations were done with the results taken between $10 - 20$ seconds. It can be seen that reducing the base size while keeping the inner iterations at 25 reduced the overall average C_d. The C_d, however, has converged at approximately 0.63, 18% from the theoretical [12], even after doubling the number of total mesh elements. This indicated that mesh dependence was achieved at 25 inner iterations. The custom sizes used on the volume controls were relative to the base size. This meant that all the volume controls were refined with the overall mesh refinement. This ensured that the mesh was refined in important and applicable locations.

The inner iterations had to be increased to ensure a true inner iteration independent solution of C_d. Figure A.5 gives the average C_d of base sizes 0.2 D_{cyl} to 0.05 D_{cyl} from 25 inner iterations to 55 inner iterations. Increasing the inner iterations on the average C_d was most apparent at base size 0.2 D_{cyl}, with a reduction of 22%. Inner iteration

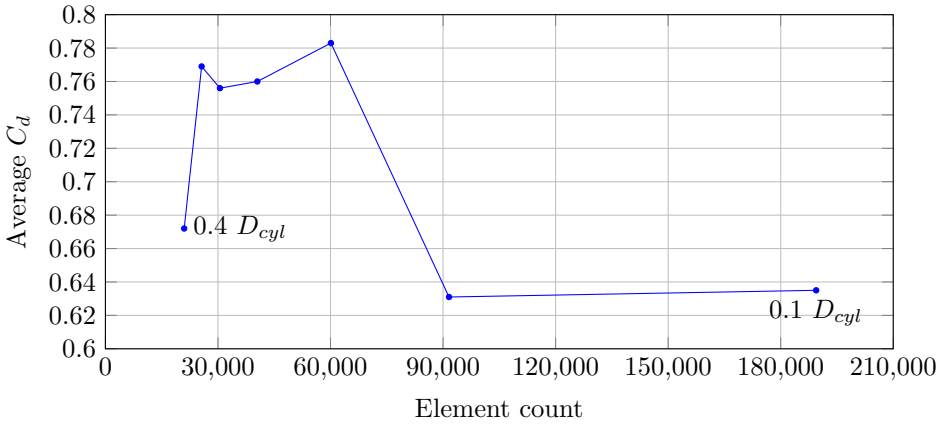

Figure 3.19: Average C_d values at base sizes 0.4 D_{cyl} - 0.1 D_{cyl} using 25 inner iterations

dependence for base sizes 0.2 D_{cyl} and 0.1 D_{cyl} was achieved at 50 inner iterations, and 45 inner iterations for base sizes 0.15 D_{cyl} and 0.05 D_{cyl}.

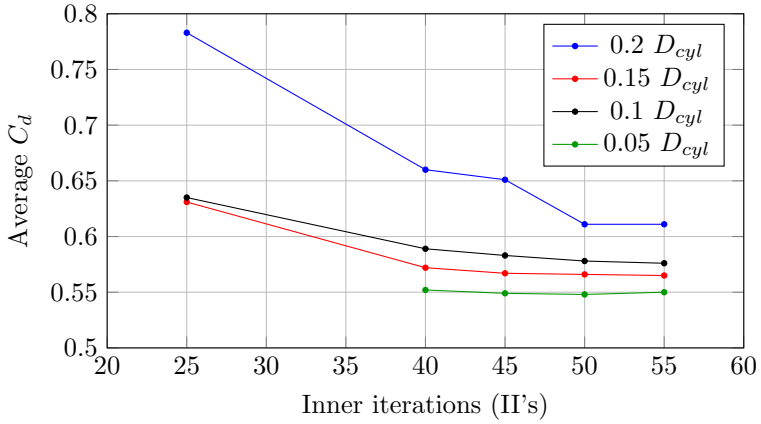

Figure 3.20: Average C_d values vs inner iterations for base sizes 0.2 D_{cyl} - 0.05 D_{cyl}

Figure A.5 shows that a fine mesh required fewer inner iterations to achieve more accurate results than a more coarse mesh with more inner iterations, assuming a constant time step. The time step independent results for all of the studies are summarised in Table 3.15 with Figure 3.21 visually illustrating the convergence of the solution as the mesh refined.

Table 3.15: Results of the mesh and inner iteration dependency studies of a circular cylinder at Re = 3.6×10^6

Base size [m] (% D_{cyl})	Element count	Inner iterations	f_{vs} [Hz]	Average C_d
0.1 (40%)	20997	25	2.0996	0.672
0.085 (35%)	25644	25	2.1996	0.769
0.075 (30%)	30530	25	2.1996	0.756
0.0625 (25%)	40500	25	2.1996	0.760
0.05 (20%)	60113	50	1.9996	0.611
0.0375 (15%)	91587	45	2.0996	0.567
0.025 (10%)	189454	50	1.9996	0.578
0.0125 (5%)	672708	45	1.9984	0.549
Reference CFD [12]				0.535

The simulation of the mesh using 5% D_{cyl} base size resulted in an average C_d of 0.549 and

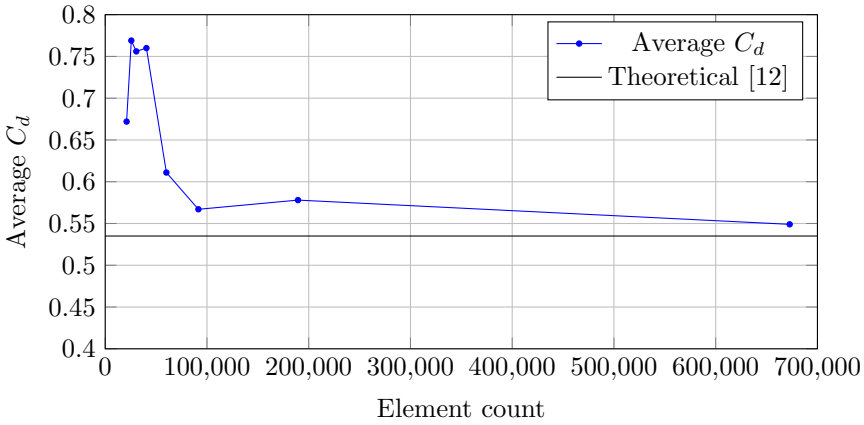

Figure 3.21: Average C_d values of different mesh sizes

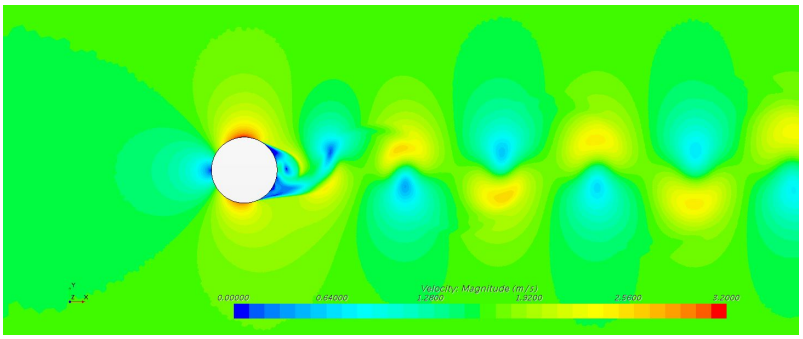

Figure 3.22: Velocity contours at 20 s with base size 5% and $Re = 3.6 \times 10^6$

a vortex shedding frequency of 1.9984 Hz. Using equation 2.8 gives a Strouhal number of 0.3107. Compared to the reference data in [12], the average C_d is within 2.6%, and the Strouhal number is within 0.1%. The slight deviation in C_d results may be due to the forces trip function used in [12], which has not been implemented in the simulations. Additionally, the reference study in [12] was 3D using a variation of the DES model.

3.4.5 Summary

Most of this section's work was on mesh refinement. The time steps and effect of the inner iteration were also prevalent in the turbulent flow regime. More inner iterations were required compared to laminar flow simulations.

The mesh in the prism layer played a more important role in the turbulent flow and required further refinement than initially started. The number of prism layer elements was an important parameter, corresponding more with the required 30 - 60 mentioned in [4]. The mesh elements in the wake, especially close to the body, were important regions to refine.

Combining the mesh refinement and the inner iteration tests ensured that the solutions were independent of these parameters. Little attention was given to the time steps, as convergence was achieved at a time step of 0.006 s. The majority of the elements had a Courant number < 50.

Figure 3.23 illustrates the delay in separation due to the higher Reynolds numbers as seen in Chapter 2.2. The significant recirculation can also be seen within 1 D_{cyl} downstream of the cylinder.

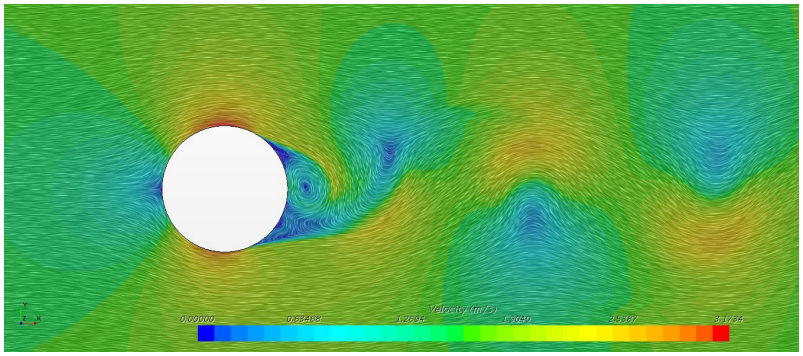

Figure 3.23: Recirculation in wake of cylinder at 20 s with base size 5% and $Re = 3.6 \times 10^6$

3.5 Square cylinder in turbulent flow

The final step in understanding unsteady simulations was to simulate the flow over a square cylinder. A square cylinder has other separation mechanisms than that of a circular cylinder. Flow separation over a square is a more accurate representation of flow over an airbrake. Therefore, it was essential to understand these mechanisms and accurately capture them before any airfoil and airbrake validation attempts were made.

The aim of this section is to apply all of the experience gained from the previous two sections to a more representative case study. Additionally, understanding the flow characteristics will allow better and faster mesh generation and physics setups in the upcoming studies.

3.5.1 Initial setup

An arbitrary initial mesh setup was done based on the volume controls and sizes of the previous section. This was to ensure starting point has a relatively close vortex shedding frequency. The numerical reference study used for comparison is also given in [12]. This reference case was used due to the square cylinder at a high Reynolds number of 2.2×10^4, which was relatively high compared to most of the available literature. The numerical results in [12] compared much better to the experimental reference case noted. The average C_d was between 1% and 15%, and the Strouhal number was within 1.5% of the experimental data.

The aerodynamic parameters used in the square cylinder validation case, also found in [12], are tabulated in Table 3.16.

Table 3.16: Aerodynamic properties used as turbulent validation baseline [12]

Reynolds number	Strouhal number	Drag coefficient
2.2×10^4	0.134	2.18

Mesh setup

An initial simulation was set up to ensure the flow characteristics were in the vicinity of the theoretical values. The boundaries and flow domain setup were kept the same as in the previous studies. The initial mesh adapted aspects of the mesh in the previous section to be more applicable to the new geometry. The mesh was generated using the automated 2D mesher. Polygonal volume mesh and the prism layer mesher were used. The additional prism layer options can be found in Table 3.17, adapted from [45]. The generated mesh had a y^+ lower than one.

Table 3.17: Prism layer options used in the initial square cylinder mesh

Property	Value [Unit]
Stretching Function	Hyperbolic Tangent
Distribution mode	Stretch Factor [-]
Gap fill percentage	25
Minimum thickness percentage	0.01
Layer reduction percentage	0.0
Boundary march angle	85
Near core layer Aspect Ratio	10

The default controls for the mesh were chosen as follows; the base size of the mesh was set to 0.2 D_{cyl}. The surface growth rate was chosen as 1.1.

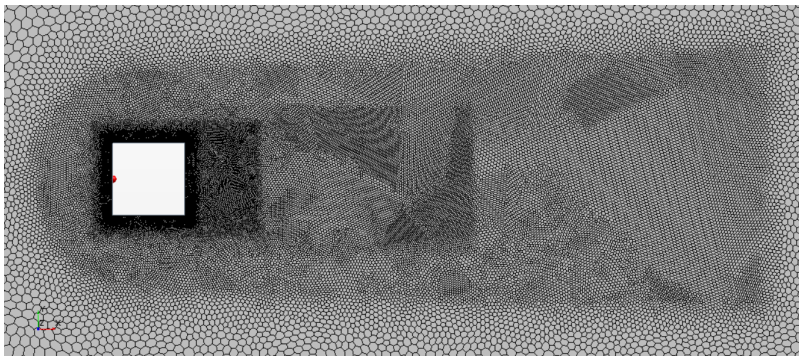

Figure 3.24: Initial generated mesh for turbulent flow over a square cylinder

Custom controls, consisting of surface and volume controls, were added to the mesh to allow for more customization. These volume controls were added to key regions around the cylinder and a surface control on the edges of the flow domain. Figure 3.24 illustrates the volume controls used in the initial mesh.

Physics setup

Similar to the previous cases, only the Reynolds and Strouhal numbers were given. The same assumptions for the diameter, density, ambient pressure and vortex shedding frequency were made as in the previous sections. A pressure of 101.325kPa and a vortex shedding frequency of 2 Hz were chosen. All physical properties used in the simulations are summarised in Table 3.18.

Table 3.18: Physical properties in the simulation of the turbulent flow over a square cylinder

Variable	Value [Unit]
Reynolds number [Re]	2.2×10^4 [-]
Strouhal number [St]	0.134 [-]
Diameter [D_{cyl}]	0.25 [m]
Density [ρ]	1 [kg/m^3]
Pressure	101.325 [kPa]
Vortex shedding frequency [f_{vs}]	2 [Hz]
Velocity [V]	3.731 [m/s]
Dynamic viscosity [μ]	4.240163×10^{-5} [Pa.s]

The physics continuum was set up identically as in Section 3.4. A 2D setup was selected using the implicit unsteady time step. Gas was used with the segregated flow solver. Constant density RANS, $k-\omega$ SST turbulence model, was used. The time steps in Table 3.19 were sufficient for the simulations in this section and thus were kept the same. The simulations were run using 25 and 40 inner iterations to identify the sensitivity of the current setup to the change in inner iterations.

Table 3.19: Time steps used at various mesh densities during initial simulation

Simulation time [s]	Time step [s]
0	0.01
5	0.008
10	0.006

The Gamma - ReTheta ($\gamma - Re_\theta$) transition model was used. The free stream edge, used in the $\gamma - Re_\theta$ model, was set to the prism layer thickness. All other properties, except for the material properties, in the physics continuum were left as default. The implicit unsteady solver was set to 2nd-order temporal discretization.

Results and discussion

Both simulations yielded similar results, with the average C_d being 2.125 and 2.128 for the 25 and 40 inner iterations, respectively. Both simulations resulted in a vortex shedding frequency of 1.8996 Hz. The average C_d values were within 2.5% of the reference case [12] with the vortex shedding frequency within 5.1%.

These values, as they are, are already very close to the reference case. This shows that

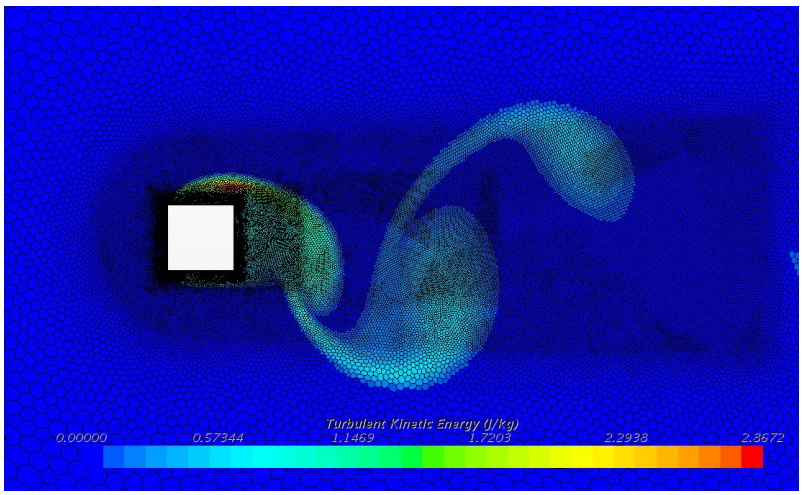

Figure 3.25: Turbulent kinetic energy (TKE) overlayed with the generated mesh

the effort spent understanding the key mesh locations, refinement and the physics setup is directly translated to similar bluff body problems without the need to follow the same extensive setup process.

Figure 3.25 shows the turbulent kinetic energy plot overlayed with the generated mesh of the initial setup. It can be seen that the mesh refinement required adjustments to fully capture the irregular vortex streets caused by the square geometry.

3.5.2 Inner iteration and mesh refinement study

Based on the initial simulation results, there were not any substantial changes that needed to be made. The mesh setup was adjusted to capture the vortices downstream of the body. The inner iteration and mesh refinement simulations were done similarly to Section 3.4.4. A mesh was generated at different base sizes, with different inner iteration studies done per base size.

The more coarse base sizes were used as a reference to compare the simulation results. More focus was placed on the finer meshes, 15% - 5% base sizes.

Mesh setup

As seen in Figure 3.25, the vortex street generated is not as narrow as behind the circular cylinders. The volume control angles in the wake were adjusted to capture these vortices better, allowing for more mesh elements in these higher gradient regions.

The base sizes varied from 0.4 D_{cyl} to 0.3 D_{cyl}, then down to 0.05 D_{cyl} in decrements of 0.05. The custom sizes for the larger volume control were 20% of the base and 16% for the smaller one. Both can be seen in Figure 3.26.

The prism layer thickness was set to 1% of the base size, with a $y^+ < 1$. A thicker prism layer was not as necessary in this case, as the flow separates at the leading edge of the

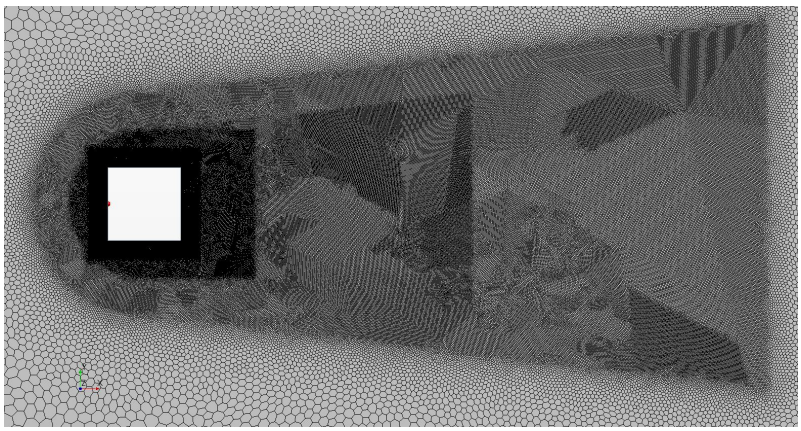

Figure 3.26: Overview of generated mesh with base size 0.1 D_{cyl}

body. The usual boundary layer does not form as on the circular cylinders. The custom volume controls around the body were set up as follows; the recirculation refinement zone was 10%, followed by 6% for the separation zone (the square mesh refinement around the body) and 4% for the four edge refinement zones. These edge refinement zones were critical in capturing the large gradients caused by the flow over the edge.

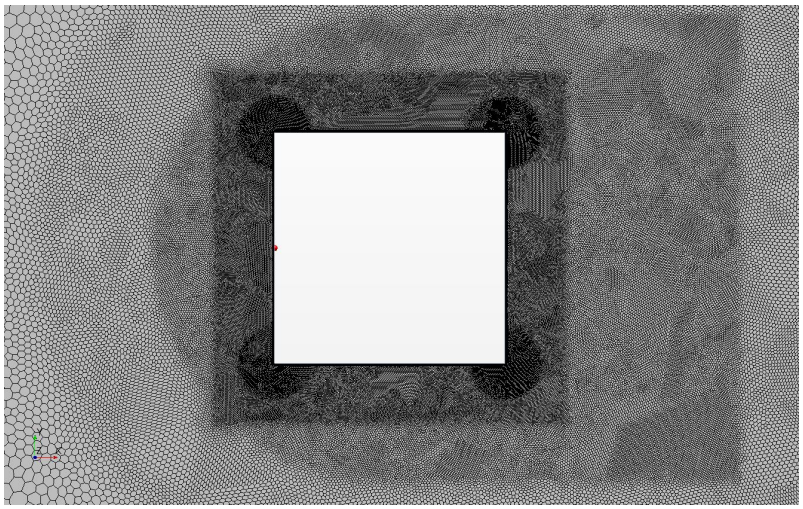

Figure 3.27: Generated mesh with base size 0.1 D_{cyl} around the body

Physics setup

The time steps varied from 0.008 s in the first 5 seconds to 0.006 s. The simulation time was set to 20 seconds, allowing full flow development. More inner iterations were used during the finer mesh studies, ensuring inner iteration independence was reached. The inner iterations used are summarised in Table 3.20.

Results and discussion

The results of all the studies are summarized in Table A.3. Figure 3.28 gives an overview of all the average C_d results for the different base sizes using only 40 inner iterations. Both

Table 3.20: Inner iterations used with various mesh setups during mesh refinement simulations

Base size [m] (% D_{cyl})	Element count	Inner iterations used
0.1 (40%)	27330	25, 40
0.075 (30%)	41217	25, 40
0.0625 (25%)	55657	25, 40
0.05 (20%)	77993	25, 40
0.0375 (15%)	124241	25, 40, 50
0.025 (10%)	251927	25, 40, 50, 60, 70
0.0125 (5%)	895236	40

simulations using base sizes 0.05 and 0.1 D_{cyl} resulted in similar average C_d and vortex shedding frequencies.

The assumption was made that due to the similar results, the results would be very similar as the inner iterations were increased. The numerical calculation time using a base size of 0.05 D_{cyl} was slow and time-consuming. This assumption allowed for conclusions to be made relatively fast, without running further simulations with more inner iterations and thus even longer calculation times.

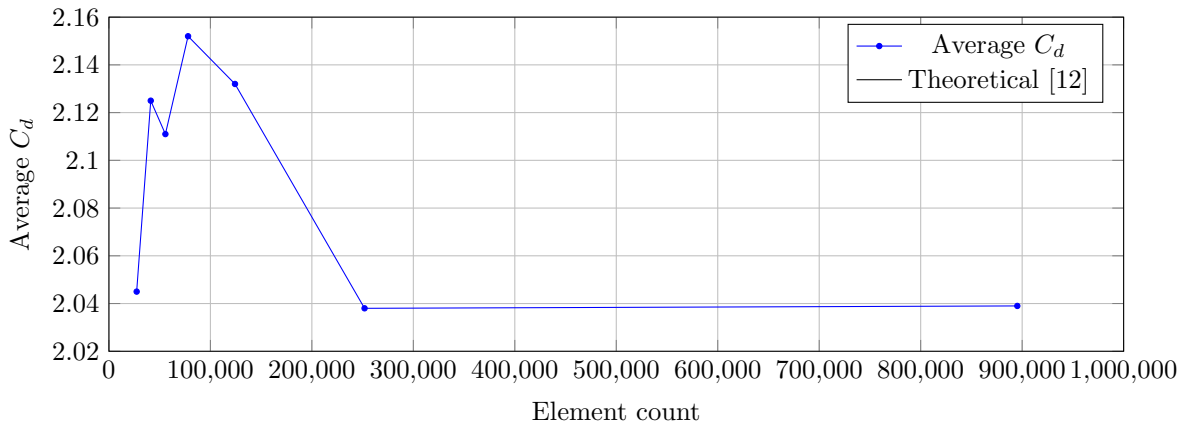

Figure 3.28: Average C_d results of different mesh sizes using 40 inner iterations

The mesh refinement and independence can be seen in Figure 3.28, where the inner iteration independence can be seen in 3.29. The 15% base size simulation converged at 40 inner iterations, whereas the 10% base size simulation started to converge at 60 inner iterations.

Compared with the numerical reference study in [12], the final results were at a base size of 0.1 D_{cyl} with 70 inner iterations. This combination of parameters resulted in an average C_d of 2.119 and a shedding frequency of 1.8996 with a Strouhal number of 0.127. This resulted in a percentage error of 5.2% for the Strouhal number and 2.8% for the average C_d.

Considering that a 2D RANS simulation was compared to a 3D DES variant, being within 5.2% of the Strouhal and 2.8% for the average C_d can be considered a success.

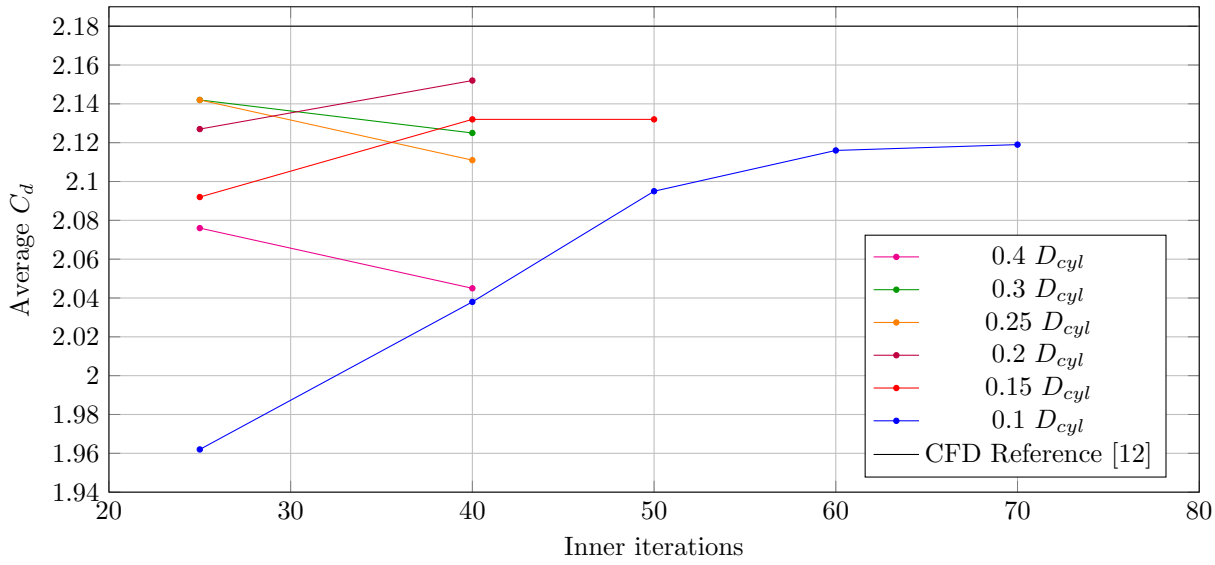

Figure 3.29: Average C_d results of different mesh sizes using 40 inner iterations

3.5.3 Summary

The simulation in this section combines everything learned in the previous sections. The work done before the turbulent square cylinder study ensured that even the initial mesh and simulation setup delivered results close to what was required.

At the finer meshes, more inner iterations were required before convergence was achieved. As the meshes became finer, the overall average C_d results started to reduce, meaning the simulations underpredicted the expected drag coefficients. The overall vortex shedding frequencies remained roughly the same from the initial simulation up to the last. There were some deviations at more coarse meshes, but that was to be expected.

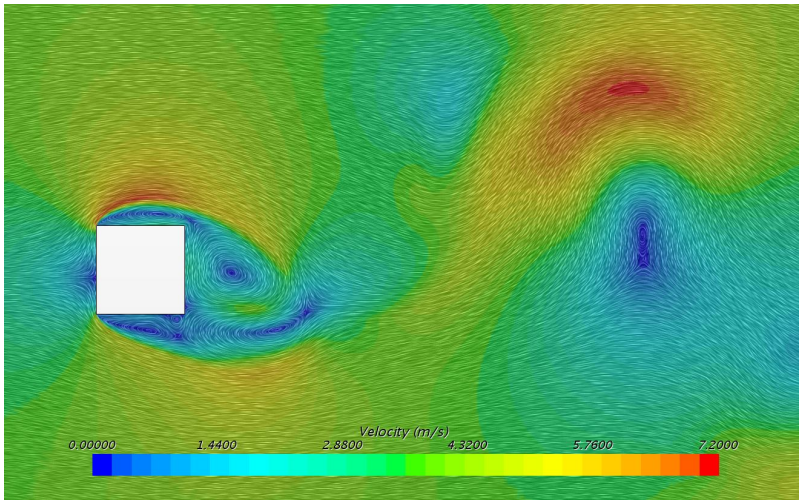

Figure 3.30: Velocity profile of flow over a square cylinder at 20 s with $Re = 2.2 \times 10^4$

The overall Courant number for the 10% base size simulation was < 50. There were sports with higher Courant numbers, especially in the high velocity regions at the leading edge corners. These high velocity regions can be seen in Figure 3.30. Even though the literature states that a Courant number < 1 is required, the combination of implicit solver and time

step independence studies meant that it was not necessary in the cases in this chapter. To achieve a lower Courant number would mean either increasing the mesh element sizes or decreasing the time step while keeping velocity constant. Both of these parameters were identified and chosen with independence studies.

It was evident, however, how computationally intense the final meshes with the high inner iterations were. The method followed in this chapter, even though it was thorough, might not be ideal in a practical engineering application where time is of the essence. The main aim was to understand the combination of parameters and know what effects each had on the overall results. This can be considered in further studies where solution time might be critical.

3.6 Conclusion

The overall aim of this chapter was to understand and correctly use the tools available to capture the flow over bluff bodies. The key and applicable parameters and their effects on the simulation results had to be understood. As with anything in the engineering field, it was evident that there was a tradeoff between accuracy and computation time. Understanding the effects of the parameters on the overall results will make the decision between accuracy and efficiency easier and where compromises can be made.

The results of the simulations in this chapter were accurate compared with the reference cases chosen. Two main properties were used to compare the results and numerical reference cases. These were the average C_d and Strouhal numbers. These are popular and practical parameters used in the literature and are simple to calculate and compare.

Three cases were studied, starting with a relatively simple case and working to more complex flow cases. Firstly flow over a 2D laminar cylinder was done at Re = 200. The average C_d and Strouhal number was 0.07% and 5% from the reference case. Secondly, flow over a cylinder in turbulent conditions was investigated at $Re = 3.6 \times 10^6$. The reference case used a 3D specific turbulence solver, namely DES. The results were within 2.6% and 0.1% of the C_d and Strouhal number values, respectively. Thirdly, flow over a square cylinder was investigated at turbulent conditions with $Re = 2.2 \times 10^4$. Similar to the turbulent circular cylinder study, the square cylinder reference case used a 3D numerical simulation with a DES variant solver. Even though these solvers are much better at solving these flow conditions, the average C_d and Strouhal number results were within 5.2% and 2.8% of the reference case.

Overall good comparisons were made with the reference cases. The identified parameters, namely the mesh refinement at critical locations, the inner iterations and the time steps, were crucial in accurate results.

The time steps were the simplest to identify and get an adequate time step. All three cases used similar vortex shedding frequencies and diameters, meaning the time steps were in the same order.

Key mesh refinement zones were also identified and studied. The most important regions were the prism layer and the wake of the bodies. This was to be expected as the flow conditions in these regions play an essential role in the drag calculation. The prism layer in the turbulent circular cylinder study required many elements to capture the boundary layer and the onset of separation due to the adverse pressure gradients. On the other hand, the square cylinder did not require that thick of a prism layer as separation happens at the LE of the body.

The key location in the wake was the recirculation zone one diameter downstream of the body. This was an important region to refine to ensure the low pressure was captured. Similarly, refinement upstream was also essential to accurately predict the high pressure. Wake refinement further down was also significant to capture the vortex sheets, ensuring that the low pressure was adequately predicted even in the wake.

The relationship between the inner iterations and the mesh refinement played the most important role in accurately capturing the flow conditions. As the mesh became finer, more inner iterations were required before the results converged. However, this parameter needs to be used cautiously, as it is possible for the number of inner iterations to drastically increase the simulation time, ultimately defeating the purpose of an efficient simulation. The compromise between accuracy and time must be made when dealing with these highly separated and turbulent flow phenomena.

Chapter 4

CFD validation on airfoil sections

4.1 Introduction

Chapter 3 was an in-depth study of the unsteady flow over various cylinders. The flow conditions started simple (laminar) and moved to more complex flows (turbulent). The next step was applying the knowledge from simpler geometries to more complex geometries, such as airfoils at high angels of attack.

In order to fully understand and numerically capture the flow around a wing section with an extended airbrake, it should first be shown that the flow over a clean airfoil could accurately be captured. The main advantage of starting with a clean airfoil is that it is simpler to replicate and understand the wind tunnel results due to the simpler geometries. This will ensure a proper interpretation of how the initial researchers captured the data. Secondly, the mesh refinement study of the airfoil will not take as much time as with the airbrake extended, as the geometry and flow conditions are relatively simple.

Two airfoils used in sailplane applications will be analysed for validation purposes, FX66-17AII-182 [19] and HPH yn1 [20]. Both these airfoils have corresponding data with the airbrakes extended in [9] and [10], respectively. This is a suitable place to start to methodically understand and build up to the end goal of analysing the airfoils with extended airbrakes in Chapter 5.

The same analysis methodology for both airfoils was followed. Firstly, an initial inviscid flow simulation was performed to determine the mesh properties required around the airfoil and the leading and trailing edge mesh refinement. Afterwards, mesh refinement was done in the wake of the airfoil. Following that, various properties of the $k-\omega$ SST Menter turbulence model were tested to refine the CFD physics model. Finally, C_l/α and C_d/α curves were plotted, validating the CFD simulation against wind tunnel data.

Thus, this chapter can be broken down into two main sections (the FX66 and HPH airfoils) with three subsections per airfoil: an inviscid mesh refinement study on the surface of the airfoil, a mesh refinement study in the wake of the airfoil, and validation of the simulated results compared to that of wind tunnel data.

4.2 FX66-17AII-182 Airfoil validation

The FX66-17AII-182 airfoil (Figure 4.1) forms part of the Wortmann family of airfoils, designed by Prof F.X. Wortmann in the early 1960's at the University of Stuttgart, West Germany. These are laminar airfoils primarily designed for use on sailplanes or other low Reynolds number applications. This airfoil has a maximum thickness of 18.2% C at 33.9% of the chord, and its maximum camber of 3.8% C at 37.1% chord [46].

This airfoil was ideal for this study, not only due to the airbrake analysis in [9] but also to understand the characteristics of laminar airfoils designed for sailplane applications. The experimental data used in this chapter can be found in [19]. Experiments were done in the Langley low-turbulence pressure tunnel in the United States of America. The aim of replicating the reference experimental data in [19] was to investigate the basic low-speed, and especially important for the current FX66 airfoil study, the 2D aerodynamic characteristics of the airfoil.

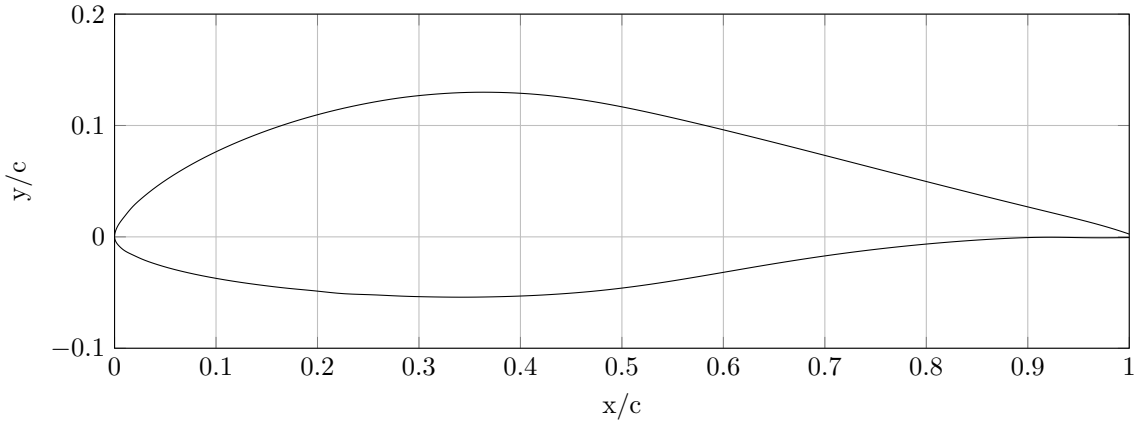

Figure 4.1: FX66-17AII-182 Section view

Various cases were discussed in the wind tunnel report, but the case used in Section 4.2 is at Re = 1×10^6 and Ma = 0.1. The geometry used in the report had a smooth finish, removing the need to consider surface roughness. The wind tunnel had a turbulence intensity of 0.034% as seen in [47].

4.2.1 FX66 airfoil mesh refinement study

The first step was to achieve a mesh independent solution for the airfoil without the wake mesh refinement by using the inviscid solver. The inviscid simulations aimed to determine the number of node points or the surface size of the body itself. In order to achieve this, the methodology followed was adapted from [48]. An inviscid simulation was used, meaning that the boundary layer is removed from the equation. Using an inviscid simulation meant the boundary conditions of the geometry exhibited slip-like conditions.

An unstructured mesh was generated without using the prism layer (similar to [48]). The inviscid nature of the simulation also meant that the y^+ was not considered, as the equation for y^+ (Eq 2.9) has a viscosity term. The prism layer is used to capture the boundary

layer and the flow gradients perpendicular to the flow on the body surface. Without the boundary layer, no momentum transfer would occur due to the frictional viscous losses between the air and the body surface.

An initial steady state inviscid simulation was set up at 0° angle of attack (AOA). The airfoil TE has been rounded to reduce errors during mesh generation. The mesh base size was reduced until the C_d function exhibited second-order convergence. More details are given in the result and discussion section below.

Geometry setup

The dimensions of the flow domain used for all of the mesh refinement studies and the validation cases are shown in Figure 4.2. All dimensions are given in terms of the airfoil chord (C). The flow domain is in the shape of a bullet containing an airfoil with chord length C. The front wall is 20 C upstream of the airfoil LE, with the top and bottom walls 20 C above and below and the back wall 40 C downstream. This large domain ensures no interference from the domain walls on the flow development and diffusion.

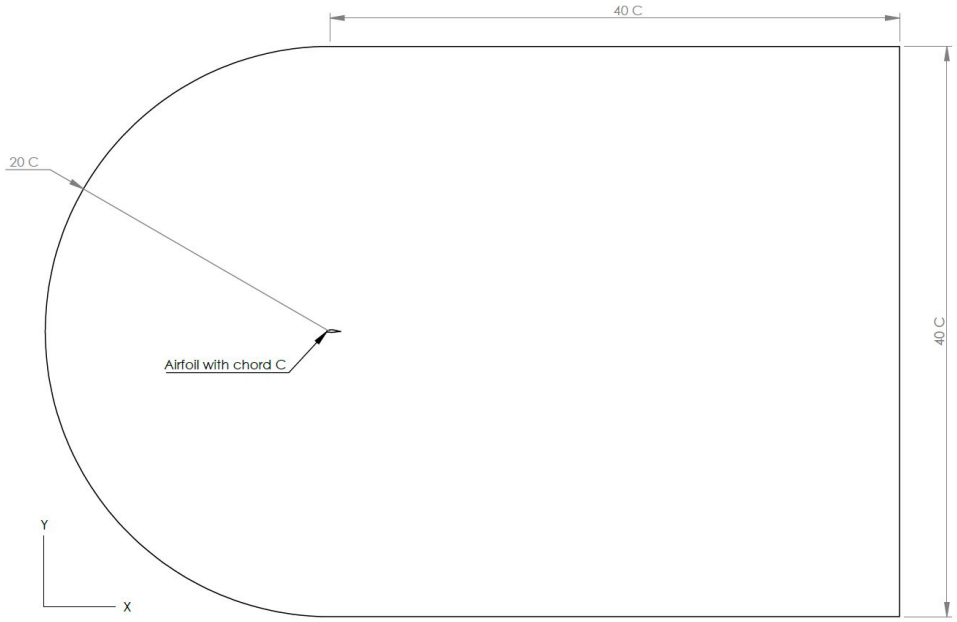

Figure 4.2: FX66-17AII-182 flow domain dimensions

Figure 4.3 shows the boundary setup. The upstream wall was set as a velocity inlet, with the downstream wall as a pressure outlet. Both upper and lower wall boundary conditions are set as slip walls.

Flow physics setup

The Reynolds and Mach numbers were given from the wind tunnel tests in [19]. A velocity of 34.3 m/s was calculated using equation 4.1 and using the speed of sound through air at standard conditions (343 m/s). The density used in the simulation was calculated using

Figure 4.3: FX66-17AII-182 flow domain boundary setup

the equation for Reynolds number (2.1) with a chord length of 0.6 m. The wing section in [19] was mounted between the wind tunnel wall and an end plate, allowing for the assumption that the results are close to a 2D setup.

$$Ma = \frac{V}{c} \tag{4.1}$$

Table 4.1 below summarises the physical properties used in this section.

Table 4.1: FX66-17AII-182 simulation properties

Variable	Value [Unit]
Reynolds number [Re]	1×10^{6} [-]
Mach number [Ma]	0.1 [-]
Airfoil chord [l]	0.6 [m]
Density [ρ]	1.225 [kg/m^3]
Velocity [V]	34.3 [m/s]
Dynamic viscosity [μ]	1.681×10^{-5} [Pa.s]

A 2D, steady simulation with constant density was set up using the inviscid flow regime, in essence, allowing the surface to have slip conditions, in other words, no viscous interaction of the fluid on the walls. To increase the accuracy, the second-order convection scheme was selected.

Mesh setup

An unstructured polyhedral mesh was used as this mesh type performs well in anisotropic flow conditions, prevalent at the higher angles of attack [26]. The airfoil surface refinement was 2%, with 0.05% on the leading edge and 0.1% on the trailing edge. Further volume refinements of 2% and 1% were set up in the region surrounding the leading and trailing edges, respectively. All the surface and volume controls were set up as a % of the base mesh size.

During the mesh refinement study, the mesh size was changed by only altering the base mesh size, initially set to 30% of the airfoil chord length (0.18m) down to 1.5%. The refinement steps, in percentage of the chord, and their corresponding number of elements can be seen in Table 4.2.

Figures 4.4 and 4.5 show the overall generated mesh as well as the generated mesh close to the airfoil with base size 10% of airfoil chord, respectively.

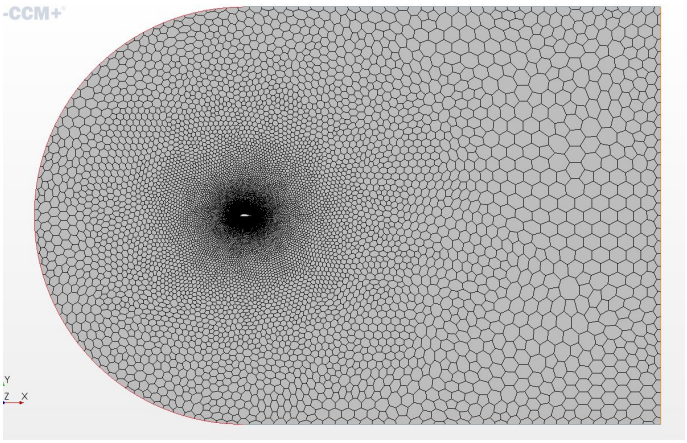

Figure 4.4: FX66-17AII-182 Generated mesh on overall flow domain - base size 10% C

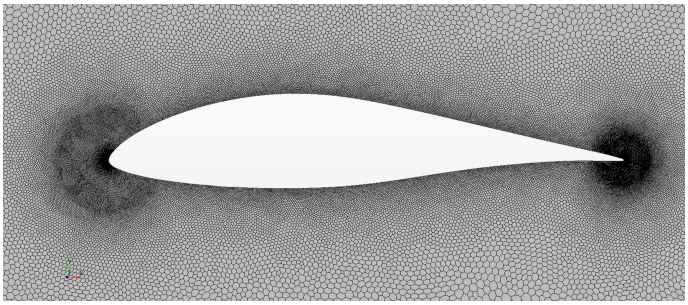

Figure 4.5: FX66-17AII-182 Generated mesh surrounding airfoil - base size 10% C

Results and discussion

The methods used and explained in this section will also be used during the mesh refinement studies of Sections 4.3, 5.2 and 5.3. This method is adapted from [48] and is used to ensure an acceptable mesh refinement has been achieved.

The representative mesh spacing (Δ_x) was calculated according to Equation 4.2.

$$\Delta_x = \left(\frac{1}{n_{total}}\right)^{1/2} \tag{4.2}$$

Equation 4.2 was derived from the Δ_x equation used in [48], with the exception that the right part of the equation is to the power 1/2 and not 1/3 due to the current study being in 2D whereas [48] was for a 3D flow domain.

The Grid Convergence Index (GCI) [49] was used to evaluate pairs of meshes. The GCI, Equation 4.4, gives an error band for mesh pairs to evaluate and relate different mesh densities.

The grid refinement factor (r) can be defined as

$$r = \frac{\Delta x_2}{\Delta x_1} \tag{4.3}$$

where the subscript 1 refers to the finer, and 2 the coarser of the two meshes. It is recommended in [50] that r be 1.3, whereas [51] recommends a value greater than 1.3. Taking this into account, all the r values (in Table 4.2), excluding the first mesh refinement step (%30 - %20), adhere to this recommendation.

The GCI for the finer mesh can then be defined as Equation 4.2 below

$$GCI = F_s \left| \frac{(f_2 - f_1)/f_1}{1 - r^2} \right| \tag{4.4}$$

The function f_2 is the coarse-grid solution obtained by using mesh spacing Δx_2. Function f_1, on the other hand, is the fine-grid solution obtained by using mesh spacing Δx_1. The lift coefficient of the airfoil C_l was set equal to function f.

The relaxation factor (F_s) can be seen as a safety factor for the GCI evaluation. The use of $F_s = 1.25$ is recommended in [49] when executing a mesh convergence study with three or more grid size solutions. Roach recommends a more conservative safety factor ($F_s = 3$) when only running a two-grid study. This can be the case when time is of the essence in more practical engineering applications.

The simulation was run for 10000 iterations, with the residuals fully converged at 1500 iterations. Figure 4.6 shows the residual plot and convergence. All of the residuals converged at a value below 0.0001.

The numerical result plot can be considered second-order if the function, C_l in this case, tends towards a straight line as the grid spacing tends towards zero. This is the case as shown in Figure 4.7b and is a similar approach to what was discussed in [48]. The significance of the second-order behaviour in Figure 4.7b is that C_l has reached the asymptotic regime. This is also evident in Figure 4.8 as the plot tends to converge. Table 4.2 summarises the results of the inviscid simulation. The Richardson Extrapolated value can be derived from the linear line given in Figure 4.7b.

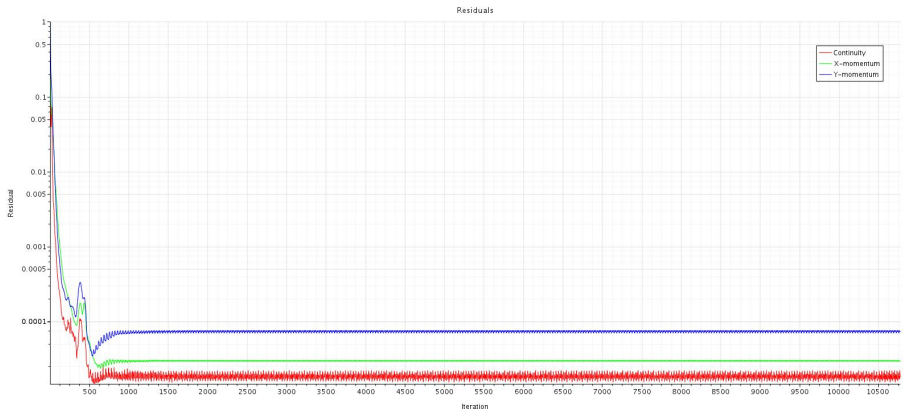

Figure 4.6: Residual convergence of inviscid simulation - base size 10%

Table 4.2: FX66-17AII-182 initial inviscid mesh refinement study base sizes at 0° AOA

Base size [% of C]	Element count [-]	C_l	Δ_x	r	GCI	% Error
30%	37300	0.5158	0.0052	-	-	0.37%
20%	46120	0.5176	0.0047	1.112	1.83%	0.03%
10% *	79701	0.5138	0.0035	1.315	1.25%	0.75%
5%	170962	0.5148	0.0024	1.465	0.21%	0.56%
2.5%	436287	0.5162	0.0015	1.597	0.21%	0.30%
1.5%	1034566	0.5171	0.0010	1.540	0.16%	0.12%
Richardson extrapolated C_l		0.5177				

* Representing the chosen parameter for following studies

The method described above uses the second-order convergences of the C_l vs Δ_{x^2} plot to predict the Richardson extrapolated value. The Richardson extrapolated value approximates the theoretical C_l value if the mesh refinement tends to an infinitely fine mesh. This is used to evaluate the current mesh and the theoretical mesh results if the current mesh refinement trend is followed. The theoretical and current C_l values are compared and used to evaluate if the current mesh is fine enough for the application or at what point the mesh would be adequately refined. This is only theoretical due to numerical errors that would appear as the mesh becomes finer. However, this is a great tool to evaluate the current mesh setup.

Using the extrapolated C_l value of 0.5177, an error of 0.75% and 0.12% were calculated for meshes of base sizes 10% C and 1.5% C, respectively. This also gave a GCI of between 1.25% and 0.16%.

A base size of 10% C was selected as the starting point for the subsequent investigation. Although the chosen base size has the largest % Error and GCI, these values are well within the acceptable ranges to obtain adequate results. The convergence of C_l in Figure 4.7b also gives the confidence to continue the study with the chosen initial mesh setup.

The converging nature of Figures 4.7 and 4.8 shows that mesh independence has been reached or can be predicted with the Richardson extrapolation technique. This lays the foundation for the subsequent studies on the FX66-17AII-182 airfoil and the studies with airbrakes extended on both FX66 and HPH yn1 airfoils. +

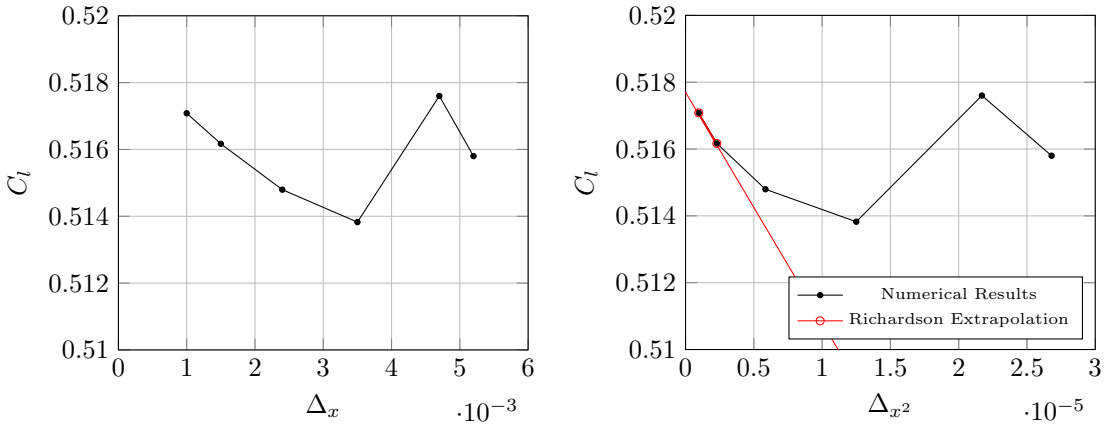

(a) C_l vs relative mesh spacing

(b) Richardson extrapolated spacing

Figure 4.7: Mesh convergence of C_l at an AOA of 0° for the inviscid flow over a FX66-17AII-182 airfoil

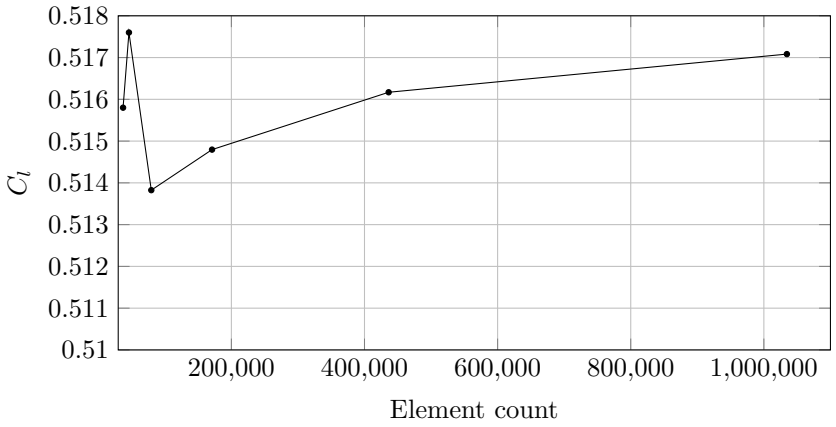

Figure 4.8: C_l vs Element count of FX66-17AII-182 - Inviscid flow regime

4.2.2 FX66 wake mesh refinement study

The work done in 4.2.1 gave a starting point for the wake mesh refinement. With the number of nodes around the airfoil selected, the next step was to finalise the wake mesh setup.

The wake mesh refinement plays an integral part in any CFD mesh setup. The aim of mesh refinement remains to have the least amount of mesh elements with the most accurate results. This is important when refining the mesh in the wake of an airfoil, where it is crucial to capture the flow wake, as this directly affects the simulation results. This section serves as the final mesh refinement study before validating the simulated C_l vs α and C_l vs α plots with the experimental results given in [19]. The overall aim of the section is to understand the flow at higher angles of attack. This understanding will also carry over when applying these techniques discussed in Chapter 3 on a more complex geometry, such as an airfoil at higher angles of attack, which are close to, and around the stall angle.

Mesh setup

The LE and TE refinement and airfoil surface refinement parameters, used in the mesh refinement study in the previous Section (4.2.1), were kept the same in this investigation. In this section, the influence of the prism layer settings on the results is determined. The first layer thickness was chosen such that the y^+ value is <1 at all the points along the airfoil. The prism layer thickness was calculated to be the same as the theoretical boundary layer thickness at the end of the airfoil calculated with Eq 2.4. Due to the added prism layer, the Re_θ wall function was set to 0.006 m, adequately capturing the boundary layer. To study the effect of variations of the wake refinement, a volume control was added to the wake region behind the airfoil allowing the control of the wake mesh density. This volume control was cone-shaped with a length of 7.5 C downstream. The volume control was set at 10% of the base mesh size. The size reduction can be seen in Table 4.3.

Figures 4.9 through 4.11 illustrate the generated mesh for 20% base size. Figure 4.9 gives an overview of the wake refinement zone. Figure 4.10 shows the overall prism layer, whereas Figure 4.11 shows, in more detail, the LE of the airfoil and the refinement chosen in the previous section.

Flow physics setup

Before choosing the flow regime and the turbulence model, the physical flow characteristics at the point of study needs to be understood. When looking at the C_l/α plot of the experimental data [19] in Figure 4.15, it shows that the chosen angle of attack of 12° is higher than the stall angle ($C_{l_{max}}$) at 9.1°. This indicates that separated and highly turbulent flow with transient flow behaviour can be expected. Due to this, the viscous flow regime, particularly the unsteady RANS (URANS) turbulence model, was chosen for this study. The transient time steps in the CFD simulation also play an essential role

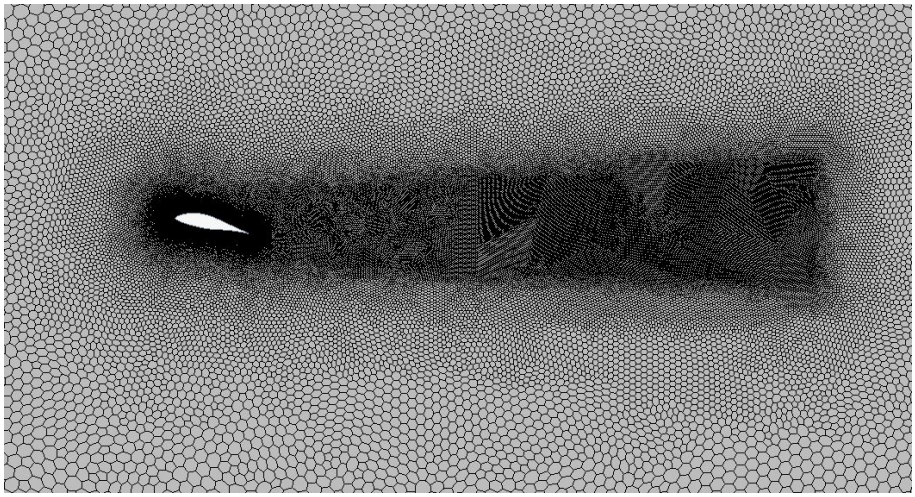

Figure 4.9: Generated mesh of wake refinement study showing wake refinement zone - base size 20% C

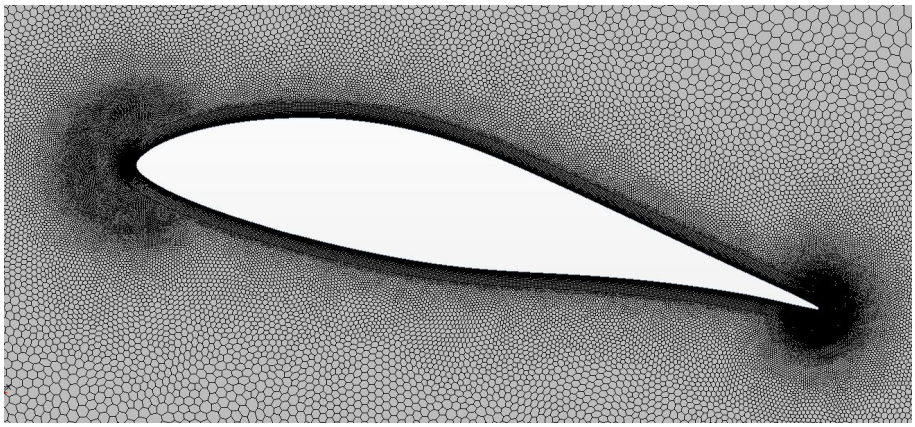

Figure 4.10: Close up view of generated mesh around airfoil - base size 20% C

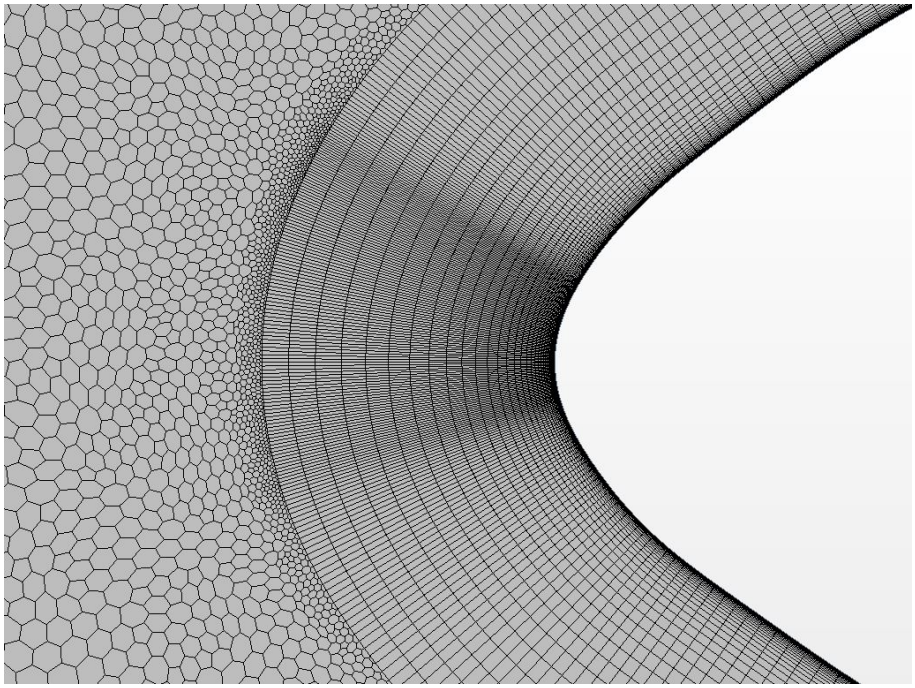

Figure 4.11: Detailed view of LE PL refinement - base size 20% C

when choosing the URANS turbulence model. Although the GCI method can be used, a time step sweep has been done.

As mentioned in Section 3.6, the inner iterations (II) play a significant role in accurately predicting separated flows. The inner iterations were set to 20 and 30 to compare and understand the effects on flow over a high angle of attack airfoil. More detail on the choice of time step and inner iterations on airfoils in these conditions is discussed in Section 4.3.2.

Both the FX66 and the HPH airfoils have similar flow velocities, chord lengths and airfoil geometries. This implies that similar meshes will be generated and that similar mesh properties could be used. These similarities allow for the same order of time steps and inner iterations as a starting point. The $k-\omega$ SST turbulence model was used with $\gamma - Re_\theta$ Transition and Second-order convection scheme.

Results and discussion

Figure 4.12 shows the results of the time steps independence study at different mesh base sizes. To give a clear view, the focus was on time steps 0.001 s - 0.00005 s. Even though the mesh with a base size of 0.3 C did not converge, good convergence for meshes with base size 0.2 C - 0.05 C at a time step of 0.0001 s were seen. A time step of 0.0001 s was taken and used in the studies to follow.

Table 4.3 summarises the results at the chosen time step of 0.0001 s. An additional mesh was generated with a base size of 0.25 C. This was to ensure a mesh independent solution was obtained.

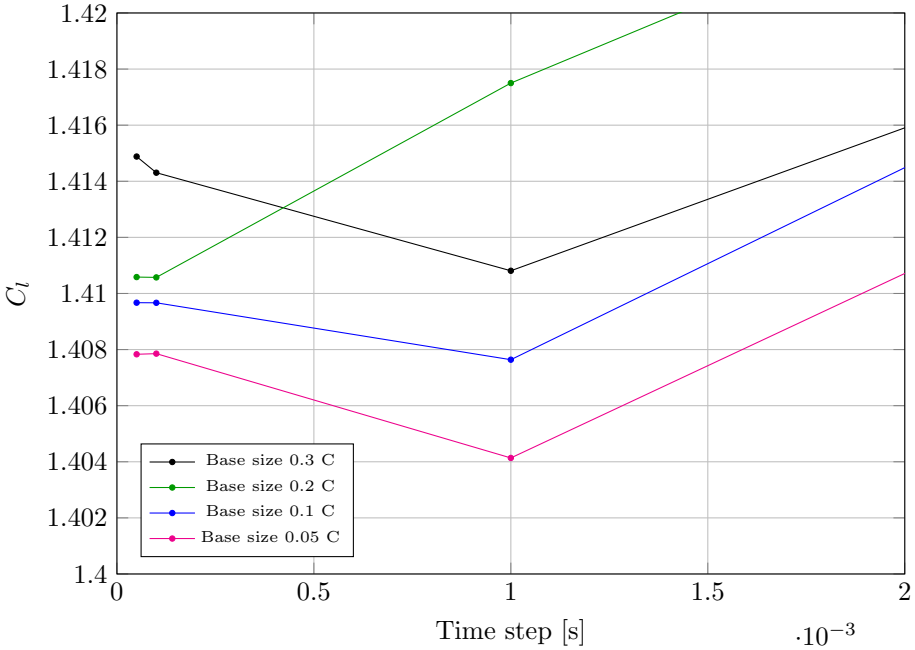

Figure 4.12: Time step convergence at various base sizes using 20 inner iterations

Figure 4.13a shows the C_l vs Δ_x plots of simulations with 20 and 30 inner iterations and time steps 0.001 s and 0.0001 s. None of the 0.001 s time step plots even came close to

Table 4.3: FX66-17AII-182 Wake mesh refinement study for 20 inner iterations at a time step of 0.0001 s and AOA 12°

Base size [% of C]	Element count [-]	C_l	Δ_x	r	GCI	% Error
30%	153610	1.4143	0.0187	-	-	0.63%
20%*	177379	1.4106	0.0178	1.049	3.29%	0.37%
10%	293124	1.4097	0.0151	1.182	0.20%	0.30%
5%	722810	1.4079	0.0111	1.351	0.20%	0.17%
2.5%	2350484	1.4065	0.0075	1.482	0.10%	0.08%
Richardson extrapolated C_l		1.4054				

* Representing the chosen parameter for following studies

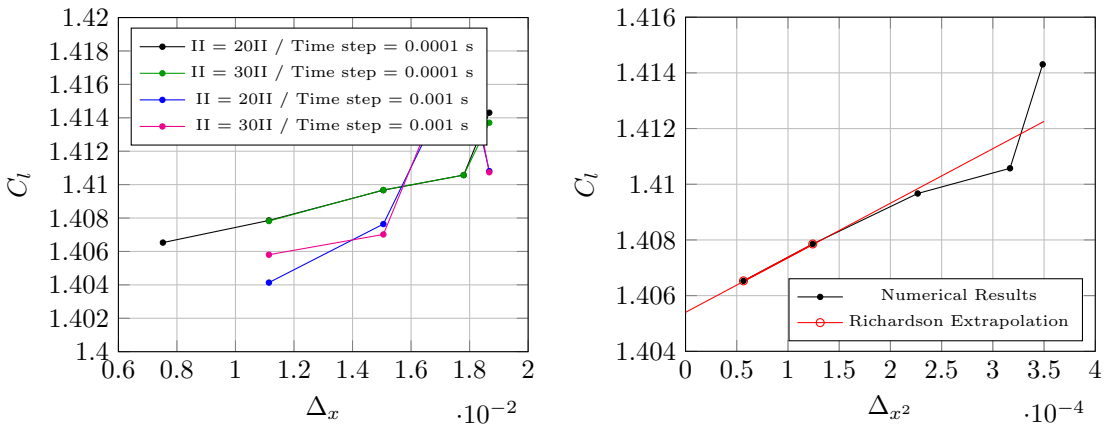

(a) C_l vs relative mesh spacing

(b) Richardson extrapolated spacing

Figure 4.13: Mesh convergence of C_l at an AOA of 12° for the flow over a FX66-17AII-182 airfoil

the required asymptotic convergence and thus was not taken into further consideration. Figure 4.13b only shows the CL vs Δ_{x^2} plot of the simulation with parameters 20 inner iterations and 0.0001 s time step.

Both 0.0001 s time step simulations converge towards a straight line as expected. It is also clear that both 20 and 30 inner iterations yielded the same plot, indicating that 20 inner iterations are enough to capture the conditions. All of the C_l are within 0.63% of the Richardson extrapolated value (1.4054) and within a GCI of 0.033%. This indicates that even a relatively coarse mesh of base size 30% of the base would have been sufficient to understand and accurately predict the flow. However, 20% of the base size was selected for the validation study in Section 4.2.3, given the GCI of 3.29%. This gives the confidence that the validation can be continued using 20 inner iterations, a time step of 0.0001 s and a base mesh size of 20% C.

The wake refinement length wasn't studied in this section. A more in-depth study was done on the effects of the wake refinement length in Chapter 3. Figure 4.14 gives the C_l vs Element count of the mesh refinement study.

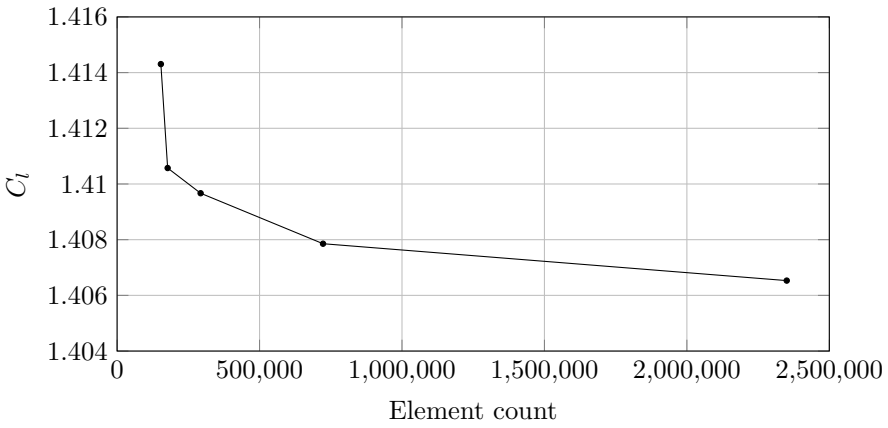

Figure 4.14: C_l vs Element count of FX66-17AII-182 - Mesh refinement study at Re = 1×10^6

4.2.3 FX66 CFD simulation validation

After both airfoil node mesh independence and wake mesh refinement studies have been done, the generated mesh can be used to start the validation simulations. These simulations are important to ensure that the results are accurate and trustworthy.

Simulation setup

The following parameters were adjusted relative to the base size of 20% C (0.12m). The LE and TE volume refinements were 1% and 0.5%. The airfoil, LE and TE surface refinements were 1%, 0.025% and 0.05%, respectively. The wake mesh refinement was set as 10% of the base size. The angles of attack varied from 0°up to 14°.

The URANS $k-\omega$ SST solver was used with a time step of 0.0001 s and 20 inner iterations. The simulation time was set to 2 seconds, ensuring that convergence and full flow development had occurred. Second-order convection and temporal discretization were selected at all angles of attack.

Results and discussion

Three sets of results were compared: the experimental data, the CFD (numerical) results, and XFoil. Somers [19] only gives the C_d values up to an angle of 9.1°. Xfoil was used to indicate the C_d characteristics from 9.1° to 14°. Figures 4.15 and 4.16 shows the results of the C_l and C_d vs α plots respectively.

As expected, both XFoil and CFD accurately predict the values and characteristics, of the flow over the FX66-17AII-182 airfoil, in the linear range (0°- 9°). The results of both C_l and C_d are less accurate after the experimental stall angle C_{lmax} as can be expected due to the highly turbulent flow conditions at the higher angle of attack.

Focusing on Figure 4.15, the simulation overpredicted C_{lmax} (1.55 vs 1.40), as well as the angle of attack 10°, compared to 9.1° in the experiment. However, the results predicted the characteristic downward slope of the experimental data after C_{lmax}.

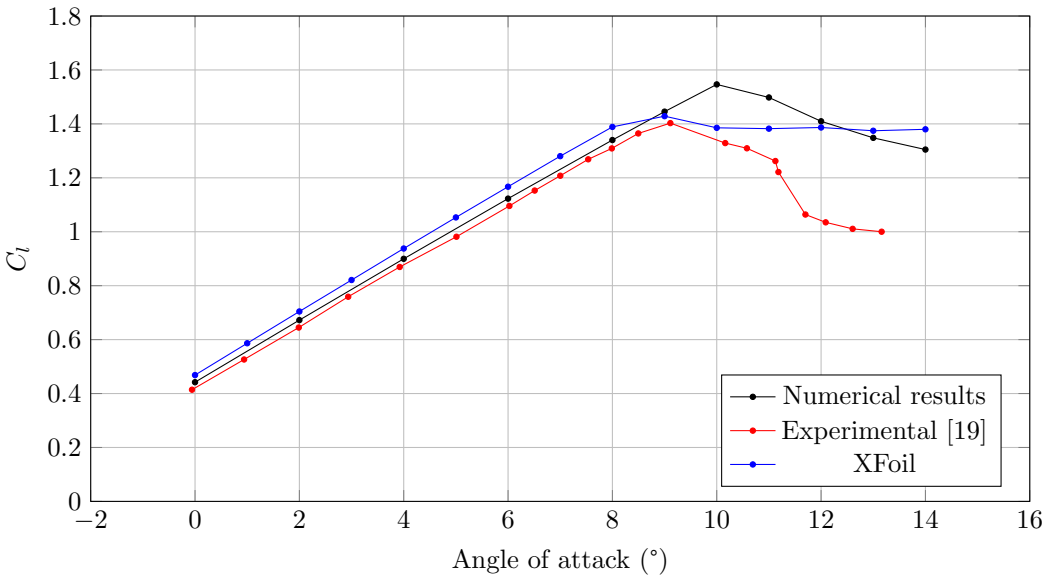

Figure 4.15: C_l vs α validation at Re = 1×10^6

Figure 4.16 shows the numerical, experimental and XFoil C_d values. Very few conclusions can be drawn about the C_d comparison at the higher angles of attack. The drag coefficient predictions were accurate in the linear range. Both CFD and XFoil predict a sudden increase in the C_d after the stall point, which is to be expected.

Figures 4.15 and 4.16 only show the results for a standard $k-\omega$ SST turbulence model, with default a_1 and C_T values and linear constitutive options. The use of the modified and variations on the $k-\omega$ SST model is described in more detail in Sections 4.3.4 and 4.3.5. Table 4.4 summarises the C_l and C_d results and % error to the wind tunnel C_l values of

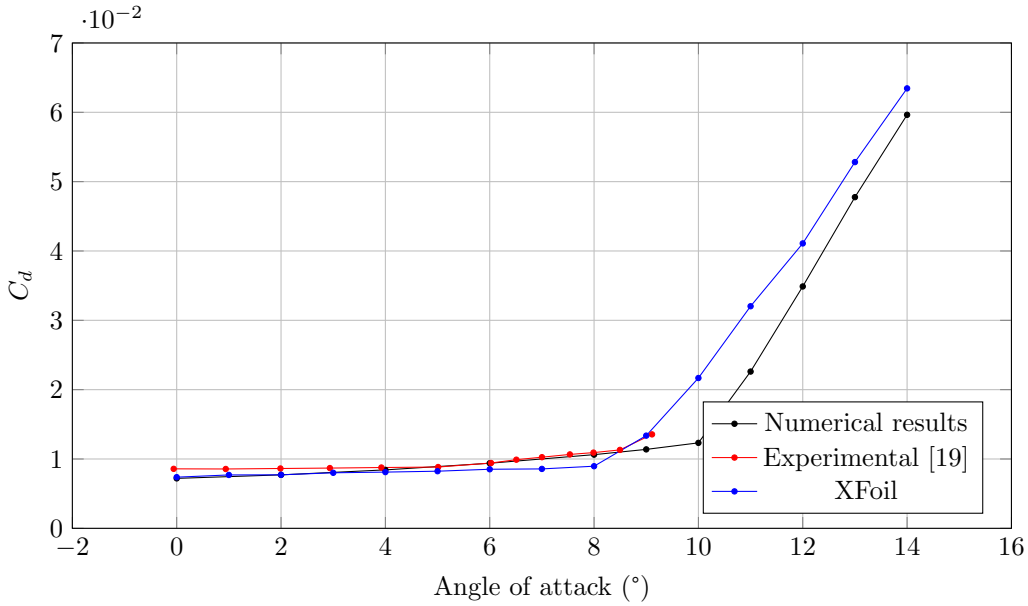

Figure 4.16: C_d vs α validation

the variations and modifications done. The standard $k-\omega$ SST setup gave the lowest C_l value where all their other variants overpredicted C_l at an angle of attack of 12°. An angle of 12° was arbitrarily chosen as an angle post the experimental stall point (± 9°). Flow conditions at this angle were much more suited for these variations and modifications. The modified a_1 and C_T values mentioned in Table 4.4, were $a_1 = 0.355$ and $C_T = 1.2$. The standard turbulence models with default parameters gave the smallest % Error and were used for the plots.

Table 4.4: FX66-17AII-182 - Results of variations on standard $k-\omega$ SST model at AOA 12°

Variation / Modification	C_l	C_l % Error to [19]	C_d
Linear, Default a_1 and C_T %	1.4097	36.2	0.0349
Linear, Modified a_1 and C_T %	1.5703	51.7	0.0345
Quadratic, Default a_1 and C_T %	1.4168	36.9	0.0299
Quadratic, Modified a_1 and C_T %	1.5248	47.3	0.0278
Cubic, Default a_1 and C_T %	1.4250	37.7	0.0338
Cubic, Modified a_1 and C_T %	1.4770	42.7	0.0326
Experimental data [19]	1.0349		

Summary

Even though the simulation overpredicted C_l, there was a good correlation of the characteristics, post-stall, between the numerical and experimental plots. Based on this, the methodology used in this section will also be followed in all coming sections. The CFD study of the extended airbrake case, in Chapter 5.1, can be conducted more confidently based on understanding the flow over the clean airfoil. The characteristics of the C_l/α plot, using the standard $k-\omega$ SST model with default parameters, matched the experimental results sufficiently. Altering the $k-\omega$ SST model did nothing to improve the results and

only served to overprediction C_l.

4.3 HPH yn1 Airfoil validation

The HPH yn1 airfoil (Figure 4.17) is a laminar airfoil used in sailplane design by the HpH Sailplane company, with a maximum thickness of 14.5% C at 43.5% C [36]. The wind tunnel data can be found in [20] and were obtained using the 3 m low wind speed tunnel with an open test section at the Aeronautical Research and Test Institute in Prague. The tests were conducted at a Reynolds number of 1.5×10^6.

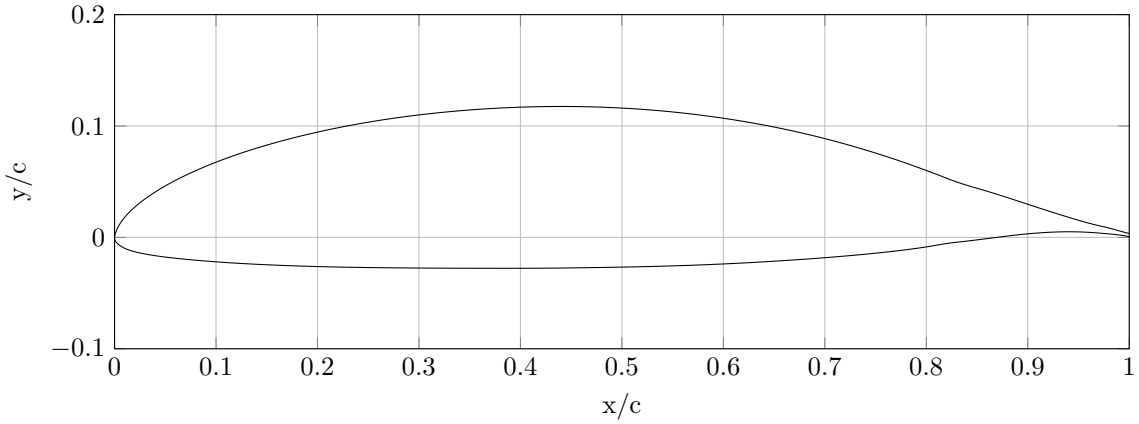

Figure 4.17: HPH yn1 section view

The methodology followed in this section is similar to that in Section 4.2. Firstly an initial inviscid simulation was done to determine the number of nodes required on the airfoil to obtain a mesh independent solution. Afterwards, the wake refinement study contained the time step and inner iteration studies.

4.3.1 HPH airfoil mesh refinement study

Similar to the FX66 airfoil, initial inviscid mesh simulations were set up to determine the minimum amount of node points on the airfoil to achieve a mesh independent solution. This solution formed the starting point for the wake mesh refinement to follow.

Simulation setup

The mesh used in this section was generated using an unstructured polyhedral mesher. The overall mesh base size was varied as per Table 4.6. The angle of attack used was 0° with the airfoil surface size selected as 2% and the LE and TE sizes 0.05% and 0.1%, respectively. In addition to the surface refinement, volume refinements were added to the region surrounding the LE and TE. These volume refinements had a target surface size of 2% and 1%, respectively. Figures 4.18 and 4.19 give an overview of the overall generated mesh and a more detailed view of the mesh around the airfoil, respectively.

Figures 4.18 and 4.19 show the generated meshes at base size 10%.

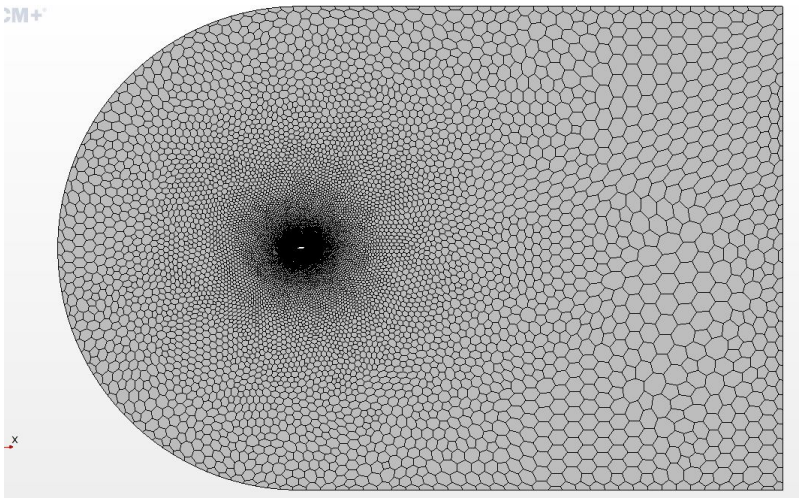

Figure 4.18: HPH yn1 Generated mesh on overall flow domain at base size 10%

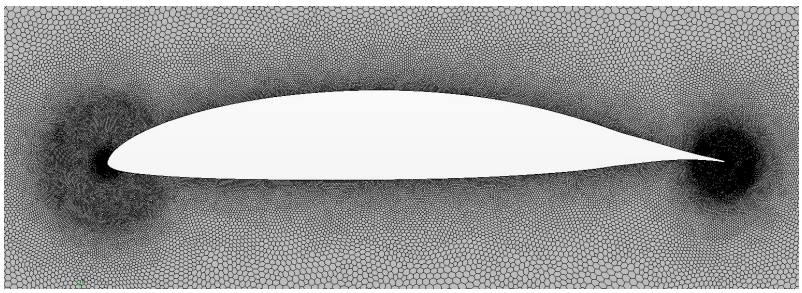

Figure 4.19: HPH yn1 Generated mesh surrounding airfoil at base size 10%

The physics continuum setup remained the same as in Section 4.2.1 except for the properties in Table 4.5. The physical flow properties were derived from the Reynolds number and using the Reynolds number equation (Eq 2.1). The chord and density values were kept the same by changing the velocity.

Table 4.5: HPH yn1 simulation properties

Variable	Value [Unit]
Reynolds number [Re]	1.5×10^{6} [-]
Airfoil chord [l]	0.6 [m]
Density [ρ]	1.225 [kg/m^3]
Velocity [V]	36.776 [m/s]
Dynamic viscosity [μ]	1.802×10^{-5} [Pa.s]

Results and discussion

Table 4.6 summarises the results of the invisicid simulation with Figure 4.20 giving the C_l vs Δ_x and Δ_{x^2} plots.

Base size 0.1 C was selected to be used in the following steps, resulting in a GCI of 0.28% with a % error of 0.89% relative to the Richardson extrapolated C_l value of 0.6138.

Table 4.6: HPH yn1 initial inviscid mesh refinement study base sizes at AOA 0°

Base size [m] (% of C)	Element count [-]	C_l	Δ_x	r	GCI	% Error
0.18 (30%)	37179	0.6168	0.0300	-	-	0.49%
0.12 (20%)	45960	0.6199	0.0279	1.073	4.14%	0.99%
0.06 (10%)*	80050	0.6193	0.0232	1.203	0.28%	0.89%
0.03 (5%)	171417	0.6169	0.0180	1.289	0.73%	0.51%
0.015 (2.5%)	462149	0.6154	0.0129	1.392	0.33%	0.26%
Richardson extrapolated C_l		0.6138				

* Representing the chosen parameter for following studies

As shown in Figure 4.20b, the C_l point at 0.1 C is nearly inline with the Richardson extrapolated linear line, indicating a very good fit and that grid independence has been achieved.

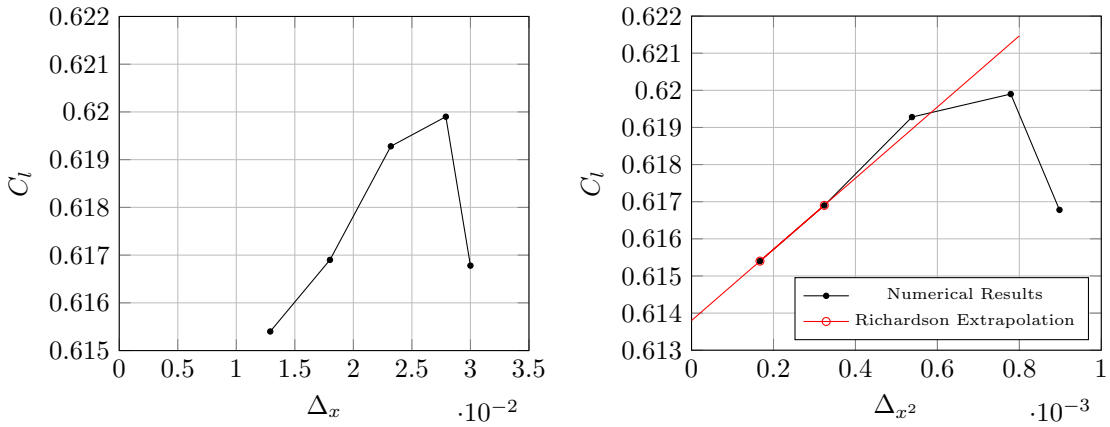

(a) C_l vs relative mesh spacing

(b) Richardson extrapolated spacing

Figure 4.20: Mesh convergence of C_l at an AOA of 0° for the inviscid flow over a HPH yn1 airfoil

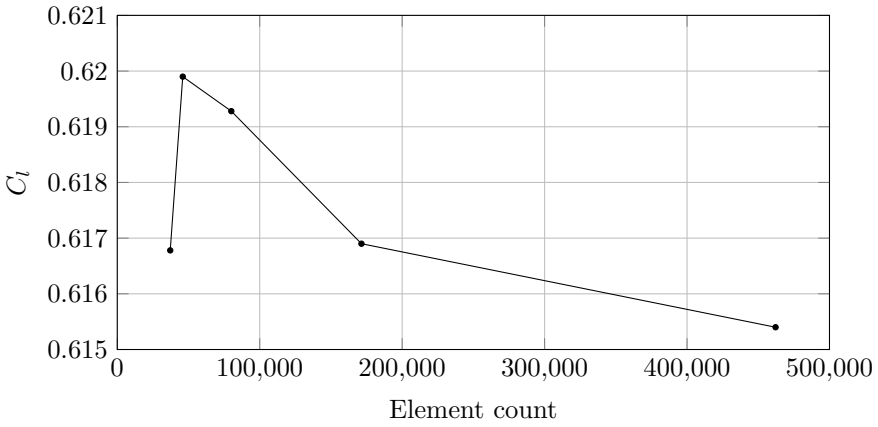

Figure 4.21: C_l vs Element count of HPH yn1 - Inviscid flow regime at AOA 0°

4.3.2 HPH wake mesh refinement study

In the wake mesh refinement study, the results of the HPH inviscid study were used as the starting point for the wake refinement study. Wake volume controls were added, and simulations were run to achieve a mesh independent solution.

Simulation setup

This study was conducted at an angle of attack of 22°. Figures 4.22 and 4.23 show the refinements of the generated mesh of base size 10%. These additional refinement zones were set to be 1, 2 and 8 chord lengths downstream with refinement sizes 8%, 10% and 15% of the mesh base size. The added volume controls gave more control over the refinement of the airfoil wake by allowing different sizes to be used. This allowed the mesh to capture secondary recirculating flows close to the airfoil without using an overly fine mesh. Chapter 3.4.3 went into more detail on the effects wake refinement, and the downstream distance had on the results.

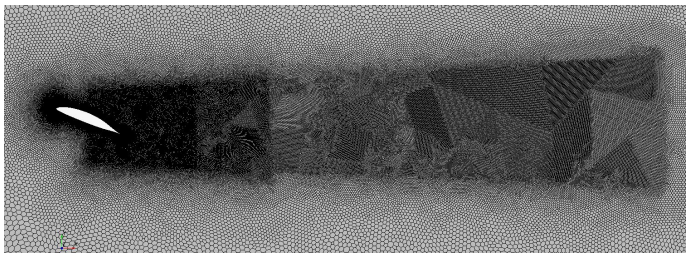

Figure 4.22: HPH yn1 Generated mesh of wake volume refinement at base size 10%

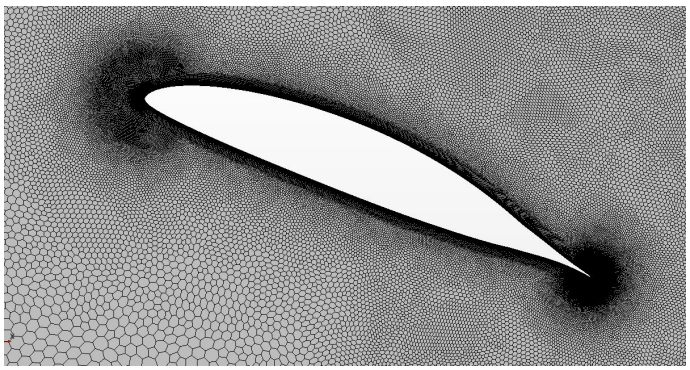

Figure 4.23: HPH yn1 Generated mesh surrounding airfoil at base size 10%

The prism layer thickness was chosen by calculating the boundary layer thickness at the end of the airfoil using Equation 2.4. The initial prim layer thickness was selected such that the y^+ values on the airfoil is < 1.

The simulation was set up using URANS $k - \omega$ SST Menter with $\gamma - Re_\theta$ transition modelling. A second-order convection scheme was selected with the linear constitutive option. Due to the high angle of attack, a $\gamma - Re_\theta$ free stream edge of 8mm was chosen. The geometry, free stream velocity and mesh settings were similar as in Section 4.2, and thus the same time step (0.0001 s) was used. The inner iterations were varied due to the

high angle of attack and the effect on the results.

Results and discussion

The wake mesh refinement study results are summarised in Table 4.7. The results in Table 4.7 are only of the 30 inner iterations and time step 0.0001 s case. A time step independence was achieved as a time step of 0.00005 s was also tested for each base size, with the force coefficient results being within 0.13% of that of time step 0.0001 s. This means that reducing the time steps also gave the same results as the chosen 0.0001 s time step, irrespective of the mesh base size.

Table 4.7: HPH yn1 wake mesh refinement study base sizes at AOA 22°

Base size [% of C]	Element count [-]	C_l	Δ_x	r	GCI	% Error
30%	152130	1.7948	0.0026	-	-	1.53%
20%	170079	1.7924	0.0024	1.057	1.39%	1.39%
10%*	258635	1.7904	0.0020	1.233	0.27%	1.28%
5%	580443	1.7785	0.0013	1.498	0.67%	0.61%
2.5%	1798126	1.7713	0.0007	1.760	0.24%	0.20%
Richardson extrapolated C_l		1.7678				

* Representing the chosen parameter for following studies

Figure 4.24 gives both the C_l values vs Δ_x and Δ_{x^2}. Figure 4.24a gives the results of both 20 inner iterations and 30 inner iterations. It is clear that the 20 inner iterations plot does not conform to the required linearity evident in the 30 inner iterations plot; thus, 30 inner iterations were chosen. Figure 4.24b clearly shows the linearity with the Richardson extrapolated plot. A Richardson extrapolated C_l value of 1.7678 was derived from the trend line.

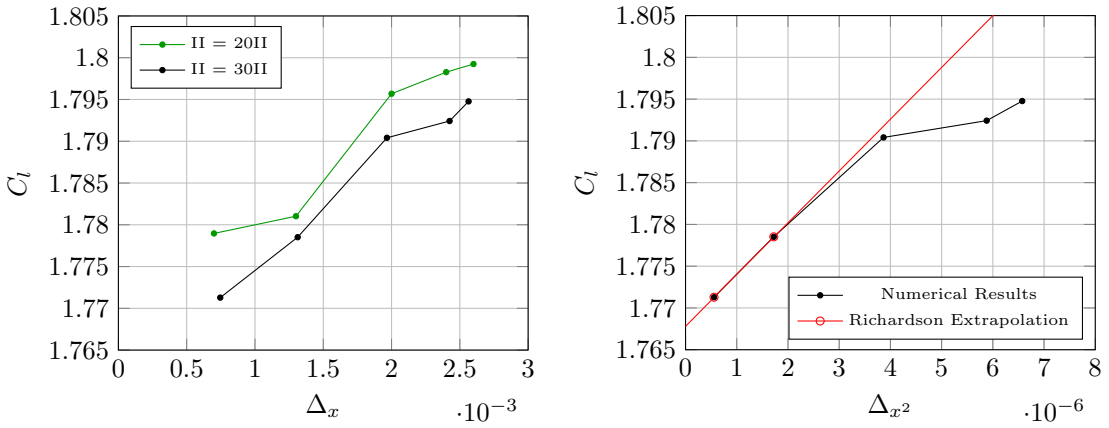

(a) C_l vs relative mesh spacing

(b) Richardson extrapolated spacing

Figure 4.24: Mesh convergence of C_l at an AOA of 22° for the flow over a HPH yn1 airfoil

A base size of 10% of the chord was selected to do the validation study in the following section. The CGI and the % error fell way below the required 5%. Figure 4.25 plots the C_l vs number of elements of the study. The plot shown is of the chosen combination of parameters, 30 inner iterations using a time step of 0.0001 s.

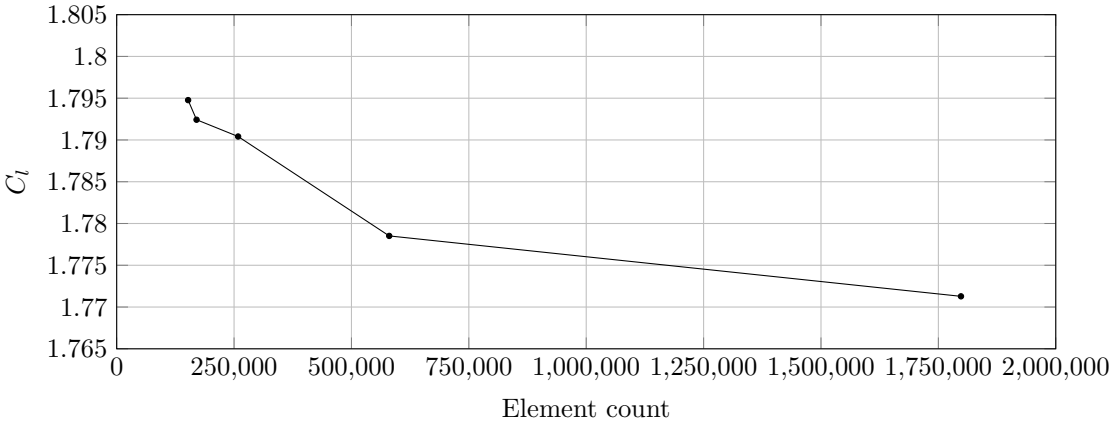

Figure 4.25: C_l vs Element count of HPH yn1 - Mesh refinement study

The second-order convergence of the plot in Figure 4.24b indicates that C_l convergence has been met and that a mesh and time step independent solution was obtained.

4.3.3 HPH CFD simulation validation

This is an essential section because both the clean airfoil and the airfoil with the extended airbrake were tested in the same wind tunnel. Accurate results increased the confidence in the simulation setup, that the force coefficients calculations are done correctly and that the airfoil geometry is sufficiently modelled.

Simulation setup

An angle of attack sweep from, -6° up to 22° was done in order to achieve accurate C_l and C_d vs α plots. A simulation at a certain angle of attack was run until the residuals, and the force coefficients converged; thereafter, a successive angle of attack was selected, the simulation was remeshed, and the process repeated. All mesh and standard physics parameters were kept the same as the previous simulations, excluding the following parameters that formed the focus of this section.

- Standard $k-\omega$ SST $\gamma - Re_\theta$ model with Linear constitutive option.
- Variations on $k-\omega$ SST $\gamma - Re_\theta$ model using quadratic and cubic constitutive options.
- Modifications of the shear stress limiter (a_1) and realizability coefficient (C_T) [52].

Results and discussion

In order to understand the effects of these variations, firstly, the standard linear constitutive $k-\omega$ SST was used. Following that, changes have been made to the constitutive

options available in Star CCM+, namely linear, quadratic and cubic. Further modifications to these variants were made by altering the shear stress limiter (a_1) and realizability coefficient (C_T). In Section 4.2.3, a brief mention of the variations and modifications on the $k-\omega$ SST turbulence model was made. These variations will be discussed in more detail in Sections 4.3.4 and 4.3.5.

Standard linear $k-\omega$ SST

Starting off, the standard linear $k-\omega$ SST model with a_1 and C_T kept at default (0.31 and ≈ 0.6, respectively) was used. Figures 4.26 and 4.27 show the standard $k-\omega$ SST model was accurate in the linear range (angle of attack -6° to 5°) on both C_l/α and C_d/α plots, which was to be expected. The CFD simulations started overpredicting C_l from 5° up to 22°.

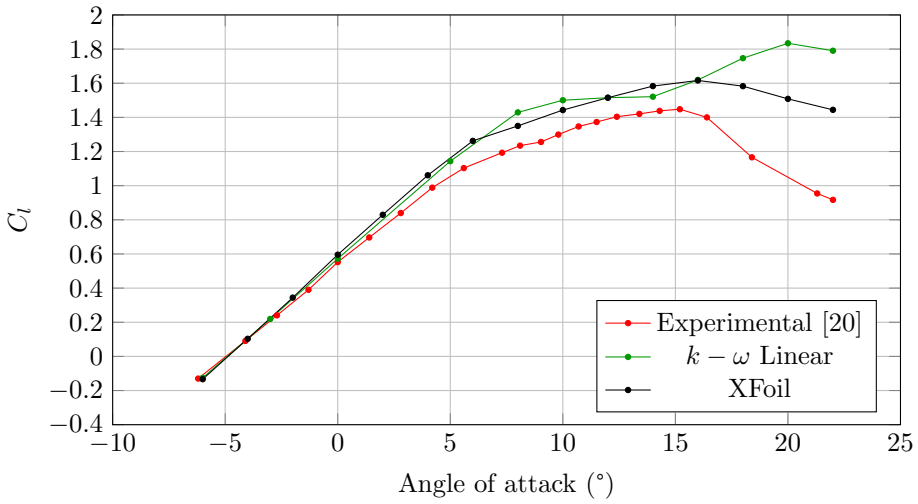

Figure 4.26: C_l vs α validation

On the other hand, the simulations more closely predicted the expected C_d trend than that of C_l. The numerical results were accurate up to 12°, where the CFD simulations started underpredicting the drag coefficient.

Accurately predicting the force and pressure coefficients at the lower angles of attack gave sufficient confidence that the CFD setup and the interpretation of the experimental results were correct. The noticeable overprediction of the C_l started at 8°. This can be seen in the C_p plot (Figure 4.28), giving the time averaged pressure coefficient distribution on the airfoil surface. Figure 4.28 shows the CFD plots have a lower pressure on the upper airfoil surface than the expected experimental results. The difference between the pressure on the upper and lower surfaces generates the lift. This means that a deviation from the experimental pressure difference will directly affect the C_l results of the simulations. Various parameters were adjusted, altered and investigated to correct the deviation; however, none gave the desired results.

These parameters included:

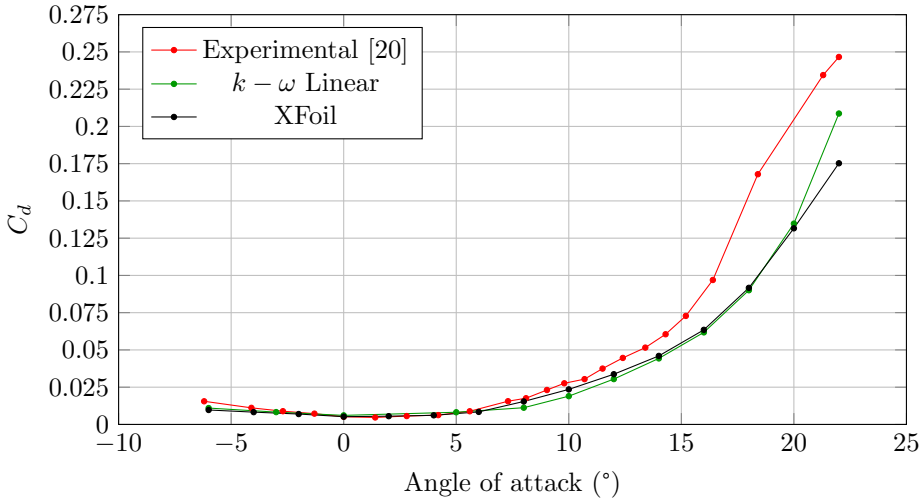

Figure 4.27: C_d vs α validation

- increasing the number of nodes on the airfoil spline using xfoil, increasing the geometric quality of the foil.
- running the simulation using Star CCM+'s double precision solver to reduce numerical errors.
- Increasing and decreasing the prism layer thickness.
- Increasing and decreasing the $\gamma - Re_\theta$ wall function.
- Incrementally increasing the AOA in steps of 0.2° around the problematic angle.
- Altering the geometry of the airfoil TE.
- Increasing and decreasing the mesh density around the airfoil leading edge.

As can be seen in Figures 4.30 and 4.33, the variations on the constitutive option and modifications of both the shear stress limiter and realizability coefficient had no significant effect.

Summary

The simulation captured the linear range of the plots accurately. The $C_l\alpha$ plot started to deviate as the angles increased until a large overprediction of the lift coefficients started at 8°.

Multiple attempts with different simulation parameters were performed to try and improve the C_l results at the angle of attack 8°and every angle after that. None of these ventures improved the results. This led to the investigation and use of the $k-\omega$ SST alterations and modifications described below.

The Courant numbers for the generated mesh and time step of 0.0001 s were < 10, except for the high-velocity regions around the leading and trailing edges. Despite the relatively high Courant number, a time step independent solution was achieved.

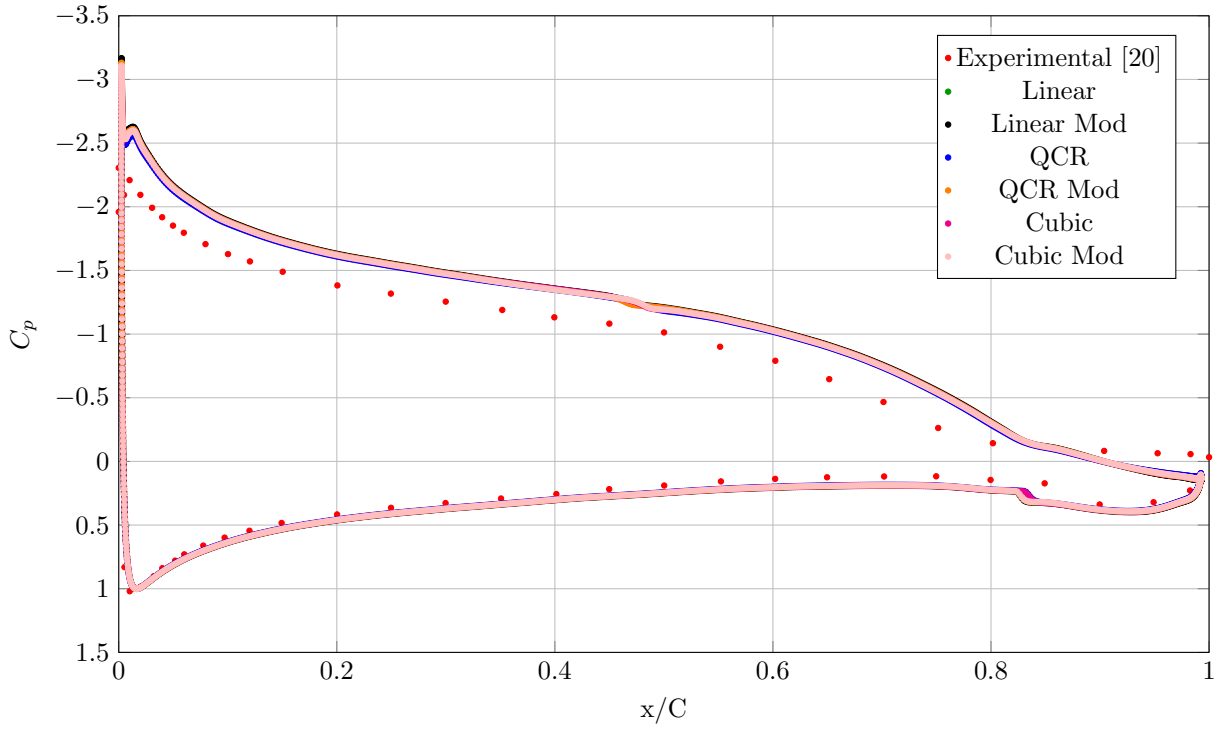

Figure 4.28: C_p vs α validation

The poor correlation between the validation simulations and the wind tunnel results required further investigation. The identified parameters to investigate were variations to the standard $k-\omega$ SST model, modifications to the model and a 2.5D study. These three studies are described in more depth in the following sections.

4.3.4 Variations on $k-\omega$ SST

Other options that were looked at, as mentioned in [10], were variations in the $k-\omega$ SST solver. These variations are to change the constitutive option from linear to cubic (as used in [10], or quadratic. Even though [10] only used cubic, [5] also mentions that the quadratic option would help with the anisotropic turbulence. The overprediction and the unexpected trend of the C_l/α plots required further investigation to obtain more accurate results.

The Hellsten $k-\omega$ explicit algebraic Reynolds-stress turbulence model was used in the airbrake extended CFD study of [10]. This variation is available in Star CCM+ as the cubic constitutive option. The other non-linear option is the quadratic (QCR) option [5]. Menter modified the linear constitutive $k-\omega$ turbulence model, naming it the $k-\omega$ SST model. The problem with only using the linear relation between the Reynolds stresses and the mean strain rate was the trend to considerably underpredict the anisotropy of the turbulence [5].

Turbulence, in the majority of the complex flows, is anisotropic. Examples of these flows are streamlined curvatures: boundary layer flows, the shear layer and strong secondary flows. All of these above mentioned flows are strongly prevalent in the high angle of

attack and extended airbrake cases studied. [5]. The addition of the quadratic and cubic constitutive options allows Star CCM+ to account for the anisotropy of turbulence in these complex flow conditions by including the non-linear functions of the strain and vorticity-rate tensors, in these relations [53]. The cubic relation expands on the quadratic relation by adding additional terms in the form of cubic functions. These terms are beneficial specifically to streamline curvatures by improving the sensitivity of the turbulence model.

These variations will improve the turbulence prediction of flow conditions with strong secondary flows such as recirculation, separation or vorticities. External aerodynamic cases, especially cases sensitive to separation such as high angle of attack studies, shows improved drag prediction in particular [53]. Secondary flows can be described as flows that form normal to the main direction of flow. Figure 4.29 illustrates the low velocity secondary, separated and recirculating flow at angle of attack of 22°. The flow conditions illustrated were fully developed and repeated at 1 second.

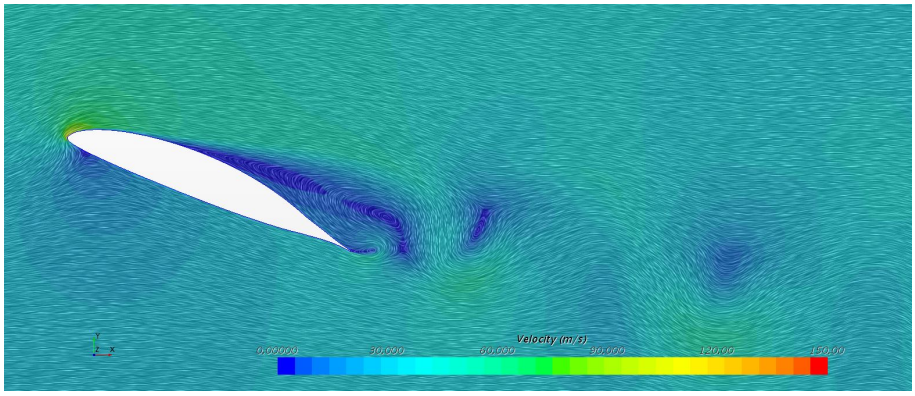

Figure 4.29: HPH yn1 Velocity plot at 1 s and AOA 22°

The cubic constitutive relation represents an Explicit Algebraic Reynolds Stress Model (EARSM), as it is derived from a Reynolds stress transport model (RST). RST models perform better in anisotropic turbulent flows than eddy viscosity models (such as the standard $k-\omega$ SST model). RST is much more unstable in these complex flows [5], where $k-\omega$ SST with the non-linear constitutive options is a good compromise and, thus, was used.

In [53], the study goes further and demonstrates that the default linear option overpredicts the separation region of a NACA 4412 at angle of attack of °13.87 and $Re = 1.52 \times 10^6$. However, the value of the a_1 coefficient was changed from 0.31 to 1, as discussed in more depth in Section 4.3.5. The addition of the quadratic option significantly increased the accuracy of the velocity profiles at the points in question (along the trailing edge), where the cubic option closely matched the experimental results.

Results and discussion

The C_l and C_d plots of linear, cubic and quadratic constitutive options are shown in Figures 4.30 and 4.31. When comparing these results to the standard linear $k-\omega$ SST $\gamma - Re_\theta$ results, it is clear that the cubic option performs similarly to the linear option.

The quadratic option slightly improves the C_l predictions at angle of attack 12° and 22°. However, the other angles have a similar or higher C_l.

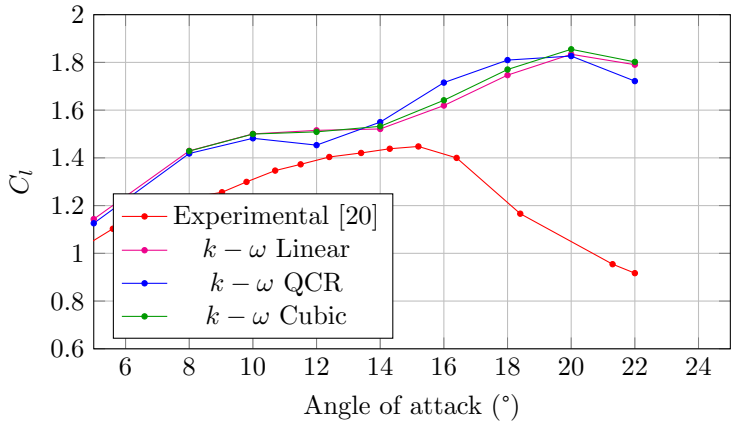

Figure 4.30: C_l vs α validation of Linear, Quadratic and Cubic constitutive options

Using this variation of the constitutive option did little to improve the characteristics and overprediction of the C_l/α curve. On the other hand, the quadratic relation did improve the C_d prediction of the entire sweep, especially at 22 °. The characteristics of the entire C_d/α plot more accurately resemble the expected experimental results.

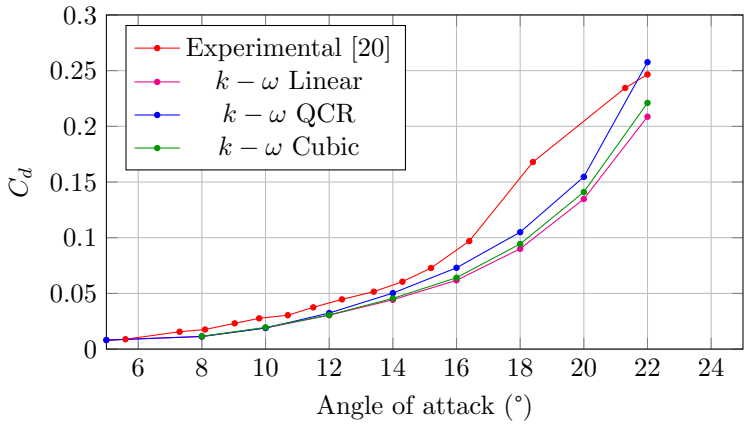

Figure 4.31: C_d vs α validation of Linear, Quadratic and Cubic constitutive options

[54] mentions that not accurately capturing the secondary flows can lead to underprediction of the losses. However, even though linear, quadratic and cubic constitutive options were used, C_d was still underpredicted during the entire angle of attack sweep up to 20°. The quadratic constitutive option gave the best C_d value, (4.3%) of the experimental, at 22° were linear and cubic were only 18.2% and 11.5% respectively, contrary to the findings in [53]. More concerning is the continued overprediction of C_l at the high angle of attacks. Those results lead to using various other methods more suited to the highly turbulent and separated flow at these higher angles of attack.

4.3.5 Modified $k-\omega$ SST

Another method to further improve separated flow conditions is by modifying the standard $k-\omega$ SST model. The modification done in [53] was to change the value of the shear

stress limiter (a_1) from 0.31 to 1. The effects of changing the a_1 coefficient are described in more detail in [55].

The shear stress limiter can significantly impact the accuracy of solutions by limiting the product of the a_1 coefficient and the turbulent kinetic energy inside the boundary layer. The default value ($a_1 = 0.31$ was derived empirically for attached flows [55] by Menter [52]. This can be altered depending on the application and flow conditions. An investigation on the effects altering the a_1 coefficient has on a NACA 4412 airfoil at an angle of attack 13.87 ° and Re $= 1.52 \times 10^6$ was conducted in [55].

The study done in [55], similar to that in [53], examines the effect on the velocity profiles along 6 line probes on the trailing edge. The study shows that a default value of $a_1 = 0.31$ gives better agreement with the experimental velocity profiles than $a_1 = 1$. The study in [55] concludes that even though altering the a_1 value can be beneficial in highly separated flows. There is not a specific a_1 value that should be used, and a sensitivity study should be run when changing the parameters.

However, [52] investigated the effect of altering the a_1 and realizability coefficient (C_T) that improved results of especially separated flows in canonical cases. Cases that were investigated in [52], that have similar characteristics of flow over a high angle of attack airfoil are: a 2D diffuser, a periodic hill, 2D NASA wall mounted hump with separated flow and NASA 3D high lift flow physics. A summary of the results of the various cases studied in [52] is given below:

- 2D diffuser - Velocity profiles of $a_1 = 0.31$ more accurately compared to the experimental results than that of $a_1 = 0.34$. The separation point was more accurately predicted using $a_1 = 0.34$, but the flow reattached too early.
- Periodic hill - Skin friction coefficient of $a_1 > 0.34$ case was much closer to that of the LES (Large Eddy Simulation) results. Due to the larger adverse pressure gradients present, the velocity profile of $a_1 = 0.36$ much closer resembled that of a DNS (Direct Numerical Simulation) model.
- NASA wall mounted hump separated flow - A more relevant case than the previous two. Flow separation and reattachment points are more accurate using $a_1 = 0.36$ than $a_1 = 0.31$. The skin friction and pressure coefficients across the surface also much closer resembles that if the experiment using $a_1 = 1$ than $a_1 = 0.31$.
- NASA 3-D High lift flow physics - A $C_T = 1.2$ was used for both $a_1 = 0.31$ and $a_1 = 1$ studies. It was found that the default, $C_T = 0.6$, was too restrictive and caused early separation. The C_L/α and C_D/α plots much closer resemble the experimental results using $a_1 = 1$ than $a_1 = 0.31$. The effect is especially noticeable at high angle of attack $\pm$ 20° to $>$ 35°.

It was concluded in [52] that changing the shear stress limiter (a_1) above 0.35 reduces the separation region. The default $k - \omega$ SST ($a_1 = 0.31$) tends to overpredict the separation region and underpredict the turbulent viscosity ratio in the recovery ratio leading to

inaccurate results. In addition to changing a_1, the realizability constant (C_T) also needed to be adjusted, being too restrictive on default settings (from 0.6 to 1). It is finally concluded that the modified $k-\omega$ SST model yields accurate results for both bluff bodies and wings.

Results and discussion

As suggested in [55], a sensitivity study was done on the HPH yn1 airfoil and the results are given in Figure 4.32. The a_1 coefficient used was 0.31, 0.355, 0.5, 1.0 and 1.5, using the cubic constitutive option with C_T left at 0.6.

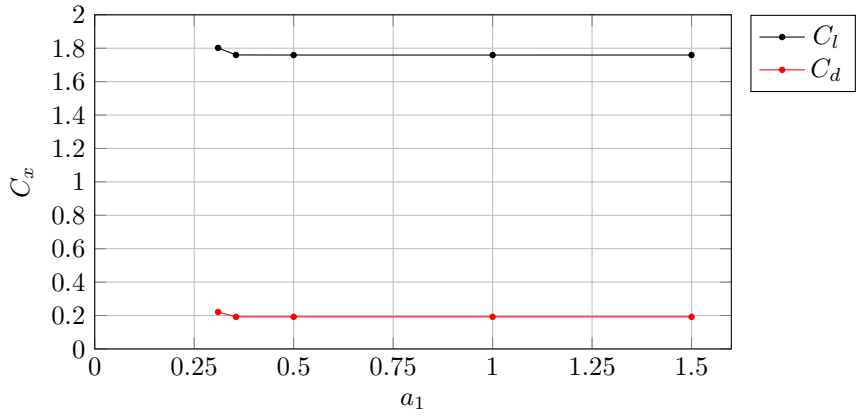

Figure 4.32: C_l and C_d vs a_1 values of HPH yn1 airfoil at 22° AOA

Both C_l and C_d values remain constant from $a_1 = 0.355$. The results for the are given in the C_l/α and C_d/α plots in Figures 4.33 and 4.34.

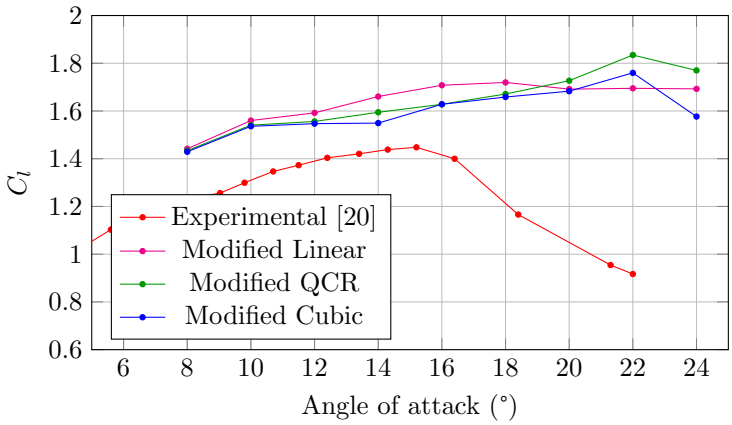

Figure 4.33: C_l vs α validation of Linear, Quadratic and Cubic constitutive options with modified $k-\omega$ SST solver

The C_l values in the current study were overpredicted using the default $k-\omega$ SST setup. The modified $k-\omega$ SST only served to further increase and exaggerate this error. The underprediction of C_d in Figure 4.34 aligns with what is expected when the separation point is delayed, contrary to what was found in the 3D NASA case in [52].

Using the modified $k-\omega$ to improve results was more applicable in the 3D NASA High lift

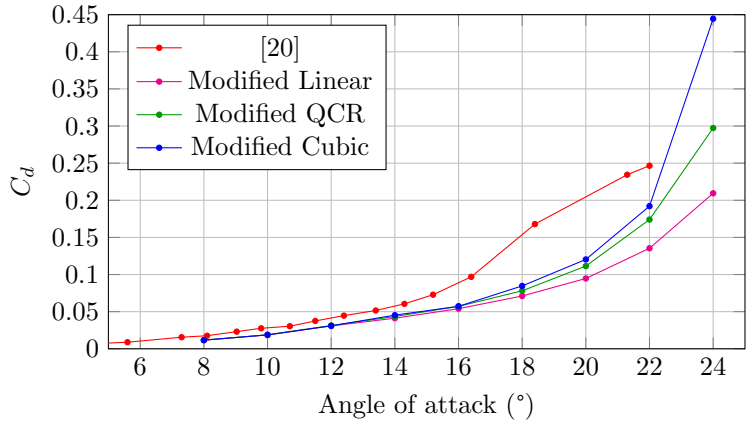

Figure 4.34: C_d vs α validation of Linear, Quadratic and Cubic constitutive options with modified $k-\omega$ SST solver

case in [52] than in the current study. The default $a_1 = 0.31$ results in [52] underpredicted the C_l/α plot, which illustrates an overestimated separation point. On the other hand, the results in [52] showed an underprediction of the C_D/α curve using $a_1 = 0.31$ and much more accurate results after using the modified turbulence model.

This was not the case in the results shown in Figures 4.33 and 4.34. The initial overprediction of C_l was only further exaggerated when increasing the a_1 value above the default. Modifying the standard $k-\omega$ SST turbulence model by changing the shear stress limiter has benefits and drawbacks. The benefits can be seen in [52] where the modification of a_1 and C_T increased the accuracy of canonical aerodynamic cases by reducing the overprediction of the separation point. The example in [53] combines the modification of these coefficients with variations on the constitutive options available using the $k-\omega$ SST model, namely the quadratic and cubic relations. There are drawbacks to these modifications, as can be seen in [55] as well as in the results in Figures 4.33 and 4.34.

The studies in [53] and [55] both used NACA 4412 airfoils at a $Re = 1.52 \times 1^6$ and Mach number = 0.09. The difference is that [53] also changed the constitutive options, whereas [55] used the linear option. These modifications and variations to the $k-\omega$ SST model did not yield the same level of increased accuracy expected and, on the contrary, only decreased the accuracy of the simulations. The results can be expected as the benefit of changing the a_1 value is delaying the separation point. This delay will keep the flow attached to the airfoil surface for longer and thus increase C_l and decrease C_d, which is exactly what was observed. The QCR constitutive option gave the best C_l and C_d results, especially at the higher angles of attack, when taking the coefficient values and the overall curve characteristics into account.

4.3.6 HPH Airfoil - 2.5D URANS

All of the studies up to this point have been 2D URANS, and the effects using different variations and modifications on the standard $k-\omega$ SST turbulence models had on the results. The problem with making the 2D assumption is that turbulence is inherently a

3D phenomenon. Turbulence can be identified by high levels of vorticity variations and rotational movement. These vorticity fluctuations can not be maintained in 2D. This is due to the vortex stretching, an important vorticity maintenance mechanism, not being present in 2D flows [56]. In addition to vortex stretching, stain also plays a part in the formation of vortices and the dissipation thereof. Figure 4.35, adapted from [57], illustrated the vortex stretching and strain.

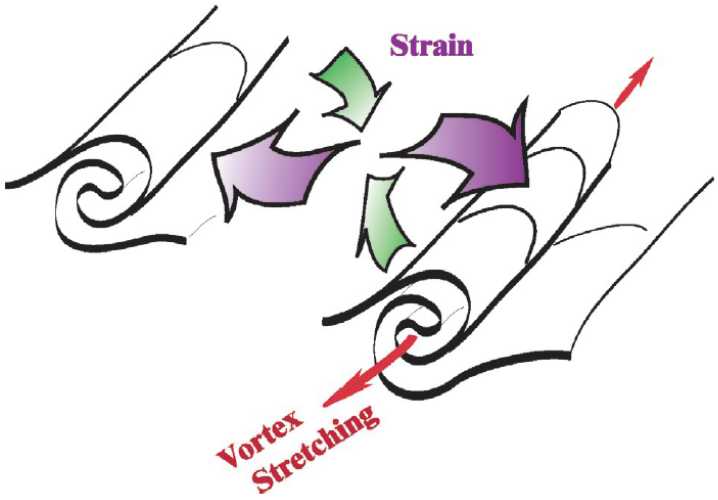

Figure 4.35: Line vortices with strain and vortex stretching affecting the vortex geometry.

Another aspect reducing the 2D accuracy is the restriction on flow dissipation. The viscous shear stresses reduce the kinetic energy of the systems [56]. Limiting flow to only 2D reduces the dissipation, altering the characteristics of the simulations. This means that using only 2D simulations suppresses the flow characteristics and development over the body, leading to inaccurate results. There are various advantages and disadvantages to using 3D over 2D. Some advantages are:

- Access to turbulence models more suited to separated flow cases such as Large Eddy Simulations (LES) and Direct Eddy Simulations (DES).
- Simulation setup more closely reflects real world conditions.

The main disadvantages to running 3D simulations, especially for separated flow cases, are how computationally expensive the simulations can get. In order to fully and accurately capture the characteristics of the turbulent and separated flow, various criteria need to be met. These include:

- Ensuring mesh size is small enough based on Taylor and Kolmogorov scales to accurately capture eddies in their applicable scales.
- Ensuring the flow domain is large enough to develop flow structures without interference from domain limits fully.

- Ensuring time steps are small enough to sufficiently capture and define a moving particle based on CFL value and allow eddies to form fully.

The disadvantages of a fully 3D CFD study outweighed the advantages for the current 2D airbrake study and is one of the reasons the focus was on a 2D approach. The other reason is that the CFD validation of both the FX66 [9] and HPH [10] extended airbrake studies are 2D.

After exploring various parameters and approaches to improving the CFD results in 4.3.3, 4.3.4 and 4.3.5, it was worth briefly investigating the effects of a 3D simulation. The method combined the speed of 2D simulations with the geometric advantages of 3D in a so-called 2.5D mesh. A 2.5D mesh, for this study, is a 2D mesh that has been extruded in the spanwise direction giving depth to the geometry and mesh setup. The 2.5D study was not meant to be an in-depth study but served as a base for what effect changing the simulation setup from 2D to 3D will have on the results and serve as a starting point for future studies. The geometry used as the 2D HPH yn1 airfoil with a span length of twice the chord, 1.2 m.

Mesh setup

The mesh was generated using the direct meshing method in Star CCM+. A 2D source mesh was extruded in the spanwise direction and divided into several sections, giving the simulation depth and allowing the use of the 3D physics continuum. The source mesh used was similar to the final mesh chosen in Section 4.3.3. The minor differences between the source mesh and the generated mesh used in Section 4.3.3 did not alter the overall 2D simulation results. Figure 4.36 illustrated the 2D source mesh.

in [12]

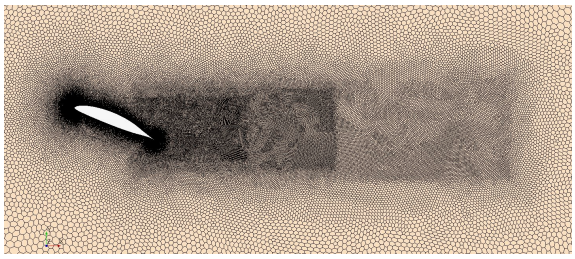

Figure 4.36: Generated 2D source mesh used in 2.5D simulation study at AOA 22°

As this study was only done to investigate the effects of a 3D simulation, the mesh was divided equally into 5, 10, 20 and 40 spanwise elements. Figure 4.37 shows the spanwise mesh distribution. In comparison, the 3D mesh in [12] had a spanwise length of 2 diameters with a spanwise mesh distribution of 20 cells per diameter, 40 in total.

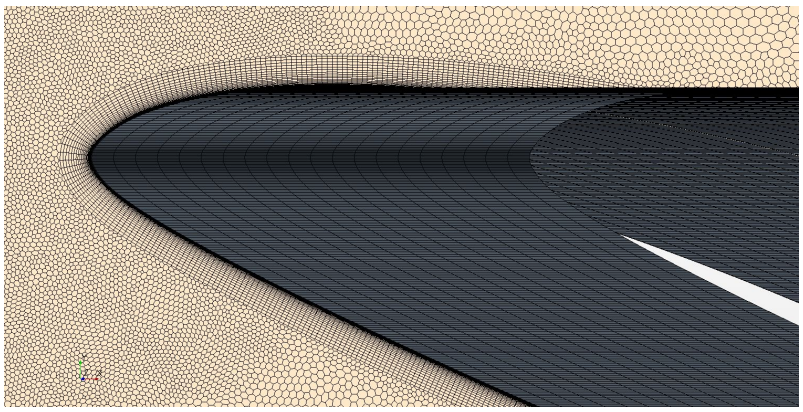

Figure 4.37: HPH yn1 Generated mesh of 2.5D simulation using 40 spanwise elements - spanwise element distribution at AOA 22°

Physics setup

The most significant change between the current 32.5D airbrake study and the 2D airbrake studies in this chapter was using the 3D physics continuum. Even though using 3D physics allowed for more powerful and applicable turbulence models, such as LES and DES, URANS was still the model of choice. The time steps and inner iterations were kept at $1x10^{-4}$ and 30, respectively. Both linear and cubic constitutive options were used, and the a_1 and C_T coefficients were left on default with the second-order upwind scheme. Both linear and cubic constitutive options were used to see what effect they would have on the results.

Results and discussion

The element counts for the generated meshes used for the mesh dependence study are summarised in Table 4.8. The mesh dependence study was done at an angle of attack of 22° using both Linear and Cubic Constitutive options. All of the mesh independence study C_L results fell within 7.4% and 16.6% of each other using linear and cubic constitutive options, respectively. The C_D results were within 13.5% and 13.2% of each other using linear and cubic constitutive options, respectively. The C_L and C_D results were close to each other, regardless of the spanwise mesh density distribution. Both linear and cubic constitutive options gave the same C_l at 14°. The cubic variant overpredicted C_l at 16°. The C_l results were close enough for exploratory purposes of the study: thus 10 spanwise elements were chosen for the simulations.

Table 4.8: Mesh dependence element count

Spanwise element count	Total element count
5	747515
10	1495030
20	2990060
40	5981020

The % error of the C_L and C_D results were 13.3% and 1.8% relative to the wind tunnel data

in [20]. Figures 4.38 and 4.39 gives the C_L/α and C_D/α results for the 2.5D simulation as well as the 2D results shown in Figures 4.26 and 4.27.

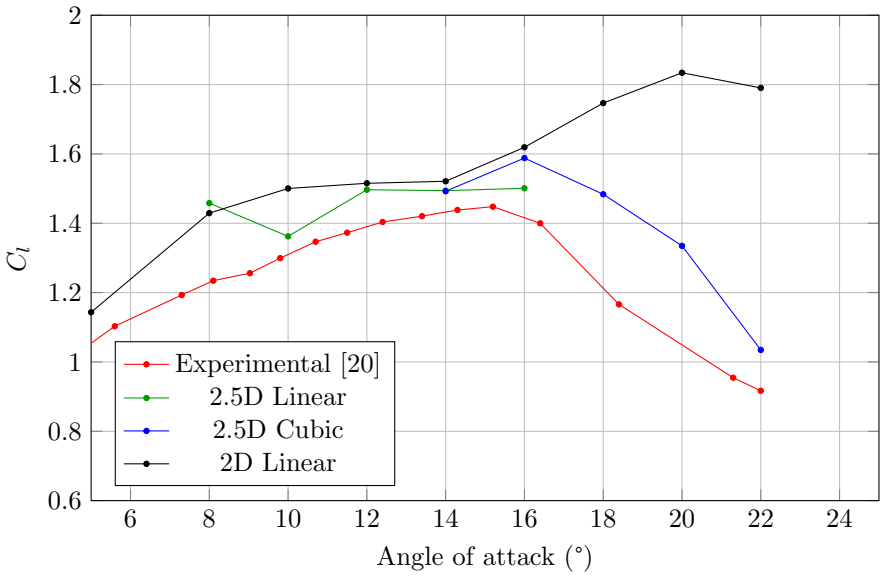

Figure 4.38: C_l vs α validation of 2.5D simulation using 10 spanwise elements

The differences between the 2D and 2.5D simulations are immediately evident at the higher angle of attacks. Even though C_L is still overpredicted, it is not nearly as extreme as using only 2D. The stall point $C_{L_{max}}$ was also closer to the experimental values, from 20° to 16° as expected.

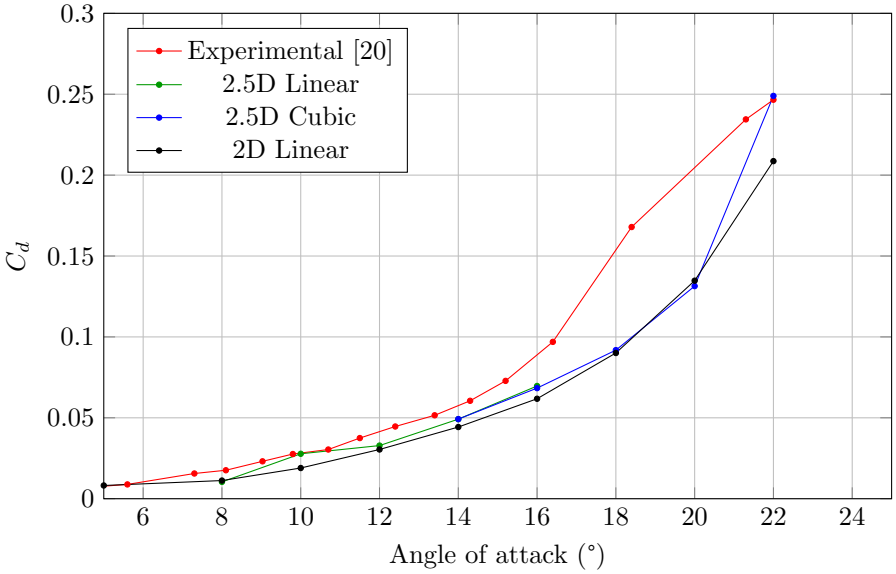

Figure 4.39: C_d vs α validation of 2.5D simulation using 10 spanwise elements

Similarly, the C_D values at 22° are within 1.8% of the wind tunnel data. The simulations still tend to underpredict the C_D between 14° and 20°.

The improved C_L results, on its own, make using a 3D simulation worth the extra computational time when accuracy at the higher angle of attack is important. The 2.5D approach in this section is not as computationally expensive as a full 3D simulation and was worth the effort to achieve these results. Depending on the application, there are benefits to

using a 2.5D simulation over that of a 2D simulation.

4.4 Conclusion

Two airfoils were studied in this section, the Wortmann FX66-17AII-182 and the HPH yn1 airfoils. These airfoils were designed for sailplane applications and thus made for suitable airfoils to do an airfoil validation study.

Both airfoil studies followed the same methodologies. Firstly a steady inviscid simulation was done to determine the number of nodes on the airfoil surface. Afterwards, a URANS mesh refinement study was done on a high angle of attack airfoil configuration. Both airfoil validation studies focused on mesh refinement in the wake and achieving a time step and inner iteration independent solutions. After the mesh and simulation properties had been identified, the validation cases for these airfoils were done using wind tunnel data as a reference.

The first study was the FX66-17AII-182 using the standard $k-\omega$ SST turbulence model. After the conclusion of the validation study, good conformance was achieved to that of the experimental data. The lift coefficient's overprediction was expected as the flow conditions were separated, highly turbulent, and difficult to capture using numerical methods. Nevertheless, the drop in the lift coefficient was predicted to be similar to that of the experimental data.

Secondly, the HPH yn1 airfoil was studied. Initially, the $k-\omega$ SST turbulence model was used during the validation study. Poor results meant that further investigation needed to be done to try and improve the results. These investigative studies used variations and modifications to the standard $k-\omega$ SST model. These variations were the use of the quadratic and cubic constitutive options, which could better capture anisotropic flows but did not improve simulation accuracy. These options allow for the better capture of anisotropic flows. These variations did not improve simulation accuracy. After that, modifications were made to the $k-\omega$ SST model, which included modifying the sheer stress limiter a_1 and constitutive option C_T coefficients.

An additional study was done using a 2.5D URANS simulation setup. The 2D mesh used in the other studies was used and extruded in the spanwise direction giving a pseudo 3D mesh. The C_d results were very similar to that of the 2D simulations. On the other hand, a significant increase in the overall flow characteristics was seen at the higher angles of attack (10° - 22°). This indicated the presence and confirmation of 3D spanwise flows directly affecting the force coefficients, especially that of C_l.

Chapter 5

CFD validation on sailplane airbrakes

5.1 Introduction

In Chapter 4, the mesh refinement, inner iteration and time step independence studies and validation of the FX66-17AII-182 and the HPH yn1 airfoils were done. The next and final step is to use the experience gained on a more complex geometry by adding the extended airbrake. This is the final step in the overall aim of simulating the flow over an airfoil and airbrake.

This chapter focuses on the CFD flow simulation over two cases of airfoils with extended airbrakes. These are the FX66-17AII-182 and HPH yn1 airfoils. Both airfoils share the Schempp-Hirth airbrake configuration used on the JS3 sailplane and are thus apt geometries to study.

The goal of this chapter is to apply the methodologies and parameters identified in both Chapters 2 and 3 on an airfoil with extended airbrakes and to investigate its effects on the CFD validations. These geometries are more complex than the canonical cases in Chapter 3 and the airfoils in Chapter 4, resulting in more complex flow phenomena and flow structures.

Both airfoil studies follow the same methodology. Firstly, adding the extended airbrake to the geometry led to additional mesh refinement in this region. The work done on the square cylinder in Section 3.5 was directly relevant to the extended airbrakes. Both geometries interact similarly to flow with high shear at the corners. This was followed by mesh refinement in the wake. The separated flow caused by the airbrake leads to vortex shedding, which needs to be captured to calculate the force coefficients accurately.

Following the mesh refinement studies, validation studies were done on both airfoil geometries. The reference data used for the FX66-17AII-182 validation was obtained from [9]. The airbrake data for the HPH airfoil is from the research of [20] with the CFD reference study done in [10].

5.2 FX66-17AII-182 Airbrake validation

The reference airbrake configuration in [9] was used in this section and represents the geometry used in the wind tunnel tests. This configuration is simply a flat plate extending vertically out of the airfoil body at a position of 0.5 C with an airbrake height of 0.11C. The airfoil had an angle of attack of 0°. The airfoil and airbrake geometry can be seen in Figure 5.1. The numeric and experimental C_l at these conditions are -0.568 and -0.649, respectively.

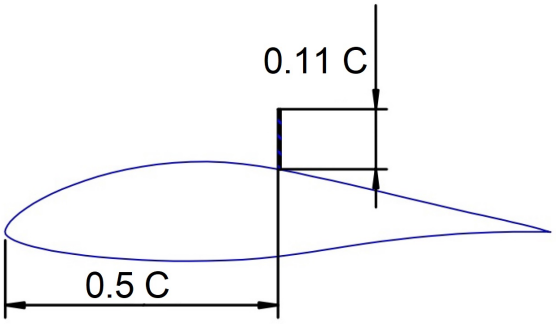

Figure 5.1: FX66-17AII-182 airfoil and airbrake configuration used in this section adapted from [9]

The simplicity of the geometry made it a suitable case to simulate. Additionally, and most importantly, the numerical C_l vs α results were compared to wind tunnel results, with a good correlation achieved between these results.

5.2.1 FX66 Airbrake mesh refinement study

The mesh used on the clean airfoil was used as the starting point of the FX66 mesh refinement study. Initially, the mesh was refined in the airbrake region. This is an important region for mesh refinement as the vortices that are formed directly affects the pressure distribution over the upper airfoil surface, thus affecting the C_l results. Additionally, the pressure differential upstream and downstream of the airbrake directly affects the total drag. These flow structures and high gradients need to be captured correctly.

Mesh setup

The flow domain and boundary conditions used were similar to that in Chapter 4. An unstructured polyhedral mesh with added prism layer was used. Three rectangular volume controls were added to the upper surface of the airbrake, with a fourth circular volume control around the tip of the airbrake blade. These volume controls can be seen in Figures 5.2 and 5.3.

The custom volume control sizes were set to 0.5%, 1%, 2% and 4% relative to the base size. The prism layer thickness was 7.5mm, half of the turbulent boundary layer thickness. A stretching factor of 3.3 was used with 45 prism layer cells, resulting in $y^+ < 1$. The

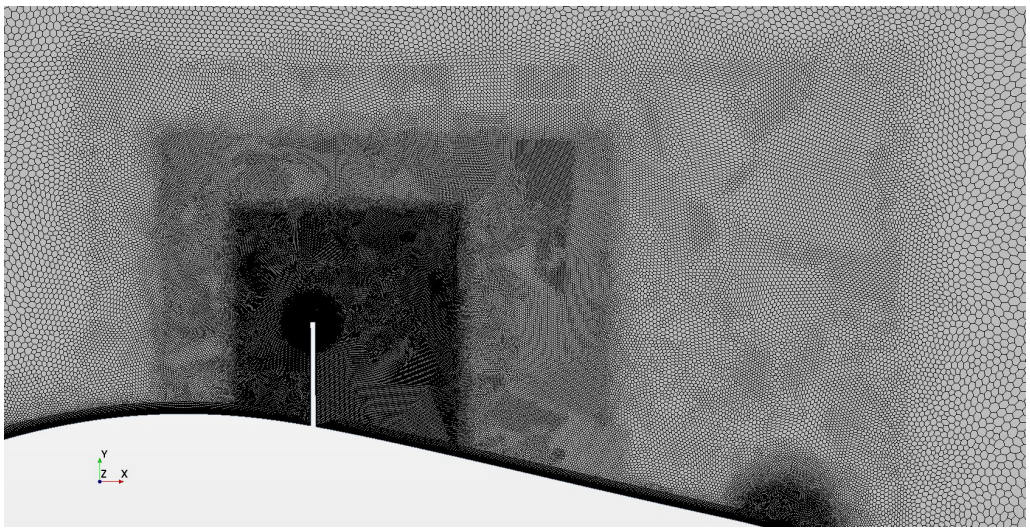

Figure 5.2: Mesh generated around FX66-17AII-182 airbrake using base size 0.1 C

base sizes for this mesh refinement simulations varied from 0.3 C down to 0.05 C as seen in Table 5.5.

Figure 5.2 shows a close-up view of the volume refinements added to the upper part of the airfoil. Figure 5.3 shows the overall generated mesh using a base size of 0.1 C.

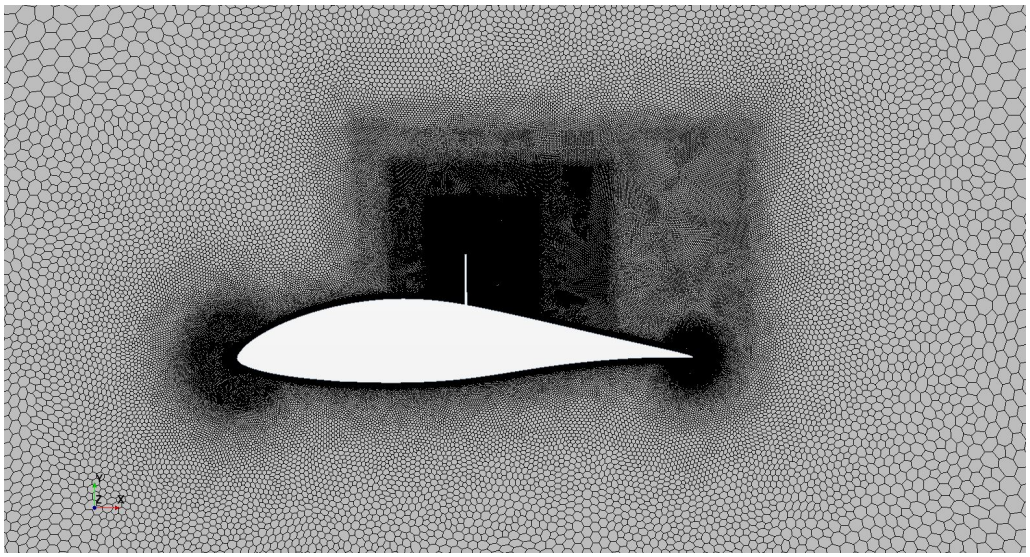

Figure 5.3: Overall mesh generated around FX66-17AII-182 body with base size 0.1 C

Physics setup

The physical flow properties, seen in Table 5.1, were derived using Eq 2.1 using a Reynolds number of 1.5×10^6 [9]. These properties are used in all the simulations in Section 5.2.

The URANS $k-\omega$ SST turbulence model was selected with the $\gamma - Re_\theta$ transition model. The inner iterations used were 20 and 30, with time steps ranging from 0.01 s to 0.00005 s. All coefficients were left at default, and the linear constitutive option was used. The second-order temporal and convective discretization schemes were used for all of the sim-

Table 5.1: FX66-17AII-182 with extended airbrake simulation properties

Variable	Value [Unit]
Reynolds number [Re]	1.5×10^{6} [-]
Airfoil chord [l]	0.6 [m]
Density [ρ]	1.225 [kg/m^3]
Velocity [V]	36.776 [m/s]
Dynamic viscosity [μ]	1.802×10^{-5} [Pa.s]

ulations in this section.

The time steps and inner iteration independence tests are done during the current mesh refinement simulations. The finest meshes are generated in the region downstream of the airbrake at this stage. The mesh refinement studies in the wake region (Section 5.2.2) will not affect the time step and inner iteration independent solutions as the wake meshes are more coarse. Additionally, the separation and recirculation flow occur downstream of the airbrake, where the current mesh refinement is done. The large vortex streets will not alter the time and inner iteration requirements.

Results and discussion

The results for the 30 inner iteration simulation at a time step of 0.0001 s are given in Table 5.5. The C_l results started converging at 0.0001s, with the results at 0.000005 s being within 2% of the 0.0001 s case. Figure 5.4a shows the C_l vs Δ_x tends of both 20 and 30 inner iterations at a time step of 0.0001 s.

Table 5.2: FX66 airfoil and airbrake wake mesh refinement study for 30 inner iterations and time step 0.0001 s

Base size [% of C]	Element count [-]	C_l	Δ_x	r	GCI	% Error
30%	161182	-0.3856	0.0025	-	-	12.7%
20%	176399	-0.3719	0.0024	1.046	48.78%	8.7%
10%*	277614	-0.3580	0.0019	1.255	8.52%	4.6%
5%	672535	-0.3487	0.0012	1.556	2.34%	1.9%
Richardson extrapolated C_l		-0.3422				

* Representing the chosen parameter for following studies

The C_l using 40 inner iterations at a times step of 0.0001 s was 2% from 30 inner iterations, indicating convergence at 30 inner iterations. Additionally, the 30 inner iteration simulation results tended much more to the asymptotic convergence compared to the 20 inner iterations. Figure 5.4b shows the linear line predicting a Richardson extrapolated C_l value of -0.3422. Using this value and the Grid Convergence Index (GCI), a mesh with a base size of 0.1 C was chosen. Even though the GCI for this mesh is slightly high, the % error to the Richardson extrapolated C_l was within 5% and within the required range.

Table 5.10 summarises the C_l vs Element count plot at 30 inner iterations and time step 0.0001 s. The TKE scene of the flow over the airbrake can be seen in Figure 5.6. This visually confirms that the chosen mesh was sufficient due to adequate mesh refinement in

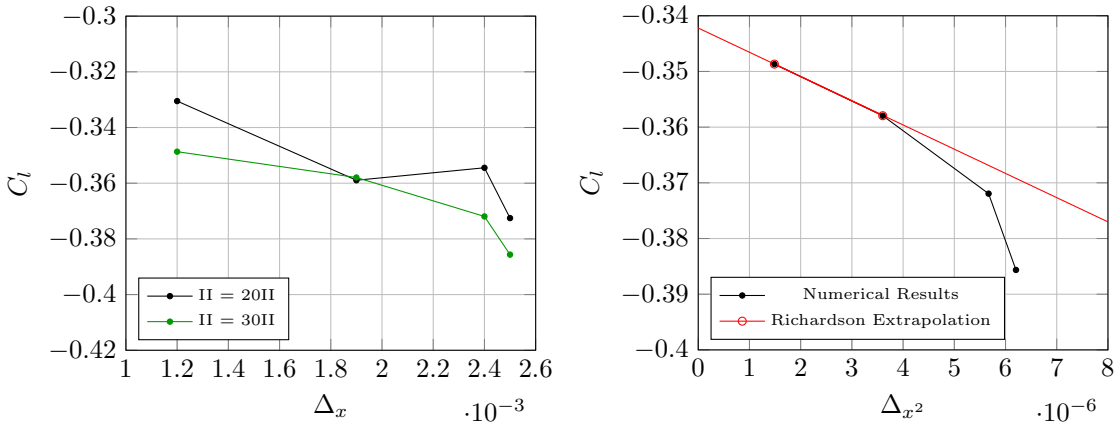

(a) C_l vs relative mesh spacing (b) Richardson extrapolated spacing

Figure 5.4: Mesh convergence of C_l at an AOA of 0° for the flow over a FX66-17AII-182 airfoil with extended airbrake and 30 inner iterations.

the high-pressure gradients, especially the shear layer emerging from the airbrake blade tip.

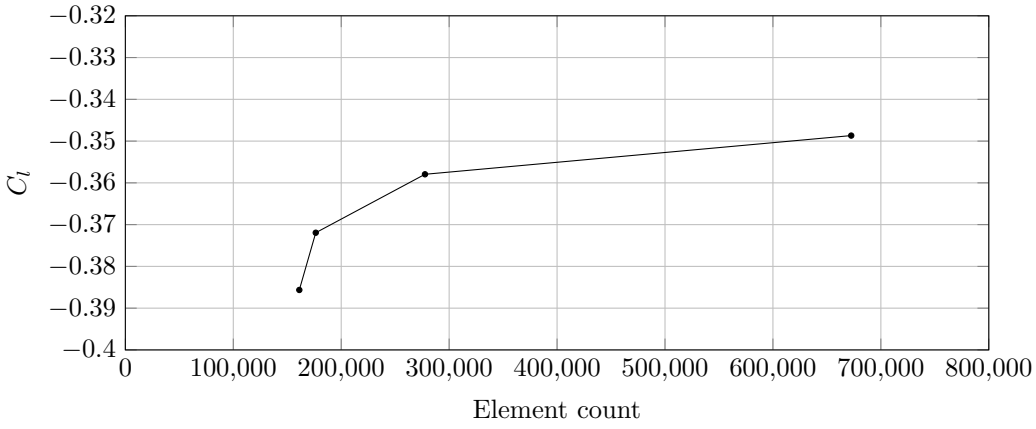

Figure 5.5: C_l vs Element count of FX66-17AII-182 airfoil with airbrake - airbrake refinement study

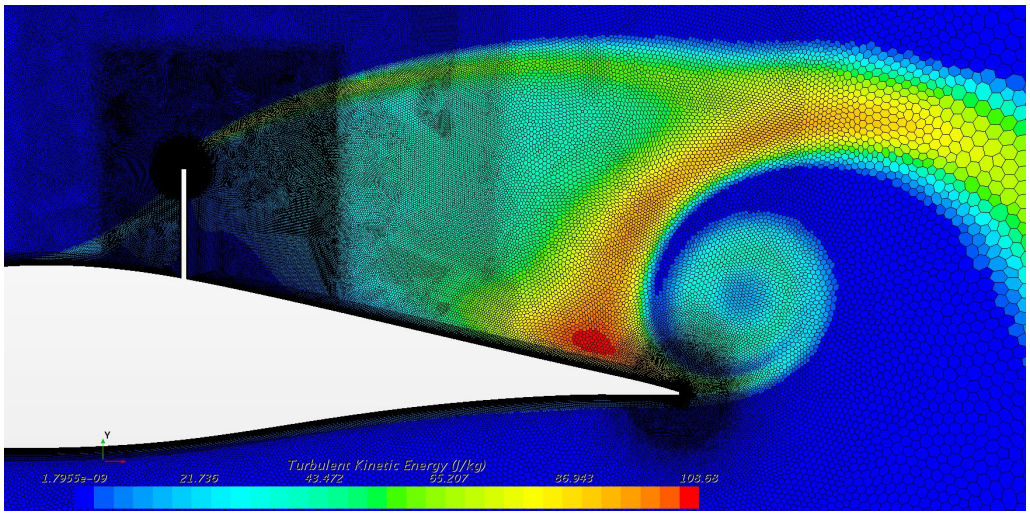

Figure 5.6: TKE plot of downstream flow with a generated mesh of 0.1 C base size

5.2.2 FX66 Wake refinement mesh independence study

The refinement around the airbrake regions forms the first part of the overall mesh refinement process. The airbrake region refinement was crucial in ensuring accurate results due to the high gradients, recirculation and separation. The wake refinement is also an essential part as this is used to capture the vortex street formed by the separation.

Simulation setup

The second part of the mesh refinement study was the addition of volume controls in the body's wake. Four wake refinement volume controls were added, three rectangular refinement zones and a larger tapered refinement zone.

The rectangular refinement zones had lengths downstream from the airbrake of 2C, 3C and 4C, with custom sizes 11%, 13% and 15% relative to the base size, respectively. These custom sizes were arbitrarily chosen but were refined uniformly by altering the overall mesh base size. The tapered wake refinement zone had a length of 8C with a custom size of 25%. Additionally, all wake refinement regions were made wide enough to capture the vortex shedding at the higher angles of attack, where the downwash from the airfoil can cause the vortex streets to form lower than at lower angles of attack. The generated meshes at base size 0.05 C of the rectangular and taped wake refinement zone can be seen in Figures 5.7 and 5.8 respectively.

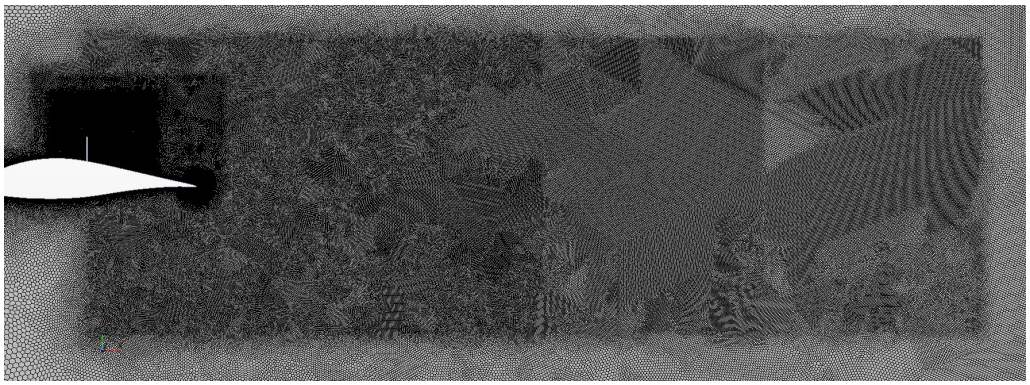

Figure 5.7: Mesh generated around FX66-17AII-182 in the near wake using base size 0.05 C

Results and discussion

Table 5.3 summarises the results of the wake refinement simulations. Figure 5.9 gives the Richardson extrapolation plot with the Richardson extrapolated C_l value of -0.3394.

The chosen base size for this simulation was 0.05 C. This base size has a GCI of 2.2% and is within 4.1% of the Richardson extrapolated C_l. However, there is an anomaly at base size 0.1 C that may be attributed to a numerical or mesh generation error. The following plots returned to the expected upward trend. The anomaly does not affect the overall

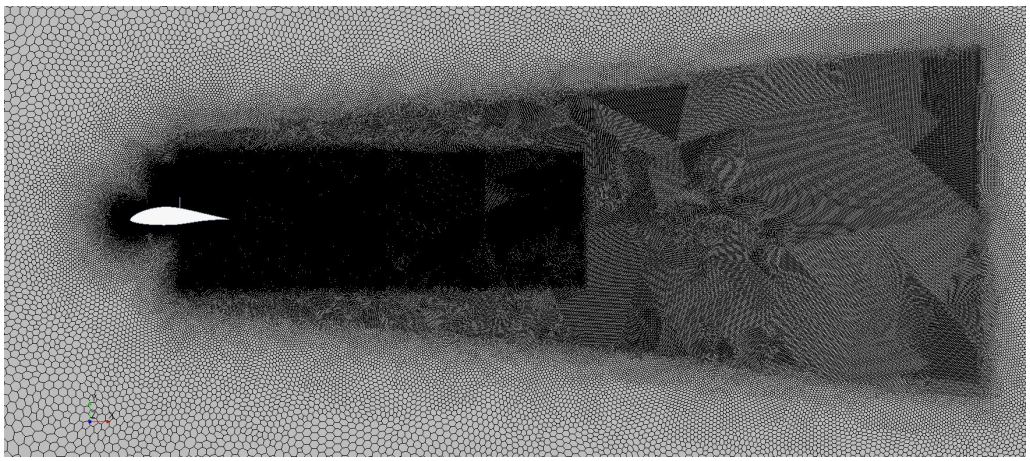

Figure 5.8: Overall mesh generated in wake of FX66-17AII-182 using base size 0.05 C

Table 5.3: FX66 airfoil and airbrake wake mesh refinement study for 30 inner iterations and time step 0.0001 s

Base size [% of C]	Element count [-]	C_l	Δ_x	r	GCI	% Error
30%	288606	-0.3626	0.0019	-	-	6.8%
20%	301205	-0.3589	0.0018	1.022	1.3%	5.8%
10%	362210	-0.3594	0.0017	1.097	0.7%	5.9%
5%*	598659	-0.3532	0.0013	1.286	2.2%	4.1%
2.5%	1504065	-0.3481	0.0008	1.585	1.8%	2.6%
Richardson extrapolated C_l		-0.3394				

* Representing the chosen parameter for subsequent studies

trend of the Richardson extrapolation plot, as shown in Figure 5.9. The point at base size 0.2 C lies precisely on the linear trend line, indicating a good fit.

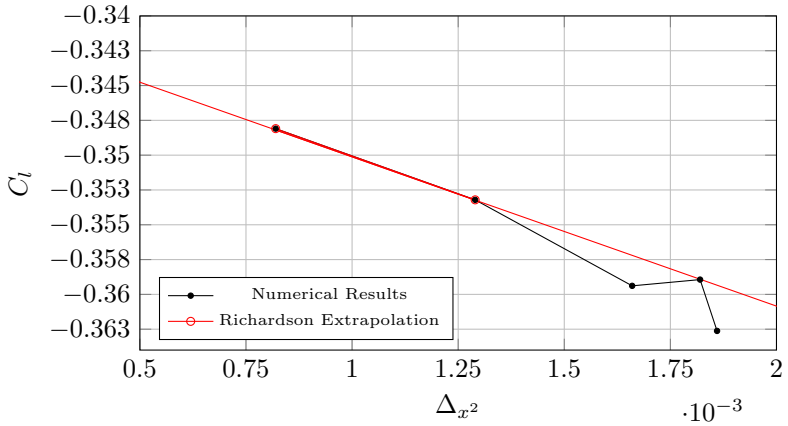

Figure 5.9: Richardson extrapolation of wake refinement study with airbrake extended

Figure 5.10 gives the C_l vs Element curve of the wake refinement simulations at a time step of 0.00001 s and 30 inner iterations. The generated mesh completely captured the fully developed vortex streets at 1 second, as shown in Figure 5.11.

The combination of mesh and physics parameters in Sections 5.2.2 and 5.2.2 suggests that the chosen mesh setup could confidently be used in the validation study done next. The asymptotic trend shown in Figure 5.9 indicates that second-order convergence has been

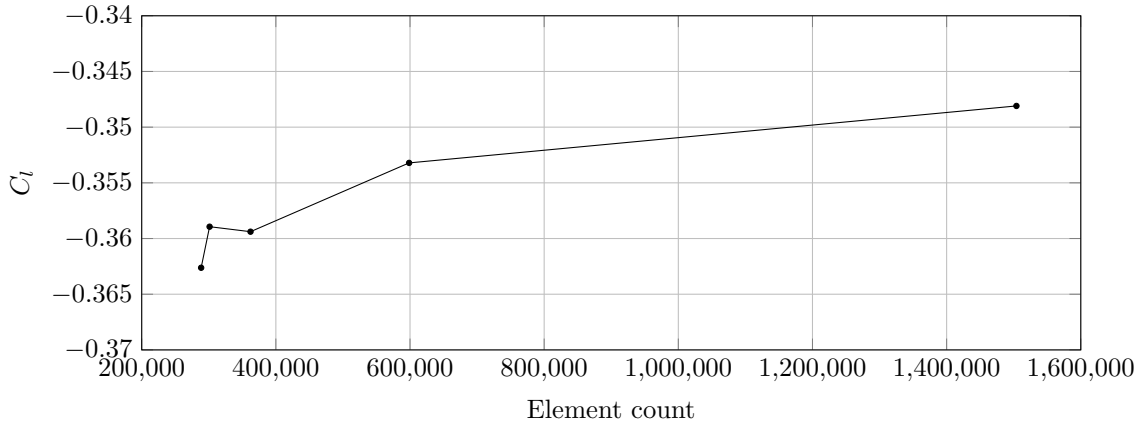

Figure 5.10: C_l vs Element count of FX66-17AII-182 airfoil with airbrake - Wake Mesh refinement study

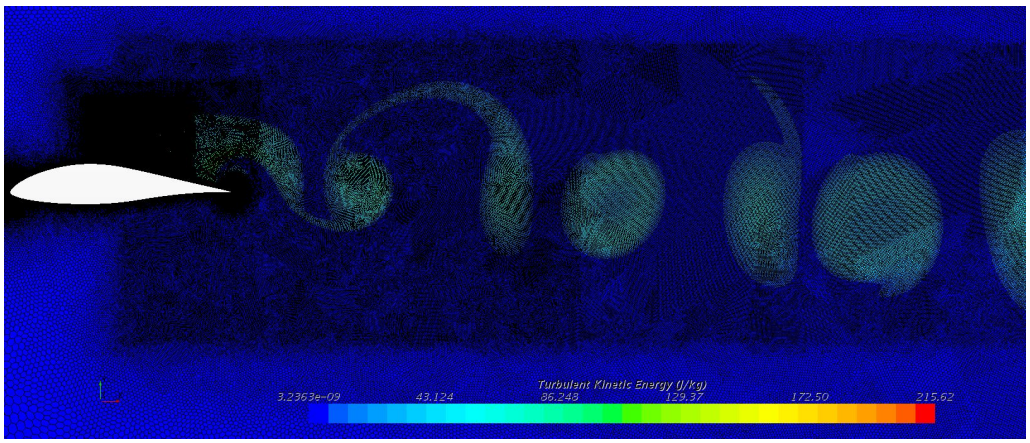

Figure 5.11: TKE scene of overall mesh at 1 s with AOA 0° and base size 0.05 C

achieved. The error percentage and GCI results of base size 0.05C were also acceptable.

5.2.3 FX66 Validation study

After the conclusion of the wake refinement, the simulation setup was ready for the validation simulations. The parameters (mesh setup, time steps and inner iterations) used in this section were derived from Sections 5.2.2 and 5.2.2. The reference study [9] gave both wind tunnel and numerical results of only C_l and was used in this validation section.

Simulation setup

The mesh setup of volume controls around the airbrake and the choice of inner iterations and time steps were described in more detail in Section 5.2.2. This was to ensure that the separation and recirculation were captured accurately and that the effects of these flow occurrences on the airfoil were representative of real-world phenomena.

The wake refinement mesh setup is described in Section 5.2.2. These refinement zones were added to ensure the vortex streets were captured entirely and accurately. The mesh

is similar to Section 5.2.2, combining the airbrake and wake volume controls.

Until this point, an angle of attack of 0° was used. The angle of attack in the FX66 validation study ranges from 0° to 20° in increments of 4°. The linear and cubic constitutive options were also used with a custom shear stress limiter (a_1) and realizability coefficients (C_T). The effects of these parameters are described in more detail in Sections 4.3.4 and 4.3.5, respectively.

Results and discussion

The results for the validation studies are summarised in Table 5.4 and compared with both the experimental (WT) and numerical (CFD) results given in [9]. Both cubic variants gave results less accurate than the linear options. This was unexpected as the cubic option is better at capturing the anisotropic flows present behind the airbrake [5]. The cubic variant was also used in a similar case study in [10].

Table 5.4: FX66 airfoil and airbrake results of various constitutive options at 0° AOA

Constitutive option	C_l	% Error WT	% Error CFD
Linear	-0.3532	45.6 %	37.8 %
Cubic	-0.3362	48.2 %	40.8 %
Linear $a_1 = 1$ $C_T = 1.2$ *	-0.4628	28.7 %	18.5 %
Cubic $a_1 = 1$ $C_T = 1.2$	-0.4327	33.4 %	23.8 %
Wind tunnel data [9]	-0.6490		
CFD Reference [9]	-0.5680		

* Representing the chosen parameter for following studies

Based on the results in Table 5.4, the combination of the linear variant with the modified a_1 and C_T values were used in the FX66 validation study. Even though the C_l results were overpredicted, a good trend was achieved. This trend is similar to the linear trends for the wind tunnel and numerical results shown in [9].

Most cells had a Courant value of less than 20, except for the high-velocity regions on the leading and trailing edges and the airbrake blade tip. The Courant number was not a problem as the results converge at a time step of 0.0001 s, indicating that further decreasing the time steps will not have an effect. Figure 5.13 shows the velocity over the airfoil and airbrake at 0°. The recirculation is evident in the regions downstream of the airbrake blade.

Figures 5.14 and 5.15 give the TKE plots at angles 0° and 20°. A low-pressure vortex can be seen on both cases' trailing edges. The generated vortex is similar to those shown in [9], indicating similar flow characteristics.

Conclusion

The simulations in Section 5.2 were divided into mesh refinement and validation simulations. The mesh refinement was broken down into mesh refinement around the airbrake

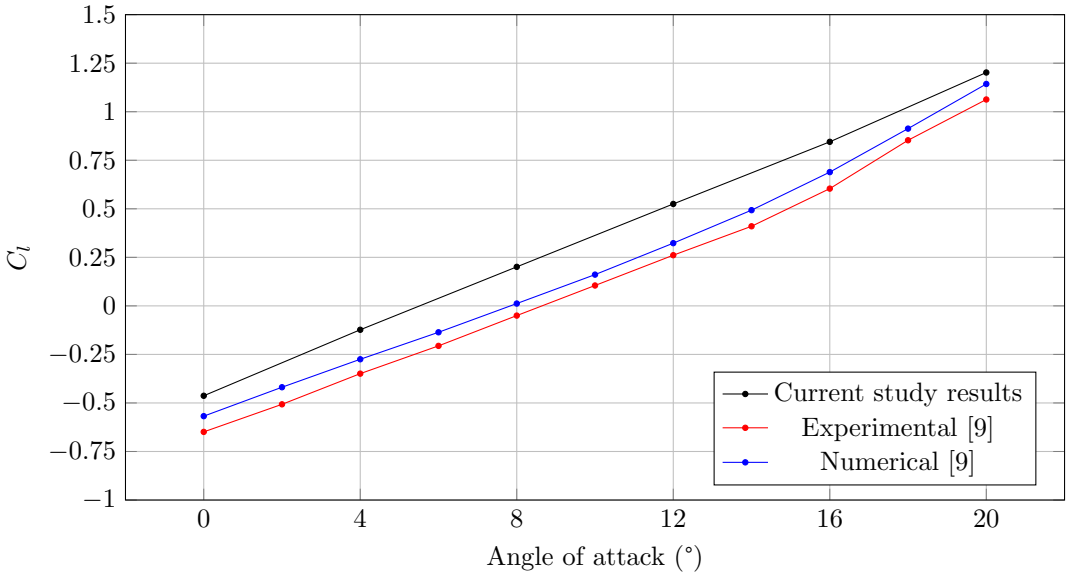

Figure 5.12: C_l vs α validation

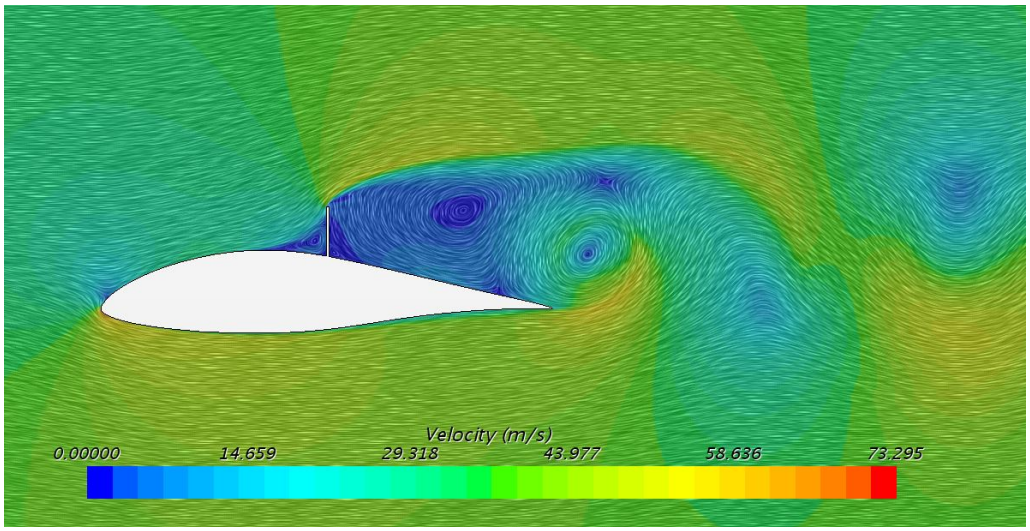

Figure 5.13: Velocity scene at 1 s and an angle of attack 0°

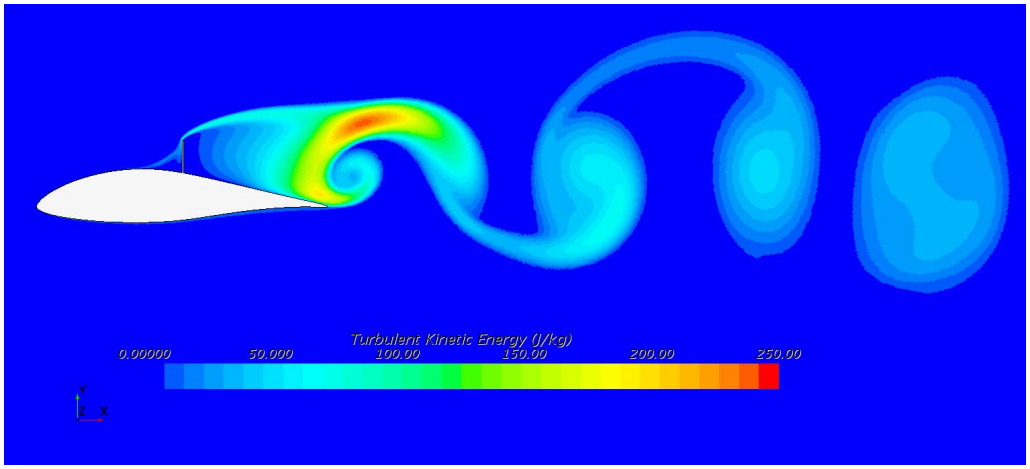

Figure 5.14: TKE scene at 1 s with AOA 0° and base size 0.05 C

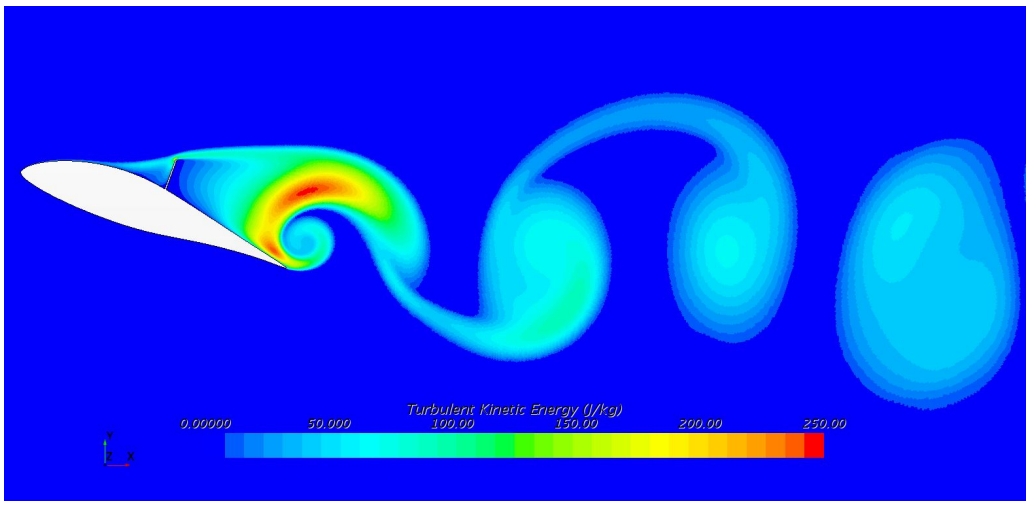

Figure 5.15: TKE scene at 1 s with AOA 20° and base size 0.05 C

and in the wake of the geometry.

After the mesh refinement setup was finalised, the effects of the $k-\omega$ variants and modifications were tested. Based on the results of the modified turbulence models, the angle of attack sweep was done, giving the final results.

Ultimately the validation simulations were done using the linear constitutive option with $a_1 = 1$ and $C_T = 1.2$. These parameters resulted in the most accurate C_l values, within 18.5% of the numerical and 28.7% of the experimental results [9].

The methodology followed yielded satisfactory results. In Figure 5.12, it can be seen that the lift coefficients were overpredicted during the entire angle of attack sweep. However, the overall upward trend closely matched the reference numeric and experimental trends.

5.3 HPH yn1 Airbrake Validation

The HPH yn1 airfoil followed the same process as the FX66 airfoil. The airbrake and wake mesh refinements, inner iterations and time step independence studies were done separately, building on the step before. After the refinement had been completed, the airbrake validation simulations were done.

The second airfoil geometry that will be validated is that of the HPH yn1 airfoil with extended airbrakes. Compared to the configuration in Section 5.2, which is only a vertically extended flat plate, this geometry is more complex. The airbrake configuration shown in Figure 5.16 represents the geometry used and tested in [20]. The airbrake blade is positioned at 0.5 C from the leading edge and does not have a gap between the airbrake blade and the airfoil surface but has an airbrake cap. Additionally, the airbrake does not take the airbrake cavity inside the airfoil into account.

The CFD study in [10] was done at an angle of attack of 5°. The physical flow properties and wind tunnel conditions in this section are similar to that in Section 4.3 and is given

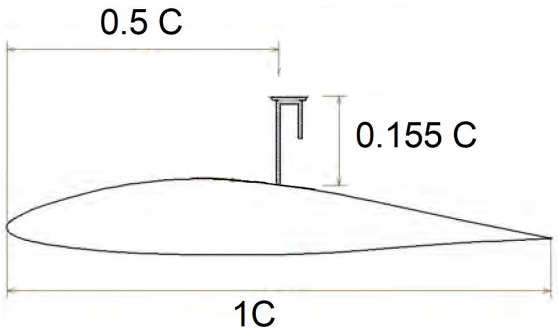

Figure 5.16: HPH yn1 airfoil and airbrake configuration used in this section adapted from [10]

in Table 4.5. Only experimental force coefficients are available from [20] with a pressure coefficient plot of the numerical results given in [10]. At these conditions, the experimental results of C_l and C_d are -0.5382 and 0.2649, respectively.

5.3.1 HPH airbrake mesh refinement study

Simulation setup

The simulation setup is similar to Section 5.2.1 except that 20, 30 and 40 inner iterations were used. The time steps, turbulence models and other settings were kept the same. The generated mesh using base size 0.2 C can be seen in Figure 5.17.

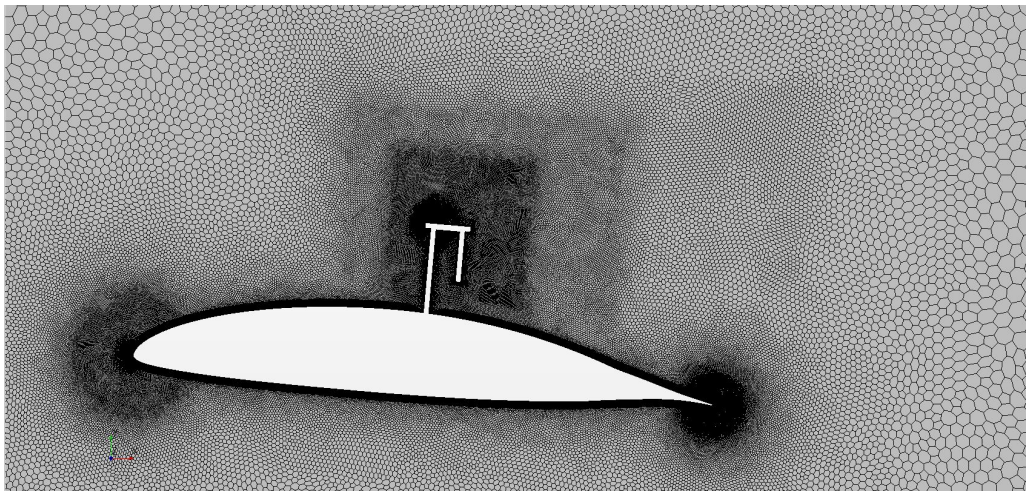

Figure 5.17: Generated mesh around the airbrake with base size 0.2C at 5° AOA

The prism layer thickness used on the airfoil surface was 7.5mm, and 0.7mm on the airbrake blade. The airfoil had 45 prism layer cells with a stretch factor of 3.3, and the airbrake blade had 35 with a stretch factor of 3.2. All the y^+ values were < 1.

Results and discussion

Figure 5.18 shows the time step independence study at time steps 0.0001 s and 0.00005 s. The C_l results converged at time step 0.0001 s in the simulation using a base size of 0.05 C. The time step convergence at 0.0001 s corresponds with all the previous studies. The time step is similar, even with the addition of relatively more complex geometry.

Table 5.5: HPH airfoil and airbrake wake mesh refinement study for 40 inner iterations and time step 0.0001 s

Base size [% of C]	Element count [-]	C_l	C_d	Δ_x	r	GCI (C_d)	% Error (C_d)
30%	182084	-0.0288	0.1980	0.0023	-	-	2.58%
20%*	201493	-0.0173	0.2021	0.0022	1.052	24.0%	0.54%
10%	324143	-0.0110	0.2030	0.0018	1.268	0.8%	0.13%
5%	806825	-0.0040	0.2031	0.0011	1.578	0.1%	0.04%
Richardson extrapolated coefficient		0.0006	0.2032				

* Representing the chosen parameter for following studies

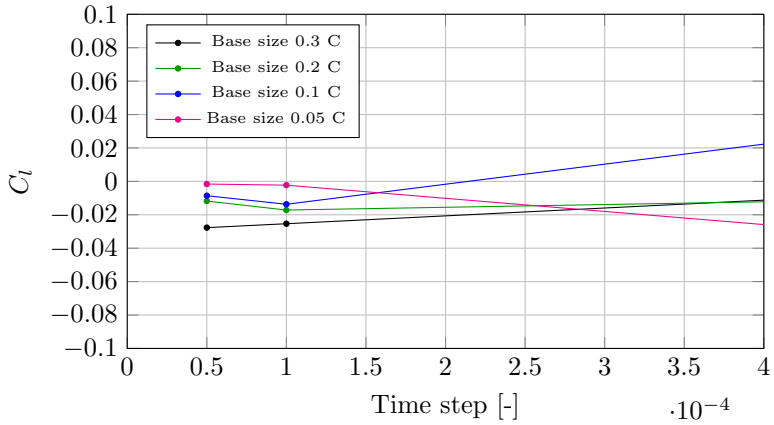

Figure 5.18: Time step convergence at various base sizes using 30 inner iterations

Table 5.5 summarises the results of 40 inner iterations and time step 0.0001 s. Due to a numerical error when calculating % Error and GCI using the C_l results, the C_d results were used in these calculations. The Richardson extrapolated value of approximately 0 caused the numerical errors.

Even though the GCI is high, the % error to the Richardson extrapolated C_d (0.2032) is within 0.6%. This was small enough to use a base size of 0.2 C for the airbrake refinement zones. Nevertheless, the C_l results were still used for the asymptotic and Richardson convergence studies shown in Figure 6.8.

As can be seen in Figure 5.19a, 20 and 30 inner iterations did not give the required asymptotic convergence. The 40 inner iterations plot gave a good asymptotic line. This indicated that 40 inner iterations were sufficient for this case.

The overall Courant number for the airbrake mesh refinement study was below 10. As expected, higher Courant numbers were seen at the high-velocity regions, such as the leading and trailing edges and especially at the shear later at the airbrake cap leading edge.

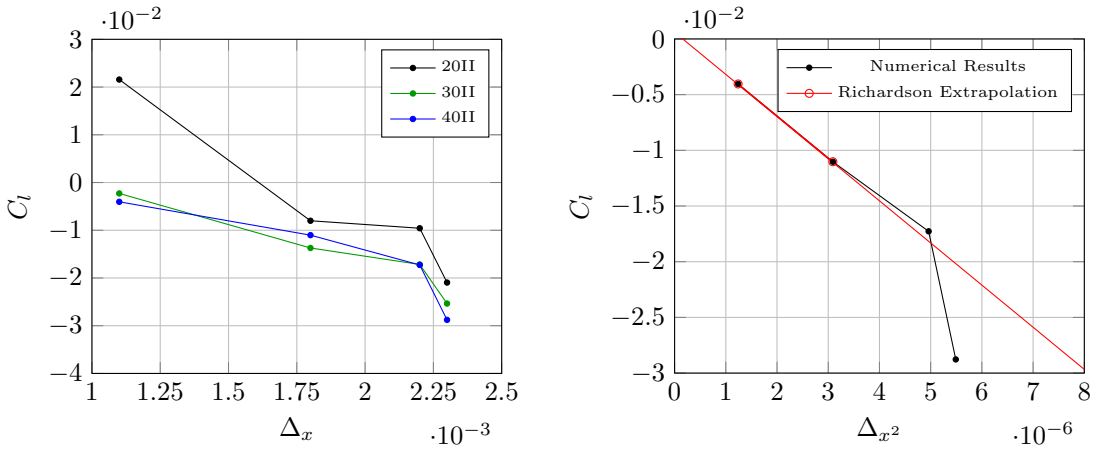

(a) C_l vs relative mesh spacing

(b) Richardson extrapolated spacing

Figure 5.19: Mesh convergence of C_l at an AOA of 5° for the flow over a HPH yn1 airfoil with extended airbrake

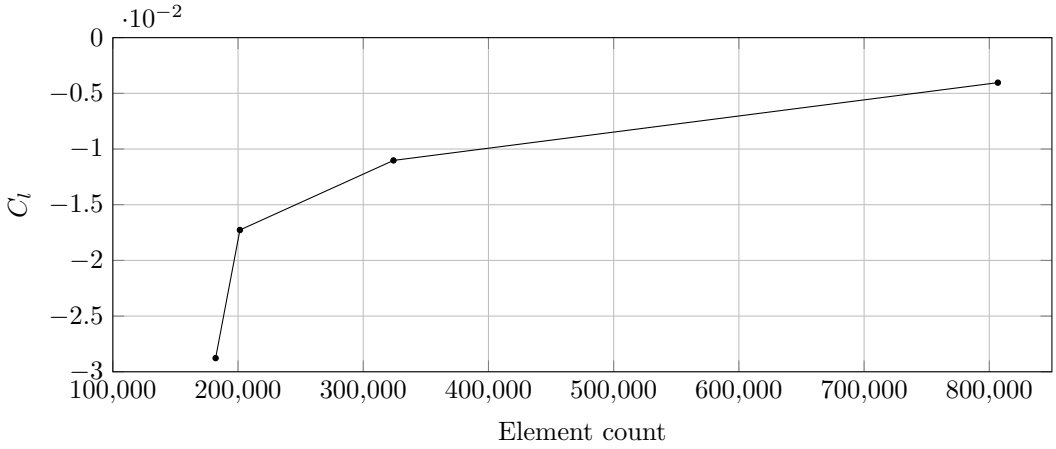

Figure 5.20: C_l vs Element count of HPH yn1 airfoil with airbrake - airbrake Mesh refinement study

Table 5.20 gives the C_l vs element count of the simulation using 40 inner iterations and a time step of 0.0001. Figure 5.21 shows a TKE scene with the generated mesh overlayed. The generated mesh adequately captures all the flow gradients and is fit for purpose.

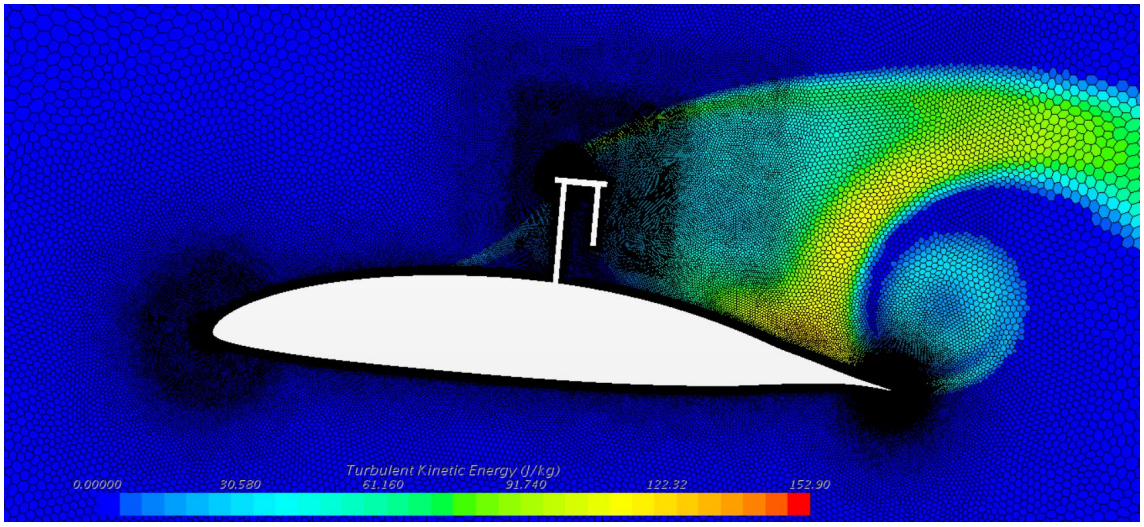

Figure 5.21: TKE around airbrake generated mesh at 1 s with 5° AOA and base size 0.2C

5.3.2 HPH wake refinement mesh dependent study

Completing the airbrake region refinement study keeps the airbrake volume controls, time steps and inner iterations constant for the next step. The wake refinement simulations used these parameters for use in the validation simulations to follow.

Simulation setup

The wake refinement volume controls used in this section were different than in Section 5.2.2. As shown in Figure 5.22, there are three wake refinement zones, all of them tapered. These zones start at the airbrake blade with downstream lengths of 2 C, 3 C and 8 C. The custom sizes were 8%, 10% and 15% of the base size, respectively. The base sizes were set up and varied as shown in Table 5.6.

Results and discussion

The simulation results are summarised in Table 5.6. Due to the higher level of inner iterations, the simulation results converged using fewer mesh elements than in Section 5.2.

The asymptotic convergence of the wake mesh refinement study can be seen in Figure 5.23. Similar to Section 5.2.2 (Figure 5.9), there was an anomaly in the results at the coarser meshes, but this was also not a problem as the asymptotic behaviour continued after the anomaly. The Richardson extrapolated values for C_l, and C_d were 0.0022 and 0.2097, respectively. A base size of 0.1C was chosen to do the validation study. The GCI and % error for C_d was 1.7% and 3.49%, respectively. These values are well below 5%.

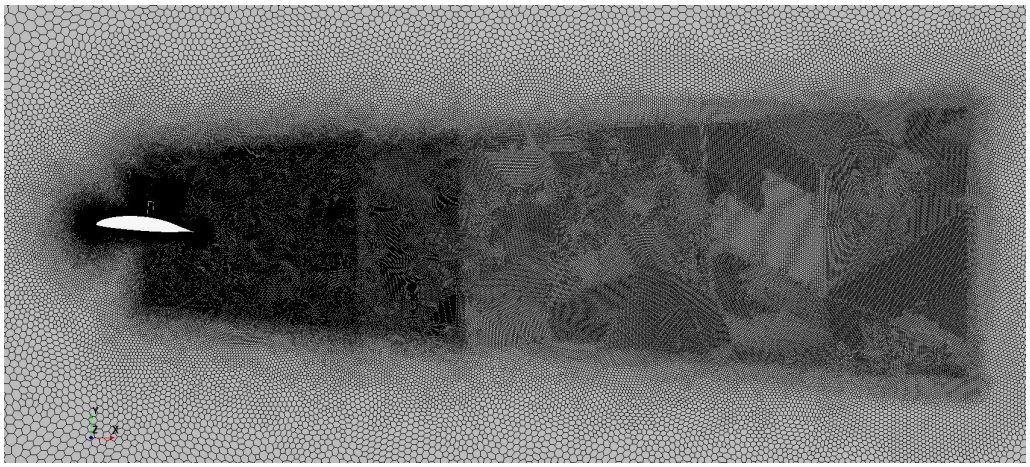

Figure 5.22: Overall generated mesh of HPH yn1 airfoil and airbrake geometry using base size 0.1C

Table 5.6: HPH airfoil and airbrake wake mesh refinement study for 40 inner iterations and time step 0.0001 s

Base size [% of C]	Element count [-]	C_l	C_d	Δ_x	r	GCI (C_d)	% Error (C_d)
30%	224294	-0.0152	0.2022	0.0021	-	-	3.58%
20%	251928	-0.0176	0.2010	0.0020	1.060	5.9%	4.14%
10%*	375200	-0.0078	0.2024	0.0016	1.220	1.7%	3.49%
5%	839218	-0.0022	0.2064	0.0011	1.496	2.0%	1.56%
Richardson extrapolated coefficient		0.0022	0.2097				

* Representing the chosen parameter for following studies

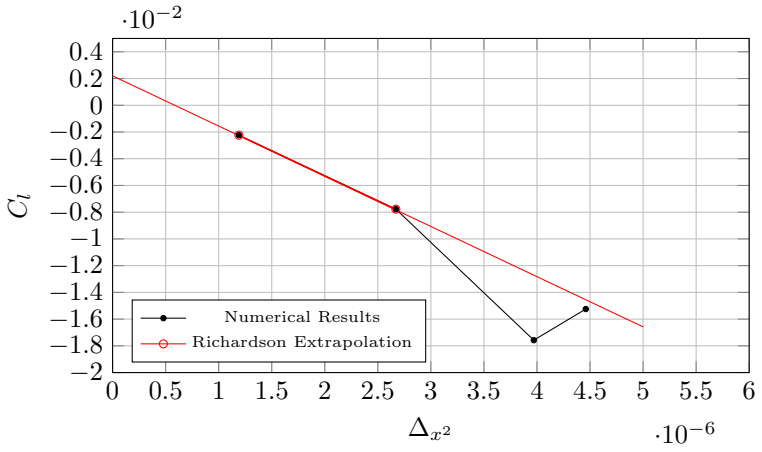

Figure 5.23: Richardson extrapolation of wake refinement study airbrake extended

Figure 5.24 shows the C_l results at the various number of mesh elements. The TKE plot with the overlayed generated mesh using base size 0.1C is shown in Figure 5.25. The wake refinement volume controls completely captured the vortex streets. Overall the combinations of simulation parameters and mesh refinement regions yielded good convergence.

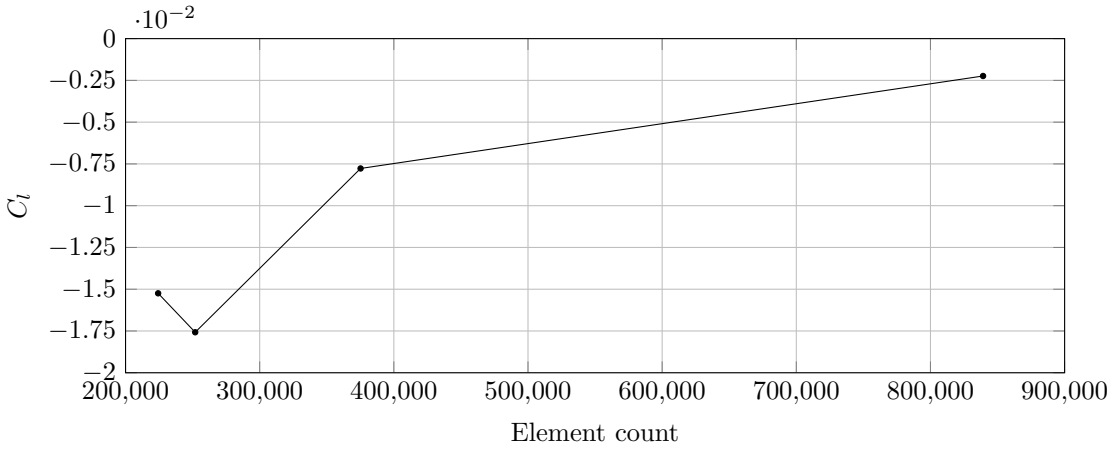

Figure 5.24: C_l vs Element count of HPH yn1 airfoil with airbrake - Wake Mesh refinement study

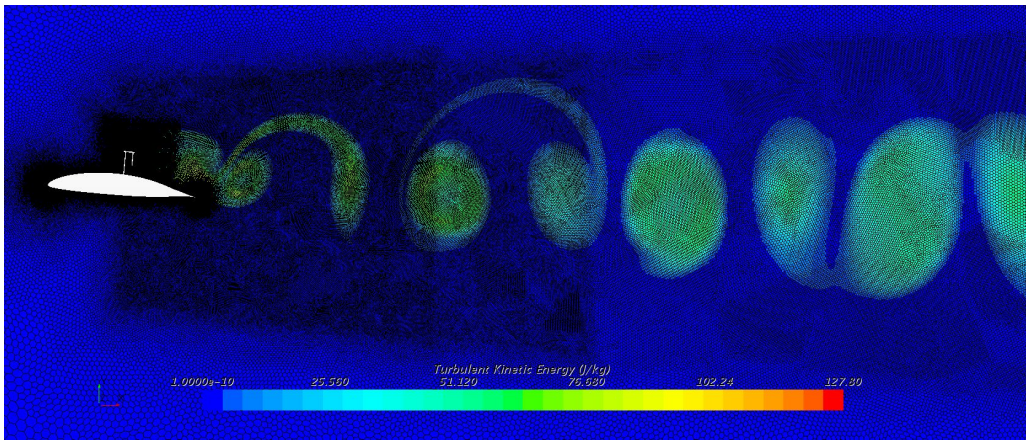

Figure 5.25: TKE scene of the overall mesh at 1 s with 5° AOA and base size 0.1 C

5.3.3 HPH validation study

The conclusion of both the airbrake region and wake refinement studies allowed for the airbrake validation simulations to be done. This was an essential step as the clean airfoil simulations gave poor results compared to the experimental data available.

Simulation setup

The final step in this section was to combine everything done in the refinement studies and apply it to the validation study. The mesh refinement around the airbrake and the selection of time steps and inner iterations are described in more detail in Sections 5.3.1. The wake refinement and final mesh base size are given in 5.3.2.

The linear constitutive option with default $k-\omega$ SST coefficients was used. The validation study was done at angles of attack between -3° to 20°. The simulation was run for 1 second, which was ample time to achieve convergence and full-flow development.

Results and discussion

Figures 5.26 and 5.27 shows the results of the C_l and C_d vs α plots. The validation resulted in a poor correlation between the numerical results and the experimental data.

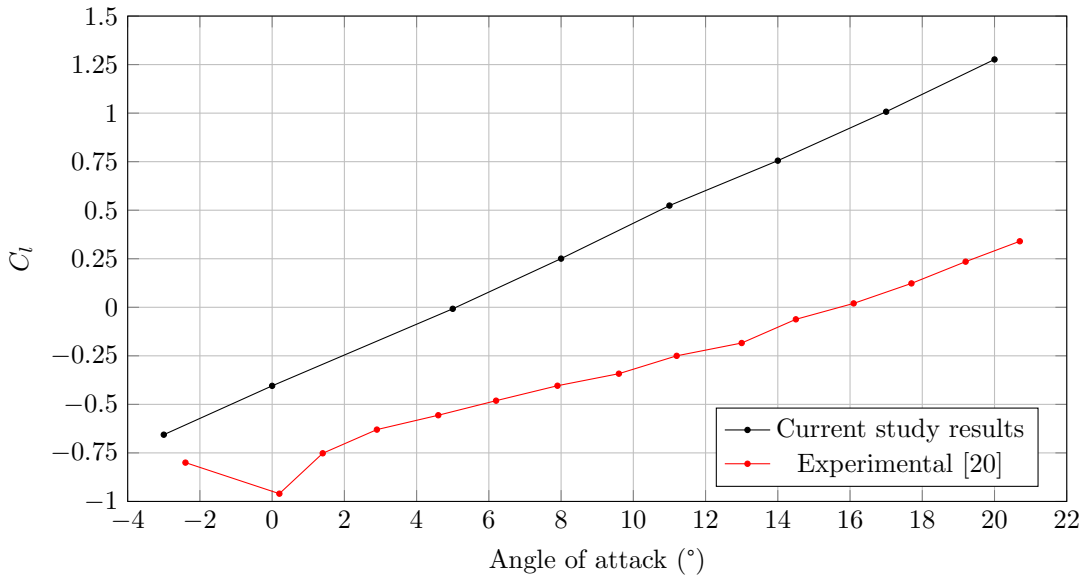

Figure 5.26: C_l vs α validation

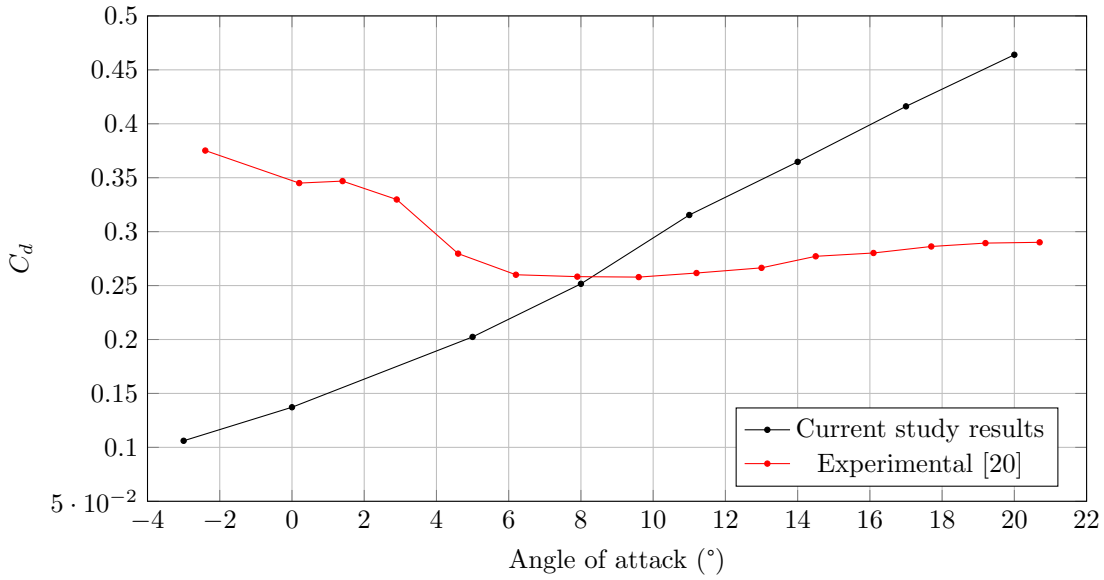

Figure 5.27: C_d vs α validation

Unfortunately, the only reference CFD results given in [10] is the pressure coefficient over the airfoil and extended airbrake at an angle of attack of 5°. The time-averaged pressure coefficients of the wind tunnel [20], reference CFD and current validation simulation results are given in Figure 5.28.

The pressure coefficient on the leading edge upper surface is lower than that of both experimental and numerical results in [20], and [10], respectively. Care was taken on the leading edge refinement region in the airfoil mesh refinement study in Section 4.3.1. This region was investigated to ensure flow conditioning upstream of the body and in the stagnation region, with decent results obtained during the low angles of attack. This indicated that the mesh refinement was sufficient in this region. The pressure coefficient on the lower surface corresponds to that of both reference cases.

The results of the current validation study predicted a very low-pressure region on the airfoil's trailing edge. The flow at the bottom of the airfoil corresponds well with what was expected. Unfortunately, no simulated results were visualised of the flow conditions at the airfoil's trailing edge with an airbrake gap of 0 mm. This made it challenging to compare flow conditions at this location visually. Figure 5.29 shows the low-pressure vortex on the airfoil trailing edge at an arbitrary point in the simulation. The time-averaged result can be seen in the pressure plots.

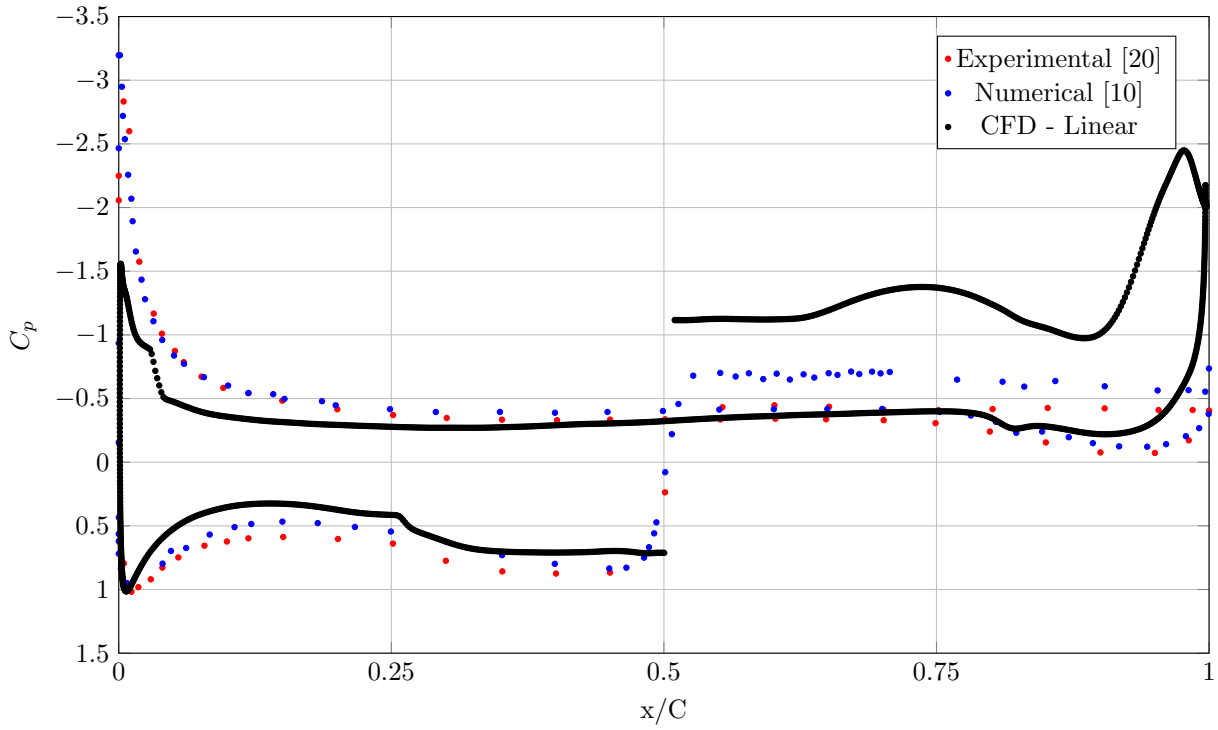

Figure 5.28: C_p vs x/C for HPH airfoil and airbrake validation study at AOA 5°

The velocity plot of the current and reference numeric results are compared in Figure 5.30. This was at an angle of attack of 0°. There are good correlations between the streamlines and velocity contours between the two figures. This can also be seen in the pressure coefficient plot (Figure 5.28), even though the pressure of the validation simulations are lower downstream of the airbrake.

The unsteady conical cases and the good results obtained in Chapter 3 indicated that the software was used correctly. The acceptable results of the clean airfoil at low angles of attack (Section 4.3) meant that the force coefficients from the wind tunnel results were accurately calculated.

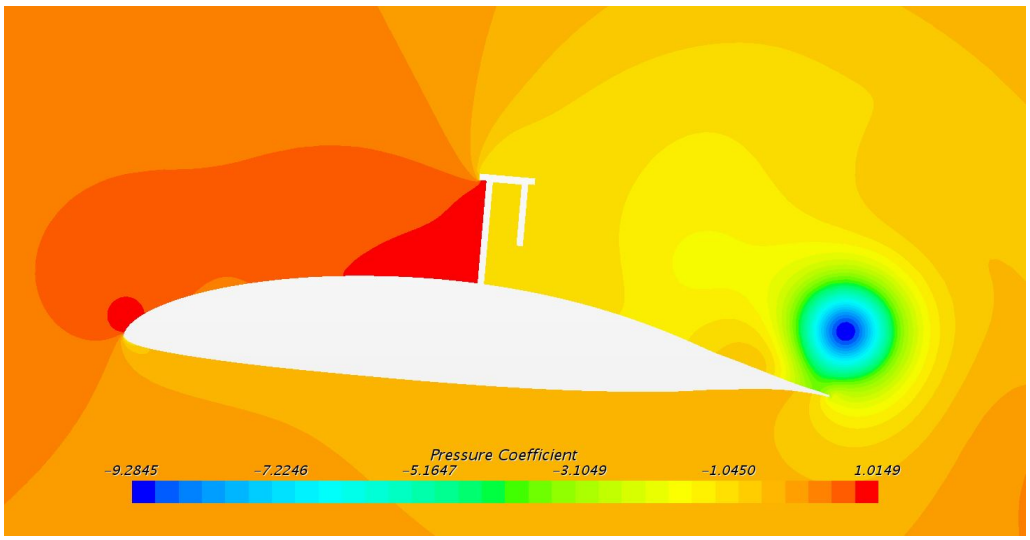

Figure 5.29: Pressure coefficient on overall mesh base size 0.1 C

The convergent results of the mesh refinement, time step and inner iteration studies (Sections 5.3.1 and 5.3.2) gave the confidence that an adequate mesh was set up and generated. This also meant that a further decrease in these parameters would not change the simulation results significantly.

In addition, the FX66-17AII-182 airbrake refinement study in Section 5.2 uses the same methodology as in this section. The results in Section 5.2 gave much better results compared to the simulations done on the HPH yn1 airfoil and airbrake.

The geometry of the airfoil (the addition of rounded edges) and finer mesh refinements, inner iterations and time steps were run without increasing result accuracy. The following additional simulation variations were done in order to try and increase the simulation accuracy, but all gave similar results:

- Variations on prism layer thicknesses, the number of cells and stretch factors
- Various $\gamma - Re_\theta$ free stream edges were tested
- The compressible solver, as well as the absence of a transition model, were investigated

5.3.4 HPH validation study - Further investigation

The poor correlation between the C_l and C_d vs α plots required further investigation and can broadly be divided into the following categories; variations on the $k-\omega$ SST turbulence model, the use of different turbulence models and alternative considerations during mesh generation in unsteady flow simulation. All the simulations in the following sections had the same time steps, inner iterations and mesh setups unless stated otherwise. This was to keep the simulations similar to that in Section 5.3.3 and to isolate the test parameters.

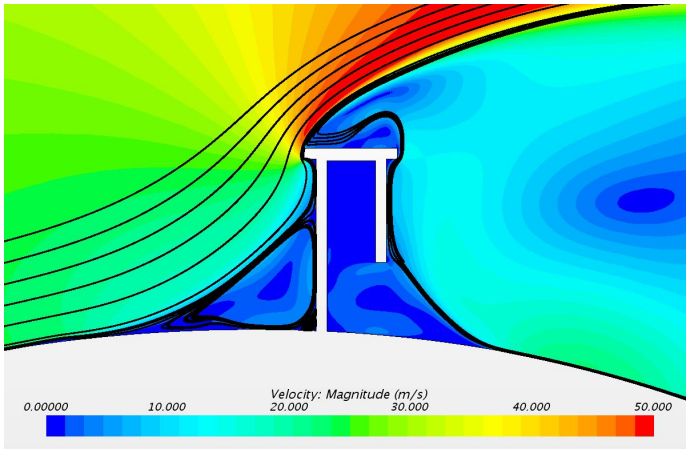

(a) HPH Validation study

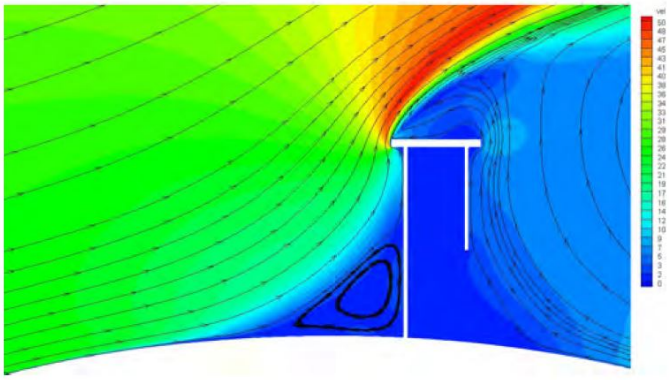

(b) Reference CFD [10]

Figure 5.30: Velocity plot with streamlines of flow over HPH airbrake at AOA 0°

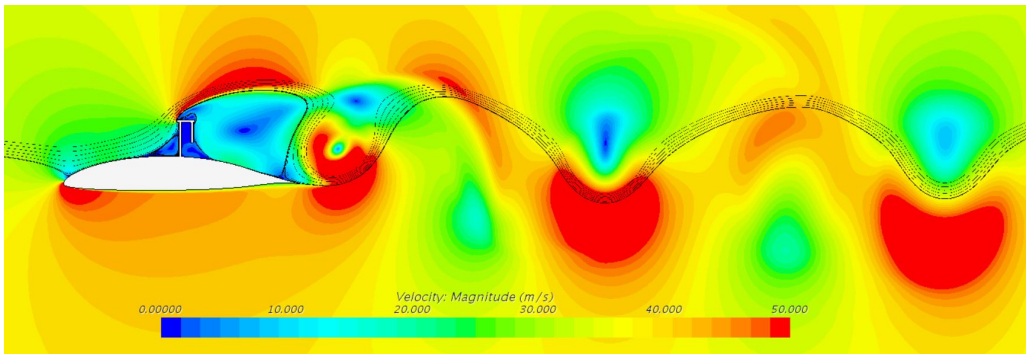

Figure 5.31: Velocity plot with streamlines in the wake of the airfoil and airbrake at 0° AOA and 1 s

$k-\omega$ SST variations

The results of the different variations and modifications made to the $k-\omega$ SST turbulence model are tabulated in Table 5.7. The variations made were using Linear, Quadratic (QCR) and Cubic constitutive options with the coefficient modifications being $a_1 = 1$, $C_T = 1.2$. More details on the effects of altering the constitutive options and modifying the shear stress limiter a_1 and realizability coefficient C_T are given in Section 4.3.

Table 5.7: $k-\omega$ SST variations and modifications investigation on the HPH yn1 airfoil with extended airbrake

Test parameter	C_l	C_d	% Error C_l	% Error C_d
Linear, Default	-0.0078	0.2024	98.6	23.6
Linear, Modified a_1 and C_T	-0.0757	0.1879	85.9	29.1
Quadratic, Default	0.0358	0.2155	106.6	18.7
Quadratic, Modified a_1 and C_T	0.0351	0.1878	106.5	29.1
Cubic, Default a_1 and C_T	0.0351	0.2152	106.5	18.8
Cubic, Modified a_1 and C_T	-0.0686	0.1904	87.3	28.1
Wind tunnel data [20]	-0.5382	0.2649		

As shown in Table 5.7, the drag coefficient predictions are relatively close compared to the lift coefficients. The CFD simulations greatly overpredicted the lift coefficients.

The same low-pressure region on the airfoil's trailing edge can be seen in the pressure coefficient plots in Figure 5.32. The modified Quadratic and Cubic solvers increased the trailing edge vortex pressure coefficient to a degree. However, the results of the modified quadratic solver were less accurate. The C_l accuracy was slightly increased when using the modified cubic solver, whereas the C_d results were less accurate. The leading edge on the upper and lower sections behaved roughly the same between all the solvers.

Alternative turbulence models

The variations and modifications to the standard $k-\omega$ SST turbulent models did not increase the accuracy of the simulations to a noticeable extent. In this section, other available turbulence models were used. These models were the standard $k-\epsilon$, Spalart–Allmaras, Lag Elliptical Blending (LEB) $k-\epsilon$ and Reynolds Stress Transport (RST) turbulent models.

The Lag Elliptical Blending $k-\epsilon$, according to [5], gives good predictive capabilities for unsteady flows with high streamline curvatures, vortex shedding and separation. This model contains terms that model the anisotropic effects in simulated flows, making it a suitable solver for separated flow over an airbrake.

The RST turbulence model used was that of the linear pressure strain two-layer variant. The two-layer variant was used to capture the boundary layer flow accurately. The effects of streamline curvature, high strain stresses, turbulent anisotropy and swirl rotations are naturally accounted for in the transport equations in the RST model. This makes this model also very applicable to separated flows over airbrakes. The downside, however, is

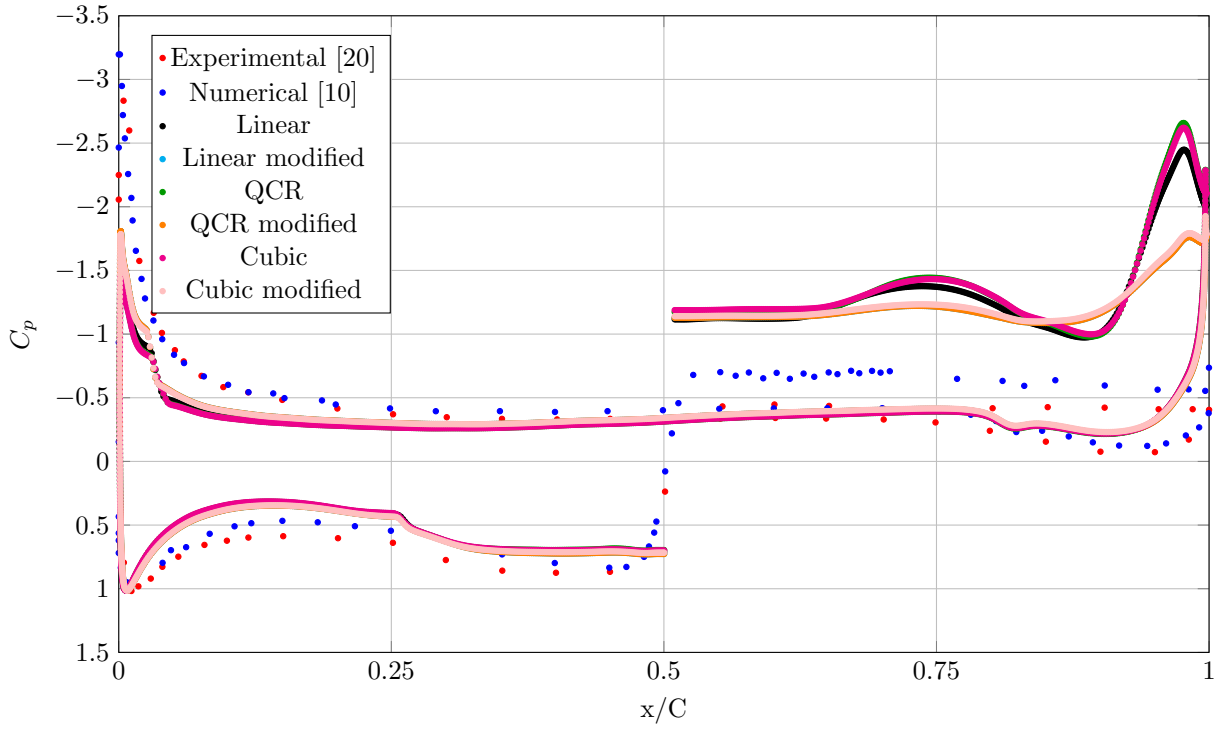

Figure 5.32: C_p vs x/C for $k-\omega$ SST modification and variation investigation at AOA 5°

that the RST model is very computationally expensive as seven equations must be solved, compared to only two of the $k-\omega$ and $k-\epsilon$ models [5].

Table 5.8: Alternative turbulence model investigation on the HPH yn1 airfoil with extended airbrake

Test parameter	C_l	C_d	% Error C_l	% Error C_d
$k-\epsilon$	-0.2136	0.1613	60.3	39.1
Spalart–Allmaras	-0.0939	0.1852	82.5	30.1
Lag EB $k-\epsilon$	0.0305	0.2189	105.7	17.4
RST - Two layer	-0.1437	0.1691	73.3	36.2
Wind tunnel data [20]	-0.5382	0.2649		

The time-averaged pressure coefficients of the simulations using the turbulence models referenced in Table 5.8 are shown in Figure 5.33. Even though the low-pressure region on the trailing edge was not as prevalent in the $k-\epsilon$, Spalart–Allmaras and RST simulations, the force coefficients results were still not close to what is required. The phenomenon where one of the two force coefficient results is closer to that of the wind tunnel results, and the other result is further away can be seen in the $k-\epsilon$, Lag EB $k-\epsilon$ and RST results.

Even though both RST and Lag EB $k-\epsilon$ turbulence models are suited for the flow conditions, in this case, they did not increase the accuracy of the results. The results were in the same order as that of the $k-\omega$ SST model. This eliminates using the wrong turbulent model from the possible causes of obtaining poor agreement with the experimental results.

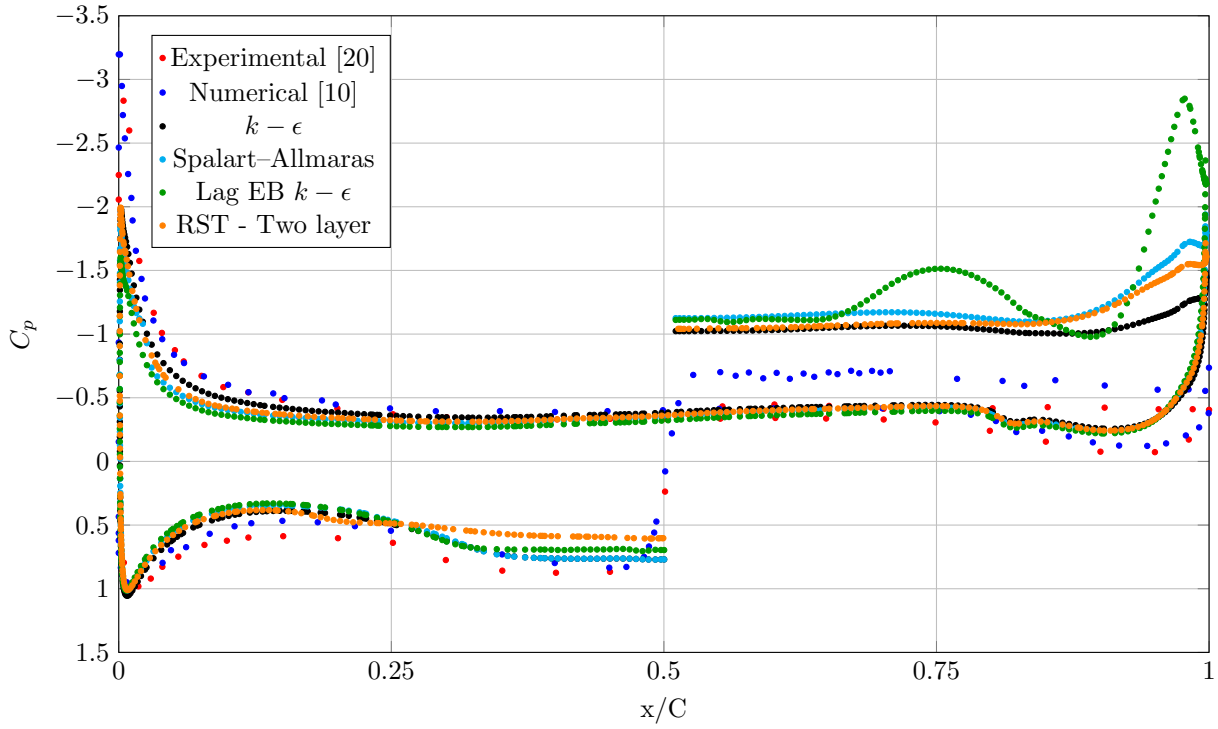

Figure 5.33: C_p vs x/C for alternative turbulence models investigation at AOA 5°

Alternative considerations

The studies in Section 5.3.4 investigated the physics of the simulation by modifying the $k-\omega$ SST turbulence model or using different turbulence models. None of these alterations made a noticeable change in the accuracy of the force coefficient predictions. The final two aspects to consider are ensuring the CFL < 1 for all elements in the simulation and generating a mesh that takes Tylor micro scales into account.

Up to this point, time step and mesh refinement studies were done to ensure the time step converged for a given mesh density. All of these parameters resulted in a Courant number higher than one. A simulation was done that ensured the Courant number was < 1 at all mesh elements. The generated mesh was similar to that in Section 5.3.3 with 40 inner iterations. The time step was changed to 1×10^{-6} s, and the simulation was run until the force coefficients converged.

Secondly, Taylor micro scales were considered. Taylor and Kolmogorov scales go hand in hand when generating an unsteady mesh with high expected eddies. The Kolmogorov length scale indicates the smallest scales present in the turbulent spectrum. Simulations at these spectrums tend toward Direct Numerical Simulations (DNS), which will not be discussed here. The Taylor micro scale, on the other hand, is an upper limit in mesh sizes. Scales that fall below the Taylor micro scale are largely viscous-driven. Limiting the maximum cell size during mesh generation based on the Taylor micro scales will yield good scale-resolving simulation results [5].

Thus, the ideal cell size would lie between the Kolmogorov length scale and Taylor micro scales. For this simulation, the focus was only on generating mesh elements smaller than

the Taylor micro scales and investigating the effects on the simulation. In addition to the updated meshes, the time step was also set to 1×10^{-6} s ensuring that the local Courant numbers were < 1.

Table 5.9 gives the results for the Courant number < 1, the Taylor micro scale and the standard linear $k-\omega$ SST studies. As a comparison, the standard linear $k-\omega$ SST results, obtained in Section 5.3.3, were added in Table 5.9.

Table 5.9: Tyalor micro scale and CFL < 1 investigation on the HPH yn1 airfoil with extended airbrake

Test parameter	C_l	C_d	% Error C_l	% Error C_d
Standard Linear $k-\omega$	-0.0078	0.2024	98.6	23.6
Courant number < 1	0.0005	0.2056	100.1	22.4
Taylor micro scale	-0.0055	0.2045	99.0	22.8
Wind tunnel data [20]	-0.5382	0.2649		

As can be seen in Table 5.9, the results are very similar to that of the linear $k-\omega$ SST. This gives even further confidence that the mesh generated, time steps and inner iterations used were correct and further altering these parameters would not have made a noticeable difference in the results.

The simulations described in this section were computationally expensive and time-consuming with the available resources. Even though these studies are important for accurate results, this is not viable in engineering applications where rapid turnaround times and design iterations are essential.

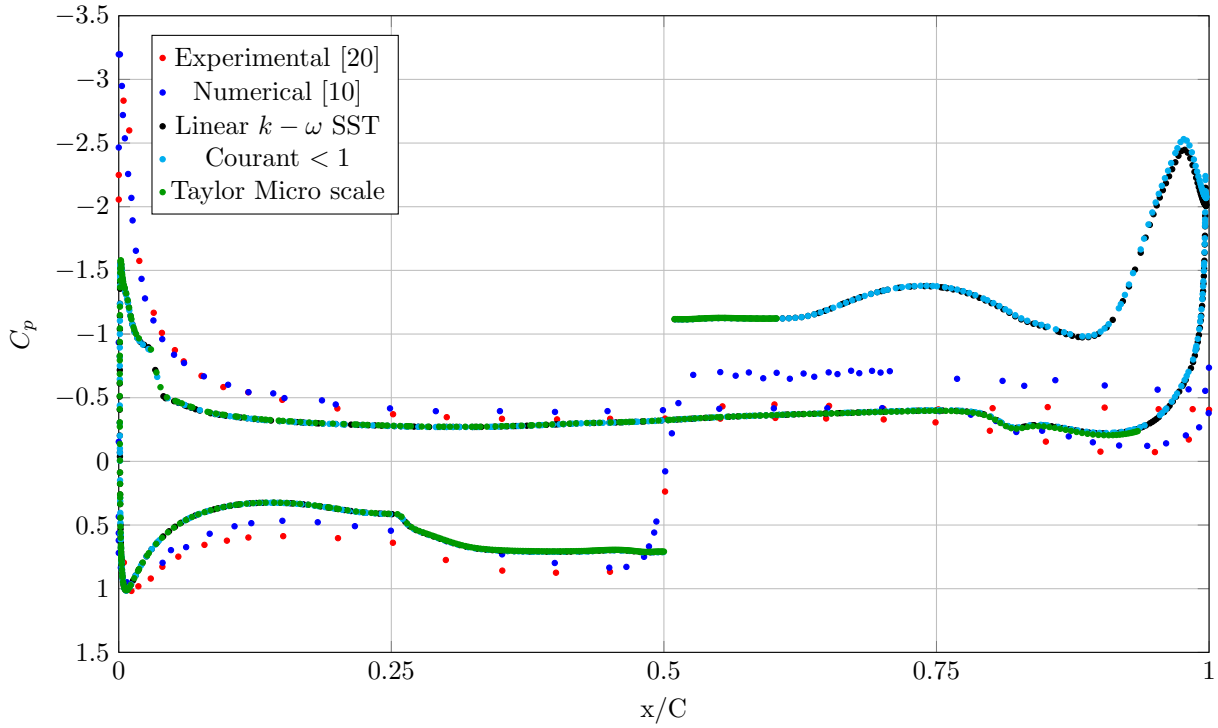

Figure 5.34: C_p vs x/C for alternative considerations investigation at AOA 5°

Figure 5.34 shows the pressure coefficients of the Courant < 1, Taylor micro scale and

Linear $k-\omega$ SST studies. The pressure distributions are almost identical, as reflected in the similar force coefficients.

5.3.5 HPH validation - 2.5D URANS Study

All the investigative simulations done up to this point in Section 5.3 were 2D. As shown in Section 4.3.6, the flow conditions present in this case are not 2D. There are tangible effects present when the flow domain has depth, and the 3D solvers are used.

A similar simulation was done as in Section 4.3.6. A 2D mesh was generated and extruded in the spanwise direction using 20 spanwise elements The 2D source mesh was not the same as in Section 5.3.3; however, the results were similar to that at an angle of attack of 8° in Section 5.3.3. The simulation used a time step of 0.0001 s with 20 inner iterations at an angle of attack of 8°.

This simulation only serves as an exploratory study to see what effects the 3D simulation would have on the extended airbrake simulations. The jump from 2D to 3D was significant in Section 4.3.6, and it was worthwhile to see if this was the case in the current section.

Table 5.10 and Figure 5.35 summarise the simulation results. The low-pressure region on the trailing edge can be seen in Figure 5.35. The time-averaged pressure coefficients were taken over the entire span and not just at a single point, indicating the presence of this low-pressure vortex on the entire span. This gives the confidence that the flow characteristics in the 2D simulations correspond to that of the 2.5D simulation, where natural flow dissipation is allowed to occur.

Even though the drag coefficient is relatively close to the wind tunnel results, the lift coefficient prediction is very inaccurate. This was similar to the 2D simulations prior to this 2.5D simulation study.

Table 5.10: 2.5D investigation on the HPH yn1 airfoil with extended airbrake

Test parameter	C_l	C_d	% Error C_l	% Error C_d
Standard Linear $k-\omega$ 2.5 D	0.1557	0.2262	138.2	12.4
Wind tunnel data [20]	-0.4120	0.2584		

5.4 Conclusion

The methodologies studied in Chapters 3 and 4 were applied to two airfoils with extended airbrake, the FX66-17AII-182 and HPH yn1 airfoils. The specific geometry used in the FX66 study was that of a vertically extended plate, where the HPH airbrake geometry had an airbrake cap.

The methodology used is built on the airfoil validations in Chapter 4. The addition of the extended airbrake required mesh refinement in the airbrake region as well as inner iteration and time step independence studies. Following this, the mesh refinement study was done

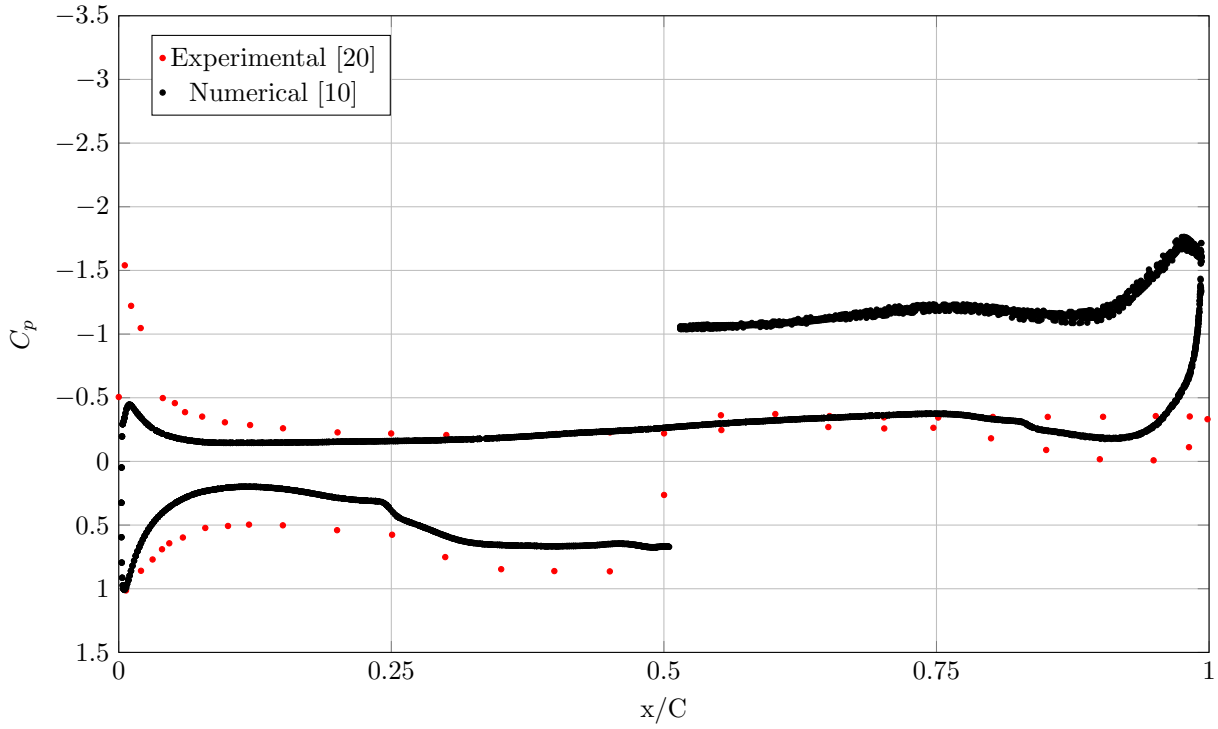

Figure 5.35: C_p vs x/C for 2.5D simulation investigation at AOA 8°

in the wakes of the two airfoils, ensuring the vortex shedding was captured accurately. After the simulation setup's conclusion, both airfoils' validation cases were done.

The results for the FX66-17AII-182 geometry were sufficiently accurate when considering the complex nature of the flow characteristics. The C_l vs α trends corresponded to that of both wind tunnel and numerical reference data given in [9]. The C_l results were within 28.7% of the wind tunnel results and 18.5% of the numerical reference case at an angle of attack at 0°.

The HPH yn1 airbrake study followed the methodology of the FX66 airfoil and airbrake study. After the conclusion of the validation study, the simulation results were very poor compared to the wind tunnel data in [20]. The only numeric reference available for the chosen simulation conditions was a pressure coefficient plot at an angle of attack at 5° given in [10]. Neither the C_l nor C_d results were accurate, and the C_l and C_d vs α plots did not behave as expected.

These poor correlations required further investigation. In addition to the modifications and variations on the $k-\omega$ SST model, described in more detail in Section 4.3, other turbulence models were used that were also suited for the anisotropic flows present in this case. Additionally, the generated mesh was altered to ensure a local Courant number < 1 and that all cell sizes were smaller than the Taylor micro scale limit required.

Neither of these investigations substantially altered the results obtained in the validation study. The final 2.5D simulation was done based on the significant results obtained in Section 4.3.6. A 2.5D simulation was set up with similar parameters as in Section 4.3.6. Even though a more accurate C_d was obtained, C_l was greatly overpredicted. All the

studies done in Section 5.3 point to an overprediction of C_l and an underprediction of C_d.

Chapter 6

FX66-17AII-182 Airbrake with cap

6.1 Introduction

A discrepancy was identified, in Chapter 5, during the study where the force coefficient results of the FX66 CFD simulations were much more accurate than the HPH simulations. The difference between these studies was that the FX66 airbrake had a vertically extended flat plate as an airbrake, whereas the HPH airbrake had an airbrake cap. These airbrake configurations can be seen in Figures 5.1 and 5.16.

In this section, the airbrake and cap configuration in [9] was simulated. This was done to investigate what effect the addition of the cap had on the overall results. Two meshing techniques were used, namely structured and unstructured meshes. The studies in Chapter 3 - 5 used the unstructured polyhedral mesh with a structured prism layer. On the other hand, the numerical reference study in [9] used a structured mesh. It was essential to eliminate the effect of the mesh type during the investigation in this chapter.

6.1.1 Unstructured mesh simulation

The first natural step was to use the mesh and simulation setup in Section 5.2.3 and adapt it for the new geometry. The main aim of this section was to identify if the airbrake cap was the cause of the discrepancy or not.

Simulation setup

The geometry used in this chapter was obtained from [9]. The only difference between the geometry used in this part of the study and Section 5.2 is the addition of the airbrake cap. The dimensions of the airbrake are shown in Figure 6.1.

The mesh used was similar to that used in Section 5.2.3. The mesh was adapted for the airbrake cap, but similar mesh refinements, flow domain and custom controls were used. The simulation used a mesh base size of 0.05 C with 30 inner iterations and a time step

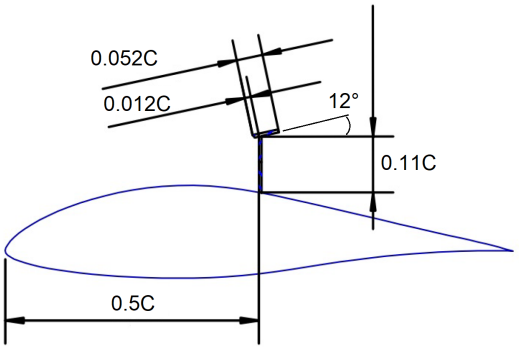

Figure 6.1: FX66-17AII-182 airfoil and airbrake with cap from [9]

of 0.0001 s. Figure 6.2 shows the generated mesh around the airbrake.

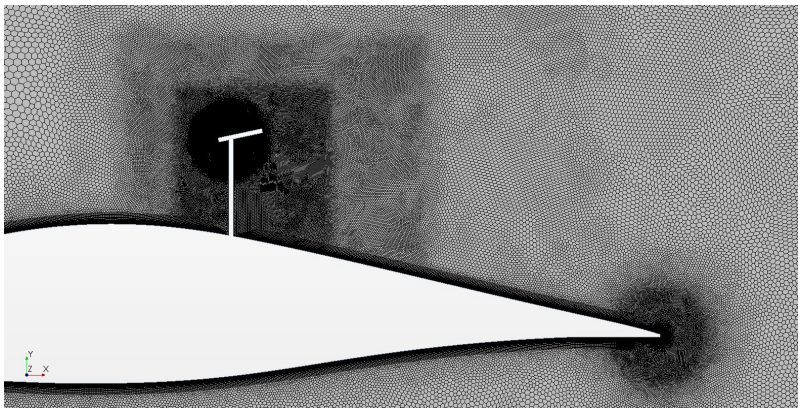

Figure 6.2: Generated mesh using base size 0.05C

The simulation used the linear $k-\omega$ SST URANS turbulence model. Two simulations were done, one using the default shear stress limiter a_1 and realizability coefficients C_T, and the other using modified a_1 and C_T coefficients.

Results and discussion

The results of the two studies are given in Table 6.1 and compared to the results in [9]. The simulation underpredicted both the C_l and C_d values. The C_d values of the default linear and modified linear studies were within 14% and 31%, respectively. The C_l values were inaccurate compared to the numerical reference values.

Table 6.1: 2.5D investigation on the HPH yn1 airfoil with extended airbrake

Turbulence model used	C_l	C_d	C_d/C_l
Linear, Default	-0.391	0.126	-0.321
Linear, Modified a_1 and C_T	-0.517	0.1	-0.195
CFD Reference [9]	0.0292	0.1463	5

Figure 6.3 shows the pressure coefficients and streamlines for both the reference case and the default linear CFD simulation. The modified and default linear simulations had similar pressure coefficient plots. The difference in pressure coefficients upstream of the

airbrake between the simulation and numerical reference case is apparent. Figure 6.3 shows the region upstream of the airbrake in the CFD simulation (6.3a) had lower pressure coefficients, ≈ 0.6, compared to ≈ 0.9 in the same region in the reference case (6.3b).

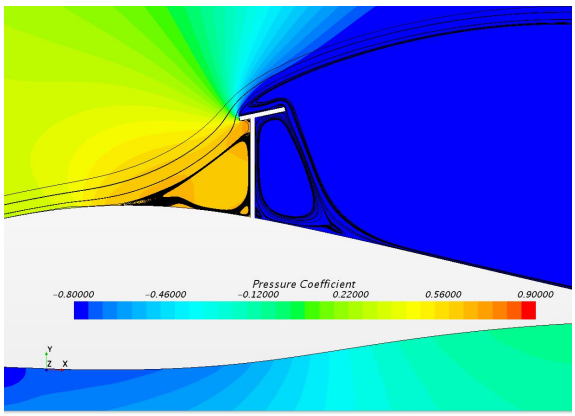

(a) Current study - Linear, Default

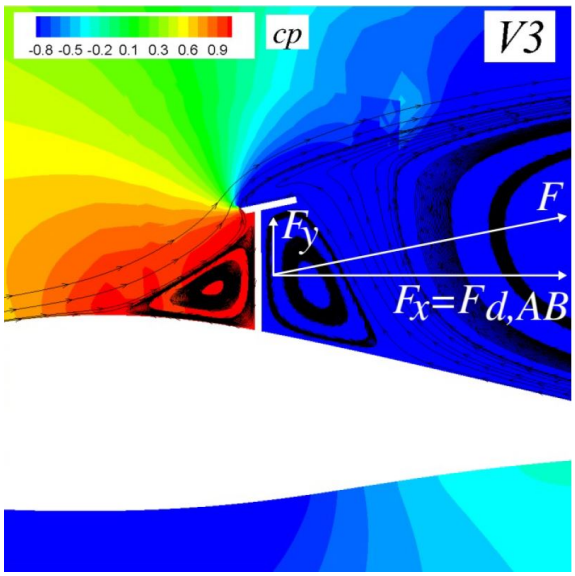

(b) Pressure coefficient plot of reference numerical study in [9]

Figure 6.3: Pressure coefficient plot comparison of airbrake with a cap at 0° AOA

The vortex formation downstream of the airbrake can better be seen in Figure 6.4. This Vortex corresponds with that seen in 6.3b. Overall, the flow pattern is similar to that of the reference case.

Figure 6.5 below shows the flow structure at three points during the flow period, at maximum and minimum C_l value and the point in between these two. The trailing edge vortex development is clear to see between these three figures.

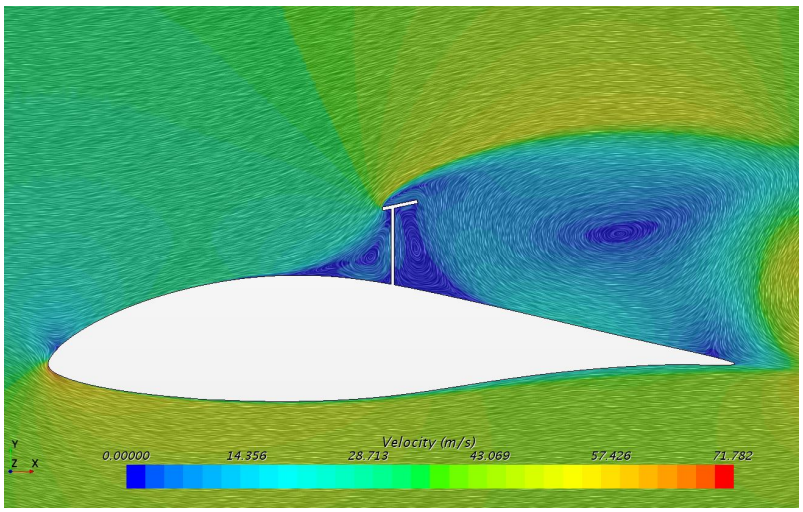

Figure 6.4: Velocity scene of the default linear $k - \omega$ SST simulation

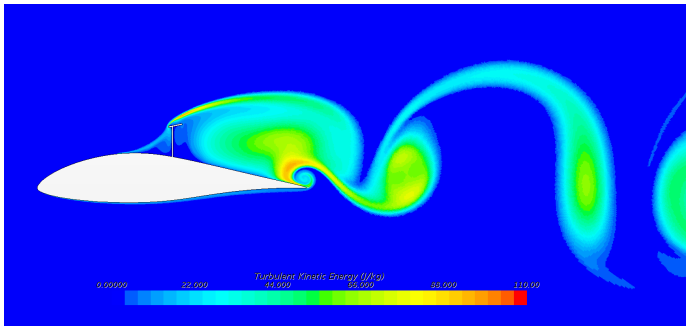

(a) TKE scene at maximumum C_l and 1.4633 s

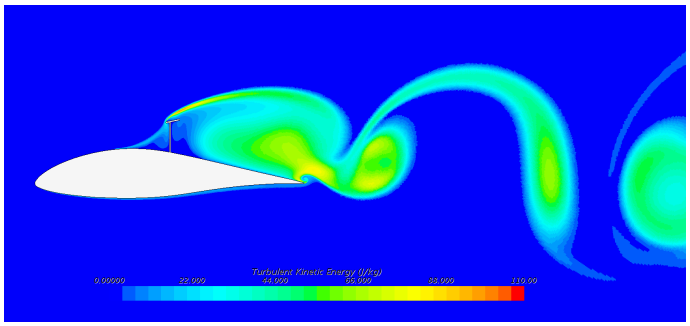

(b) TKE scene between maximum and minimum C_l and at 1.4673 s

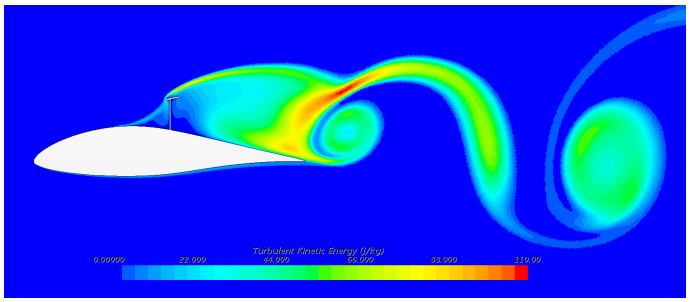

(c) TKE scene at minimum C_l and at 1.4733 s

Figure 6.5: Flow development over three points of the unstructured simulation of FX66 airbrake with a cap

6.1.2 Structured mesh simulation

The numerical studies in [9] used an overset structured mesh. Due to the poor results in Section 6.1.1, a structured mesh was generated to study the effects of the mesh on the final results. The aim of this section was only to set up and generate a mesh similar to what was used in [9] and study if that may be a cause of the poor simulation accuracy.

Simulation setup

Three structured meshes were set up for this structured simulation. As these simulations were only to observe the results of a structured mesh and if substantial changes would be obtained, three meshes were sufficient for the grid independence study. The GCI was used using a factor of safety (F_s) of 3 as suggested in [49]. A F_s of 3 was selected above the 1.25 in Chapters 4 and 5, as only three meshes were tested and required a larger safety factor to ensure the generated meshes are suitable.

The entire flow domain was divided into two sections, the area around the airbrake and the larger flow area. The two meshes were generated and combined to form the final mesh used in the simulation. This was done to increase the customizability of the mesh, especially around the airbrake region.

The mesh setup in the flow area was generated as follows; the coarse grid had 245 points on the body surface and 110 in the normal direction, the medium mesh had 308 and 138 points, and the fine mesh had 365 and 167 points, respectively. The generated fine mesh for the flow area is shown in Figure 6.6a.

The points on the airbrake flow area were as follows; the coarse mesh was generated using 210 points on the body surface with 190 points in the direction normal to the flow, the medium mesh used 263 and 238 and the fine mesh used 311 and 290 points, respectively. The generated fine mesh for the airbrake area is shown in Figure 6.6b.

The combined generated fine mesh, as well as the mesh used in [9], are shown in Figure 6.7. This mesh, however, is only a representation and not the same as the reference data used. The generated mesh had a $y^+ \approx 1$. The meshes are functionally similar, as seen in Figure 6.7. The main difference between the two meshes is that the reference mesh used an overset mesh, whereas the generated mesh in this section used an interface between the meshes. In both cases, the region where both meshes merge is not as smooth and gradual as preferred. This is one of the disadvantages of using structured mesh compared to an unstructured one, as used in Chapter 5.

The time steps and inner iterations used in the structured simulations were 0.0001 s and 30, respectively. The smallest mesh sizes in both the structured and unstructured meshes were similar, thus there was no need for time step or inner iteration independence studies. The default linear $k - \omega$ SST turbulence model was used.

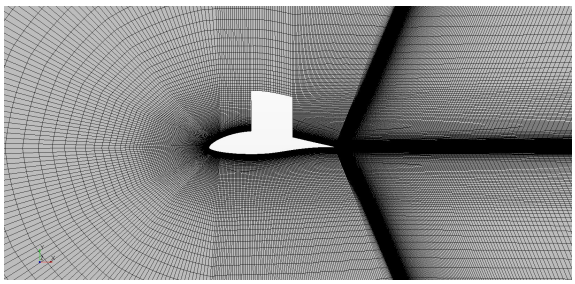

(a) Fine mesh generated in flow area

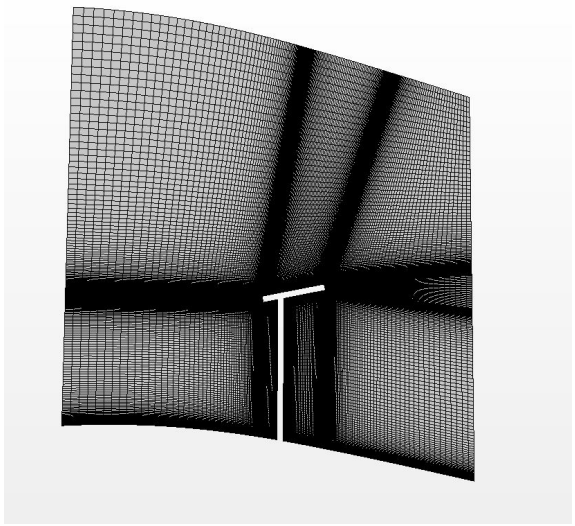

(b) Fine mesh generated in airbrake area

Figure 6.6: Generated meshes using the fine mesh parameters for both the flow and airbrake areas

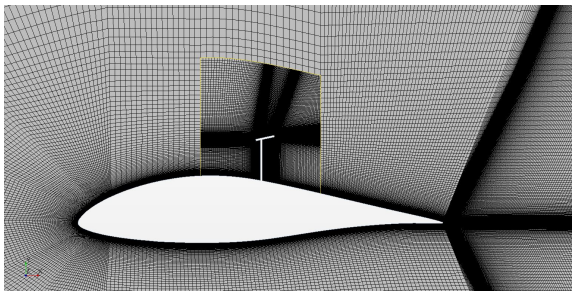

(a) Fine mesh generated for final flow domain used in simulation

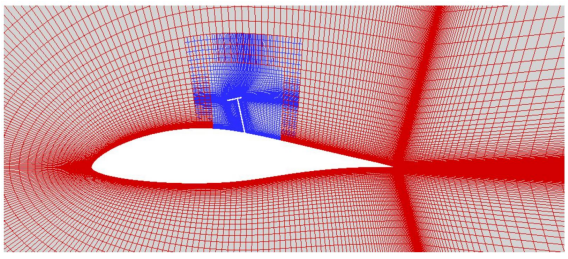

(b) Mesh used in the numerical study in [9]

Figure 6.7: Comparison between the generated mesh used in this simulation and an example of the reference mesh

Results and discussion

Table6.2 summarise the results of the unstructured mesh study. Figure 6.8a shows the asymptotic convergence of the generated meshes. With the Richardson extrapolation results in Figure 6.8b, the chosen mesh was sufficient for this structured simulations.

The GCI and % error of the fine mesh was 5.9% and 5.1%, respectively. This was sufficient for the purposes of this structured mesh study, identifying what effects if any, an unstructured mesh had on the overall results of the airbrake with the cap.

Table 6.2: Structured mesh simulations with airbrake cap at 30 inner iterations and time step 0.0001 s

Mesh size	Element count [-]	C_l	C_d	Δ_x	r	GCI	% Error
Coarse	133747	-0.4622	0.2616	0.0027	-	-	4.14%
Medium	208704	-0.4766	0.2588	0.0022	1.560	6.3%	7.39%
Fine	303825	-0.4663	0.2633	0.0018	1.456	5.9%	5.08%
CFD Reference [9]		0.0292	0.1463				

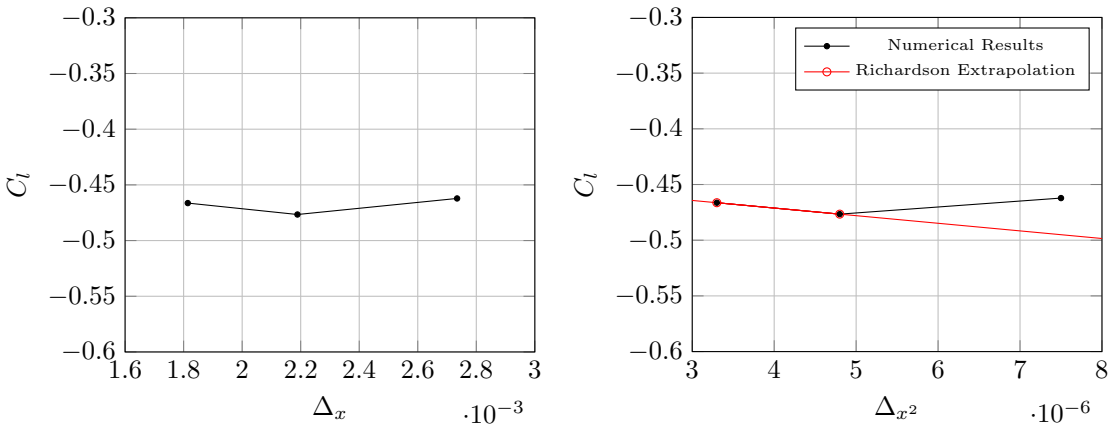

(a) C_l vs relative mesh spacing

(b) Richardson extrapolated spacing

Figure 6.8: Mesh convergence of C_l using a structured mesh for the FX66-17AII-182

The structured fine mesh C_l results were within 19.3% and 9.8% of the unstructured default linear and modified linear simulations in Table 6.1. The structured C_d results were further out than both unstructured simulations, 109.0% and 163.3%, respectively.

Neither the C_l nor the C_d results of the structured mesh were close to the numerical results given in [9]. Based on these results, the difference in meshes used between the current structured mesh study and that of [9] did not lead to the poor accuracy in Section 6.1.1.

6.2 Conclusion

In Chapter 5, the same simulation methodology was applied to two airfoil and airbrake cases, one (FX66-17AII-182 Airbrake) was a plain flat plate, and the other (HPH yn1) had an airbrake cap. The simulation accuracy of the FX66 airfoil was relatively good, unlike

that of the HPH airfoil simulations.

Both simulations had similar flow conditions, methodologies and simulation setups. The difference was the airbrake cap on the HPH compared to the flat plate of the FX66 airfoil. The overall aim of this section was to study the effect of the airbrake cap on the FX66 airfoil and airbrake and to identify if the addition of the cap would cause the loss of simulation accuracy when using similar methodologies.

The C_d results, in Section 6.1.1, were relatively accurate where the C_l results were not. Both the modified and default linear $k-\omega$ SST solvers were used and using other solvers were not deemed necessary based on the results in Section 5.3.4.

A structured simulation was set up with a functionally similar mesh to the one in the reference case [9]. The results of the structured mesh in Section 6.1.2 were also inaccurate compared to the numerical reference results. These simulations were done to eliminate the possibility that the different meshes used played a significant role in the accuracy of the simulations.

Based on these results, it can be said with relative confidence that the addition of the airbrake cap might play a role in the accuracy of the simulations in Chapters 5 and 6. Comparing the streamlines of both cases (Figure 5.30 and Figure 6.3) indicates that the flow structures around the airbrakes are relatively similar.

It is difficult to pinpoint an exact cause as the methodologies explored in this chapter gave accurate results in Chapters 3, 4 and Section 5.2. Additionally, the literature available does not detail the various turbulence model coefficients used, if any. All the standard parameters mentioned in the literature were taken into account in these studies.

Chapter 7

Conclusions and recommendations

The following chapter summarises the research objectives and how they were met, a discussion and conclusion of the work done and recommendations for further research based on the findings of this study.

7.1 Objective outcomes

The objectives set in Chapter 1 and are discussed below;

Validated unsteady canonical flow cases

Three unsteady flow cases were identified and studied in Chapter 3: laminar flow over a circular cylinder, turbulent flow over a circular cylinder and turbulent flow over a square cylinder. CFD simulation results from existing literature were replicated for each case and used as a reference. The CFD study in [11] was used as the laminar flow reference CFD case. The CFD simulation results were within 0.07% and 5% of the C_d and Strouhal numbers, respectively. Both turbulent circular and square cylinder CFD data were given in [12]. The C_d and Strouhal number results of the circular cylinder were within 2.6% and 0.1%, respectively. The square cylinder C_d and Strouhal number results were within 5.2% and 2.8%. These conditions were considered accurate, and the objective was met.

Validate flow over a clean airfoil

Two airfoils were identified and studied in Chapter 4. These airfoils had wind tunnel data available on the clean airfoils and with airbrakes extended. Additionally, these airfoils were designed for sailplane applications, making them suitable for this study. The wind tunnel data for the first airfoil, the FX66-17AII-182 airfoil, was given in [19]. The CFD validation study to replicate the wind tunnel results were accurate in the linear range but over predicted C_l after the stall angle.

The wind tunnel data of the second airfoil, HPH yn1, was given in [20]. The CFD results were accurate in the linear region but overpredicted C_l and underpredicted C_d. The

variations and modifications to the $k-\omega$ SST solver to try and increase the prediction accuracy had little effect on the overall results.

Validate flow over an airfoil with extended airbrakes

Both FX66 and HPH airfoils had wind tunnel and CFD results available to validate the CFD simulations in Chapter 5. The FX66 wind tunnel and CFD data used were given in [9]. The FX66 airbrake configuration used as a validation case was a vertically protruding flat plate. The CFD validation simulations were sufficiently accurate and predicted the C_l vs α trend accurately. Additionally, the CFD results of FX66 airfoil with the airbrake cap were compared to the CFD data given in [9]. The CFD simulation poorly predicted the force coefficients compared to the reference values.

The HPH yn1 CFD data, given in [10], was a pressure coefficient plot at 5°. The wind tunnel data, given in [10], gave full C_l and C_d vs α plots. The HPH validation study, done at 5°, had poor accuracy, even though the C_d was within 23.6%, the C_l results were 98.6%. Various parameters were investigated to try and improve the simulation results without any apparent success. These parameters included modifications and variations of the $k-\omega$ SST turbulence model, using different turbulence models and generating a mesh with elements smaller than the Taylor microscales.

7.2 Conclusion

The same methodology was used during all validation simulations. Firstly the mesh refinement around key locations was done. These locations were identified as regions with high gradients or eddies, such as behind a bluff body, at airbrake corners or on leading and trailing edges of airfoils. In conjunction with the mesh refinement studies, time step and inner iteration independence studies were done to identify the time step and inner iteration independent solutions. Once both time step, mesh and inner iteration independence solutions were obtained, the validation studies were done. This methodology resulted in good correlation in the canonical unsteady validation simulations in Chapter 3 as well as the FX66 simulations in Chapters 4 and 5.

The methodology proved successful by the accurate FX66 airfoil and airbrake validation correlation: however, the HPH simulation accuracy was poor, even though the same methodology was followed. The inaccurate airfoil validation results started to appear at high angles of attack, where the simulations overpredicted the C_l. The overprediction of the C_l was prominent in all the validation cases using both airfoils; however, the HPH airfoil validation C_l vs α curve did not match the expected curve.

The HPH airbrake validation results were very poor, even with more advanced solvers and techniques primarily used in anisotropic turbulence, such as those in highly separated and recirculating flows. The addition of the quadratic and cubic constitutive options did not significantly increase the accuracy of the HPH airbrake simulations. Combining these variations with the shear stress limiter and realizability coefficients did not improve the

simulation accuracy. Using more complex solvers, such as the Lag Elliptical Blending $k-\epsilon$ and RST turbulence models, specifically meant for anisotropic flows, did not improve the results. Additionally, not even using the 2.5D simulation increased the accuracy of the HPH airbrake CFD results, which was the case with the HPH airfoil.

It can be stated with reasonable certainty that the presence of the airbrake cap played a role in the poor correlation of the HPH airbrake studies. This can be seen in Chapter 6, where adding the airbrake cap on the FX66 airfoil resulted in inaccurate results. Additionally, both [9] and [10] used in-house CFD programs and not easily commercially available software such as ANSYS or Star CCM+. Commercial CFD packages focus on robustness and ease of use over accuracy, which could lead to results that are not similar compared to in-house software. Getting results to match or correspond to these in-house packages is difficult if none of the more in-depth solver coefficients and calibrations is given. The differences in pressure coefficient plots between the results in [10] and that found in the current study, indicate further CFD setup that was not mentioned or reported on.

Three overall parameters played a significant role in the accuracy of the simulations above all else, and these were the mesh density, time steps used and inner iterations. All three of these parameters needed to be tested and refined together for the simulation to be independent of these parameters. By understanding these parameters, choices can be made on the combination of these parameters that would lead to the most efficient simulation. Increasing any of these parameters would increase simulation time.

There is a tradeoff to be made between simulation accuracy and speed. The use of 2D simulations is more than capable of being used as a design and engineering tool when rapid prototyping or analysis is required. However, when the main aim is the complete understanding of the flow and force coefficient accuracy, 3D simulations are a better option. The 3D turbulent effects are only in 3D simulations. A good alternative is that a 2.5D mesh can be used, combining the benefits of 3D with the ease of mesh generation of 2D.

The use of the methodologies in this study can confidently be used on similar canonical unsteady cases, even simple sailplane airbrakes or airfoils at high angles of attack. It would, however, be advised that before this methodology is used on more complex airbrakes, the discrepancies with the airbrake cap need to be understood and studied.

This study serves as a starting point, identifying and summarising the essential aspects required to set up a reasonably accurate and robust simulation for cases similar to flow over bluff bodies or, more specifically, sailplane airbrakes. The available literature on sailplane airbrakes CFD studies does not go in-depth about how the simulations were set up and the coefficients used. The poor correlation with the HPH airbrake simulation results should not discourage the use of this methodology but serve as a starting point to fully understand the reasons for the discrepancies.

7.3 Recommendations

The following points were identified as points of interest for future research studies:

- Investigate the discrepancies between die CFD and wind tunnel results of the HPH airfoil. The discrepancies formed at a relatively low angle of attack (8°) in the absence of high turbulent and separated flows.
- A wind tunnel and CFD study together to understand and validate the methods used in this study and to eliminate any possibility of unknown parameters and obscurity.
- A Validation study of airfoils at higher angles of attack to further understand the causes of the discrepancies identified in this study.
- Investigate the discrepancies between the HPH airbrake validation CFD and wind tunnel results. In particular, the formation of the low-pressure vortex on the airbrake trailing edge.
- Investigate the flow phenomena caused by the addition of the airbrake cap in the FX66 that could lead to poor results.
- Validate that methodology used in this study on other bluff body studies to identify and study the poor correlation with the HPH wind tunnel and the anomalies in the results.

Bibliography

[1] "What are spoilers and what are they used for?" Dec 2018. [Online]. Available: https://www.airlineratings.com/did-you-know/what-are-spoilers-and-what-are-they-used-for/

[2] S. F. Hoerner, "Fluid-dynamic drag," *Hoerner fluid dynamics*, 1965.

[3] B. W. McCormick, "Aerodynamics, aeronautics, and flight mechanics," 1995.

[4] J. Tu, G. H. Yeoh, and C. Liu, *Computational fluid dynamics: a practical approach*. Butterworth-Heinemann, 2018.

[5] *Simcenter STAR-CCM+ Documentation*.

[6] H. K. Versteeg and W. Malalasekera, *An introduction to computational fluid dynamics: the finite volume method*. Pearson education, 2007.

[7] "Courant number in cfd," Apr 2022. [Online]. Available: https://www.idealsimulations.com/resources/courant-number-cfd/

[8] *Introduction to ANSYS solver Fluent*. [Online]. Available: https://home.agh.edu.pl/ jaszczur/doc/cfd/L2/FLUENT(heat%20transfer-unsteady).pdf

[9] M. Greiner and G. Bangga, "Dilemma resolved: Airbrakes tamed," *Technical Soaring*, vol. 42, no. 4, pp. 23–30.

[10] Z. Pátek, J. Červinka, and P. Vrchota, "Wind tunnel and cfd study of airfoil with airbrake," in *28th Congress of the International Council of the Aeronautical Sciences ICAS 2012*, 2012, pp. 1–9.

[11] N. Mahir and Z. Altaç, "Numerical investigation of convective heat transfer in unsteady flow past two cylinders in tandem arrangements," *International Journal of Heat and Fluid Flow*, vol. 29, no. 5, pp. 1309–1318, 2008.

[12] S.-C. Lo, K. A. Hoffmann, and J.-F. Dietiker, "Numerical investigation of high reynolds number flows over square and circular cylinders," *Journal of Thermophysics and Heat Transfer*, vol. 19, no. 1, pp. 72–80, 2005.

[13] N. Hall, "Gliders - glenn research center," Jul 2022. [Online]. Available: https://www1.grc.nasa.gov/beginners-guide-to-aeronautics/gliders/

[14] F. Thomas and J. Milgram, *Fundamentals of sailplane design.* College Park Press College Park, MD, 1999, vol. 3.

[15] J. Gedeon, "A few words on airbrakes," *Technical Soaring*, vol. 31, no. 4, pp. 110–113, 2006.

[16] N. Hall, "Spoilers interactive - glenn research center," Jul 2022. [Online]. Available: https://www1.grc.nasa.gov/beginners-guide-to-aeronautics/spoilers-interactive/

[17] ——, "Flaps and slats interactive - glenn research center," Jul 2022. [Online]. Available: https://www1.grc.nasa.gov/beginners-guide-to-aeronautics/flaps-and-slats/

[18] "Certification specifications for sailplanes and powered sailplanes cs-22," European Aviation Safety Agency, Tech. Rep., 03 2009.

[19] D. M. Somers, "Experimental and theoretical low-speed aerodynamic characteristics of a wortmann airfoil as manufactured on a fiberglass sailplane," 1977.

[20] J. Červinka, Z. Pátek, and M. Zabloudil, "Wind-Tunnel measurements of wing airfoil section equipped with airbrake," VZLU, Czech aerospace research centre, Tech. Rep. R-5177, 2011.

[21] B. R. Munson, T. H. Okiishi, W. W. Huebsch, and A. P. Rothmayer, *Fluid mechanics.* Wiley Singapore, 2013.

[22] J. Tu, G. H. Yeoh, and C. Liu, *Computational fluid dynamics: a practical approach.* Butterworth-Heinemann, 2018.

[23] H. Schlichting and K. Gersten, *Boundary-layer theory.* Springer, 2017.

[24] T. Nakamura, S. Kaneko, F. Inada, M. Kato, K. Ishihara, T. Nishihara, N. W. Mureithi, and M. A. Langthjem, *Flow-induced vibrations: classifications and lessons from practical experiences.* Butterworth-Heinemann, 2013.

[25] M. W. Bern and P. E. Plassmann, "Mesh generation." *Handbook of computational geometry*, vol. 38, 2000.

[26] I. Sadrehaghighi, *Mesh Generation in CFD*, 01 2020.

[27] T. Cebeci, J. P. Shao, F. Kafyeke, and E. Laurendeau, *Computational fluid dynamics for engineers: from panel to Navier-Stokes methods with computer programs.* Springer, 2005.

[28] F. R. Menter, "Two-equation eddy-viscosity turbulence models for engineering applications," *AIAA journal*, vol. 32, no. 8, pp. 1598–1605, 1994.

[29] P. Catalano, M. Wang, G. Iaccarino, and P. Moin, "Numerical simulation of the flow around a circular cylinder at high reynolds numbers," *International journal of heat and fluid flow*, vol. 24, no. 4, pp. 463–469, 2003.

[30] D. S. Holloway, D. K. Walters, and J. H. Leylek, "Prediction of unsteady, separated boundary layer over a blunt body for laminar, turbulent, and transitional flow," *International Journal for Numerical Methods in Fluids*, vol. 45, no. 12, pp. 1291–1315, 2004.

[31] A. Benim, E. Pasqualotto, and S. Suh, "Modelling turbulent flow past a circular cylinder by rans, urans, les and des," *Progress in Computational Fluid Dynamics, An International Journal*, vol. 8, no. 5, pp. 299–307, 2008.

[32] A. Guissart, T. Andrianne, G. Dimitriadis, and V. E. Terrapon, "Numerical and experimental study of the flow around a 4: 1 rectangular cylinder at moderate reynolds number," *Journal of Wind Engineering and Industrial Aerodynamics*, vol. 189, pp. 289–303, 2019.

[33] J. Ke, "Rans and hybrid les/rans simulations of flow over a square cylinder," *Advances in Aerodynamics*, vol. 1, no. 1, pp. 1–24, 2019.

[34] M. I. Khan and S. A. Masood, "A numerical investigation of vortex shedding and flow around a smooth circular cylinder in upper transition regime by using urans," *Technical Journal*, vol. 25, no. 01, pp. 15–21, 2020.

[35] N. Souckova, M. Matejka, and L. Popelka, "Experimental investigation and numerical analysis of flow past airfoils with spoilers and high lift devices," *Technical soaring*, vol. 34, no. 4, pp. 110–117, 2010.

[36] Z. Pátek, J. Červinka, R. Kulhánek, and P. Vrchota, "Experimental study of aerodynamics of an airfoil with airbrake," *Technical Soaring*, vol. 44, no. 1, pp. 2–13.

[37] T. Mulyanto and M. Zulkarnain, "Computational fluid dynamics analysis and aircraft performance studies of gl-1's spoiler extension," in *AIP Conference Proceedings*, vol. 2366, no. 1. AIP Publishing LLC, 2021, p. 030005.

[38] ——, "Indonesian glider gl-1 spoiler preliminary design and computational fluid dynamics analysis using easa cs-22 performance requirements," in *IOP Conference Series: Materials Science and Engineering*, vol. 1173, no. 1. IOP Publishing, 2021, p. 012048.

[39] W. L. Oberkampf and T. G. Trucano, "Verification and validation in computational fluid dynamics," *Progress in aerospace sciences*, vol. 38, no. 3, pp. 209–272, 2002.

[40] "Guide for the verification and validation of computational fluid dynamics simulations."

[41] *Simcenter STAR-CCM+ Verification Suite.*

[42] C. Stoll, "Fft vs psd: What's the difference?" Sep 2022. [Online]. Available: https://vibrationresearch.com/blog/fft-psd-difference/

[43] R. Oshana, *DSP software development techniques for embedded and real-time systems.* Elsevier, 2006.

[44] M. Cunningham and G. Bibby, "11 - electrical measurement," in *Electrical Engineer's Reference Book (Sixteenth Edition)*, sixteenth edition ed., M. Laughton and D. Warne, Eds. Oxford: Newnes, 2003, pp. 11–1–11–43. [Online]. Available: https://www.sciencedirect.com/science/article/pii/B9780750646376500113

[45] P. Ewing, "Best practices for aerospace aerodynamics," Jun 2015.

[46] H. Riblett, "What are wortman airfoils," *EAA*, no. 29576, 1988.

[47] G. V. Selby, "Boundary-layer measurements on a high reynolds number three-element airfoil," *Hampton Univ., NASA (American Society for Engineering Education (ASEE) Summer Faculty Fellowship Program 1992 p 171-172 (SEE N93-16760 05-80)*, 1992.

[48] D. M. Changfoot, A. G. Malan, and J. Nordström, "Hybrid computational-fluid-dynamics platform to investigate aircraft trailing vortices," *Journal of Aircraft*, vol. 56, no. 1, pp. 344–355, 2019.

[49] P. J. Roache, "Quantification of uncertainty in computational fluid dynamics," *Annual review of fluid Mechanics*, vol. 29, no. 1, pp. 123–160, 1997.

[50] ——, *Verification and validation in computational science and engineering*. Hermosa Albuquerque, NM, 1998, vol. 895.

[51] I. B. Celik, U. Ghia, P. J. Roache, and C. J. Freitas, "Procedure for estimation and reporting of uncertainty due to discretization in cfd applications," *Journal of fluids Engineering-Transactions of the ASME*, vol. 130, no. 7, 2008.

[52] S. Evans and S. Lardeau, "Validation of a turbulence methodology using the sst k-ω model for adjoint calculation," in *54th AIAA Aerospace Sciences Meeting*, 2016, p. 0585.

[53] (2017) Rans turbulence using non-linear constitutive relationships including qcr. [Online]. Available: https://support.sw.siemens.com/knowledge-base/KB000032422$_E N_U S$

[54] (2018) What are secondary flows, when do they occur, and how do i capture them? [Online]. Available: https://support.sw.siemens.com/knowledge-base/KB000031985$_E N_U S$

[55] (2018) What is the a1 coefficient in the menter sst turbulence model? [Online]. Available: https://support.sw.siemens.com/knowledge-base/KB000037700$_E N_U S$

[56] H. Tennekes, J. L. Lumley, J. L. Lumley *et al.*, *A first course in turbulence*. MIT press, 1972.

[57] W. Smyth and J. Moum, *Three-dimensional (3D) turbulence*. Academic Press, 2009.

Appendix A

Appendix Chapter

A.1 Appendix A

Lam Surface size study

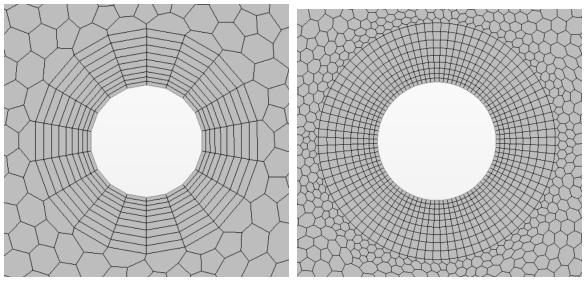

Figure A.1: Prism layer comparison of different surface sizes; a) 15%, b) 3%

Table A.1: Results of the surface size variation

Surface size [%]	Element count	F_{vs} [Hz]	Average C_d
15	1506	1.699	1.325
12	1734	1.799	1.324
9*	2000	1.898	1.334
6	2445	1.898	1.340
3	3460	1.898	1.351
Theoretical value [11]		2	1.367

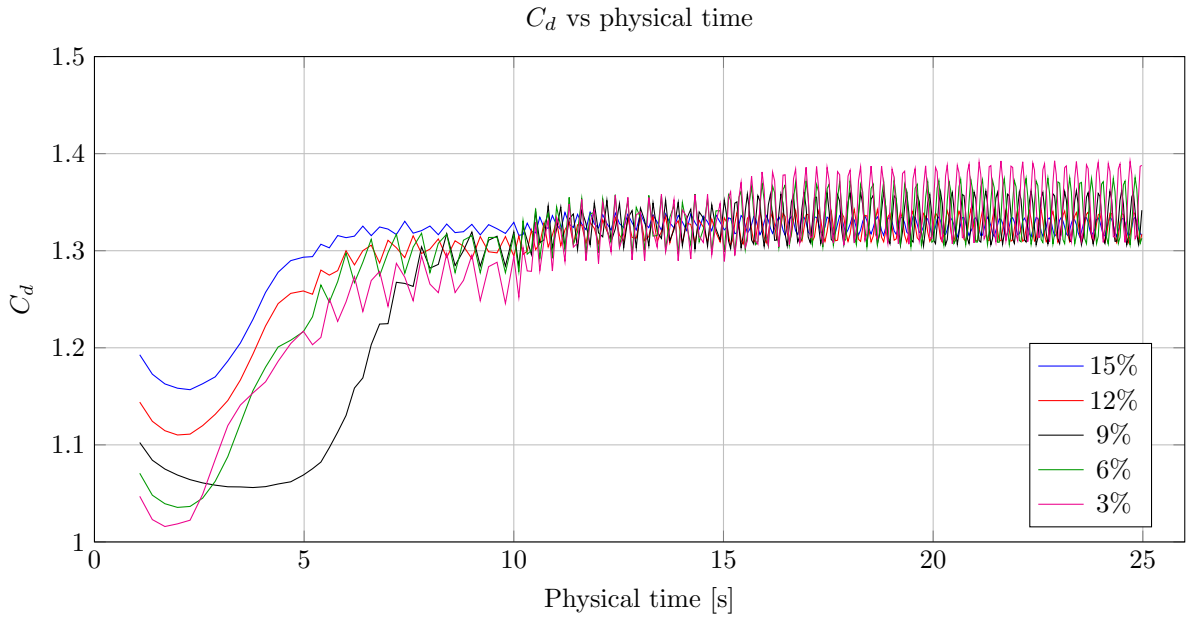

Figure A.2: Drag coefficient comparison of various surface sizes

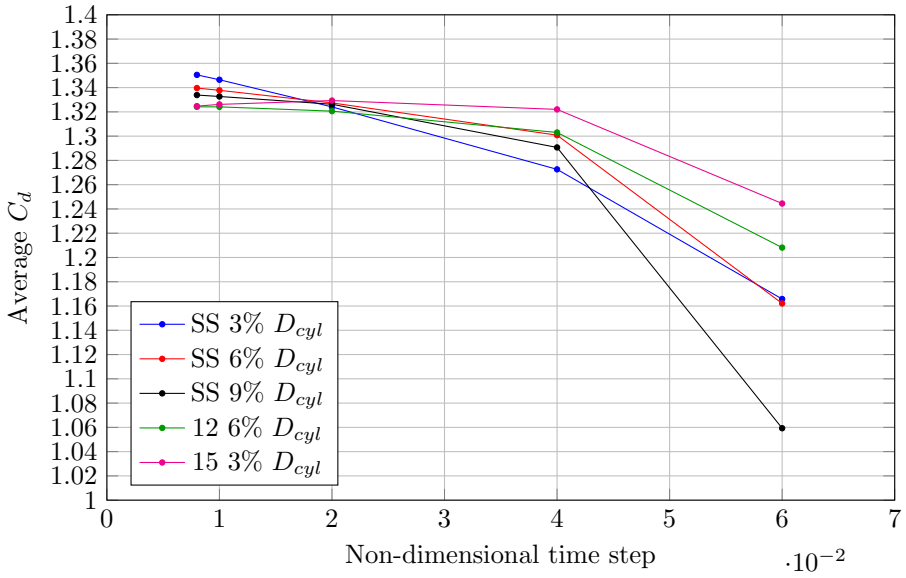

Figure A.3: Average C_d values vs inner iterations for base sizes 20% D_{cyl} - 5% D_{cyl}

Lam prism layer mesh study

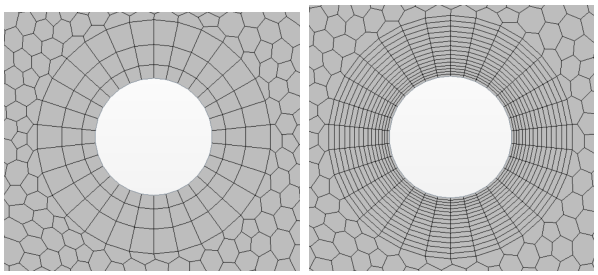

Figure A.4: Comparison of different number of prism layer cells; a) 3%, b) 15%

Table A.2: Results of the number of cells in the prism layer

Number of PL cells	Element count	F_{vs} [Hz]	Average C_d
3	1820	1.898	1.130
6	1910	1.898	1.349
9*	2000	1.898	1.334
12	2090	1.898	1.327
15	2180	1.898	1.324
Theoretical value [11]		2	1.367

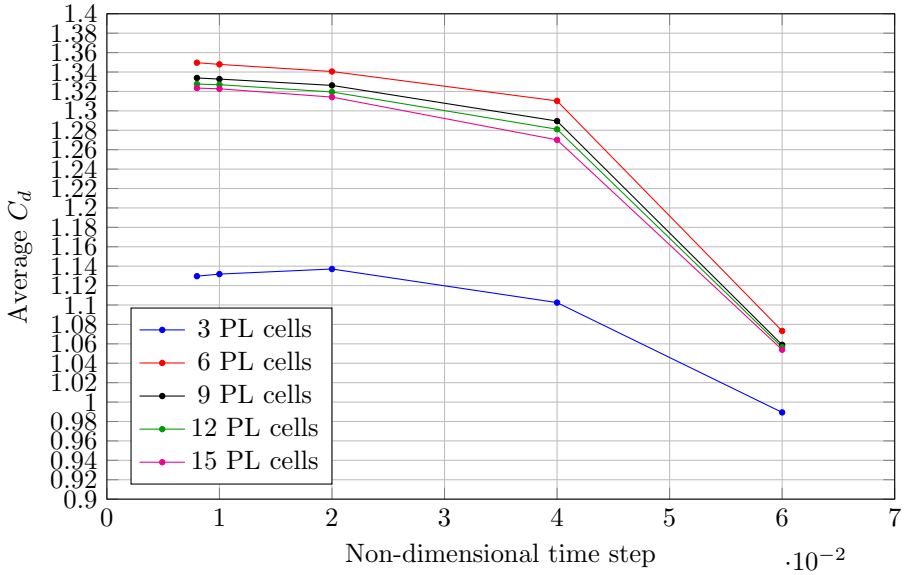

Figure A.5: Average C_d values vs inner iterations for base sizes 0.2 D_{cyl} - 0.05 D_{cyl}

Lam cylinder wake length study results

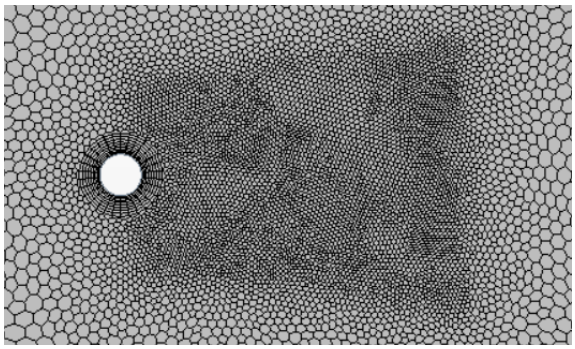

Figure A.6: Generated mesh using cone shaped volume control with mesh size 10% of base size and length 8 D_{cyl}

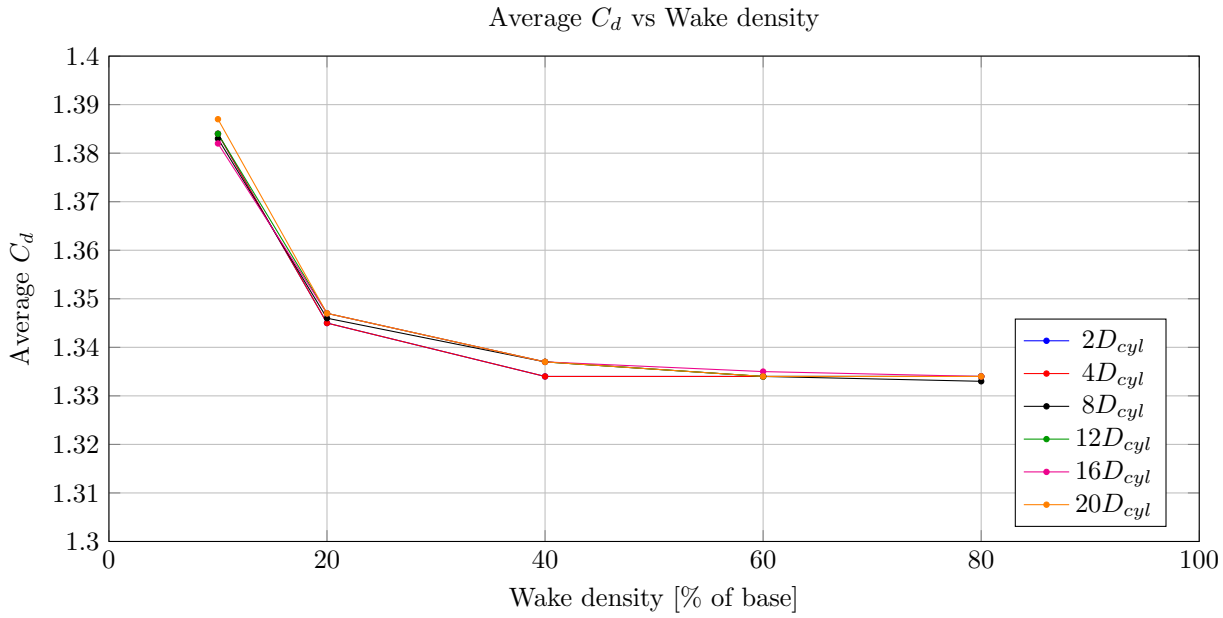

Figure A.7: Drag coefficient comparison of various surface sizes

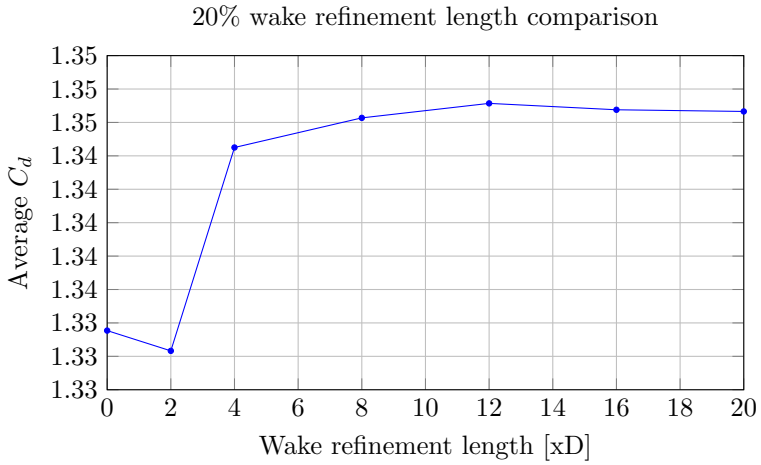

Figure A.8: Drag coefficient comparison of various surface sizes

A.2 Appendix B

Prism layer stretch

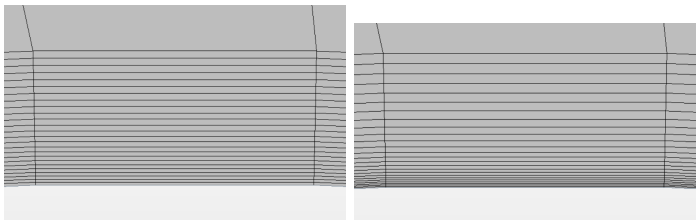

Figure A.9: Prism layer comparison of different stretch factor; a) 1.05 , b) 1.8

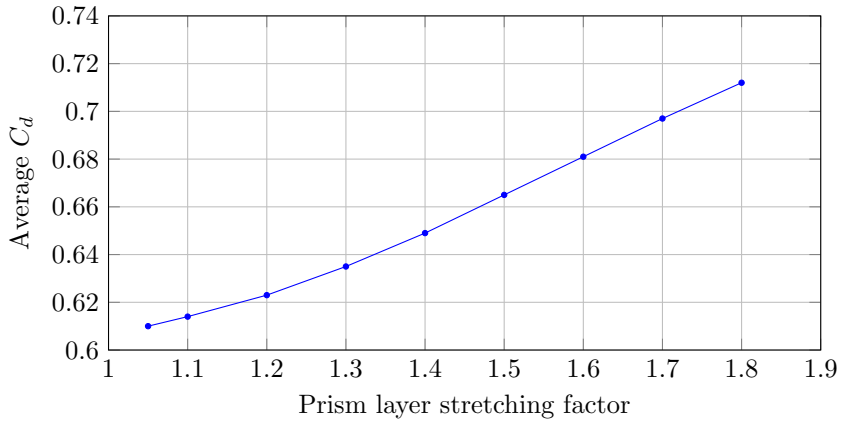

Figure A.10: Average C_d values at various prism layer stretch factors

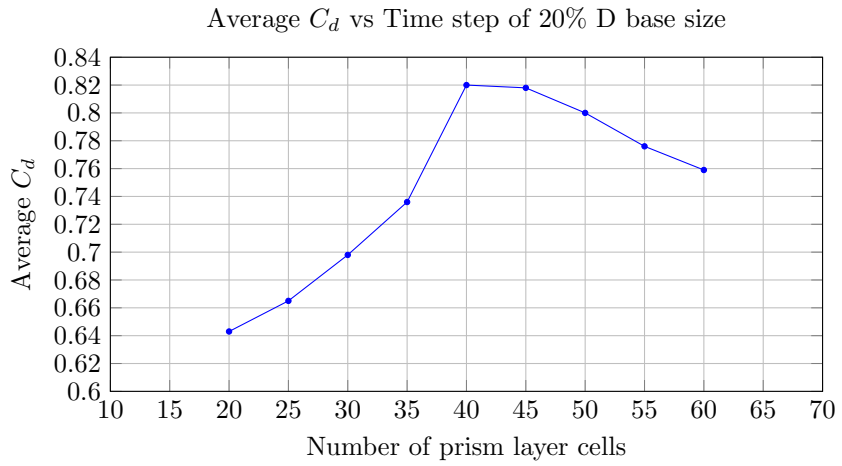

Figure A.11: Average C_d values at various prism layer stretch factors

Separation zone

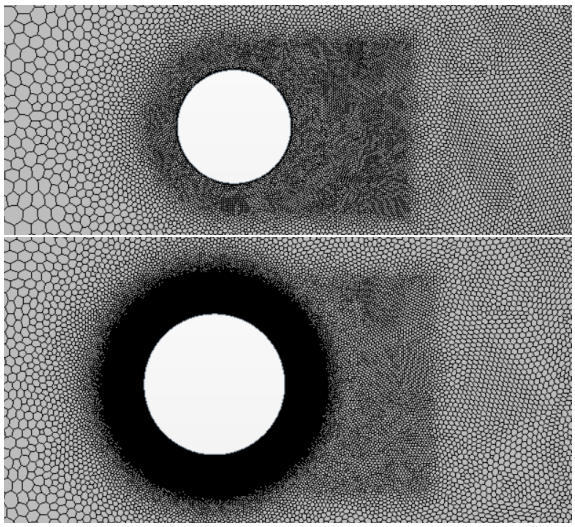

Figure A.12: Mesh comparison of different volume control base sizes; a) 10%, b) 1%

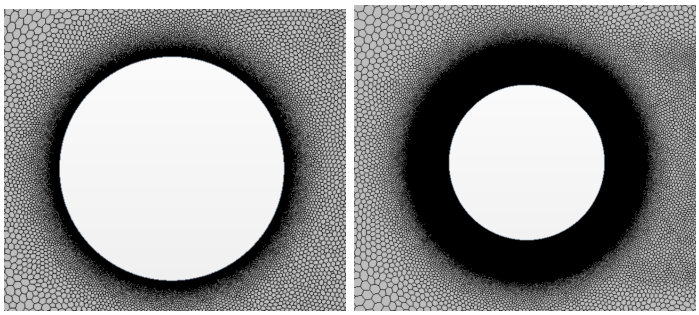

Figure A.13: Mesh comparison of different volume control radius dimensions; a) 1.05R, b) 1.5R

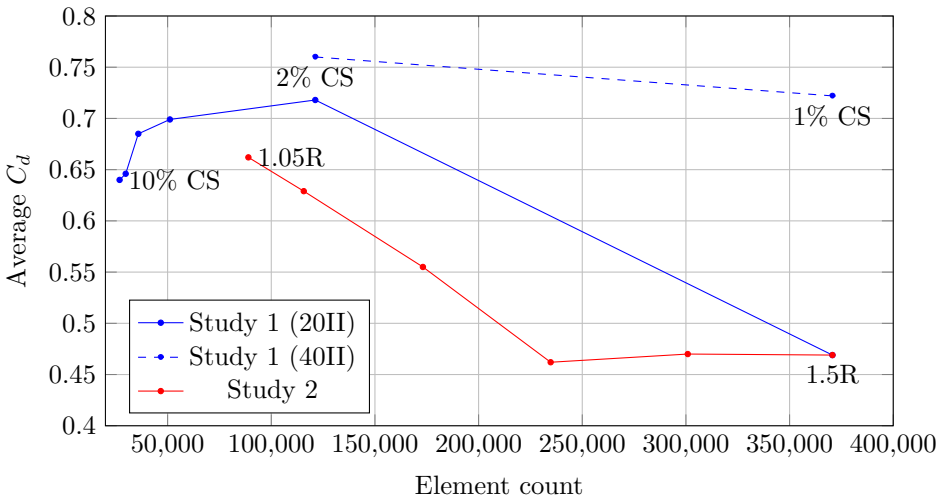

Figure A.14: Average C_d values for separation region mesh refinement study

Recirculation zone

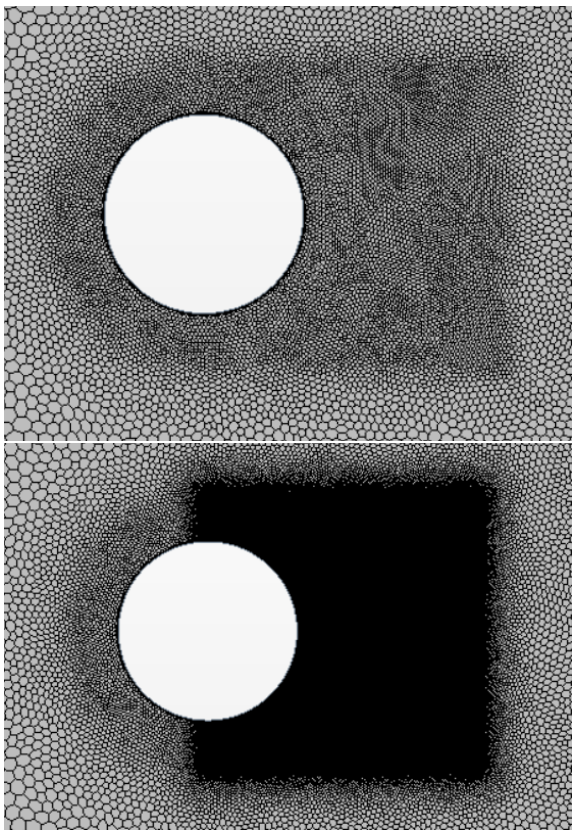

Figure A.15: Mesh comparison of different custom sizes; a) 10%, b) 1%

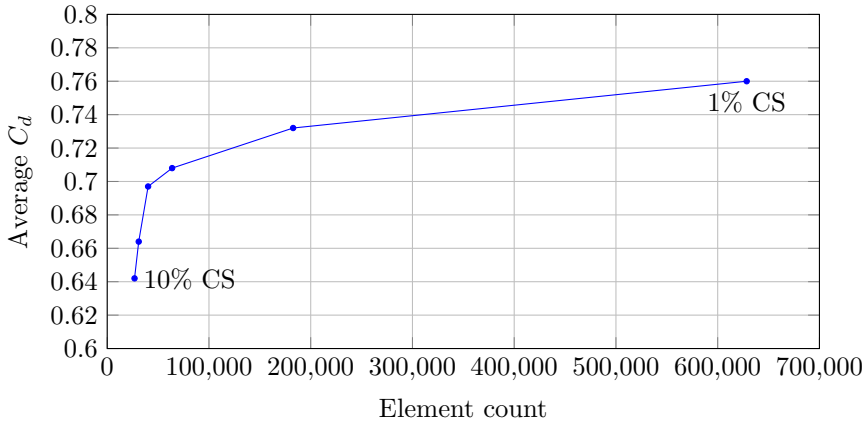

Figure A.16: Average C_d values at various volume control parameters

Wake refinement region

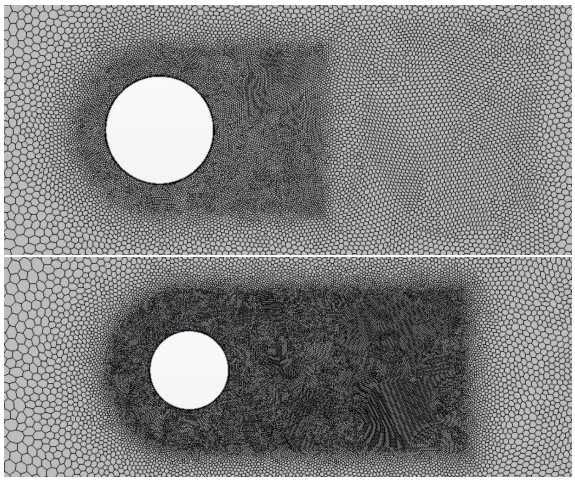

Figure A.17: Mesh comparison of different custom sizes; a) 20%, b) 10%

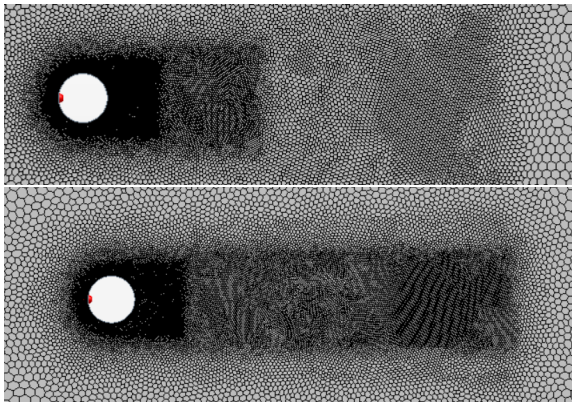

Figure A.18: Mesh comparison of different mesh refinement lengths sizes; a) 3D%, b) 8D%

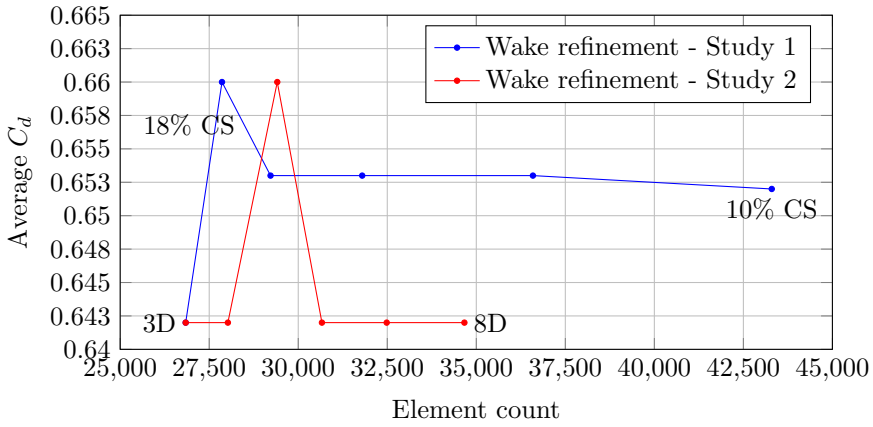

Figure A.19: Average C_d values at wake mesh refinement parameters

A.3 Appendix C

Table A.3: Results of the mesh and inner iteration dependency studies of circular cylinder at Re = 3.6×10^6

Base size [m] (% D_{cyl})	Element count	Inner iterations	f_{vs} [Hz]	Average C_d
0.1 (40%)	27330	25	1.8996	2.076
		40	1.8996	2.045
0.075 (30%)	41217	25	1.8996	2.142
		40	1.7996	2.125
0.0625 (25%)	55657	25	1.8996	2.142
		40	1.8996	2.111
0.05 (20%)	77993	25	1.8996	2.127
		40	1.8996	2.152
0.0375 (15%)	124241	25	1.7996	2.092
		40	1.8996	2.132
		50	1.8996	2.132
0.025 (10%)	251927	25	1.8996	1.962
		40	1.9996	2.038
		50	1.7996	2.095
		60	1.8996	2.116
		70	1.8996	2.119
0.0125 (5%)	895236	40	1.8996	2.039